Polythiophene and Dye Blends for the Photo-electrocatalytic Production of Hydrogen

Chun Hin Ng

Bachelor of Engineering (with Honours)
Bachelor of Science

A thesis submitted for the degree of
Doctor of Philosophy

Monash University,
Department of Materials Science and Engineering

12th August 2015

Copyright Notice

<div align="right">
Chun Hin Ng

12th August 2015
</div>

"There's nothing worse than being lazy..."

Mum

Errata and Addenda

Page 117, para 2, line 4; change "*0.222 V vs SHE*" to "0.207 V vs SHE"

Page 118, Fig. 7; change y-axis units from "$\mu A\ mW^{-1} cm^{-2}$" to "$\mu A\ cm^{-2}$"

Page 220, para 1, line 3; remove "*being*"

Page 222, para 2, line 3; change "*fig S3*" to "fig S4"

Page 113, para 2, line 5; add "in energy" between "*significantly lower...than that*"

Page 118, Fig. 7; add "The catalytic response has been normalised to the photo-intensity (in mW) at each wavelength"

Page 126, para 2, line 3; add "different" between "*slightly...behaviour*"

Abstract

The main finding of this thesis is the discovery of poly(2,2'-bithiophene) (PBTh) as a novel photo-electrocatalyst for the hydrogen evolution reaction (HER). This finding for PBTh is supplemented by studies showing remarkable long term stability, high Faradaic efficiencies, and successful operation over a wide pH range. In-depth mechanistic studies were also conducted and reveal significant insight into the thermodynamic and kinetic mechanism of the PBTh catalyst.

The challenge of tackling climate change requires the rapid development of new technologies for sustainable energy use. To this end, hydrogen shows much promise as an alternative for fossil fuels, however, the absence of an efficient H_2 generation method has thus far limited commercial applications. Significant research has been directed towards the development of new catalysts for the HER though none have yet achieved the desired performance requirements. In this study, we utilise the inherent electrochemical and photo-active properties of conducting polymers to tackle this long-standing problem.

Initial studies on conducting polymer:dye blends were inspired by earlier research but revealed little catalytic activity. Subsequent in-depth characterisation studies allowed the identification of key issues, whilst revealing promising alternative conducting polymer:dye combinations for further investigation; namely, PBTh and Cresol Red. It was eventually discovered that PBTh displayed photo-electrocatalytic activity towards the HER even without the dye component. As a result, research was redirected to focus on pure PBTh to better understand this novel behaviour.

The investigations on PBTh films revealed a range of desirable catalytic properties such as the successful operation in neutral aqueous environments, good stability over 12 days and an onset potential of 0.3 V *below* E^0. The PBTh system also showed significant scope for further improvements which included the threefold increase in the catalytic activity when changing film thickness. This potential for enhancement, together with the inherent desirable catalytic properties, presents PBTh as a particularly exciting photo-electrocatalyst.

In the final part of this study, in-depth mechanistic studies were undertaken to elucidate the chemistry behind the catalytic behaviour. Key findings included the exclusion of iron as a possible contaminant, confirmation of the photo-dependence to the optical properties of PBTh

and assignment of an equivalent circuit to yield insight into the electrical properties of the PBTh electrode. Most importantly, in-situ Raman spectroscopy analysis was able to reveal the formation of an S—H def. band (at $985\,\mathrm{cm}^{-1}$) which confirmed the proposed intermediate state of a PBTh chain protonated at a sulphur atom (PBTh(S-H)$^+$). Subsequent computational studies supported these findings and revealed promising charge transfer states of the excited PBTh(S-H)$^+$ species. A tentative reaction mechanism is thus put forward, though further experimental data is required to confirm the scheme.

The studies presented herein represent the beginnings of the development of PBTh as a photo-electrocatalyst for the HER. These promising initial results have led to the publication of three papers and generated considerable scope for future studies. As it stands, the full potential of the PBTh system has yet to be realised but given the promising performance observed thus far, it is hoped that the eventual optimised system would yield a low-cost and efficient catalyst for the commercial production of H_2.

Acknowledgements

First and foremost, my deepest and most profound thanks to my supervisors, A/Prof. Bjorn Winther-Jensen and Dr C. André Ohlin.

Bjørn, I cannot say how truly grateful I am for your wonderful support, help and guidance for the past three and a half years. Every time I come out of a meeting with you, I am filled with renewed hope and purpose...no matter how fleeting that may be at times. I did not believe it when you first told me, all those years ago, that by the end of the PhD I would know more about my project than you – whether or not that's true – thank you for having that belief and desire for me. Your gentle but steady push to encourage me to seek out science, to think outside the box and to question everything has inspired and shaped me as a researcher and I will take that away with me for life. Moreover, you held me steady when I wavered, gave me lifelines at dead-ends, and allowed me the freedom to explore and find my own path, I truly could not have asked for a better supervisor.

I think the line *"it wasn't an aspirational target – I gave you a deadline"* pretty much sums up our relationship Andy... But in all honesty, your guidance has been phenomenal, even if I didn't appreciate it at the time. Thank you for all your hard work and patience, I realise that as soul crushing as it was for me to see your comments, it must've been just as frustrating and time consuming for you to make them. My publications are a testament to your efforts and I am truly grateful for that. Last but not least, thank you for opening my eyes to a world beyond Windows and MS Office, I have not always embraced your open-sourced madness but even I must admit that they can be ganska jättebra. Until the next time I forget how to compile LaTeX, I will take these skills and treasure them.

I must also mention a big thank you to Doug. Although time on both our parts was often in short supply, I have appreciated the opportunity to work with and learn from you and your group of diverse and talented people. The topics that I have been exposed to has been an insightful and fascinating experience; not to mention the wondrous world of fishkeeping!

To Orawan, thank you for teaching me so much in the lab, I know our research paths did not cross often but even so, you always took the time to help whenever I had questions. Your lessons on care, attention to detail and good note-taking were truly appreciated by this super

forgetful student. Thank you for keeping me from losing my mind when trying to figure out what went wrong.

I also need to thank Vanessa, you were such an integral part in my first year of PhD. My questions and issues were endless and each time, no matter how stressed you were, you would come over and help regardless. And when nothing worked, as it often did, you were always there to commiserate with and offer words of advice. Thank you for giving me perspective and inspiring me to always work harder.

To Bartek, Matt, Dave, Rob, Shravan, Ciaran, Alison, Mega, Matze, Santosh and so many more, you guys made PhD all the more bearable. Whether as someone to vent to, to share ideas, to have a laugh or beers or *winning trivia*! Thank you for all the good times.

Also a special thank you to Edna! I cannot begin to say how appreciative I am of your abilities to just make things happen. Thank you for going above and beyond to make things run so smoothly for all of us.

To my brother and sister who have had to put up with me and my crazy work habits throughout the PhD. I'm sorry for waking you guys up at 2 am while I search for food and all the days which I would steal all the left overs for lunch. Thank you for being so understanding and supportive and proof reading my thesis! I promise to return the favour.

To my mum and 師父

我真的要感謝你和你的功夫。你努力的態度是我的好榜樣,也是我的目標。謝謝你的教導和愛心,成日叫我用『Science』的諗法。我希望我可以令你和爹哋開心。冧師父,阿彌陀佛!我又學業進步了!

To my friends from undergrad and beyond, the 1 o'clock lunch is the only reason I go into uni sometimes. Thank you for keeping me sane with those 1, 1.5...ok, 2 hours of mindless fun and important life lessons; the answer's always 'c', it's always false and the concept of hashing, bubble sorting and pruning trees. I could not think of a nerdier, smarter or more enjoyable group of people.

And last but not least, to my Anna, my rock (who gives me rocks) throughout my PhD and beyond. I don't know how I would have coped without you. Thank you for being a source of joy, wisdom, encouragement and strength...ㄦ愛ㄩ...we made it!

Contents

General Declaration

PART A: General Declaration for thesis based on conjointly published work

In accordance with Monash University Doctorate Regulation 17.2 Doctor of Philosophy and Research Master's regulations the following declarations are made:

I hereby declare that this thesis contains no material which has been accepted for the award of any other degree or diploma at any university or equivalent institution and that, to the best of my knowledge and belief, this thesis contains no material previously published or written by another person, except where due reference is made in the text of the thesis.

This thesis includes 3 original papers published in peer reviewed journals. The core theme of the thesis is the use of "Polythiophene and Dye Blends for the Photo-electrocatalytic Production of Hydrogen". The ideas, development and writing up of all the papers in the thesis were the principal responsibility of myself, the candidate, working within the Department of Materials Science and Engineering under the supervision of A/Prof. Bjorn Winther-Jensen, Dr C. André Ohlin and Prof. Douglas MacFarlane.

The inclusion of co-authors reflects the fact that the work came from active collaboration between researchers and acknowledges input into team-based research. In the case of chapters 3, 4 and 5 my contribution to the work involved the following:

Thesis Chapter	Publication Title	Publication Status	Nature and Extent of Candidate's Contribution
3	Characterisation of a series of tri-arylmethane dyes as light harvesters for photo-electrochemical systems	Published	All experimental work, analysis of the results and writing of the manuscript
4	Photo-electrocatalytic H_2 evolution on poly(2,2'-bithiophene) at neutral pH	Published	Experimentation and analysis on the catalyst film and writing of the manuscript
5	Exploration and optimisation of poly(2,2'-bithiophene) as a stable photo-electrocatalyst for hydrogen production	Published	All experimental and analytical work into the nature of the films, writing of the manuscript

I have not renumbered sections of submitted or published papers in order to generate a consistent presentation within the thesis.

Signed:

Date:

Nomenclature

ΔE_{CV} Electrochemical band gap

ΔE_{opt} Optical band gap

ΔG Gibbs free energy

η Overpotential

h^+ Hole

TiO_2 Titanium Dioxide

Acn   Acetonitrile

Ag/AgCl   Silver Chloride Electrode

Brilliant Blue   Coomassie Brilliant Blue G250

CA   Chronoamperometery

CB   Conduction Band

CdS   Cadmium Sulphide

CE   Counter Electrode

COSMO   Conductor-like Screening Model

CPE   Constant Phase Element

CV   Cyclic Voltammetry

DCM   Dichloromethane

DFT   Density Functional Theory

DSSC   Dye Sensitised Solar Cell

E_g Electronic Band Gap

E_{onset} Onset Potential

E_{ox} Oxidation potential

E_{red} Reduction potential

E_{we} Working Electrode Potential

ECCE   Extensible Computational Chemistry Environment

EDTA   Ethyldiaminetetraacetic Acid

EDX   Energy Dispersive X-ray Spectroscopy

EF   Excimer Fluorescence

EIS   Electrical Impedance Spectroscopy

ESP   Electrostatic Potential

Fl   Fluorescence

FTO   Fluorine-doped Tin Oxide

GC   Gas Chromatography

HER   Hydrogen Evolution Reaction

HOMO   Highest Occupied Molecular Orbital

HPLC   High Pressure Liquid Chromatography

IC   Internal Conversion

ICP   Intrinsically Conducting Polymer

LUMO   Lowest Unoccupied Molecular Orbital

MS   Mass Spectroscopy

NHE   Normal Hydrogen Electrode

OLED   Organic Light-emitting Diode

OPV   Organic Photovoltaic Cell

ORR   Oxygen Reduction Reaction

P3HT   Poly(3-hexylthiophene)

PB   Phosphate Buffer

PBTh   Poly(2,2'-bithiophene)

$PBTh(C_\beta\text{-H})^+$ Protonated PBTh at the β-carbon

$PBTh(C\text{-H})^+$ Protonated PBTh at the α-carbon

$PBTh(S\text{-H})^+$ Protonated PBTh at the sulphur

PC   Propylene Carbonate

PCBM   Phenyl-C61-butyric-acid-methyl Ester

PEDOT   Poly(3,4-ethylenedioxythiophene)

PEM   Proton Exchange Membrane

PTSa   Para-toluene Sulphonic Acid

PTTh   poly(2,2':5',2"-terthiophene)

RE   Reference Electrode

RGO   Reduced Graphene Oxide

RHE   Reversible Hydrogen Electrode

rr-P3HT   Regioregular-Poly(3-hexylthiophene-2,5-diyl)

S_0 Singlet Ground State

SCE   Saturated Calomel Electrode

SEM   Scanning Electron Microscopy

SHE   Standard Hydrogen Electrode

SiC   Silicon Carbide

T_1 Triplet State

TD-DFT   Time Dependent Density Functional Theory

TEOA   Triethanolamine

TOF   Turn-Over-Frequency

TON   Turnover Number

VB   Valence Band

VPP   Vapour Phase Polymerisation

WE   Working Electrode

Z   Impedance

Z_{Im} Imaginary Impedance

Z_{Re} Real Impedance

ZPE   Zero-point Energy

Note on References

Due to the use of individual chapter bibliographies and the inclusion of publications in this thesis, some references may be listed more than once with different reference numbers between each chapter.

Chapter 1

Introduction and Literature Review

1.1   General Context

The Fifth Assessment Group from the International Panel on Climate Change considers the warming of our planet as "unequivocal" and would require "substantial and sustained reductions of greenhouse gas emissions" to avoid dangerous climate change.[1] In light of this, hydrogen has been proposed in recent decades as a zero-carbon energy medium for a variety of applications which range from replacing petrol in transportation, batteries in energy storage and coal/gas in power generation.[2] In particular, H_2 can be used in conjunction with intermittent renewable energy sources such as wind and solar to store energy (when in excess) and supply electricity (when inactive), thus forming a strong partnership that harnesses the strengths of both technologies.[3] As a result, hydrogen power has seen significant developments in both research and industry.[4]

Despite the promising potential of H_2, widespread commercial use has been hindered, amongst other things, by the lack of a sustainable hydrogen production method.[5] The current fossil fuel based approach using the steam methane reformation process is effective and low cost but ultimately runs counter to achieving a carbon neutral energy economy.[6] Of the alternative production techniques, electrolysis is perhaps the most established. First discovered in 1800 by Nicholson and Carlisle,[7] it was found that the passing of a voltage between two immersed electrodes was able to split water via the electrochemical reaction: $2\,H_2O \longrightarrow 2\,H_2 + O_2$ (see Figure 1.1).

Overall
$2H_2O \rightarrow 2H_2 + O_2$

Reduction   **Oxidation**
$2H^+ + 2e^- \rightarrow H_2$ **$2H_2O \rightarrow O_2 + 4H^+ + 4e^-$**

H_2O

Cathode   Anode
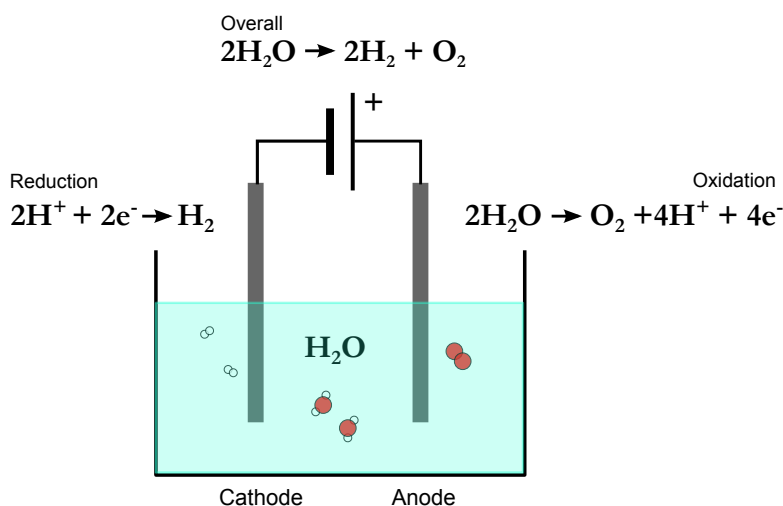
Figure 1.1: Electrolysis of water. A voltage is applied across two electrodes, splitting water into its elemental constituents (hydrogen and oxygen) via electrochemical reaction.

Currently, the majority of commercial electrolysers are limited to the small scale with operational capacities between 0.1 kg to 1000 kg per day[5,8] and is insufficient for industrial applications. This is a direct result of several factors and include the use of expensive catalyst materials (such at Pt), the requirements of harsh chemical environments and the limited access to cheap renewable energy resources.[9]

To address some of these shortcomings — primarily the use of platinum — this project builds on work carried out by the Winther-Jensen group on intrinsically conducting polymers (ICP) as a catalytic electrode material.[10] The principle reaction investigated is the reduction half-reaction, also known as the hydrogen evolution reaction (HER) (see Eq 1.1); the E^0 of this reaction is commonly listed as 0 V vs SHE but is dependent on pH via the Nernst equation (Eq 1.2).

$$2\,H^+ + 2\,e^- \longrightarrow H_2 \tag{1.1}$$

$$E_{H^+/H_2} = E^0_{H^+/H_2} + \frac{RT}{nF} \ln \frac{[H^+]^2}{P_{H_2}} \tag{1.2}$$

In current electrolysers, platinum electrodes are used for the HER due to their excellent performance, but the rarity of Pt renders them prohibitively expensive for industrial applications.[11] As such, alternative, platinum-free catalysts for the HER have been heavily investigated in recent decades. Unfortunately, these catalysts have their own failings and include instability, the requirement of acidic or organic electrolytes, the addition of sacrificial electron donors and significantly higher activation energies.

This project builds on previous findings, where blends of PEDOT:PEG were able to successfully electrochemically catalyse the production of hydrogen (Figure 1.2).[10] By expanding on this concept, this study attempts to address some of the key issues of the HER catalysis by examining the novel idea of embedding dyes into conducting polymers to form a photo-active blend; thereby reducing the total energy requirements for the HER. While the role of each component has been successfully applied in their respective fields – dyes as light harvesters and ICPs as conductive substrates – their combination may prove to be a unique solution to this long-standing problem. Supported by computational simulations, we explore the multiple facets in the design of this electrode system including its feasibility, selection of materials, operating parameters and the working mechanics.
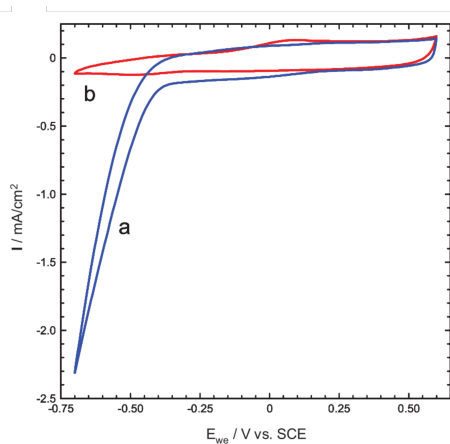
Figure 1.2: The catalytic activity of a PEDOT:PEG blend (blue) compared to a PE-DOT:polymethylvinylether blend (red), in $1\,\text{mol}\,\text{L}^{-1}$ H_2SO_4 at $5\,\text{mV}\,\text{s}^{-1}$ on Ti foil.[10]

Literature Review

The overall scope of the project encompasses several fields, key of which is the area of water electrolysis. However, as a multicomponent electrode, concepts and hence literature is also drawn from the fields of dye sensitised solar cells (DSSC), organic photovoltaics, computational chemistry and conducting polymers. The following literature review will hence highlight key developments in the aforementioned fields and their relationship to the focus of this project: the investigation of light enhanced conducting polymer:dye blends for the HER.

1.2   Overview of Electrolysis

1.2.1   History of Electrolysis

The history of electrolysis began in the early 1800's and its potential to provide energy was recognised as early as 1874 by Jules Verne where he predicted that "water will be the coal of the future".[12] The first commercial electrolysers — a device that splits water into hydrogen and oxygen via electricity — were built in 1902[13] and they provided hydrogen for the majority of the early 20th century. However as demand continued to increase, the cheaper steam methane reformation process eventually superseded electrolysis and remains the main source of hydrogen today.[14]

Nonetheless, development on electrolysis and electrolysers continued. Key milestones included the commercialisation of pressurised electrolysers (1951), the discovery and use of Raney Nickel electrodes (1957), and the development of both the solid polymer electrolyte electrolyser (1966) and the solid oxide electrolysis cell (1972). The Oil Crisis of 1973 and the growing recognition of man's environmental impact has since stimulated research. However, despite steady advancements, long standing issues such the use of platinum, corrosive operating conditions and limited access to cheap renewable energy still remain.[15,16]

1.2.2   Proton Exchange Membrane Electrolysers

Of the aforementioned breakthroughs, the development of the proton exchange membrane (PEM) electrolyser was perhaps the most influential. This was the direct result of General Electric's work in developing a fuel cell for the Gemini space program[17] and brought numerous advantages over the earlier alkaline type electrolysers. While the operation of a PEM electrolyser (Figure 1.3) remains reliant on the same basic chemical reactions, the use of a solid proton conducting polymer membrane (eg: Nafion)[13,18] altered the operational conditions significantly. The net result is an electrolyser that is capable of fast start up/response times and higher current densities, traits which synergise well with the intermittency of renewable resources.[5] The PEM electrolyser also eliminates the various issues associated with the use of concentrated alkaline solutions and allows for a very robust and low maintenance electrolysis system.[16,19,20]
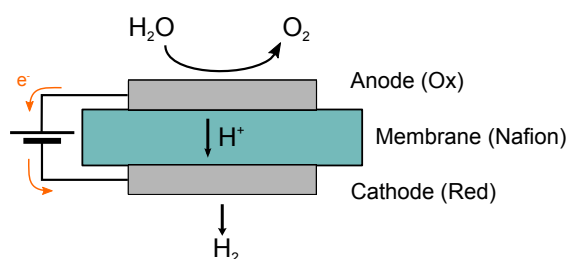
Figure 1.3: Schematic of a PEM electrolysis cell

As a result of their advantages, PEM electrolysers have been successfully commercialised since the 1990's.[20–23] Unfortunately, their reliance on the rare and expensive platinum group metals such as iridium, ruthenium and platinum have restricted their applications to small scale and specialised situations. However, as interest grew around the shift to a hydrogen economy,[2, 24–26] the research and development of cheaper and more efficient catalytic electrodes for electrolysis gained momentum.

1.3 Alternative Electrochemical Catalysts

An effective HER catalyst requires a balance between proton adsorption and H_2 release. It needs to bind H^+ strongly enough to enable their adsorption and subsequent reaction on the catalyst surface, but not so strongly that it is unable to release the produced H_2 gas.[27] This is the underlying reason for the high performances of platinum and biological catalysts such as Hydrogenase and Nitrogenase as they strike the correct balance for H_2 formation (where $\Delta G_H \approx 0$).[28] This is phenomenon is illustrated in Figure 1.4. The same figure also shows how materials that require substantial energies to bind H^+ such as Au, or to release the H_2 such as Ni, Mo, are not efficient catalysts.[29]
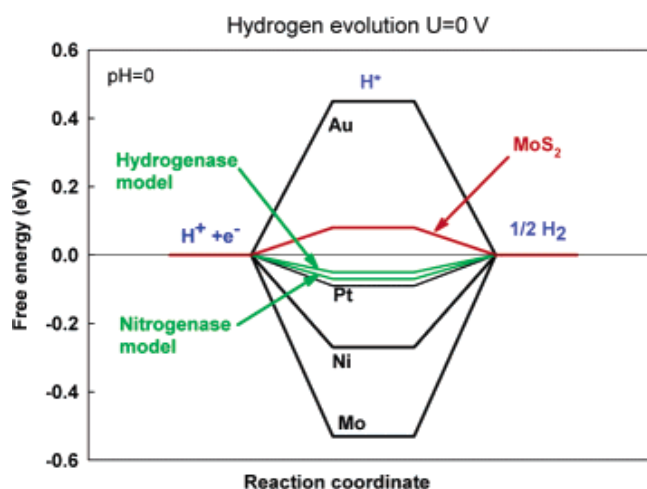
Figure 1.4: Free energy diagram for H_2 evolution calculated by Hinnemann *et al.*, the most successful catalysts have a free energy close to zero for easy adsorption and desorption of H_2[29]
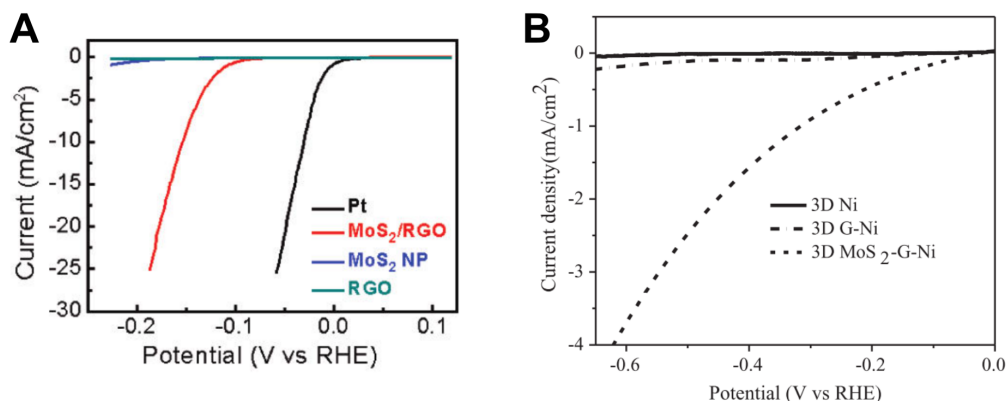
Figure 1.5: Cyclic voltammetry (CV) showing the performance of MoS_2 catalysts. **A:** Comparison of the MoS_2 catalyst on reduced graphene oxide (RGO) and solution grown MoS_2 nanoparticles (NP) to a commercial platinum catalyst.[35] **B:** The catalytic performance of MoS_2 deposited on a graphene-Ni network in $0.1\,mol\,L^{-1}$ KOH, pH 14.[38]

1.3.1 Molybdenum Sulphides (MoS_2)

Researchers at the Technical University of Denmark recognised this energy requirement and used computational techniques to identify MoS_2 as a potential electrode material.[29,30] Since then, research has continued on investigating and developing MoS_2 and related sulphides such as WS_2.[31,32] These include the identification of the active edge sites,[33] structure modifications to improve conductivity and active sites[34] and the synthesis of MoS_2 on reduced graphene oxide (RGO)[35] (Figure 1.5A) and carbon nanospheres[36] to increase catalytic surface area. More recent work includes the development of $[Mo_3S_{13}]^{2-}$ nanoclusters with excellent HER activity,[37] as well as the ability to perform the HER in extreme alkaline conditions using MoS_2 (on graphene-nickel 3D stuctures), see Figure 1.5B.[38]

Interest with these catalysts have been significant as both molybdenum (USD 25.5 per kg) and tungsten (USD 63.9 per kg) are non-precious metals that are far cheaper and more abundant than platinum (USD 45 800 per kg).[39] However, outstanding issues remain and include the lack of long term testing, the absence of photo-activity for the HER (thus requiring higher electrochemical potentials) and the requirement of nanoparticles with a high number of edge sites for good catalytic activity.[31]   Nevertheless, MoS_2 is a promising candidate as a low cost catalyst for the HER with significant scope for further developments.[40]

1.3.2 Biological and Bio-Inspired Approaches

Other approaches take inspiration from naturally occurring enzymes such as hydrogenase and nitrogenase to catalyse the HER (Figure 1.6). In nature, these enzymes are vital for anaerobic metabolism and are responsible for driving the reduction reactions of carbon dioxide, sulphate,
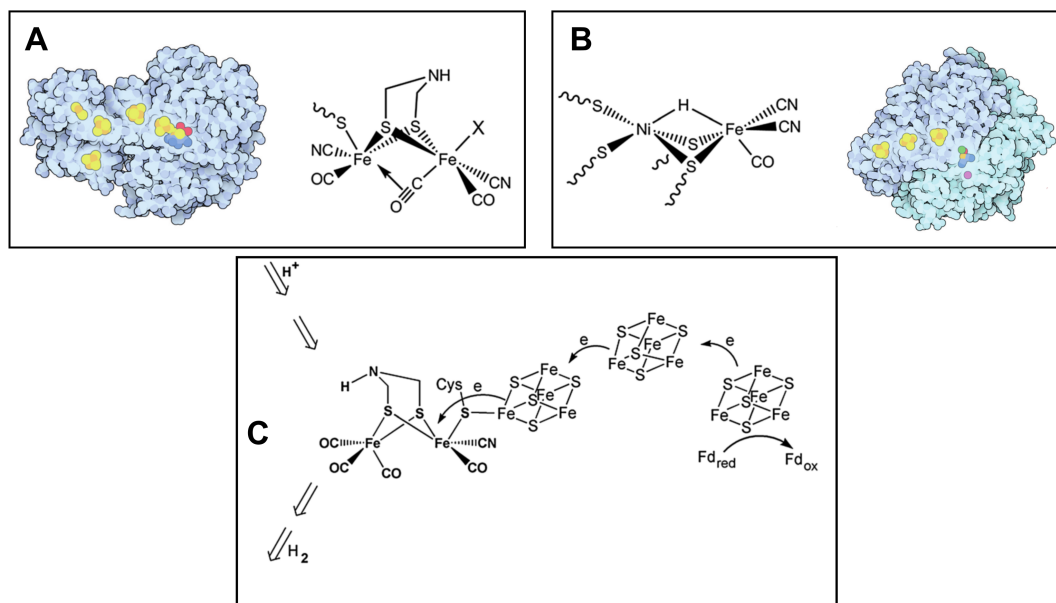
Figure 1.6: The catalytic metal centre of the [FeFe]- and [NiFe]-hydrogenase in **A** and **B** respectively. A cartoon representation of the hydrogenase enzyme is also included, showing the [Fe-S] clusters that transport electrons from the ferredoxin redox mediator (F_d) to the catalytic centre. A schematic of this process is presented in **C** for the [FeFe]-hydrogenase.[11,43]

nitrate *etc.* via the reversible reaction $2\,H^+ + 2\,e^- \rightleftharpoons H_2$.[41] Like MoS_2, these enzymes follow the same reaction thermodynamics where the free energy the HER is close to 0 – see Figure 1.4 – and possess performances on par with platinum.[42] Because of their high reactivity, investigation into [NiFe]- and [FeFe]-hydrogenases and the development of a synthetic analogue has been an area of rapid development.[11]

One approach taken is the incorporation of enzymes into various substrates to harness their catalytic activity. A direct adsorption approach has been trialled[44,45] and while useful for fundamental electrochemical study, the enzyme was found to be unstable and unsuitable for commercial purposes.[46] Stability was improved with the entrapment of hydrogenase by viologen containing polypyrrole films on carbon electrodes, which allowed for hydrogen evolution and uptake.[47,48] Other methods include the covalent grafting of hydrogenase onto functionalised carbon electrodes and nanorods, and has demonstrated sustained catalytic current for over a week.[49,50] However, these investigations have focused on hydrogen oxidation (not the HER) primarily due to the use of [NiFe]-hydrogenase which are more robust under aerobic conditions but display a lower activity for hydrogen evolution.[51]

In general, while the use of hydrogenase present an intriguing method for the production of H_2, it is difficult to achieve due to their instability. [FeFe]-hydrogenases present the most promising potential but they tend to degrade when exposed to O_2, on the other hand, [NiFe]-hydrogenases are more stable in air but have much lower activities.[46] It is also possible to biologically produce hydrogen using microbes such as cyanobacteria that contain the hydrogenase enzyme.[52]

However, its implementation is non-trivial due to (once again) sensitivity to oxygen and the need to regenerate the redox mediator (ferredoxin) through processes such as respiration or nitrogen fixing.[52,53] In conclusion, though the use of enzymes in a "bio-hybrid" type catalyst could reveal excellent information on the mechanisms for the HER, it has been identified that a more likely breakthrough would be with "bio-inspired" catalysts.[54]

1.3.3 Metal Complexes

The use of metal complexes represent a significant area of research and development due to their facile redox reactions and options for customisability using ligands. Moreover, their vital role as the active site in biological enzymes have resulted in a large range of bio-inspired catalysts showing promising performance without the inherent instability of the enzyme. An overview of some of these promising metallic complexes with iron, nickel, molybdenum and cobalt metal centres are described below.[55–59]

Iron (Bio-mimics)

Interest in Fe catalytic centres are in a large part due to their presence in the active site of hydrogenase, and as such, many of these complexes contain a di-iron [FeFe] centre. Initial studies of a simple diiron dithiolate complex showed poor catalytic performance[60,61] though the addition of proton relay sites were able to significantly bring down the required overpotentials.[11,62] However, for many of the [FeFe] catalysts, strong acids and organic solvents are still required and overpotentials remain high.[11,55] Research has since continued with developments including the use of diphosphine ligands,[63,64] the move to mononuclear iron species[65] and the development of unsaturated, pentacoordinate iron complexes.[64,66,67] Despite these developments, catalysis performance on par with that of biological systems have remained elusive and the instability, low water solubility and high overpotentials of these catalysts remain problematic.

Nickel

Similar to Fe, Ni is also found in the catalytic centre of hydrogenase and has promising potential for the HER catalysis. One such bio-inspired example is the nickel bisdiphosphine (NiP_4) catalyst family developed by DuBois *et al.*[68–70] These combine the functional features of both [NiFe]- and [FeFe]-hydrogenases and have resulted in impressive catalytic capabilities which include a turn-over-frequency (TOF) of over $100\,000\,s^{-1}$ using a NiP_4 complex, see Figure 1.7.[71] Strong acidic conditions, organic solvents and a sacrificial proton donor was still required but importantly, it revealed the critical role of pendant amines and their role as proton relays.[11,71] A large body of research has since further improved the NiP_4 catalysts and
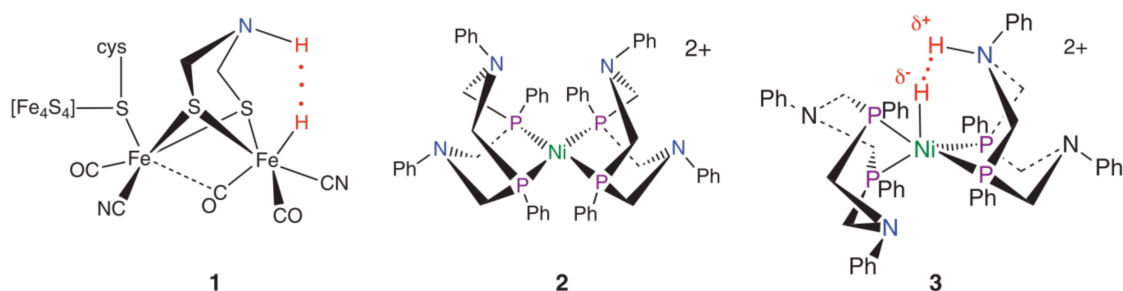
Figure 1.7: (1) The [FeFe]-hydrogenase centre. (2) The NiP_4 catalyst developed by DuBois *et al.* for H_2 production. (3) Proposed transition state of the NiP_4 during H_2 production; (1) and (3) show the role of the pendant amine group as a proton relay.[71]

include an increased stability in aqueous environments, enhanced catalytic activity as well as an improved understanding of the system.[72–78]

Molybdenum

Moving away from enzymes and their bio-mimic centres, other catalysts have taken inspiration from the activity of MoS_2 with the use a molybdenum centre. These include the related $[Mo_3S_4]^{4+}$ cubane-type cluster where a similar catalysis performance was observed (Fig. 1.8A, B);[31,79] it is particularly interesting as the molecular nature lends itself to further functionalisation. Molybdenum-oxo catalysts have also demonstrated significant catalytic activity in aqueous solutions and a neutral pH (Figure 1.8C, D);[56,57] this is particularly noteworthy due to its potential for use in electrolysers without the need for sacrificial additives, exotic media or harsh chemical environments. Subsequent studies based on the Mo-oxo complex was able to realise a MoS_2 mimic showing impressive catalytic HER performance in aqueous (acidic) electrolyte.[80]
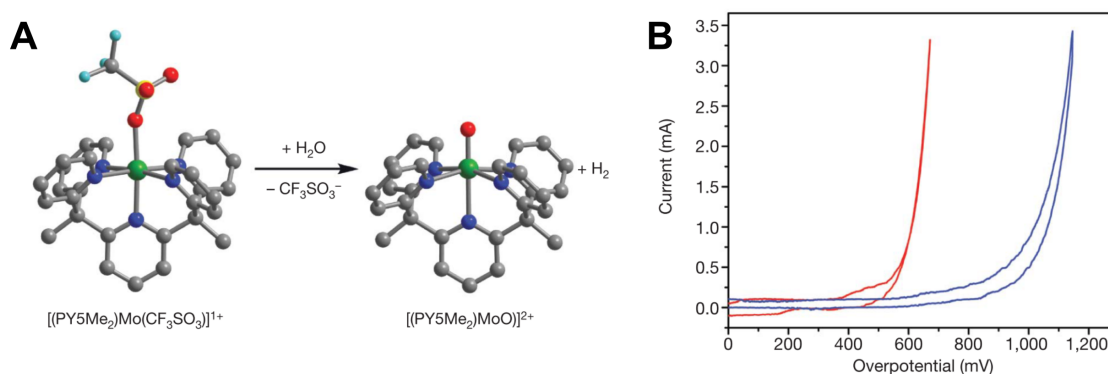
Figure 1.8: A: The molybdenum-oxo catalyst and the reaction to produce H_2, and **B:** its performance ($7.7\,\mu mol\,L^{-1}$, red trace) as shown by CV in a $0.6\,mol\,L^{-1}$ phosphate buffer at pH 7, $50\,mV\,s^{-1}$;[56] the neat background is shown in the blue trace. Cathodic current is being presented here in positive values.

Cobalt

Cobalt is another very commonly used catalytic centre and cobaloxime complexes have been shown to exhibit very low overpotentials with high turnover rates.[55] Unfortunately, they require organic solvents or acidic environments for optimal performance[81–83] and these conditions are typically avoided for industrial processes (where possible). Nonetheless, more recent studies on cobaloximes have shown electrochemical HER activity in aqueous solutions with promising scope for further improvements.[84–86] Cobalt polypyridyls are another promising catalyst where advances have progressed from initial studies in organic media,[87] to catalysis in H_2O,[88] to the incorporation of photo-sensitizers.[89] They are not without limitations which include the need for sacrificial electron donors and the use of significant overpotentials (>0.3 V). Nevertheless, developments are continuing on these highly tunable Co systems (Figure 1.9), key of which include the incorporation of photo-active components and these are further discussed below in Section 1.4.
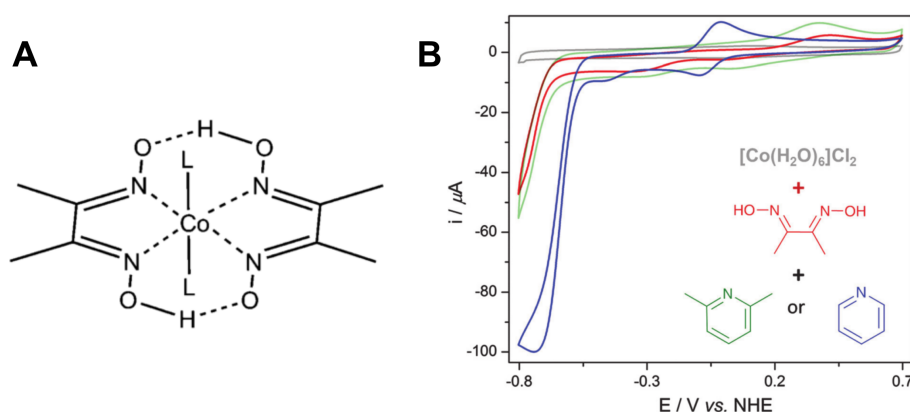
Figure 1.9: A: The general structure of cobaloxime showing the two axial sites (L) for attachment of ligand and reaction with H^+. **B:** CVs showing how the catalytic performance of cobaloxime changes with different ligands; conducted in 0.1 mol L^{-1} phosphate buffer, pH 7 at 100 mV s^{-1}.[85]

1.3.4 Nickel Electrodes

Nickel electrodes in the form of Ni foam has been used in alkaline electrolysers for their low cost and high surface area[90] though they suffer from deactivation under the strong alkaline conditions.[20] Numerous techniques have been trialled for improving catalytic lifetime and these include the development of alloys,[91,92] the addition of an iron coating[93] and adding dissolved vanadium.[94] Promising results have also been obtained for modified $Ni(OH)_2$ electrodes where they show a four-fold increase in catalytic activity over plain nickel (Figure 1.20) and substantially better performance than other 3d metal hydroxides (Co, Mn and Fe).[95–97]
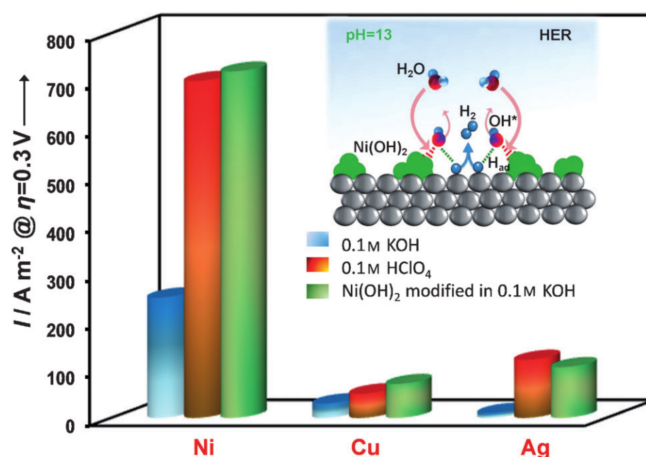
Figure 1.10: A comparison of the HER performance of Ni, Cu, Ag metal electrodes in different electrolytes and with the Ni(OH)$_2$ modification. The activities reported were taken from the first polarisation curve at an overpotential of 0.3 V.[97]

Despite their promising performance, these nickel based electrodes are optimised for alkaline electrolysers. While they are a potential solution for sustainable hydrogen production, they have numerous other issues that include high overpotentials, insufficient charge transport and gas bubble resistance.[20,98]

Summary of Electrochemical Catalysts

Despite the development of numerous promising electrodes and catalysts, research thus far has yet to produce an ideal alternative for platinum. An inherent problem of electrocatalytic materials is that they can only operate with the application of a potential, an issue that requires cheap renewable energy in order to achieve the goal of environmentally sustainable hydrogen production. Furthermore, even the most efficient electrochemical catalysts cannot catalyse the HER below the theoretical value of E^0. These combined factors have resulted in the investigation and development of photo-electrocatalysis, where light is harnessed to help drive the electrolysis reaction.

1.4 Light Enhanced Electrodes

The development of a photo-driven or a photo-enhanced-electrochemical electrode for electrolysis is not a new idea. Its roots can be traced to the early 70's when Fujishima and Honda first reported the evolution of hydrogen and oxygen from their titanium dioxide (TiO$_2$) electrode with the illumination of UV light.[99] While the need for UV light proved too impractical for commercial use, the idea spawned a new way of addressing the catalysis problem. Here, a
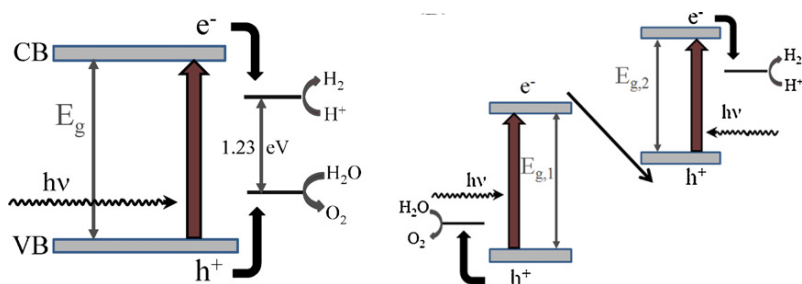
Figure 1.11: Left: The ideal band structure of a photodriven semi-conductor system for water splitting . **Right:** A multi-component system used for the same reaction. In both cases, conduction and valence bands must be positioned correctly for electron injection and withdrawal respectively.[104]

range of different photo-catalytic systems using a variety of light-harvesting and chemical mechanisms are described; some are completely photo-driven while others require an application of electrochemical potential.

1.4.1 Semi-Conductors

The principles behind a light-driven electrode rely on the correct positioning of each component's electronic band energy structure, see Figure 1.11. Various semi-conductor based materials satisfy this criteria and include TiO_2, cadmium sulphide (CdS) and silicon carbide (SiC) .[100–102] There are however, several issues to this semi-conductor approach, and include photo-corrosion, fast recombination of electron/hole pairs and the inability to harness light from the visible spectrum.[103] Thus, the realisation of a successful semi-conductor photo-catalyst is not trivial, though various materials have shown promise and they are presented below.

TiO_2 is a prime candidate due to its abundance and stability. However, its large band gap (3.2 eV)[100] prevents the material from harnessing lower energy photons and it is thus unable to utilise a significant portion of the solar energy spectrum. To counter this, some groups have attempted to narrow the TiO_2 bandgap using methods such as the doping of TiO_2 with anions[100] and modification with carbon atoms via controlled combustion.[102] While yielding promising initial results, the anion doped electrode has so far only demonstrated the successful photo-decomposition of various organic molecules while the combustion modified TiO_2 requires further investigation to increase photo-conversion efficiency (see Figure 1.12).[105] A part of this issue is the short hole lifetime where recombination of the photo-excited electron/hole pair occurs before oxidation of H_2O.[106]

Cadmium sulphide is another much investigated semi-conducting material since it has a smaller band gap of 2.4 eV. This allows it to both harness photons from the visible spectrum and still have the appropriate conduction and valence band energies to split water.[107] Unfortunately, CdS suffers from photo-corrosion via the reaction, Eq 1.3. Approaches to counter this include
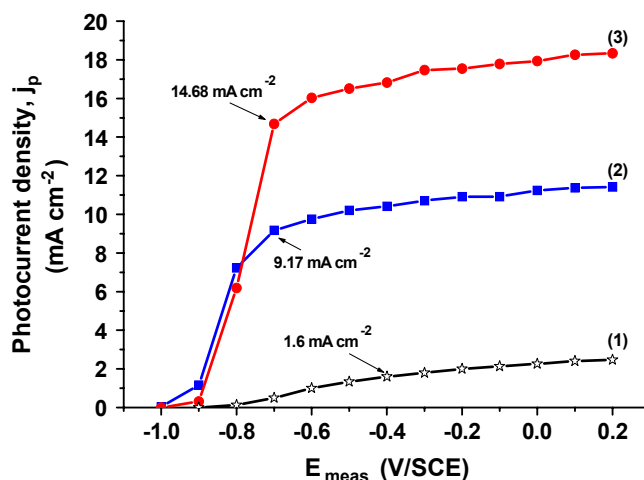
Figure 1.12: Photocurrent density (j_p) of various TiO_2 electrodes as a function of measured potential; Unmodified TiO_2 (1), TiO_2 modified by thermal flame oxidation (2) and TiO_2 modified by spray flame (3). Illumination was provided by a white light with intensity of $100 \, mW \, cm^{-2}$.[105]

the addition of sacrificial species such as EDTA and S^{2-}/SO_3^{2-} to scavenge valence band holes.[108,109] Other approaches such as platinization and the use of Nafion has also met with some success though the overall requirement for sacrificial additives currently hold back the commercialisation of CdS based photo-catalysts.[107,110]

$$CdS + 2\,h_{vb}^+ \longrightarrow Cd^{2+} + S \tag{1.3}$$

More exotic semiconductors are have also demonstrated photo-catalytic activity and include TaON,[111] $Y_2Ta_2O_5N_2$,[112] $(Zn_{(1+x)}Ge)(N_2O_x)$,[113] and $Sm_2Ti_2S_2O_5$.[114] Despite their ability for photodriven water splitting, their complicated synthesis techniques, use of sacrificial donors/acceptors and reliance on Ru, Ir, and Pt particles currently limit their application to laboratory work and development.

1.4.2 Biological Photo-systems

The addition of a photosensitiser for light driven catalysis has been used as a way to expand the capabilities of bio-catalysts; previously mentioned in Section 1.3.2. Approaches have utilised both biological and synthetic components and include novel ideas such as the joining of Photosystem I to hydrogenase (or platinum) via a "molecular wire".[115] A similar approach conducted by Krassen *et al.* combines a modified subunit of Photosystem I from *Synechocystis* with [NiFe]-hydrogenase into a hybrid complex capable of light-induced hydrogen evolution; albeit at the low rate of 10^{-10} moles per second.[116] Other new ideas include the coupling of
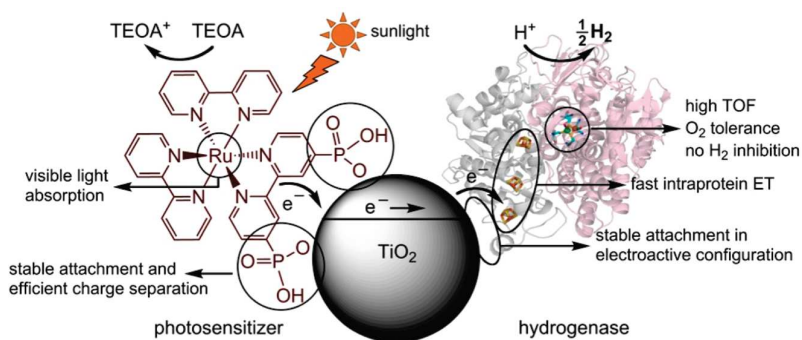
Figure 1.13: Representation of the enzyme-TiO$_2$ hybrid system with photosensitiser developed by Armstrong *et al.* Aspects that are desirable for H$_2$ production are shown.[117]

hydrogenase directly to a Ru dye-sensitised TiO$_2$ photosystem (Figure 1.13). Impressive turn-over-frequencies of up to 50 mol H$_2$ s^{-1} (mol enzyme)$^{-1}$ were shown for the system although it suffers from photo-instability.[46, 117]

1.4.3 Chemical Photo-systems

Heterogeneous Catalysis

Chemical H$_2$ evolution catalysts have also been adapted for photo-enhancement, common methods include the attachment of dyes, incorporation onto semiconductors and use of other photosensitisers. Simple systems combining catalysts and semiconductors/dyes have been investigated since the mid 1980's where a combination of p-type silicon and [1.1]ferrocenophane achieved H$_2$ evolution under illumination with a 300 mV underpotential.[118] Developments since then have progressively moved towards aqueous and more neutral environments and include the work of Nann, Pickett *et al.*, where a nano-photocathode system was reported to achieve a photo-*electro*chemical efficiency of over 60% (potential was applied).[119] Their system, based on a [FeFe]-hydrogenase analogue and a network of crosslinked indium phosphide, was able to produce H$_2$ at an applied potential of -400 mV vs Ag/AgCl in a neutral aqueous solution (Figure 1.14). This corresponds to an underpotential of *ca* 200 mV and is a significant step in the development of an efficient photo-elelctrocatalyst; though it should be mentioned that currents remain very poor.

Other studies have combined CdS with a molecular Ni-complex[120] and a MoS$_2$-polyaniline composite[121] to produce successful photo-catalytic systems. More exotic hybrid combinations using CdSe/ZnS quantum dots with cobaloxime catalysts have resulted in high turnover numbers (TON) with respect to the photocatalytic generation of H$_2$.[122] The molecular [Mo$_3$S$_4$]$^{4+}$ catalyst has also lent itself to be incorporated into photo-active materials such as NaTaO$_3$[123] and silicon[124] to photo-catalytically produce H$_2$. Key issues that remain for these photo-systems
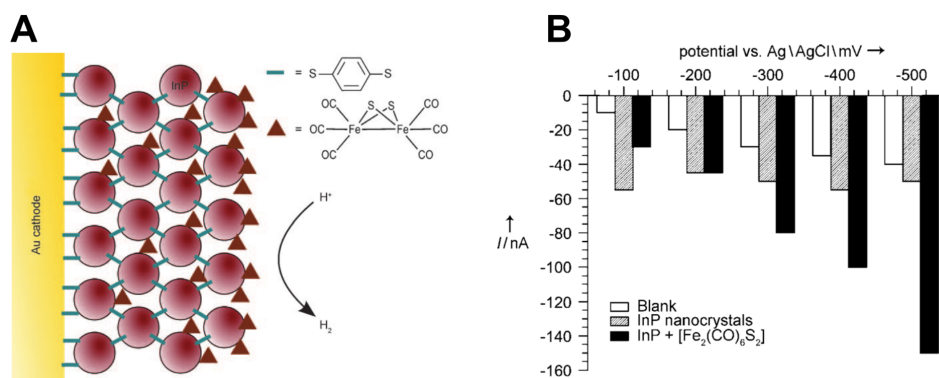
Figure 1.14: The nano-photocathode system developed by Nann, Pickett *et al.* **A:** Schematic cross-section diagram of the photo-system showing the InP nanocrystal modified gold cathode and adsorbed $[Fe_2S_2(CO)_6]$ catalyst. **(Right)** Comparison of the photocurrent responses of various electrodes at different bias potentials.[119]

however, include the need for sacrificial electron donors such as triethylamine, strong acidic environments and the absence of long-term testing.

Homogeneous Catalysis

Homogeneous catalysis is another approach investigated with interest centred on the development of non-precious metal based photo-catalysis.[125] Examples of such research include the bio-inspired supramolecular photocatalyst created by Sun *et al.*[126] and involves the non-covalent assembly of a metalloporphyrin to an iron hydrogenase active site mimic (Figure 1.15 left). While the TON is low (0.2) it is attractive due to the lack of noble metals and the use of bio-inspired molecules.[125] Nickel catalysts have also been investigated with one such example reporting the photo-driven production of H_2 with a high TON of 7300, though again, requires a sacrificial electron donor.[72, 127]

Photo-catalysis on cobalt based complexes have also been investigated and include the attachment of cyclometalated iridium and ruthenium photosensitisers to cobaloxime catalysts.[128–130] One such photo-catalyst is shown in Figure 1.15 (right), and was able to achieve quantum yield values of 16% with high TOF ($50\,h^{-1}$) and moderate stability (TON $= 273$). Studies have since continued to increase TON, reaction rates, quantum efficiency, pH performance and operation in pure aqueous environments, nonetheless there is the need for further improvements.[131]

There are numerous other catalysts for the homogeneous photo-driven production of H_2 and their molecular nature helps to reveal much about the photo- and chemical properties required for the HER.[125, 132, 133] However, this nature also means that it is difficult to regenerate the photo-catalyst without sacrificial additives and could potentially hinder large scale production.
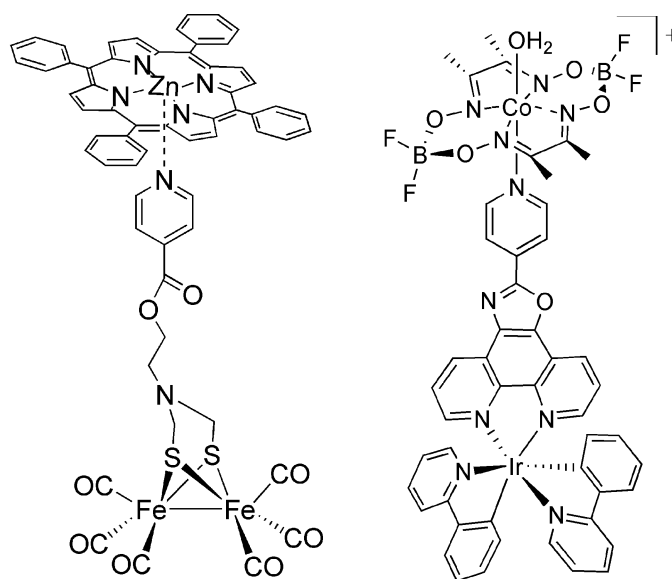
Figure 1.15: Structures of molecular photocatalysts showing catalyst and photosensitiser.[125] **Left:** Bio-inspired di-iron active catalyst with porphyrin photosensitiser and **Right:** a cobaloxime catalyst with iridium photosensitiser.

Summary of Photo-catlysts

Harnessing light for the HER and water splitting is a promising and energy efficient method in which to produce hydrogen. Yet, despite work progressing along numerous fields, an ideal photo-system for the production of hydrogen has yet to be realised. The key hurdles vary for each photo-catalyst though commonly encountered issues include, the reliance on rare-earth metals, the need for sacrificial donors, difficulties in aqueous environments, low H_2 evolution rates and low stability.[134, 135]

Some of these issues can be addressed through the use of hybrid photo-electrochemical systems where the light harvesting mechanism from a conventional solar cell (Si, DSSC, perovskite *etc.*) is used to drive a matched electrochemical catalyst.[46, 90, 134, 136] These systems can eliminate the need for sacrificial donors as charges can be balanced/regenerated by the redox reactions on the counter electrode. On the other hand, the incorporation and successful catalytic interaction of two different systems can be problematic and their overall usefulness remains dependent on the development of efficient catalysts. In any case, the advancement of photo-systems for the HER is ongoing along many different research directions, all with interesting properties and capabilities. Only time will tell which method will achieve the *holy grail* of water splitting/sustainable H_2 production.

1.5 Conducting Polymers

1.5.1 Overview

Conducting polymers were first discovered in 1862 by H. Letheby and his investigations on polyaniline, however, the instability of early conducting polymers limited their commercial use. Their potential as intrinsically conducting polymers (ICP) was only fully realised in the late 1980's with the development of a range of stable species using polyaniline, polypyrrole and polythiophenes.[137]

Since then, conducting polymers have been utilised for a wide range of applications, brought about by careful analysis and utilisation of the HOMO/LUMO positions (for discrete molecules) or the valence band (VB)/conduction band (CB) (for polymer films), and their associated band gap (E_g). These applications include organic light-emitting diodes (OLEDs) , anti-static coatings, organic photovoltaic cells (OPV) and field effect transistors.[138] Amongst the most commonly used ICP is the stable, highly conductive and processable poly(3,4-ethylenedioxythiophene) or PEDOT.[139] In this section, an emphasis is placed on members of the polythiophene family due to their relevance to the project.

The operating principles of ICPs is illustrated by p-doped (or oxidised) polythiophene (Figure 1.16) where the positive charge is conducted via the conjugated carbon backbone and the associated π electron system. The introduced charge is known as a polaron and is associated with the creation of an extra electronic energy level from the conduction and valence bands, see Figure 1.16.[140,141] Increased doping of the conducting polymer eventually leads to the formation of polaron bands and provides the pathway by which charges can travel. Bipolarons are also commonly observed especially in more heavily doped samples and is the combination of two same charge polarons that come together to form a spinless state.[142]

For many polythiophenes and other conducting polymers, they can swap between a neutral (undoped) semi-conductor state and an oxidised (doped) conducting state; ICPs are conducting polymers that naturally exist in this doped conducting state. However, the oxidation state of the conducting polymer is also strongly dependent on the synthesis method used as well as the chemical environment that it is exposed to. The oxidised/doped state can be brought on chemically with oxidants,[141] with applied potential[144] and with light.[145–147] The latter phenomenon is particularly important as it underpins the operating mechanisms of many conducting polymer photo-applications.

1.5.2 Photo-interactions

The band structure of ICPs and conjugated polymers enable a variety of photo-interactions. Many examples (including polythiophenes) are able to absorb light in the visible spectra via a
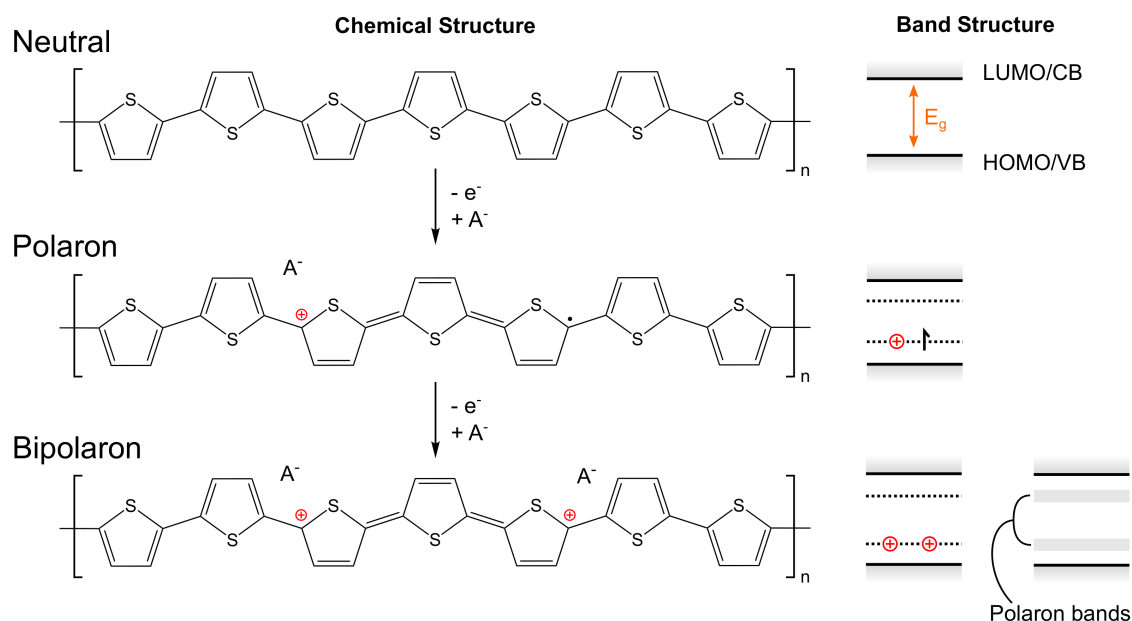
Figure 1.16: The chemical and band structure of neutral polythiophene, and p-doped polythiophene with a polaron and bipolaron, where A^- represents the counter ion. Further increases in doping levels eventually lead to the formation of polaron bands. Adapted from reference.[143]

$\pi - \pi^*$ excitation to form a photo-excited electron/hole pair (exciton). A range of different photo-physical and photo-chemical mechanisms can occur from this excited state, some of which are shown in Figure 1.17.

The most commonly known of these is perhaps fluorescence – a fast radiative relaxation between states of the same multiplicity – and has been harnessed in polythiophenes for a variety of applications such as fluorescent markers, light-emitting diodes and even lasers.[145, 148–151] Internal conversion (IC) or the loss of photo-energy via heat is another common relaxation mechanism. Other transitions include intersystem crossing which is a non-radiative transition to the triplet state (T_1) and the subsequent radiative relaxation from T_1 to the singlet ground state (S_0) via phosphorescence. The triplet processes are spin-forbidden and are typically low in population but occur over longer timescales ($>\mu s$).

The mechanism by which the photo-excited state relaxes/recombines is heavily dependent on the proximity and activity of surrounding chromophores.[152] In conjugated polymer films, the high density and overlap of π-orbitals mean that intermolecular relaxation mechanisms such as quenching, energy transfer by the movement of excitons and the formation of excimers (D) are possible; where an excimer describes the short-lived dimeric species formed by the formation of a temporary bond between a photo-excited and ground state pair. These processes are prominent in the polythiophene family due to the heavy sulphur atom which promotes non-radiative relaxation mechanisms such as interchain interactions and intersystem crossing.[150, 153]
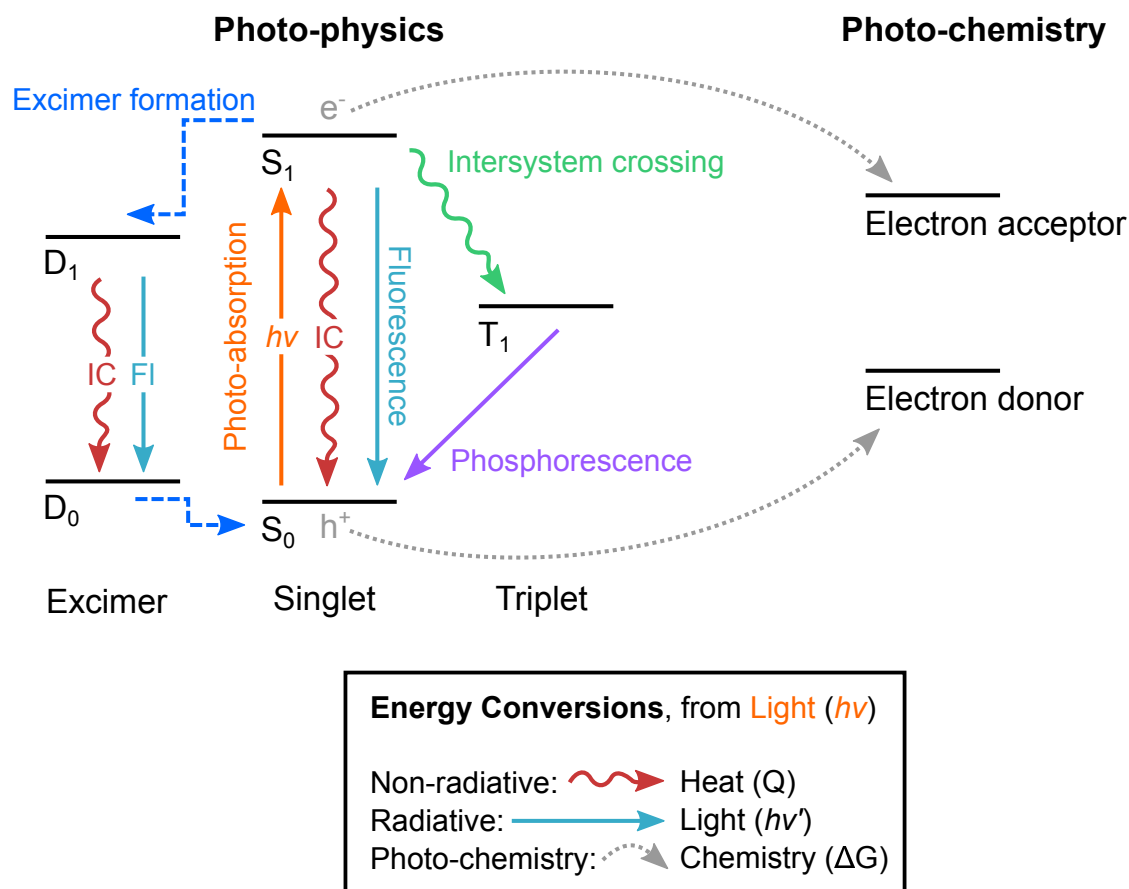
Figure 1.17: The various photo-physics and photo-chemical interactions that are commonly observed with conducting polymers. These include the non-radiative processes of internal conversion (IC) and intersystem crossing, the radiative processes of fluorescence (Fl) and phosphorescence, and the formation of excimers (D) (adapted from reference[152]).

As a result, the triplet states and interchain transfers play a much more important role in the photo-physics of polythiophenes.[154, 155]

The photo-chemistry of ICPs is also important to understand as photo-excitation often leads to degradation via photo-oxidation and chain scission, especially in the presence of O_2.[152, 156] However, when utilised properly, this photo-activity can be employed for a wide range of useful reactions. This includes the formation of charge transfer complexes and photo-induced electron transfers for photo-electrochemistry and photovoltaic applications.[141, 157, 158]

1.5.3 Polythiophenes

Polythiophene was first synthesised in the early 1980's. In its most basic form, polythiophene was known as a stable and moderately conducting polymer (when doped with iodine)[159] but did not really exhibit any other particularly notable properties. This could have been in part

A

e⁻

hv

h⁺

Donor
(P3HT)

B

→   e⁻

→ h⁺

Donor   Acceptor
(P3HT)   (PCBM)

C

e⁻

h⁺

Anode   Donor   Acceptor   Cathode
(ITO)   (P3HT)   (PCBM)   (Al)
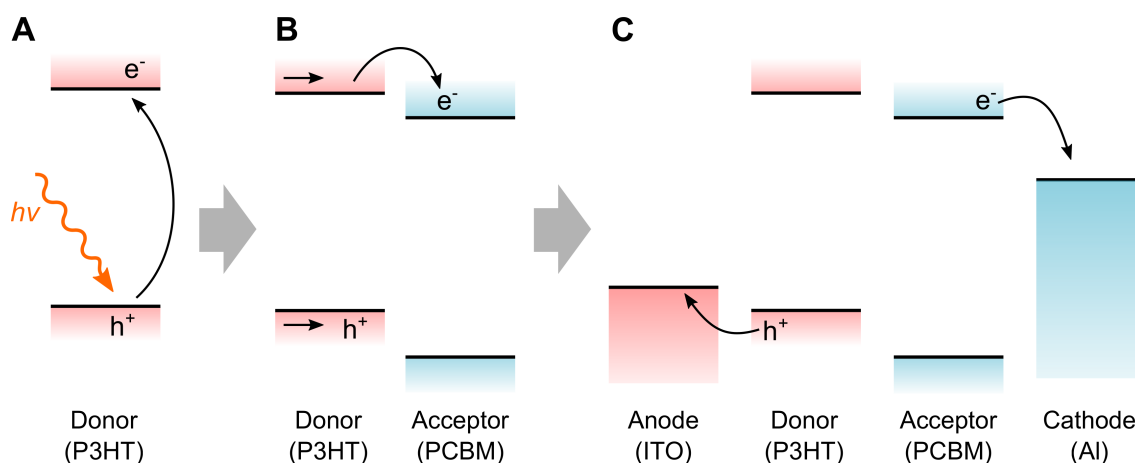
Figure 1.18: Schematic showing the operating mechanism of a typical OPV. **A:** Initial photo-excitation and formation of the exciton (electron/hole pair), **B:** diffusion of the exciton to the heterojunction interface followed by charge separation. **C:** Conduction of the separated charges to their respective electrodes and the generation of photo-current.

due to the strong π stacking of the polythiophene chains which severely reduced solubility and made initial studies difficult.[138] It wasn't until the development and synthesis of the soluble poly(3-alkylthiophene) family that allowed for a much broader range of scientific studies.

The extensive conjugated π-structure of polythiophenes and conducting polymers in general, allow them to absorb light and electronically interact with surrounding materials relatively easily. As such, they have been harnessed for photo-electric applications that include OLEDs, OPVs and as conductive substrates in a variety of photo-devices.[160–163] In these cases, success of the photo-device is dependent on the correct positioning of the polymer's electronic band energies and its ability to selectively conduct holes (positive charges).

Polythiophenes in particular, have been heavily studied due to their stability and the wide array of techniques by which they can be synthesised, modified and tuned for specific photo-electronic properties.[150, 164] This feature has been of particular interest in OPVs as it allows for a much greater flexibility when optimising for properties such as processability, stability, morphology and E_g.[138, 165, 166] One of the most well known polythiophenes to have evolved from this process is poly(3-hexylthiophene) (P3HT) where it is commonly paired with phenyl-C_{61}-butyric acid methyl ester (PCBM) to form a relatively stable and efficient OPV.[167]

The success of P3HT and related polythiophenes with respect to OPVs is due to several inherent properties with the first being their strong photo-absorption.[168] Good interchain interactions then aids in the diffusion of the generated exciton pair towards the bulk heterojunction where it can undergo charge separation and generate the desired photo-current (see Figure 1.18).[169]

1.5.4 Electrochemical Applications

The same properties that make P3HT useful for OPVs such as good conductivity and photo-activity, also makes them suited for electrochemical and photo-electrochemical applications. However alternatives to the poly(3-alkylthiophene) family is required due to their instability in the presence of O_2 and H_2O.[170,171] As such, alternative water stable polythiophenes such as PEDOT are used.

As an organic polymer network, PEDOT lends itself to various modification techniques whilst still being able to preserve its highly conductive nature. Examples include the addition of gold/platinum/iron particles to PEDOT to improve the electrochemical oxidation of various organic species[172–175] and the reduction of protons and oxygen.[176,177] Moreover, research from our group and others have shown that PEDOT and various other polythiophenes prepared via a vapour phase polymerisation (VPP)[178] has shown interesting catalytic abilities. These include the oxygen reduction reaction (ORR)[179–182] as well as the HER on PEDOT:PEG blends[10] (shown earlier in Figure 1.2); the latter of which forms the basis of this thesis project.

The VPP and solution processability of PEDOT and other polythiophenes allowed for easy deposition on functional substrates and led to the improvement of catalytic performance.[161,183,184] Examples include PEDOT on reduced graphene oxide for the ORR,[185] poly(3,4-dinitrothiophene) on carbon nanotubes as an electrocatalyst for the HER[186] and PEDOT with PEG scaffolds for the ORR which exhibited performance on par with Pt.[187] This ease of polymerisation/modification and promising electrocatalytic activity of PEDOT and polythiophenes eventually led to the progression towards the investigation of photo-active films.

Photo-enhancement

Polythiophenes have been successfully utilised for photo-enhanced electrochemical catalysis by taking advantage of their inherent optical and electronic properties.[188–190] Examples include the photo-stimulated catalytic oxidation of water using polyterthiophene (PTTh)[191,192] and PEDOT.[193] Another approach investigated a heterojunction based device for the splitting of water with the schematic being shown in Figure 1.19.[194] The photo-electrocatalytic capabilities of these conducting polymers represent the beginnings of a promising field of study; albeit a little surprising given that these polymers are generally optimised for stability and conductivity, not reactivity or photo-absorption. Studies are currently underway to better understand their catalytic mechanism, with one initial result revealing the formation of a photo-enhanced P3HT/oxygen charge transfer complex.[195]
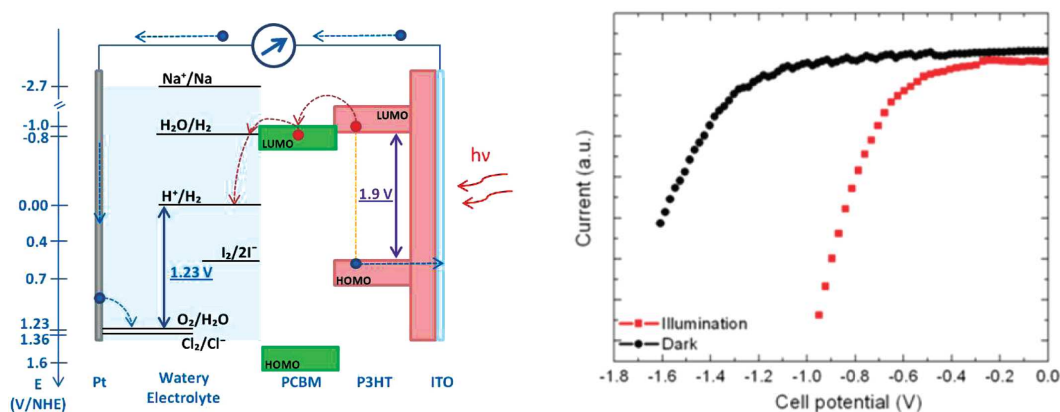
Figure 1.19: The polymer heterojunction photo-system for water splitting.[194] **Left:** Schematic diagram showing the working principle of the device and the energy levels associated with each of the components. **Right:** Comparing the dark and illuminated performance of the ITO/rr-P3HT:PCBM/NaCl/Pt device.

Summary

The ability to electronically interact with a wide range of substrates/catalysts/components affords conducting polymers such as polythiophenes a customisability that is hard found in inorganic and biological equivalents. Their inherent photo-absorbance and stability further increases their potential for successful photo-catalytic activity. Moreover, the promising initial photo/electro-catalytic results give support to the viability of our proposed photo-electrocatalytic system using ICPs and dyes.

1.6 Dyes

Dyes by their very nature are natural light absorbers and have been utilised heavily in the field of electrochemistry to enable photo-activity; the most prominent example perhaps being DSSCs. Several dye sensitised photo-systems for the HER have already been mentioned in Section 1.4.3, though they chiefly comprise of metal complex dyes. In this section, an emphasis is placed on organic dyes which have numerous advantages, key of which include easier synthesis and customisation methods, no reliance on rare-earth metals such as Ru and high absorption coefficients from the $\pi - \pi^*$ transition.[196]

Typically in dyes, relaxation of the excited state occurs via a variety of methods such a IC and fluorescence (similar to ICPs, Figure 1.17). However, given the proper excitation energy, stability of the dye and chemical interactions, it is possible for a charge transfer from the dye to another species.[58,197,198] This concept is the basis upon which we incorporate dyes.

In relation to H_2 production, some dyes, such as Safranine O, have been found to photolytically reduce hydrogen (in the presence of electron donors).[199] Further studies found that the
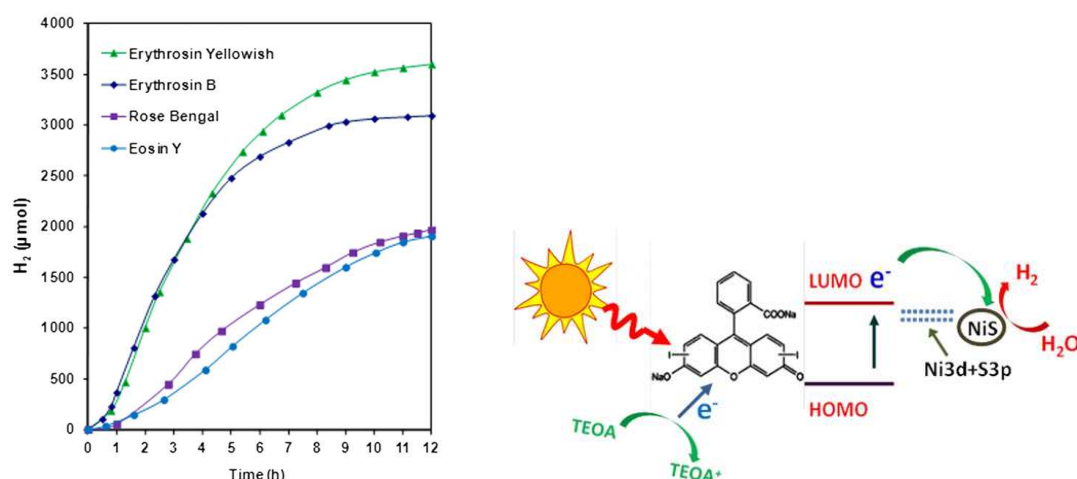
Figure 1.20: A xanthene and Ni photo-catalyst system proposed for the HER.[204] **Left:** The photo-catalytic hydrogen production with NiS-EG catalyst and xanthene dyes, $2.25\,\mathrm{mmol\,L^{-1}}$ in 15 % v/v aqueous TEOA solution, illumination wavelength >420 nm. **Right:** Schematic diagram of the Ni-Xanthene catalyst system for the photodriven generation of H_2

attachment of dye to semi-conductors created more efficient charge separation and improved catalytic performance.[103, 109, 200, 201] More recent studies include; the investigation of dye sensitised TiO_2 particles loaded with Pt for use in photodriven hydrogen generation and environmental remediation,[202] as well as the combination of Eosin Y (dye) with a synthetic [FeFe]-hydrogenase inspired catalyst to photo-catalytically produce H_2.[203] Of particular interest is the demonstration of photocatalytic H_2 evolution using xanthene dyes and nickel based catalyts,[204] a system that contains many close parallels to the photo-system envisioned for this project (Figure 1.20).

Dyes are an obvious choice for the enabling and enhancing of photo-activity, but proper understanding of their abilities and limitations is needed for the design of a successful photoelectrode. Some examples of this required working knowledge comes from the analysis of the dye's HOMO/LUMO energies, absorption spectra, excitation lifetimes and ability for charge transfer.

1.7 Computational Chemistry

The use of computational techniques has been applied in recent years to both model and develop new catalytic molecules and systems. While computational results still require the support of experimental data, careful selection of computational models and parameters can allow valuable insights into a wide range of chemical properties. Wang and Lewis were able to accurately predict the bandgap narrowing effect of anion-doped TiO_2[205] while work by Siegbahn and Head-Gordon *et al.* helped reveal the catalysis mechanism for [NiFe]-hydrogenase[28] and molybdenum-oxo catalysts[57] respectively.
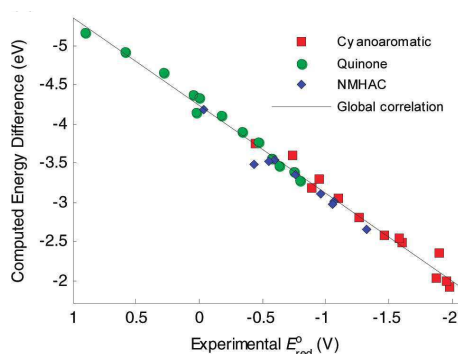
Figure 1.21: Comparison of computed and experimental reduction potentials showing good correlation for various photo-oxidants.[208]

For the purpose of photo-electrochemical catalysis, study and knowledge of properties such as the electronic band energy structure and HOMO/LUMO energy levels are vital. In recognition of this, researchers have applied computational techniques to aid in their determination. Examples include calculations of HOMO and LUMO orbital energies using time-dependent density functional theory (TD-DFT) [206, 207] and the determination of reduction potentials using a density functional theory (DFT) based approach.[208, 209] The latter of these techniques was able to achieve a significant accuracy with organic photo-oxidants and is show in Figure 1.21.

1.8   Research Aims

1.8.1   Main Research Aim

Despite the many different methods currently under development, we are yet to discover an efficient, economical and sustainable solution for the facile production of hydrogen. In light of this, we propose:

The development of a photo-electrocatalyst for the hydrogen evolution reaction utilising blends of conducting polymers and organic dyes.

1.8.2   Secondary Aims

Exploration and optimisation of the conducting polymer:dye electrode for catalytic activity toward the HER

The thorough investigation of the successful conducting polymer:dye electrode to examine how operation parameters such as pH, electrolyte, film thickness *etc.* will affect the catalytic behaviour; and if these parameters can be tuned in a way to improve catalytic response.

Development of computational models to streamline selection processes

The goal of this aim is twofold, first and foremost it will enable a rapid selection process where time consuming and costly laboratory work can be minimised. Secondly the development of a computational model whereby redox potentials can be accurately predicted will have a wide ranging impact with applications in electrochemistry and catalyst development.

Mechanistic understanding

The in-depth investigation of the conducting polymer:dye heterojunction system to better understand and further refine the electrode material. This includes the elucidation of the charge transfer mechanism, dependence on electronic energy levels and the effect of solvent. All of which are vital to the development of the electrode.

Expanding the electrode material for the catalysis of other reactants

Focus will be on the development of a photo-enhanced electrocatalyst for the HER, but the principles on which the electrode is founded will be applicable to a wide range of electrochemical reactions. Thus examinations into other processes may reveal new and interesting applications for this system.

1.9 Conclusion and Project Summary

The sustainable production of hydrogen through electrolysis is a critical milestone to the realisation of a carbon-free hydrogen economy. From the thorough review of current literature, significant progress has been made in developing more efficient and low cost electrodes though substantial hurdles remain. Electrochemical catalysts are capable of high production rates but require high overpotentials and tend to be energetically inefficient. Biological catalysts are only viable under very specific conditions and tend to become inactive and unstable when exposed to air. Photo-catalysts are able to harness light for the HER but have limited lifetime and often rely on sacrificial electron donors and/or expensive noble metals.

Conducting polymers provide a good base to address many of these issues, particularly PEDOT and variants from the polythiophene family. Their favourable properties include good stability under a wide range of chemical conditions, good hole conductivity and impressive electro- and photo-catalytic activity towards numerous reactions such as the HER and ORR. These inherent photo-interactions will be of interest to explore, though further photo-activity can be supplied with the addition of dyes which have been known to aid in the catalysis of various electrochemical reactions.

The proposed conducting polymer:dye blend for this project encompasses a wide range of fields where each one is vital to the success of its overall operation. Taking current research on photo and electrocatalysts as inspiration, the as yet untrialled incorporation of dyes into conducting polymers is hoped to reveal a new and novel photo-system. The working principles of this electrode system is displayed in Figure 1.22 and will rely on the concepts highlighted in the above literature review, including:

- The ability for efficient charge separation and transfer
- The correct matching of electronic band energies
- A low ΔG for the adsorption and release of H_2
- Good coherency between the dye and the conducting polymer
- Stability under various electrochemical environments
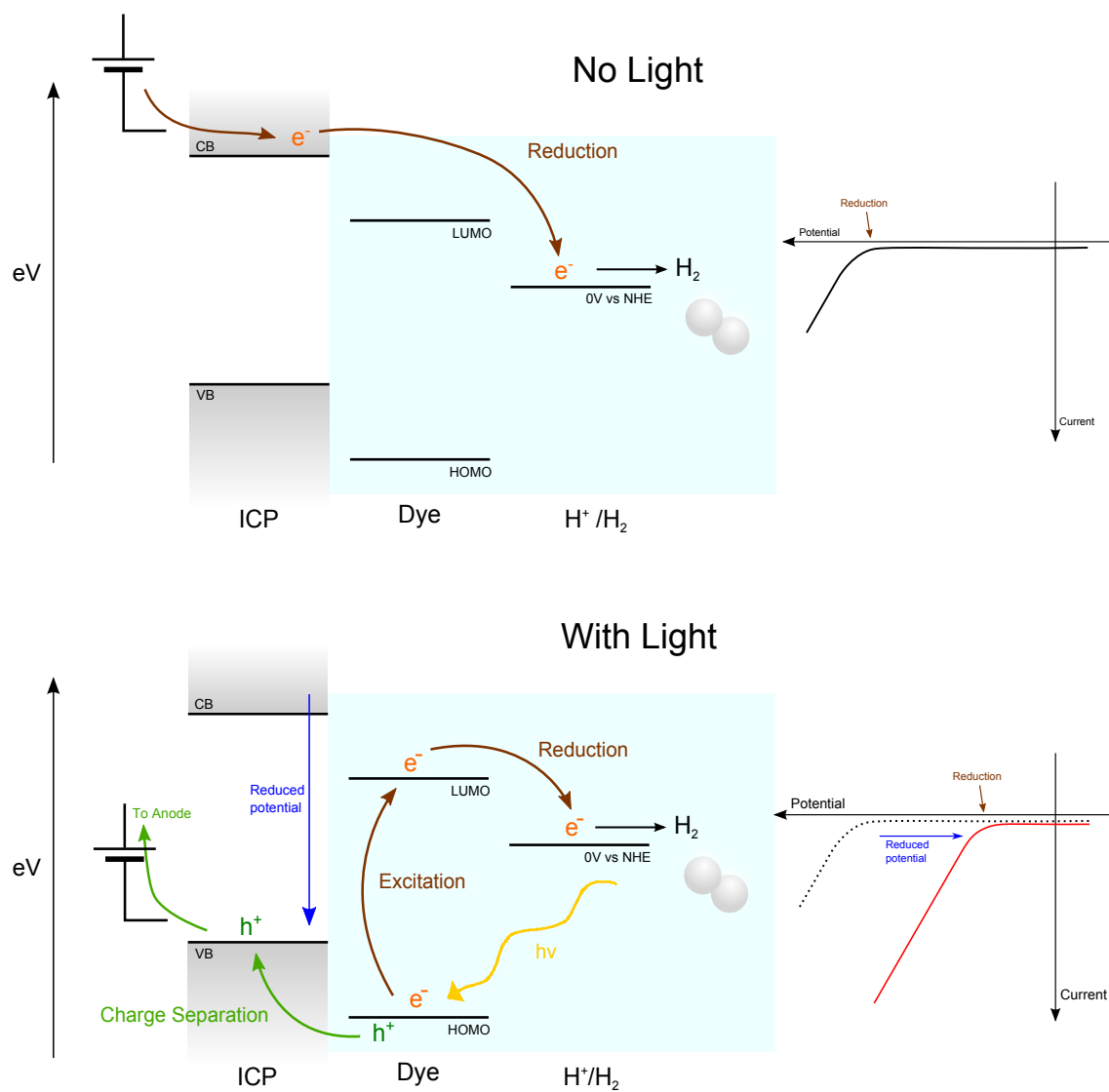
Figure 1.22: A schematic of the envisaged working principle of the light enhanced conducting polymer:dye electrode for the HER; the proposed effect on cyclic voltammograms is also shown.

Bibliography

[1] T. Stocker, D. Qin, P. G.K., T. M., K. Allen, J. Boschung, A. Nauels, Y. Xia, V. Bex and P. Midgley. "IPCC, 2013: Summary for Policymakers. In: Climate Change 2013: The Physical Science Basis. Contribution of Working Group I to the Fifth Assessment Report of the Intergovernmental Panel on Climate Change". Technical report, Cambridge University Press, Cambridge, United Kingdom and New York, NY, USA, 2013.

[2] T. Morgan, J. Rogat, D. Puig and M. Rakda. "The hydrogen economy: A non technical review". Technical report, United Nations Environment Programme, Paris, 2006.

[3] R. Lacko, B. Drobnič, M. Sekavčnik and M. Mori. "Hydrogen energy system with renewables for isolated households: The optimal system design, numerical analysis and experimental evaluation". *Energy Build.*, 2014. **80**, 106–113.

[4] M. Pagliaro and A. G. Konstandopoulos. "Solar Hydrogen Utilization". In "Sol. Hydrog. Fuel Futur.", chapter 4. Royal Society of Chemistry, 2012. pp. 119–154.

[5] K. Harrison and J. I. Levene. "Electrolysis of Water". In K. Rajeshwar, R. McConnell and S. Licht (editors), "Sol. Hydrog. Gener.", chapter 3. Springer New York, 2008. pp. 41–63.

[6] T. Riis, E. F. Hagen, P. J. S. Vie and O. Ulleberg. "Hydrogen Production and Storage". Technical report, International Energy Agency, Paris, 2006.

[7] K. Rajeshwar, R. McConnell, K. Harrison and S. Licht. "Renewable Energy and the Hydrogen Economy". In "Sol. Hydrog. Gener.", chapter 1. Springer New York, 2008.

[8] J. Ivy. "Summary of Electrolytic Hydrogen Production Milestone Completion Report". Technical Report September, National Renewable Energy Laboratory, Golden, Colorado, 2004.

[9] J. H. Guo and X. B. Chen. "Hydrogen Generation: Electrochemistry and Photoelectrolysis 1". In "Sol. Hydrog. Gener. Transistion Met. Oxides Water Photoelectrolysis", chapter 1. McGraw Hill, 2011.

[10] B. Winther-Jensen, K. Fraser, C. Ong, M. Forsyth and D. R. MacFarlane. "Conducting polymer composite materials for hydrogen generation." *Adv. Mater.*, 2010. **22**, 15, 1727–1730.

[11] P. D. Tran and J. Barber. "Proton reduction to hydrogen in biological and chemical systems." *Phys. Chem. Chem. Phys.*, 2012. **14**, 40, 13772–13784.

[12] J. Verne. *The Mysterious Island*. Modern Library, 2001, 1874.

[13] B. Kroposki, J. Levene and K. Harrison. "Electrolysis : Information and Opportunities for Electric Power Utilities". Technical report, National Renewable Energy Laboratory, 2006.

[14] A. Ursua, L. M. Gandia and P. Sanchis. "Hydrogen Production From Water Electrolysis: Current Status and Future Trends". *Proc. IEEE*, 2012. **100**, 2, 410 –426.

[15] P. Hoffmann. *The Forever Fuel: The Story of Hydrogen*. Westview Press, Boulder, Colorado, 1981.

[16] A. P. Fickett and F. R. Kalhammer. "Water Electrolysis". In K. E. Cox and K. D. Williamson (editors), "Hydrog. Its Technol. Implic.", chapter 1. CRC Press, Cleveland, Ohio, 1977.

[17] A. Konopka and D. Gregory. "Hydrogen Production by Electrolysis: Present and Future". In "10th Intersoc. Energy Convers. Eng. Conf.", IEEE Cat. No. 75CHO 987-7 TAB.

[18] Z. Yang, D. Coutinho, F. Feng, J. P. Ferraris and K. J. B. Jr. "Novel Inorganic/Organic Hybrid Electrolyte Membranes". *Prepr. Pap. - Am. Chem. Soc. Div. Fuel Chem.*, 2004. **49**, 2, 599–600.

[19] D. Stolten, D. Krieg and M. Weber. "An Overview on Water Electrolysis". In "WICaC", Institute for Fuel Cells, Juelich Research Center, Germany, Campinas, Brasil.

[20] E. Zoulias, E. Varkaraki, N. Lymberopoulos, C. N. Christodoulou and G. N. Karagiorgis. "A review on water electrolysis". Technical report, Centre for Renewable Energy Sources, Pikermi, 2004.

[21] Proton OnSite. "Proton OnSite: Who We Are", 2011.

[22] Treadwell Corporation. "Treadwell Corporation: Timeline", 2013.

[23] Claind Gas Generators. "Claind: History", 2011.

[24] National Renewable Energy Laboratory. "NREL: Hydrogen & Fuel Cells Research", 2011.

[25] P. Pillay. "Hydrogen Economy and Alternative Fuels". Technical report, IEEE, 2006.

[26] L. Barreto, A. Makihira and K. Riahi. "The hydrogen economy in the 21st century: a sustainable development scenario". *Int. J. Hydrogen Energy*, 2003. **28**, 3, 267–284.

[27] J. K. Norskov and C. H. Christensen. "Toward efficient hydrogen production at surfaces". *Science*, 2006. **312**, 5778, 1322–1323.

[28] P. E. M. Siegbahn. "Proton and Electron Transfers in Hydrogenase". *Adv. Inorg. Chem.*, 2004. **56**, 04, 101–125.

[29] B. Hinnemann, P. G. Moses, J. Bonde, K. P. Jorgensen, J. H. Nielsen, S. Horch, I. Chorkendorff and J. K. Norskov. "Biomimetic hydrogen evolution: MoS2 nanoparticles as catalyst for hydrogen evolution." *J. Am. Chem. Soc.*, 2005. **127**, 15, 5308–5309.

[30] B. Hinnemann, J. K. Nørskov and H. Topsøe. "A density functional study of the chemical differences between Type I and Type II MoS2-based structures in hydrotreating catalysts." *J. Phys. Chem. B*, 2005. **109**, 6, 2245–53.

[31] D. Merki and X. Hu. "Recent developments of molybdenum and tungsten sulfides as hydrogen evolution catalysts". *Energy Environ. Sci.*, 2011. **4**, 10, 3878–3888.

[32] T.-Y. Chen, Y.-H. Chang, C.-L. Hsu, K.-H. Wei, C.-Y. Chiang and L.-J. Li. "Comparative study on MoS2 and WS2 for electrocatalytic water splitting". *Int. J. Hydrogen Energy*, 2013. **38**, 28, 12302–12309.

[33] T. F. Jaramillo, K. P. Jorgensen, J. Bonde, J. H. Nielsen, S. Horch and I. Chorkendorff. "Identification of active edge sites for electrochemical H2 evolution from MoS2 nanocatalysts." *Science*, 2007. **317**, 5834, 100–102.

[34] J. Xie, J. Zhang, S. Li, F. Grote, X. Zhang, H. Zhang, R. Wang, Y. Lei, B. Pan and Y. Xie. "Controllable disorder engineering in oxygen-incorporated MoS2 ultrathin nanosheets for efficient hydrogen evolution". *J. Am. Chem. Soc.*, 2013. **135**, 47, 17881–17888.

[35] Y. Li, H. Wang, L. Xie, Y. Liang, G. Hong and H. Dai. "MoS2 Nanoparticles Grown on Graphene: An Advanced Catalyst for Hydrogen Evolution Reaction". *J. Am. Chem. Soc.*, 2011. **133**, 7296–7299.

[36] W.-H. Hu, G.-Q. Han, Y.-R. Liu, B. Dong, Y.-M. Chai, Y.-Q. Liu and C.-G. Liu. "Ultrathin MoS2-coated carbon nanospheres as highly efficient electrocatalyts for hydrogen evolution reaction". *Int. J. Hydrogen Energy*, 2015. **40**, 20, 6552–6558.

[37] J. Kibsgaard, T. F. Jaramillo and F. Besenbacher. "Building an appropriate active-site motif into a hydrogen-evolution catalyst with thiomolybdate [Mo3S13]2- clusters." *Nat. Chem.*, 2014. **6**, 3, 248–53.

[38] X. Geng, W. Wu, N. Li, W. Sun, J. Armstrong, A. Al-hilo, M. Brozak, J. Cui and T.-p. Chen. "Three-Dimensional Structures of MoS 2 Nanosheets with Ultrahigh Hydrogen Evolution Reaction in Water Reduction". *Adv. Funct. Mater.*, 2014. **24**, 6123–6129.

[39] Metalprices.com. "metalprices.com", 2013.

[40] J. Kibsgaard, Z. Chen, B. N. Reinecke and T. F. Jaramillo. "Engineering the surface structure of MoS2 to preferentially expose active edge sites for electrocatalysis". *Nat. Mater.*, 2012. **11**, 11, 963–969.

[41] M. W. W. Adams and E. I. Stiefel. "Biological Hydrogen Production: Not So Elementary". *Sci.*, 1998. **282**, 5395, 1842–1843.

[42] A. K. Jones, E. Sillery, S. P. J. Albracht and F. a. Armstrong. "Direct comparison of the electrocatalytic oxidation of hydrogen by an enzyme and a platinum catalyst." *Chem. Commun.*, 2002, 866–867.

[43] D. S. Goodsell. "Molecule of the Month: Hydrogenase", 2009.

[44] S. E. Lamle, K. A. Vincent, L. M. Halliwell, S. P. J. Albracht and F. A. Armstrong. "Hydrogenase on an electrode: a remarkable heterogeneous catalyst". *Dalt. Trans.*, 2003, 4152–4157.

[45] K. A. Vincent, A. Parkin and F. A. Armstrong. "Investigating and exploiting the electrocatalytic properties of hydrogenases." *Chem. Rev.*, 2007. **107**, 10, 4366–413.

[46] P. D. Tran, V. Artero and M. Fontecave. "Water electrolysis and photoelectrolysis on electrodes engineered using biological and bio-inspired molecular systems". *Energy Environ. Sci.*, 2010. **3**, 6, 727–747.

[47] S. Morozov, P. Vignais, L. Cournac, N. Zorin, E. Karyakina, A. Karyakin and S. Cosnier. "Bioelectrocatalytic hydrogen production by hydrogenase electrodes". *Int. J. Hydrogen Energy*, 2002. **27**, 1501–1505.

[48] A. A. Karyakin, S. V. Morozov, O. G. Voronin, N. A. Zorin, E. E. Karyakina, V. N. Fateyev and S. Cosnier. "The Limiting Performance Characteristics in Bioelectrocatalysis of Hydrogenase Enzymes". *Angew. Chemie*, 2007. **119**, 38, 7382–7384.

[49] O. Rüdiger, J. M. Abad, E. C. Hatchikian, V. M. Fernandez and A. L. De Lacey. "Oriented immobilization of Desulfovibrio gigas hydrogenase onto carbon electrodes by covalent bonds for nonmediated oxidation of H2." *J. Am. Chem. Soc.*, 2005. **127**, 46, 16008–9.

[50] M. A. Alonso-Lomillo, O. Rüdiger, A. Maroto-Valiente, M. Velez, I. Rodríguez-Ramos, F. J. Muñoz, V. M. Fernández and A. L. De Lacey. "Hydrogenase-coated carbon nanotubes for efficient H2 oxidation." *Nano Lett.*, 2007. **7**, 6, 1603–8.

[51] M. Frey. "Hydrogenases: hydrogen-activating enzymes." *Chembiochem*, 2002. **3**, 2-3, 153–60.

[52] P. Lindberg, P. Lindblad and L. Cournac. "Gas Exchange in the Filamentous Cyanobacterium Nostoc punctiforme Strain ATCC 29133 and Its Hydrogenase-Deficient Mutant Strain NHM5". *Appl. Environ. Microbiol.*, 2004. **70**, 4, 2137–2145.

[53] A. Magnuson, M. Anderlund, O. Johansson, P. Lindblad, R. Lomoth, T. Polivka, S. Ott, K. Stensjö, S. Styring, V. Sundström and L. Hammarström. "Biomimetic and microbial approaches to solar fuel generation." *Acc. Chem. Res.*, 2009. **42**, 12, 1899–1909.

[54] T. W. Woolerton, S. Sheard, Y. S. Chaudhary and F. A. Armstrong. "Enzymes and bio-inspired electrocatalysts in solar fuel devices". *Energy Environ. Sci.*, 2012. **5**, 6, 7470–7490.

[55] M. Wang, L. Chen and L. Sun. "Recent progress in electrochemical hydrogen production with earth-abundant metal complexes as catalysts". *Energy Environ. Sci.*, 2012. **5**, 5, 6763–6778.

[56] H. I. Karunadasa, C. J. Chang and J. R. Long. "A molecular molybdenum-oxo catalyst for generating hydrogen from water." *Nature*, 2010. **464**, 7293, 1329–1333.

[57] E. J. Sundstrom, X. Yang, V. S. Thoi, H. I. Karunadasa, C. J. Chang, J. R. Long and M. Head-Gordon. "Computational and experimental study of the mechanism of hydrogen generation from water by a molecular molybdenum-oxo electrocatalyst." *J. Am. Chem. Soc.*, 2012. **134**, 11, 5233–5242.

[58] T. Peng, D. Ke, P. Cai, K. Dai, L. Ma and L. Zan. "Influence of different ruthenium(II) bipyridyl complex on the photocatalytic H2 evolution over TiO2 nanoparticles with mesostructures". *J. Power Sources*, 2008. **180**, 1, 498–505.

[59] B. D. Stubbert, J. C. Peters and H. B. Gray. "Rapid water reduction to H2 catalyzed by a cobalt bis(iminopyridine) complex." *J. Am. Chem. Soc.*, 2011. **133**, 45, 18070–3.

[60] J. F. Capon, F. Gloaguen, F. Y. Pétillon, P. Schollhammer and J. Talarmin. "On the electrochemistry of diiron dithiolate complexes related to the active site of the [FeFe]H2ase". *Comptes Rendus Chim.*, 2008. **11**, 8, 842–851.

[61] J. F. Capon, F. Gloaguen, P. Schollhammer and J. Talarmin. "Catalysis of the electro-chemical H2 evolution by di-iron sub-site models". *Coord. Chem. Rev.*, 2005. **249**, 15-16 SPEC. ISS., 1664–1676.

[62] J. F. Capon, S. Ezzaher, F. Gloaguen, F. Y. Pétillon, P. Schollhammer and J. Talarmin. "Electrochemical insights into the mechanisms of proton reduction by [Fe2(CO)6{micro-SCH2N(R)CH2S}] complexes related to the [2Fe](H) subsite of [FeFe]hydrogenase." *Chemistry*, 2008. **14**, 6, 1954–1964.

[63] S. Lounissi, J.-F. Capon, F. Gloaguen, F. Matoussi, F. Y. Pétillon, P. Schollhammer and J. Talarmin. "Diiron species containing a cyclic P(Ph)2N(Ph)2 diphosphine related to the [FeFe]H2ases active site." *Chem. Commun. (Camb).*, 2011. **47**, 3, 878–880.

[64] M. Beyler, S. Ezzaher, M. Karnahl, M.-P. Santoni, R. Lomoth and S. Ott. "Pentacoordinate iron complexes as functional models of the distal iron in [FeFe] hydrogenases". *Chem. Commun.*, 2011. **47**, 42, 11662.

[65] S. Kaur-Ghumaan, L. Schwartz, R. Lomoth, M. Stein and S. Ott. "Catalytic hydrogen evolution from mononuclear iron(II) carbonyl complexes as minimal functional models of the [FeFe] hydrogenase active site". *Angew. Chemie - Int. Ed.*, 2010. **49**, 43, 8033–8036.

[66] A. Orthaber, M. Karnahl, S. Tschierlei, D. Streich, M. Stein and S. Ott. "Coordination and conformational isomers in mononuclear iron complexes with pertinence to the [FeFe] hydrogenase active site." *Dalton Trans.*, 2014. **43**, 11, 4537–49.

[67] S. Roy, S. K. S. Mazinani, T. L. Groy, L. Gan, P. Tarakeshwar, V. Mujica and A. K. Jones. "Catalytic Hydrogen Evolution by Fe(II) Carbonyls Featuring a Dithiolate and a Chelating Phosphine." *Inorg. Chem.*, 2014. **53**, 8919–8929.

[68] A. D. Wilson, R. H. Newell, M. J. McNevin, J. T. Muckerman, M. Rakowski DuBois and D. L. DuBois. "Hydrogen oxidation and production using nickel-based molecular catalysts with positioned proton relays." *J. Am. Chem. Soc.*, 2006. **128**, 1, 358–66.

[69] U. J. Kilgore, J. a. S. Roberts, D. H. Pool, A. M. Appel, M. P. Stewart, M. R. DuBois, W. G. Dougherty, W. S. Kassel, R. M. Bullock and D. L. DuBois. "[Ni(P(Ph)2N(C6H4X)2)2]2+ complexes as electrocatalysts for H2 production: effect of substituents, acids, and water on catalytic rates." *J. Am. Chem. Soc.*, 2011. **133**, 15, 5861–72.

[70] S. E. Smith, J. Y. Yang, D. L. Dubois and R. M. Bullock. "Reversible electrocatalytic production and oxidation of hydrogen at low overpotentials by a functional hydrogenase mimic". *Angew. Chemie - Int. Ed.*, 2012. **51**, 13, 3152–3155.

[71] M. L. Helm, M. P. Stewart, R. M. Bullock, M. R. DuBois and D. L. DuBois. "A synthetic nickel electrocatalyst with a turnover frequency above 100,000 s-1 for H2 production." *Science*, 2011. **333**, 6044, 863–6.

[72] M. P. McLaughlin, T. M. McCormick, R. Eisenberg and P. L. Holland. "A stable molecular nickel catalyst for the homogeneous photogeneration of hydrogen in aqueous solution." *Chem. Commun. (Camb).*, 2011. **47**, 28, 7989–7991.

[73] W. a. Hoffert, J. a. S. Roberts, R. Morris Bullock and M. L. Helm. "Production of H2 at fast rates using a nickel electrocatalyst in water-acetonitrile solutions." *Chem. Commun.*, 2013. **49**, 71, 7767–9.

[74] M. P. Stewart, M. H. Ho, S. Wiese, M. L. Lindstrom, C. E. Thogerson, S. Raugei, R. M. Bullock and M. L. Helm. "High catalytic rates for hydrogen production using nickel electrocatalysts with seven-membered cyclic diphosphine ligands containing one pendant amine". *J. Am. Chem. Soc.*, 2013. **135**, 16, 6033–6046.

[75] S. Raugei, S. Chen, M. H. Ho, B. Ginovska-Pangovska, R. J. Rousseau, M. Dupuis, D. L. Dubois and R. M. Bullock. "The role of pendant amines in the breaking and forming of molecular hydrogen catalyzed by nickel complexes". *Chem. - A Eur. J.*, 2012. **18**, 21, 6493–6506.

[76] P. Das, R. M. Stolley, E. F. van der Eide and M. L. Helm. "A Ni II -Bis(diphosphine)-Hydride Complex Containing Proton Relays - Structural Characterization and Electrocatalytic Studies". *Eur. J. Inorg. Chem.*, 2014. **2014**, 27, 4611–4618.

[77] R. M. Bullock, A. M. Appel and M. L. Helm. "Production of hydrogen by electrocatalysis: making the H-H bond by combining protons and hydrides." *Chem. Commun. (Camb).*, 2014. **50**, 24, 3125–43.

[78] L. Gan, T. L. Groy, P. Tarakeshwar, S. K. S. Mazinani, J. Shearer, V. Mujica and A. K. Jones. "A Nickel Phosphine Complex as a Fast and Efficient Hydrogen Production Catalyst". *J. Am. Chem. Soc.*, 2015. **137**, 3, 1109–1115.

[79] T. Jaramillo, J. Bonde and J. Zhang. "Hydrogen evolution on supported incomplete cubane-type [Mo3S4]4+ electrocatalysts". *J. Phys. Chem. C*, 2008. **112**, 45, 17492–17498.

[80] H. I. Karunadasa, E. Montalvo, Y. Sun, M. Majda, J. R. Long and C. J. Chang. "A molecular MoS2 edge site mimic for catalytic hydrogen generation." *Science*, 2012. **335**, 6069, 698–702.

[81] X. Hu, B. S. Brunschwig and J. C. Peters. "Electrocatalytic hydrogen evolution at low overpotentials by cobalt macrocyclic glyoxime and tetraimine complexes." *J. Am. Chem. Soc.*, 2007. **129**, 29, 8988–98.

[82] X. Hu, B. M. Cossairt, B. S. Brunschwig, N. S. Lewis and J. C. Peters. "Electrocatalytic hydrogen evolution by cobalt difluoroboryl-diglyoximate complexes." *Chem. Commun. (Camb).*, 2005. **1**, 37, 4723–4725.

[83] C. Baffert, V. Artero and M. Fontecave. "Cobaloximes as functional models for hydrogenases. 2. Proton electroreduction catalyzed by difluoroboryl-bis(dimethylglyoximato)cobalt(II) complexes in organic media." *Inorg. Chem.*, 2007. **46**, 5, 1817–24.

[84] N. M. Muresan, J. Willkomm, D. Mersch, Y. Vaynzof and E. Reisner. "Immobilization of a molecular cobaloxime catalyst for hydrogen evolution on a mesoporous metal oxide electrode". *Angew. Chemie - Int. Ed.*, 2012. **51**, 51, 12749–12753.

[85] D. W. Wakerley and E. Reisner. "Development and understanding of cobaloxime activity through electrochemical molecular catalyst screening." *Phys. Chem. Chem. Phys.*, 2014. **16**, 12, 5739–46.

[86] F. Lakadamyali, M. Kato, N. M. Muresan and E. Reisner. "Selective reduction of aqueous protons to hydrogen with a synthetic cobaloxime catalyst in the presence of atmospheric oxygen". *Angew. Chemie - Int. Ed.*, 2012. **51**, 37, 9381–9384.

[87] J. P. Bigi, T. E. Hanna, W. H. Harman, A. Chang and C. J. Chang. "Electrocatalytic reduction of protons to hydrogen by a water-compatible cobalt polypyridyl platform." *Chem. Commun. (Camb).*, 2010. **46**, 6, 958–60.

[88] Y. Sun, J. P. Bigi, N. a. Piro, M. L. Tang, J. R. Long and C. J. Chang. "Molecular cobalt pentapyridine catalysts for generating hydrogen from water." *J. Am. Chem. Soc.*, 2011. **133**, 24, 9212–5.

[89] Y. Sun, J. Sun, J. R. Long, P. Yang and C. J. Chang. "Photocatalytic generation of hydrogen from water using a cobalt pentapyridine complex in combination with molecular and semiconductor nanowire photosensitizers". *Chem. Sci.*, 2013. **4**, 1, 118–124.

[90] J. Luo, J. Im, M. T. Mayer, M. Schreier, M. K. Nazeeruddin, N.-G. Park, S. D. Tilley, H. J. Fan and M. Grätzel. "Water photolysis at 12.3% efficiency via perovskite photovoltaics and Earth-abundant catalysts". *Science*, 2014. **345**, 6204, 1593–1596.

[91] W. Hu and J. Lee. "Electrocatalytic properties of Ti 2 Ni/Ni-Mo composite electrodes for hydrogen evolution reaction". *Int. J. Hydrogen Energy*, 1998. **23**, 4, 253–257.

[92] W. Hu. "Electrocatalytic properties of new electrocatalysts for hydrogen evolution in alkaline water electrolysis". *Int. J. Hydrogen Energy*, 2000. **25**, 2, 111–118.

[93] A. E. Mauer, D. W. Kirk and S. J. Thorpe. "The role of iron in the prevention of nickel electrode deactivation in alkaline electrolysis". *Electrochim. Acta*, 2007. **52**, 11, 3505–3509.

[94] R. M. Abouatallah, D. W. Kirk, S. J. Thorpe and J. W. Graydon. "Reactivation of nickel cathodes by dissolved vanadium species during hydrogen evolution in alkaline media". *Electrochim. Acta*, 2001. **47**, 4, 613–621.

[95] R. Subbaraman, D. Tripkovic, K.-C. Chang, D. Strmcnik, A. P. Paulikas, P. Hirunsit, M. Chan, J. Greeley, V. Stamenkovic and N. M. Markovic. "Trends in activity for the water electrolyser reactions on 3d M(Ni,Co,Fe,Mn) hydr(oxy)oxide catalysts". *Nat. Mater.*, 2012. **11**, 6, 550–557.

[96] Z. Yin and F. Chen. "Electrochemically fabricated hierarchical porous Ni(OH)2/NiCu electrodes for hydrogen evolution reaction". *Electrochim. Acta*, 2014. **117**, 84–91.

[97] N. Danilovic, R. Subbaraman, D. Strmcnik, K. C. Chang, A. P. Paulikas, V. R. Stamenkovic and N. M. Markovic. "Enhancing the alkaline hydrogen evolution reaction activity through the bifunctionality of Ni(OH)2/metal catalysts". *Angew. Chemie - Int. Ed.*, 2012. **51**, 50, 12495–12498.

[98] K. Zeng and D. Zhang. "Recent progress in alkaline water electrolysis for hydrogen production and applications". *Prog. Energy Combust. Sci.*, 2010. **36**, 3, 307–326.

[99] A. Fujishima and K. Honda. "Electrochemical photolysis of water at a semiconductor electrode". *Nature*, 1972. **238**, 37–38.

[100] R. Asahi, T. Morikawa, T. Ohwaki, K. Aoki and Y. Taga. "Visible-light photocatalysis in nitrogen-doped titanium oxides". *Science*, 2001. **293**, 5528, 269–271.

[101] Z. Zou, J. Ye, K. Sayama and H. Arakawa. "Direct splitting of water under visible light irradiation with an oxide semiconductor photocatalyst." *Nature*, 2001. **414**, 6864, 625–7.

[102] S. U. M. Khan, M. Al-Shahry and W. B. J. Ingler. "Efficient photochemical water splitting by a chemically modified n-TiO2". *Science*, 2002. **297**, 5590, 2243–2244.

[103] M. Ni, M. K. Leung, D. Y. Leung and K. Sumathy. "A review and recent developments in photocatalytic water-splitting using TiO2 for hydrogen production". *Renew. Sustain. Energy Rev.*, 2007. **11**, 3, 401–425.

[104] C. Janáky, K. Rajeshwar, N. de Tacconi, W. Chanmanee and M. Huda. "Tungsten-based oxide semiconductors for solar hydrogen generation". *Catal. Today*, 2013. **199**, 53–64.

[105] Y. a. Shaban and S. U. M. Khan. "Carbon modified (CM)-n-TiO2 thin films for efficient water splitting to H2 and O2 under xenon lamp light and natural sunlight illuminations". *J. Solid State Electrochem.*, 2009. **13**, 7, 1025–1036.

[106] J. Tang, J. R. Durrant and D. R. Klug. "Mechanism of photocatalytic water splitting in TiO2. Reaction of water with photoholes, importance of charge carrier dynamics, and evidence for four-hole chemistry". *J. Am. Chem. Soc.*, 2008. **130**, 42, 13885–13891.

[107] M. Ashokkumar. "An overview on semiconductor particulate systems for photoproduction of hydrogen". *Int. J. Hydrogen Energy*, 1998. **3199**, 97, 427–438.

[108] A. Koca and M. \c{S}ahin. "Photocatalytic hydrogen production by direct sun light from sulfide/sulfite solution". *Int. J. Hydrogen Energy*, 2002. **27**, 363–367.

[109] K. Gurunathan, P. Maruthamuthu and M. V. C. Sastri. "Photocatalytic hydrogen production by dye-sensitized Pt/SnO2 and Pt/SnO2/RuO2 in aqueous methyl viologen solution". *Int. J. Hydrogen Energy*, 1997. **22**, 1, 57–62.

[110] A. W. Mau, C.-b. Huang, N. Kakuta, A. J. Bard, A. Campion, M. A. Fox, J. M. White and S. E. Webber. "H2 Photoproduction by Nafion/CdS/Pt Films in H20/S2- Solutions". *Am. Chem. Soc.*, 1984. **106**, 22, 6537–6542.

[111] G. Hitoki, T. Takata, J. N. Kondo, M. Hara, H. Kobayashi and K. Domen. "An oxynitride, TaON, as an efficient water oxidation photocatalyst under visible light irradiation". *Chem. Commun. (Camb).*, 2002. **2**, 16, 1698–9.

[112] M. Liu, W. You, Z. Lei, G. Zhou, J. Yang, G. Wu, G. Ma, G. Luan, T. Takata, M. Hara, K. Domen and C. Li. "Water reduction and oxidation on Pt-Ru/Y2Ta2O5N2 catalyst under visible light irradiation." *Chem. Commun. (Camb).*, 2004, 2192–2193.

[113] Y. Lee and H. Terashima. "Zinc germanium oxynitride as a photocatalyst for overall water splitting under visible light". *J. Phys. Chem. C*, 2007. **111**, 001, 1042–1048.

[114] A. Ishikawa, T. Takata, J. N. Kondo, M. Hara, H. Kobayashi and K. Domen. "Oxysulfide Sm(2)Ti(2)S(2)O(5) as a stable photocatalyst for water oxidation and reduction under visible light irradiation (lambda < or = 650 nm)." *J. Am. Chem. Soc.*, 2002. **124**, 45, 13547–53.

[115] C. E. Lubner, R. Grimme, D. a. Bryant and J. H. Golbeck. "Wiring photosystem I for direct solar hydrogen production." *Biochemistry*, 2010. **49**, 3, 404–14.

[116] H. Krassen, A. Schwarze, B. Friedrich and K. Ataka. "Photosynthetic hydrogen production by a hybrid complex of photosystem I and -hydrogenase". *ACS Nano*, 2009. **3**, 12, 4055–4061.

[117] E. Reisner, D. J. Powell, C. Cavazza, J. C. Fontecilla-Camps and F. a. Armstrong. "Visible light-driven H(2) production by hydrogenases attached to dye-sensitized TiO(2) nanoparticles." *J. Am. Chem. Soc.*, 2009. **131**, 51, 18457–66.

[118] U. Mueller-Westerhoff, A. Nazzal, H. Dreyfus and A. P. Sloan. "Ferrocenophanes as effective catalysts in the photoelectrochemical hydrogen evolution from acidic aqueous media". *J. Am. Chem. Soc.*, 1984. **106**, 5381–5382.

[119] T. Nann, S. K. Ibrahim, P.-M. Woi, S. Xu, J. Ziegler and C. J. Pickett. "Water splitting by visible light: a nanophotocathode for hydrogen production." *Angew. Chem. Int. Ed. Engl.*, 2010. **49**, 9, 1574–7.

[120] Y. Xu, X. Yin, Y. Huang, P. Du and B. Zhang. "Hydrogen Production on a Hybrid Photocatalytic System Composed of Ultrathin CdS Nanosheets and a Molecular Nickel Complex". *Chem. - A Eur. J.*, 2015. **21**, 4571–4575.

[121] R. Sasikala, a.P. Gaikwad, O. Jayakumar, K. Girija, R. Rao, a.K Tyagi and S. Bharadwaj. "Nanohybrid MoS2-PANI-CdS photocatalyst for hydrogen evolution from water". *Colloids Surfaces A Physicochem. Eng. Asp.*, 2015. **481**, 485–492.

[122] J. Huang, K. L. Mulfort, P. Du and L. X. Chen. "Photodriven charge separation dynamics in CdSe/ZnS core/shell quantum dot/cobaloxime hybrid for efficient hydrogen production". *J. Am. Chem. Soc.*, 2012. **134**, 40, 16472–16475.

[123] S. W. Seo, S. Park, H.-Y. Jeong, S. H. Kim, U. Sim, C. W. Lee, K. T. Nam and K. S. Hong. "Enhanced performance of NaTaO3 using molecular co-catalyst [Mo3S4]4+ for water splitting into H2 and O2." *Chem. Commun. (Camb).*, 2012. **48**, 84, 10452–4.

[124] Y. Hou, B. L. Abrams, P. C. K. Vesborg, M. E. Björketun, K. Herbst, L. Bech, A. M. Setti, C. D. Damsgaard, T. Pedersen, O. Hansen, J. Rossmeisl, S. Dahl, J. K. Norskov and I. Chorkendorff. "Bioinspired molecular co-catalysts bonded to a silicon photocathode for solar hydrogen evolution." *Nat. Mater.*, 2011. **10**, 6, 434–438.

[125] M. Wang, Y. Na, M. Gorlov and L. Sun. "Light-driven hydrogen production catalysed by transition metal complexes in homogeneous systems." *Dalton Trans.*, 2009, 6458–6467.

[126] X. Li, M. Wang, S. Zhang, J. Pan, Y. Na, J. Liu, B. Akermark and L. Sun. "Noncovalent assembly of a metalloporphyrin and an iron hydrogenase active-site model: photoinduced electron transfer and hydrogen generation." *J. Phys. Chem. B*, 2008. **112**, 27, 8198–202.

[127] Z. Han, L. Shen, W. W. Brennessel, P. L. Holland and R. Eisenberg. "Nickel pyridinethiolate complexes as catalysts for the light-driven production of hydrogen from aqueous solutions in noble-metal-free systems". *J. Am. Chem. Soc.*, 2013. **135**, 39, 14659–14669.

[128] A. Fihri, V. Artero, A. Pereira and M. Fontecave. "Efficient H2-producing photocatalytic systems based on cyclometalated iridium- and tricarbonylrhenium-diimine photosensitizers and cobaloxime catalysts." *Dalton Trans.*, 2008, 5567–5569.

[129] A. Fihri, V. Artero, M. Razavet, C. Baffert, W. Leibl and M. Fontecave. "Cobaloxime-based photocatalytic devices for hydrogen production". *Angew. Chemie - Int. Ed.*, 2008. **47**, 3, 564–567.

[130] C. Li, M. Wang, J. Pan, P. Zhang, R. Zhang and L. Sun. "Photochemical hydrogen production catalyzed by polypyridyl ruthenium-cobaloxime heterobinuclear complexes with different bridges". *J. Organomet. Chem.*, 2009. **694**, 17, 2814–2819.

[131] J. R. Long, C. J. Chang and F. N. Castellano. "Towards a comprehensive understanding of visible- light photogeneration of hydrogen from water using cobalt (II) polypyridyl catalysts". *Energy Environ. Sci.*, 2014. **7**, 1477–1488.

[132] S. Fukuzumi, Y. Yamada, T. Suenobu, K. Ohkubo and H. Kotani. "Catalytic mechanisms of hydrogen evolution with homogeneous and heterogeneous catalysts". *Energy Environ. Sci.*, 2011. **4**, 8, 2754.

[133] V. Artero and M. Fontecave. "Solar fuels generation and molecular systems: is it homogeneous or heterogeneous catalysis?" *Chem. Soc. Rev.*, 2013. **42**, 6, 2338–56.

[134] K. G. U. Wijayantha. "Photoelectrochemical cells for hydrogen generation". In J. A. Kilner, S. J. Kinner, S. J. Irvine and P. P. Edwards (editors), "Functional Materials for Solar Power", chapter 5. Woodhead Publishing Limited, Cambridge, 2012. pp. 91–145.

[135] M. Bowker. "Sustainable hydrogen production by the application of ambient temperature photocatalysis". *Green Chem.*, 2011. **13**, 9, 2235–2246.

[136] M. Grätzel. "Photoelectrochemical cells". *Nature*, 2001. **414**, November.

[137] A. Elschner, S. Kirchmeyer, W. Lövenich, U. Merker and K. Reuter. "The Discovery and Development of Conducting Polymers". In "PEDOT Principles and Applications of an Intrinsically Conductive Polymer", chapter 1. CRC Press, 2010. pp. 1–20.

[138] T. Skotheim and J. Reynolds. *Conjugated Polymers: Theory, Synthesis, Properties, and Characterization*. CRC Press, Boca Raton, Fl, 3rd edition, 2006.

[139] A. Elschner, S. Kirchmeyer, W. Lövenich, U. Merker and K. Reuter. "Polythiophenes: A Chance for Maximum Conductivity?" In "PEDOT Principles and Applications of an Intrinsically Conductive Polymer", chapter 3. CRC Press, 2011. pp. 31–40.

[140] A. Elschner, S. Kirchmeyer, W. Lövenich, U. Merker and K. Reuter. "Conductive Polymers versus Metals and Insulators". In "PEDOT Principles and Applications of an Intrinsically Conductive Polymer", chapter 2. CRC Press, 2011. pp. 21–30.

[141] A. J. Heeger. "Semiconducting and Metallic Polymers: The Fourth Generation of Polymeric Materials". *J. Phys. Chem. B*, 2001. **105**, 36, 8475–8491.

[142] J. Bredas and G. Street. "Polarons, bipolarons, and solitons in conducting polymers". *Acc. Chem. Res.*, 1985. **1305**, 4, 309–315.

[143] A. Pron, P. Gawrys, M. Zagorska, D. Djurado and R. Demadrille. "Electroactive materials for organic electronics: preparation strategies, structural aspects and characterization techniques." *Chem. Soc. Rev.*, 2010. **39**, 7, 2577–2632.

[144] Z.-g. Xu and G. Horowitz. "From oligomers to polymer. An insight into the electrochemical doping-dedoping of polythiophene from electrochemical data on thiophene oligomers". *J. Electroanal. Chem.*, 1992. **335**, 123–134.

[145] S. Cook, A. Furube and R. Katoh. "Analysis of the excited states of regioregular polythiophene P3HT". *Energy Environ. Sci.*, 2008. **1**, 2, 294.

[146] Y. Aoyama, T. Yamanari, N. Koumura, H. Tachikawa, M. Nagai and Y. Yoshida. "Photo-induced oxidation of polythiophene derivatives: Dependence on side chain structure". *Polym. Degrad. Stab.*, 2013. **98**, 4, 899–903.

[147] M. Springborgt. "The electronic properties of polythiophene". *J. Phys. Condens. Matter*, 1992. **4**, 101–120.

[148] R. S. Becker, J. S. de Melo, a. L. Macanita and F. Elisei. "Comprehensive investigation of the solution photophysics and theoretical aspects of oligothiophenes of 1-7 rings". *Pure Appl. Chem.*, 1995. **67**, 1, 9–16.

[149] A. Åslund, K. P. R. Nilsson and P. Konradsson. "Fluorescent oligo and poly-thiophenes and their utilization for recording biological events of diverse origin-when organic chemistry meets biology". *J. Chem. Biol.*, 2009. **2**, 4, 161–175.

[150] I. F. Perepichka, D. F. Perepichka, H. Meng and F. Wudl. "Light-emitting polythiophenes". *Adv. Mater.*, 2005. **17**, 19, 2281–2305.

[151] T. Granlund, M. Theander, M. Berggren, M. Andersson, A. Ruzeckas, V. Sundström, G. Björk, M. Granström and O. Inganäs. "A polythiophene microcavity laser". *Chem. Phys. Lett.*, 1998. **288**, 5-6, 879–884.

[152] M. S. A. Abdou and S. Holdcroft. "Photochemical Processes of Conductive Polymers". In H. S. Nalwa (editor), "Organic Conductive Molecules and Polymers: Vol. 4. Conductive Polymers: Transport, Photophysics and Applications", chapter 4. John Wiley & Sons Ltd, Chichester, UK, 1997. pp. 173–229.

[153] H. Saadeh, T. Goodson and L. Yu. "Synthesis of a Polyphenylene-co-furan and Polyphenylene-co-thiophene and Comparison of Their Electroluminescent Properties". *Macromolecules*, 1997. **30**, 16, 4608–4612.

[154] B. Kraabel, D. Moses and a. J. Heeger. "Direct observation of the intersystem crossing in poly(3-octylthiophene)". *J. Chem. Phys.*, 1995. **103**, 12, 5102–5108.

[155] D. Beljonne, Z. Shuai, G. Pourtois and J. L. Bredas. "Spin - Orbit Coupling and Intersystem Crossing in Conjugated Polymers: A Configuration Interaction Description". *J. Phys. Chem. A*, 2001. **105**, 15, 3899–3907.

[156] M. Koch, R. Nicolaescu and P. V. Kamat. "Photodegradation of polythiophene-based polymers: Excited state properties and radical intermediates". *J. Phys. Chem. C*, 2009. **113**, 27, 11507–11513.

[157] I. Haeldermans, K. Vandewal, W. D. Oosterbaan, a. Gadisa, J. D'Haen, M. K. Van Bael, J. V. Manca and J. Mullens. "Ground-state charge-transfer complex formation in hybrid poly(3-hexyl thiophene):titanium dioxide solar cells". *Appl. Phys. Lett.*, 2008. **93**, 22, 18–21.

[158] M. S. a. Abdou, F. P. Orfino, Z. W. Xie, M. J. Deen and S. Holdcroft. "Reversible Charge Transfer Complexes Between Molecular Oxygen and Poly(3-alkylthiophene)s". *Adv. Mater.*, 1994. **6**, 11, 838–841.

[159] M. Kobayashi, J. Chen, T.-C. Chung, F. Moraes, a.J. Heeger and F. Wudl. "Synthesis and properties of chemically coupled poly(thiophene)". *Synth. Met.*, 1984. **9**, 1, 77–86.

[160] F. Group. "Applications". In "PEDOT Principles and Applications of an Intrinsically Conductive Polymer", chapter 10. CRC Press, 2011. pp. 167–264.

[161] D. Bhattacharyya, R. M. Howden, D. C. Borrelli and K. K. Gleason. "Vapor phase oxidative synthesis of conjugated polymers and applications". *J. Polym. Sci. Part B Polym. Phys.*, 2012. **50**, 19, 1329–1351.

[162] X. Li, W. Lu, W. Dong, Q. Chen, D. Wu, W. Zhou and L. Chen. "Si/PEDOT hybrid core/shell nanowire arrays as photoelectrodes for photoelectrochemical water-splitting." *Nanoscale*, 2013. **5**, 12, 5257–61.

[163] N. Srinivasan, Y. Shiga, D. Atarashi, E. Sakai and M. Miyauchi. "A PEDOT-coated quantum dot as efficient visible light harvester for photocatalytic hydrogen production". *Appl. Catal. B Environ.*, 2015. **179**, 113–121.

[164] M. R. Andersson, O. Thomas, W. Mammo, M. Svensson, M. Theander and O. Inganäs. "Substituted polythiophenes designed for optoelectronic devices and conductors". *J. Mater. Chem.*, 1999. **9**, 9, 1933–1940.

[165] C. Cutler, A. Burrell, D. Officer, C. Too and G. Wallace. "Effect of electron withdrawing or donating substituents on the photovoltaic performance of polythiophenes". *Synth. Met.*, 2002. **128**, 1, 35–42.

[166] I. F. Perepichka and D. F. Perepichka. *Handbook of Thiophene-Based Materials: Applications in Organic Electronics and Photonics*. John Wiley & Sons, Ltd, Chichester, UK, 2009.

[167] J. a. Hauch, P. Schilinsky, S. a. Choulis, R. Childers, M. Biele and C. J. Brabec. "Flexible organic P3HT:PCBM bulk-heterojunction modules with more than 1 year outdoor lifetime". *Sol. Energy Mater. Sol. Cells*, 2008. **92**, 7, 727–731.

[168] G. Li, V. Shrotriya, J. Huang, Y. Yao, T. Moriarty, K. Emery and Y. Yang. "High-efficiency solution processable polymer photovoltaic cells by self-organization of polymer blends". *Nat. Mater.*, 2005. **4**, 11, 864–868.

[169] P. E. Shaw, A. Ruseckas and I. D. W. Samuel. "Exciton diffusion measurements in poly(3-hexylthiophene)". *Adv. Mater.*, 2008. **20**, 18, 3516–3520.

[170] M. Manceau, A. Rivaton, J. L. Gardette, S. Guillerez and N. Lemaître. "The mechanism of photo- and thermooxidation of poly(3-hexylthiophene) (P3HT) reconsidered". *Polym. Degrad. Stab.*, 2009. **94**, 6, 898–907.

[171] M. Jørgensen, K. Norrman, S. a. Gevorgyan, T. Tromholt, B. Andreasen and F. C. Krebs. "Stability of polymer solar cells." *Adv. Mater.*, 2012. **24**, 5, 580–612.

[172] F. Terzi, C. Zanardi, V. Martina, L. Pigani and R. Seeber. "Electrochemical, spectroscopic and microscopic characterisation of novel poly(3,4-ethylenedioxythiophene)/gold nanoparticles composite materials". *J. Electroanal. Chem.*, 2008. **619-620**, 75–82.

[173] C. Arbizzani, M. Biso, E. Manferrari and M. Mastragostino. "Methanol oxidation by pEDOT-pSS/PtRu in DMFC". *J. Power Sources*, 2008. **178**, 2, 584–590.

[174] S.-J. Wang and H.-H. Park. "Properties of one-step synthesized Pt nanoparticle-doped poly(3,4-ethylenedioxy thiophen):poly(styrenesulfonate) hybrid films". *Thin Solid Films*, 2010. **518**, 24, 7185–7190.

[175] C. Lamy, J.-M. Leger and F. Garnier. "Electrocatalytic Properties of Conductive Polymers". In H. S. Nalwa (editor), "Organic Conductive Molecules and Polymers: Vol. 3. Conductive Polymers: Spectroscopy and Physical Properties", chapter 10. John Wiley & Sons Ltd, Chichester, UK, 1997. pp. 471–493.

[176] C. Gu, B. C. Norris, F.-R. F. Fan, C. W. Bielawski and A. J. Bard. "Is Base-Inhibited Vapor Phase Polymerized PEDOT an Electrocatalyst for the Hydrogen Evolution Reaction? Exploring Substrate Effects, Including Pt Contaminated Au". *ACS Catal.*, 2012. **2**, 5, 746–750.

[177] R. Kerr, C. Pozo-gonzalo, M. Forsyth and B. Winther-jensen. "Electrochimica Acta The Reduction of Oxygen on Iron (II) Oxide / Poly (3 , 4- ethylenedioxythiophene) Composite Thin Film Electrodes". *Electrochim. Acta*, 2015. **154**, 142–148.

[178] B. Winther-Jensen and K. West. "Vapor-Phase Polymerization of 3,4-Ethylenedioxythiophene: A Route to Highly Conducting Polymer Surface Layers". *Macromolecules*, 2004. **37**, 12, 4538–4543.

[179] R. Kerr, C. Pozo-Gonzalo, M. Forsyth and B. Winther-Jensen. "Influence of the Polymerization Method on the Oxygen Reduction Reaction Pathway on PEDOT". *ECS Electrochem. Lett.*, 2013. **2**, 3, F29–F31.

[180] B. Winther-Jensen, O. Winther-Jensen, M. Forsyth and D. R. Macfarlane. "High rates of oxygen reduction over a vapor phase-polymerized PEDOT electrode." *Science*, 2008. **321**, 5889, 671–4.

[181] V. G. Khomenko, V. Z. Barsukov and a. S. Katashinskii. "The catalytic activity of conducting polymers toward oxygen reduction". *Electrochim. Acta*, 2005. **50**, 7-8, 1675–1683.

[182] P. P. Cottis, D. Evans, M. Fabretto, S. Pering, P. Murphy and P. Hojati-Talemi. "Metal-free oxygen reduction electrodes based on thin PEDOT films with high electrocatalytic activity". *RSC Adv.*, 2014. **4**, 19, 9819.

[183] B. Reeja-Jayan, P. Kovacik, R. Yang, H. Sojoudi, A. Ugur, D. H. Kim, C. D. Petruczok, X. Wang, A. Liu and K. K. Gleason. "A Route Towards Sustainability Through Engineered Polymeric Interfaces". *Adv. Mater. Interfaces*, 2014, 1–30.

[184] B. Winther-Jensen and D. R. MacFarlane. "New generation, metal-free electrocatalysts for fuel cells, solar cells and water splitting". *Energy Environ. Sci.*, 2011. **4**, 8, 2790.

[185] M. Zhang, W. Yuan, B. Yao, C. Li and G. Shi. "Solution-processed PEDOT:PSS/graphene composites as the electrocatalyst for oxygen reduction reaction". *ACS Appl. Mater. Interfaces*, 2014. **6**, 5, 3587–3593.

[186] K. Xie, H. Wu, Y. Meng, K. Lu, Z. Wei and Z. Zhang. "Poly(3,4-dinitrothiophene)/SWCNT composite as a low overpotential hydrogen evolution metal-free catalyst". *J. Mater. Chem. A*, 2015. **3**, 1, 78–82.

[187] P. P. Cottis, D. Evans, M. Fabretto, S. Pering, P. Murphy and P. Hojati-Talemi. "Metal-free oxygen reduction electrodes based on thin PEDOT films with high electrocatalytic activity". *RSC Adv.*, 2014. **4**, 19, 9819.

[188] B. Kolodziejczyk, O. Winther-Jensen, D. R. MacFarlane and B. Winther-Jensen. "Conducting polymer alloys for photo-enhanced electro-catalytic oxygen reduction". *J. Mater. Chem.*, 2012. **22**, 21, 10821–10826.

[189] M. P. Gustafson, K. Matsumoto, D. R. MacFarlane and B. Winther-Jensen. "An investigation of the properties of conducting polymer alloys for water oxidation". *Electrochim. Acta*, 2014. **122**, 166–172.

[190] M. Kaneko. "Photoelectric Conversion by Polymeric and Organic Materials". In H. S. Nalwa (editor), "Organic Conductive Molecules and Polymers: Vol. 4. Conductive Polymers: Transport, Photophysics and Applications", chapter 13. John Wiley & Sons Ltd, Chichester, UK, 1997. pp. 661–692.

[191] O. Winther-Jensen, B. Winther-Jensen and D. R. MacFarlane. "Photostimulated electrocatalysis of water oxidation by conjugated polymers". *Electrochem. commun.*, 2011. **13**, 4, 307–309.

[192] J. Chen, P. Wagner, L. Tong, G. G. Wallace, D. L. Officer and G. F. Swiegers. "A porphyrin-doped polymer catalyzes selective, light-assisted water oxidation in seawater". *Angew. Chemie - Int. Ed.*, 2012. **51**, 8, 1907–1910.

[193] J. Chen, P. Wagner, L. Tong, D. Boskovic, W. Zhang, D. Officer, G. G. Wallace and G. F. Swiegers. "A light-assisted, polymeric water oxidation catalyst that selectively oxidizes seawater with a low onset potential". *Chem. Sci.*, 2013. **4**, 7, 2797–2803.

[194] E. Lanzarini, M. R. Antognazza, M. Biso, A. Ansaldo, L. Laudato, P. Bruno, P. Metrangolo, G. Resnati, D. Ricci and G. Lanzani. "Polymer-Based Photocatalytic Hydrogen Generation". *J. Phys. Chem. C*, 2012. **116**, 20, 10944–10949.

[195] S. Bellani, D. Fazzi, P. Bruno, E. Giussani, E. V. Canesi, G. Lanzani, M. R. Antognazza, D. Fisica, D. Chimica, I. Chimica, P. Milano and P. L. Da. "Reversible P3HT/Oxygen Charge Transfer Complex Identi fi cation in Thin Films Exposed to Direct Contact with Water". *J. Phys. Chem. C*, 2014.

[196] R. K. Kanaparthi, J. Kandhadi and L. Giribabu. "Metal-free organic dyes for dye-sensitized solar cells: recent advances". *Tetrahedron*, 2012. **68**, 40, 8383–8393.

[197] P. Shen, X. Liu, S. Jiang, L. Wang, L. Yi, D. Ye, B. Zhao and S. Tan. "Synthesis of new N, N-diphenylhydrazone dyes for solar cells: Effects of thiophene-derived π-conjugated bridge". *Dye. Pigment.*, 2012. **92**, 3, 1042–1051.

[198] L. Li, L. Duan, F. Wen, C. Li, M. Wang, A. Hagfeldt and L. Sun. "Visible light driven hydrogen production from a photo-active cathode based on a molecular catalyst and organic dye-sensitized p-type nanostructured NiO." *Chem. Commun. (Camb).*, 2012. **48**, 7, 988–90.

[199] E. Lansing, Z. Bi and H. T. Tien. "Photoproduction of hydrogen by dye-sensitized systems". *Int. J. Hydrogen Energy*, 1984. **9**, 8, 717–722.

[200] K. Dhanalakshmi. "Dye sensitized hydrogen evolution from water". *Int. J. Hydrogen Energy*, 2001. **26**, 7, 669–674.

[201] R. Abe, K. Sayama and H. Arakawa. "Dye-sensitized photocatalysts for efficient hydrogen production from aqueous I- solution under visible light irradiation". *J. Photochem. Photobiol. A Chem.*, 2004. **166**, 1-3, 115–122.

[202] S. K. Choi, H. S. Yang, J. H. Kim and H. Park. "Organic dye-sensitized TiO2 as a versatile photocatalyst for solar hydrogen and environmental remediation". *Appl. Catal. B Environ.*, 2012. **121-122**, 206–213.

[203] C. Orain, F. Quentel and F. Gloaguen. "Photocatalytic hydrogen production using models of the iron-iron hydrogenase active site dispersed in micellar solution". *ChemSusChem*, 2014. **7**, 2, 638–643.

[204] W. Zhang and R. Xu. "Hybrid photocatalytic H2 evolution systems containing xanthene dyes and inorganic nickel based catalysts". *Int. J. Hydrogen Energy*, 2012. **37**, 23, 17899–17909.

[205] H. Wang and J. P. Lewis. "Second-generation photocatalytic materials: anion-doped TiO 2". *J. Phys. Condens. Matter*, 2006. **18**, 2, 421–434.

[206] J. F. Mike, K. Nalwa, A. J. Makowski, D. Putnam, A. L. Tomlinson, S. Chaudhary and M. Jeffries-El. "Synthesis, characterization and photovoltaic properties of poly(thiophenevinylene-alt-benzobisoxazole)s." *Phys. Chem. Chem. Phys.*, 2011. **13**, 4, 1338–44.

[207] A. Baheti, P. Singh, C.-P. Lee, K. R. J. Thomas and K.-C. Ho. "2,7-Diaminofluorene-based organic dyes for dye-sensitized solar cells: effect of auxiliary donor on optical and electrochemical properties." *J. Org. Chem.*, 2011. **76**, 12, 4910–20.

[208] A. L. Speelman and J. G. Gillmore. "Efficient computational methods for accurately predicting reduction potentials of organic molecules." *J. Phys. Chem. A*, 2008. **112**, 25, 5684–90.

[209] E. Lynch and A. Speelman. "and Testing a Computational Method for Predicting the Ground State Reduction Potentials of Organic Molecules on the Basis of Empirical Correlation to Experiment". *J. Org. Chem.*, 2012. **77**, 6423–6430.

Chapter 2

Materials and Methods

2.1 Materials and Preparation

The experimental methods used are described in detail below. This includes the preparation, synthesis, experimental parameters used as well as a small overview on more important and novel analysis techniques. The initial sections show the preparation and synthesis steps of the films and their various components, while the later sections focus on experimental techniques and parameters.

2.1.1 Substrates

A variety of substrates were utilised though they follow three main groups: gold substrates, glass substrates and glassy carbon substrates. The chief role of the substrate is to provide a conducting surface with which to transfer charge to the film using minimal resistance. Good adherence of the film is also important as is a clean background where the substrate is inert throughout the investigated electrochemical window.

Gold substrates

The gold substrates comprised of gold that was sputtered coated onto mylar and polytetrafluoroethylene (PTFE) film, known as the "gold mylar" and "gold Gortex" respectively. Gold mylar was acquired commercially through CPFilms Inc. USA and was used after trace amounts of dust were removed with an air gun.

The gold Goretex samples were prepared in-house via two main steps. First, a plasma treatment of the Goretex film was conducted using the deposition and polymerisation of maleic anhydride to form a binding layer. Second was the spluttering of a thin layer of gold using an SPI Sputter Coater under Ar gas to form gold Goretex. Further details on this method and the maleic anhydride plasma treatment can be found in work by the Winther-Jensen group.[1,2] Occasionally, for more conductive films such as PEDOT, the second gold spluttering step was forgone and the plasma treated Gortex film was used as is; this is referred to as the "Gortex" substrate.

Glass substrates

The glass substrates consisted of two different types, the glass slide for films that do not require electrochemistry, and fluorine-doped tin oxide (FTO) glass for electrochemical analysis that required a transparent substrate. Typically, these glass substrates would be rinsed in ethanol and acetone before being blown dry with an air gun. Occasionally, a plasma treatment of maleic anhydride would be used, this would be referred to as plasma-treated glass substrates.

Glassy Carbon

The glassy carbon substrates were polished prior to polymerisation. A 50 μm Al_2O_3/H_2O paste was first used to remove the previous film along with any scratches or defects on the glassy carbon. Once clean, a fine 1 μm diamond suspension was used to polish the glassy carbon until a mirror finish was reached. The substrate was then rinsed in water and ultrasonicated in a 1:1 mixture of H_2O and ethanol for 60 min to remove residual diamond suspension. A final rinse in ethanol and acetone followed drying with an air gun resulted in the usable glassy carbon substrate.

2.1.2 Dyes

The dyes used for initial testing were obtained from a variety of sources, namely: Sigma Aldrish (Coomassie Brilliant Blue G250, Ethyl Violet, Malachite Green, Brilliant Green and p-Rosolic Acid), the British Drug House (Crystal Violet, Cresol Red, and Catechol Violet), May and Baker (m-Cresol Purple) and Fluka AG (Phenol Red). The dyes were used as is without further purification though they were dried thoroughly at 70 °C to remove residual water contaminants.

2.1.3 Vapour Phase Polymerisation

The vapour phase polymerisation (VPP) technique was used extensively to produce the conducting polymer films. To conduct VPP, an enclosed chamber containing a small amount of the monomer is heated so that it vaporises to form an atmosphere containing monomer vapour inside the chamber. When the monomer vapour comes into contact with an oxidant coated on the substrate, it is oxidised which allows it to then undergo polymerisation with the surrounding monomers.[3,4]
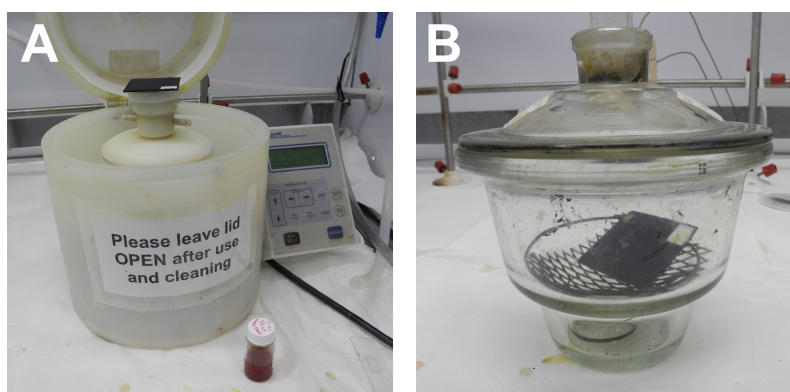
Figure 2.1: A: The spin coater used for depositing the oxidant onto the substrate and **B:** one of the VPP chambers used synthesising PEDOT.

Typically, a 40 w/v% Fe(III)PTS$_3$ in BtOH oxidant precursor solution was spin coated onto a prepared substrate at 1500 RPM for 30 s and then placed into a preheated polymerisation chamber (Figure 2.1). The chamber + substrate was then placed in a 70 °C oven and left to undergo VPP, 30 min for PEDOT, and 60 min for PBTh. The resulting polymer film was then taken out and rinsed in ethanol, followed by an overnight soak ($\approx$ 18 h) also in ethanol, to remove residual Fe species. A final rinse with ethanol was performed to remove the last traces of Fe and complete the synthesis step of the polymer film. For some films, $1\,\mathrm{mmol\,L^{-1}}$ para-toluene sulphonic acid (PTSa) was used for the wash steps instead of ethanol.

Dye blends

In the some experiments, the polymer films were blended with dyes to serve as a light harvester/catalyst. These dye/ICP blends were formed by dissolving a specified amount of dye into the oxidant solution which allows the ICP to polymerise around the dye. The amount of dye dissolved was calculated as a ratio based on the expected volume of polymer film vs volume of dye. The oxidant solution (with dye) would then be spin coated and polymerised via VPP as per usual. After the VPP step, the dye was mostly entrapped by the interlocking layers of ICP, though strong solvents could remove the dyes. Thus, the wash solutions were tailored to minimise the escape of dye; a water wash was used for organic soluble dyes, while pH adjustments were used for water soluble dyes to keep them in a non-ionic form. Once dried, dye/ICP films did not show significant leaching of dye during electrochemical experiments.

Films of Different Thicknesses

Conducting polymer films with different thickness were also prepared by diluting the original 40% Fe(III)PTS BtOH oxidant. A "half" thickness film is prepared using a 20% Fe(III)PTS BtOH oxidant solution while a "quarter" thickness is prepared using a 10% solution, see Figure 2.3A. A "double" film was made by performing two VPP process back to back, where after the first VPP, the film was taken out and another layer of precursor was deposited for the second VPP.

Films Exposed to Humidity

In general, exposure to humidity during the production step was avoided since it can lead to the formation of crystallites that affect conductivity. However, in certain studies it was necessary to expose the spin coated oxidant solution to ambient or artificial humidity. This was achieved either by exposing the oxidant to air (noting down the time, temperature and ambient humidity levels) or via placement inside a humidity chamber (Figure 2.2). The humidity chamber consisted of a saturated aqueous NaCl solution in a glass desiccator and maintained a constant humidity of 75%.[5]

Figure 2.2: The humidity chamber with saturated NaCl solution and constant humidity at 75%

2.1.4 The Standard Film

The most commonly used sample for our investigation was a PBTh film polymerised on glassy carbon using 40% Fe(III)PTS and washed in ethanol (sometimes referred to as "single" thickness), Figure 2.3B. This is assigned as the "standard film" and will be referred to thusly in the proceeding discussions.
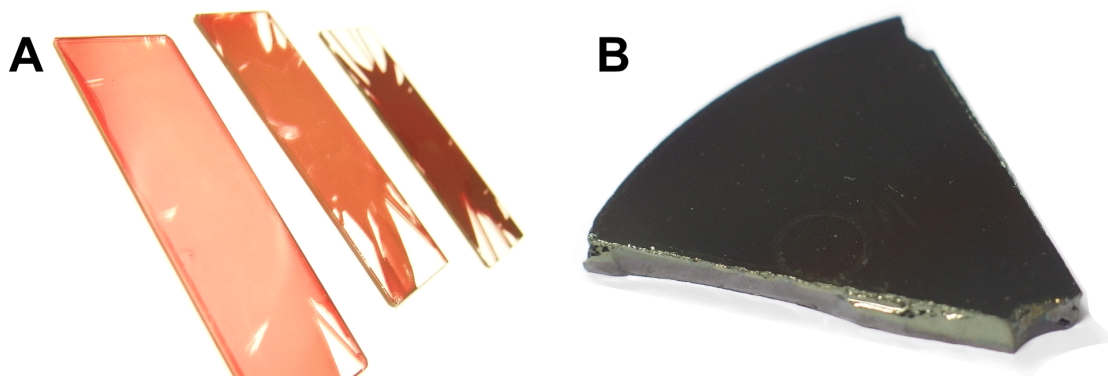
Figure 2.3: (A) PBTh of different thickness on glass slides, from left to right, a quarter, half and single film. (B) The standard film of PBTh on glassy carbon.

2.1.5 Light Source

A Leica KL2500 LCD lamp with a halogen bulb was generally used as the light source to provide illumination of the film. A setting of 4E was commonly used with an average intensity of 0.4 suns at the general working distance of our films (1.5–2 cm) as calibrated by a Si chip. However the intensity could vary depending on the age of the light bulb, hence for experiments where photo-intensity was critical, the lamp output was measured and reported. The results within the same set of experiments are generally comparable but this effect should be noted when considering longer term testing or tests conducted far apart.

2.2 Components for Electrochemistry

2.2.1 Working Electrodes

The working electrode (WE) for the most part consisted of the polymerised film – PEDOT/PBTh and their variants – on their respective substrates. For dye characterisation, the working electrode was a Pt wire immersed in the dye solution.

2.2.2 Electrolyte

Phosphate buffer (PB) was the most commonly used electrolyte for testing. Typically a $0.1 \, \text{mol} \, \text{L}^{-1}$ solution of pH 7 was prepared by mixing a 0.91:1 molar ratio of NaH_2PO_4:Na_2HPO_4; obtained from Merck and used as is. PB of different pH and buffer concentrations were also used, in which case the molar ratio and amount of NaH_2PO_4 and Na_2HPO_4 were adjusted accordingly and the desired pH was confirmed by measurements from a pH probe. Sodium chloride solutions also used and were made up by the dissolution of NaCl (from Merck) in water to the required concentration.

Non-aqueous electrolytes, namely anhydrous acetonitrile (Acn) and anhydrous propylene carbonate (PC) were used for dye and film characterisation; both solvents were obtained from Sigma Aldrich. As these solvents are hygroscopic, pre-dried 4 Å molecular sieves were added to the solutions to remove any trace amounts of water, they were then stored under a N_2 atmosphere.

2.2.3 Counter Electrodes

The counter electrode (CE) used for electrochemistry were typically titanium mesh electrodes with a mixed metal oxide coating from Savcor ART Pty Ltd. The Ti mesh electrodes were selected for their large surface area and the ease in which the water oxidation reaction could occur, thus making a good anode to compliment the reduction reactions at the working electrode. Furthermore, the absence of platinum was highly desirable as it eliminated the risk of Pt contamination. Alternative counter electrodes including Pt, stainless steel, glassy carbon and graphite counter electrodes were also utilised when the electrochemical cell set-up did not allow for a Ti mesh electrode; mainly as a result of size limitations.

2.2.4 Reference Electrodes

Two main types of reference electrodes (RE) were used in aqueous electrolytes, the saturated calomel electrode (SCE) and the silver chloride reference electrode (Ag/AgCl), these were

obtained commercially from Cole Parmer and BASi respectively; the concentration of chloride in the Ag/AgCl reference was $3\,mol\,L^{-1}$ (NaCl), thus the electrode is $207\,mV$ vs SHE. Typically, the SCE was used for earlier tests in the initial plastic cell while the Ag/AgCl electrode was used in the custom designed metal and plastic cells, see section 2.2.5 for more details.

For non-aqueous electrolytes, a platinum wire was used as a pseudo-reference electrode in conjunction with ferrocene. The required CV was first conducted vs Pt wire, Fc/Fc^+ was then added for a second CV vs Fc/Fc^+. Comparison between the two allowed the determination of the potential vs Fc/Fc^+ for the first (clean) CV.

2.2.5 Electrochemical Cells

Initial non-gas tight cells were useful for preliminary electrochemical investigations, but it was identified early in the project that a gas tight cell would be required to properly analyse any gaseous products. In recognition of this, several electrochemical cell set-ups were used in our studies: the quick, non-gas tight preliminary cells for fast, non-critical analysis and the more rigorous gas tight "standard" cells for further in-depth study.

Preliminary Cells

The preliminary cells used modified plastic tissue culture flasks (from BD Falcon) with holes cut in for the insertion of the required electrodes. An inert atmosphere was achieved by the vigorous bubbling of the solution (N_2 or Ar) but it did not allow for the collection of any gaseous products nor the incorporation of a flow through detector system, see Figure 2.4A. This cell was most used in the initial studies of PEDOT and PBTh as well as for quick electrochemical tests that did not require gas analysis.

Development of Gas Tight "Standard" Cell

For more stringent gas detection, metal cells were used. The preliminary lab metal cell (shown in Figure 2.4B) was not tailored for the thick glassy carbon substrates that were required for our studies. As a result, gas was easily lost, shorting of the electrodes was a common problem and catalytic performance in general greatly suffered, making it impossible to detect hydrogen. A commercially available Zahner photo-electrochemical cell was also explored but it was not ideal with issues such as a large head space, the use of a Pt counter electrode and general leakage when used conjunction with our films. To counter this, a series of custom designed metal cells were made for the PBTh system with the goal of providing a flexible, gas tight system with which to test a variety of sample sizes, substrate types and electrolytes.
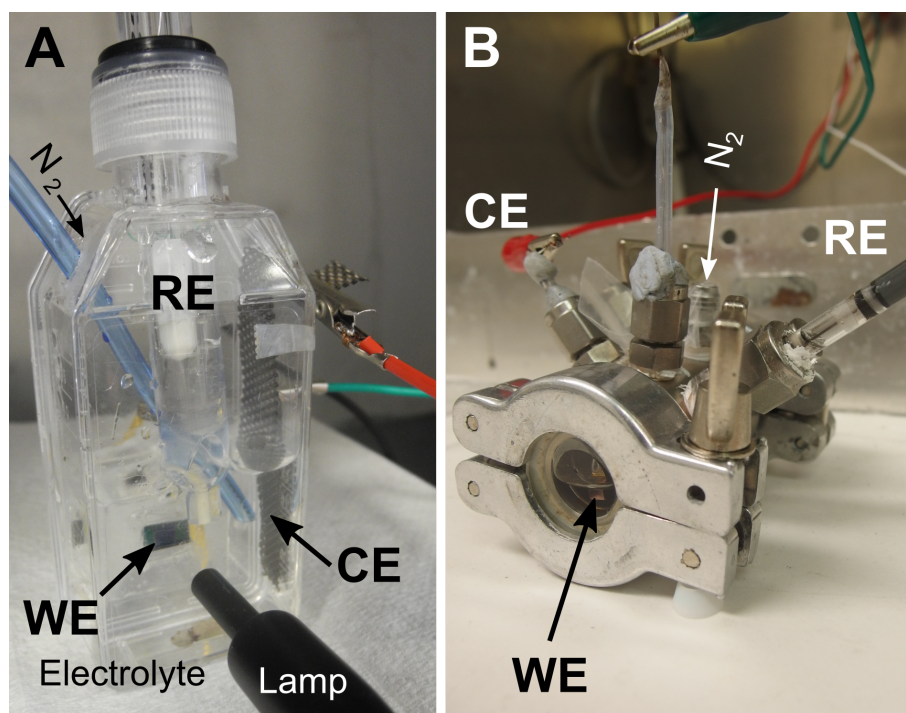
Figure 2.4: (A) A preliminary plastic cell set-up showing the electrodes and gas line for purging. (B) The preliminary lab metal cell for gas tight measurements.

The first generation of this custom cell incorporated some design elements from the Zahner cell but was more tailored to our system. Some key features include the use of a larger electrolyte chamber, the ability to interchange counter electrode types, a larger working electrode area, a more effective gas purge set-up and the relocation of the gas outlet to the top of the cell, thus avoiding leakage issues and maintaining a solution free headspace. The cell was also kept to be as thin as possible so that it would be more amenable to planned in-situ experiments. Stainless steel was used throughout the cell to minimise the escape of H_2 gas and was combined with Swagelok fittings to further reduce gas loss. This first generation cell can be seen in Figure 2.5A and ultimately culminated in a much better detection limit and allowed the first successful identification of gaseous H_2.

The custom metal cell bought many benefits, but as investigations continued, two major shortcomings were revealed; the presence of cross-over reactions from the close proximity of the counter electrode and the inability to alter the size of the working electrode. Thus, the original design was modified to include a flexible spacer plate so that different WE areas are possible and a wider counter electrode fitting so that it can be situated away from the main chamber. This second generation cell (also referred to as the *standard cell*) was made in stainless steel and PVC. The former was selected to perform high efficiency, low cross-over analysis while the latter was an inert cell for long-term analysis as well as quick studies that did not require sensitive gas measurements. The disassembled second generation plastic cell is shown in Figure 2.5B and highlights the different components; the metal cell has the same design.
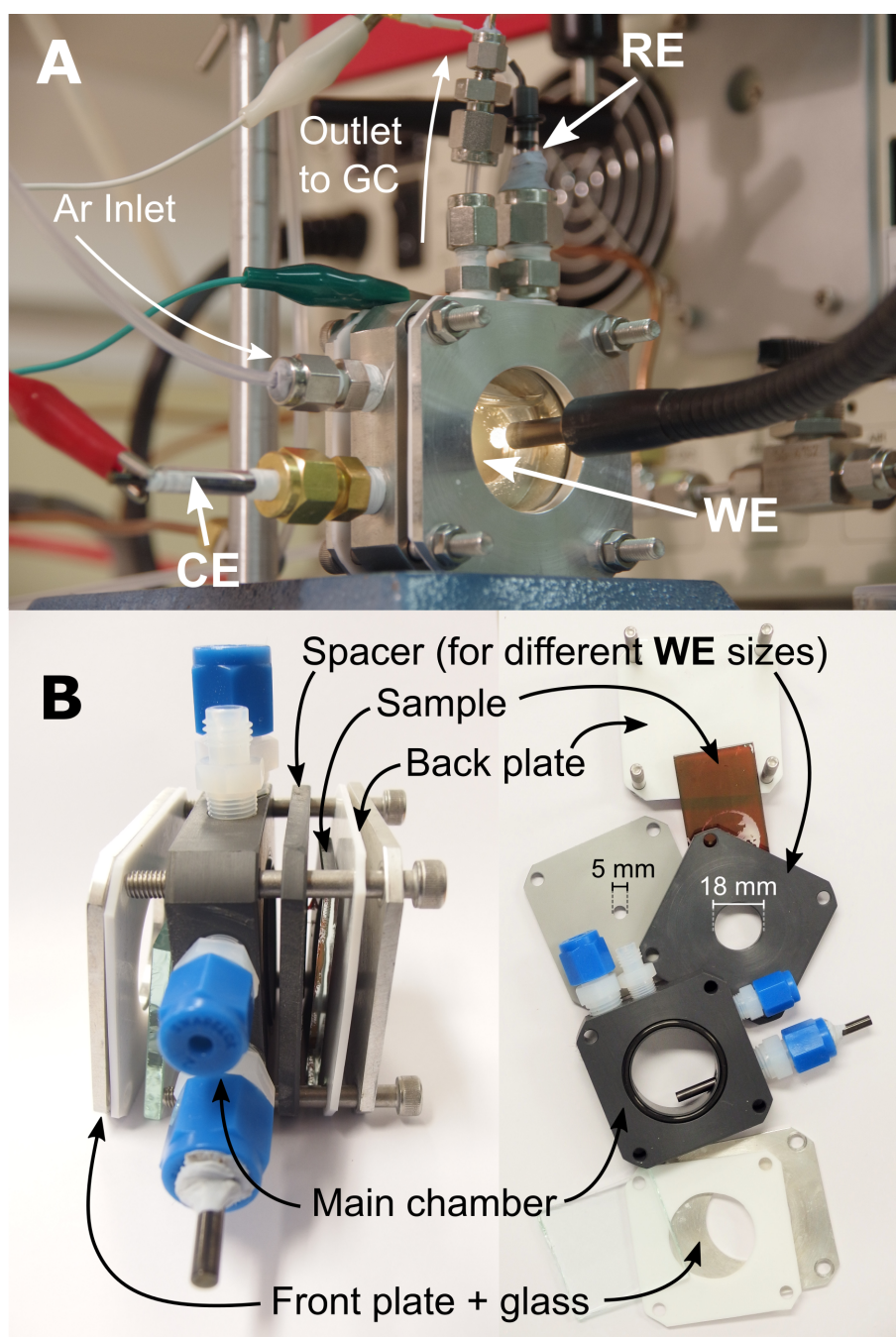
Figure 2.5: (A) The first generation custom metal cell showing it in operation with the inserted electrodes and connection for gas chromatography (GC). (B) The second generation custom cell (PVC version), showing the various components that make up the cell and how they are assembled.

Dye Characterisation Set-up

For the electrochemical characterisation of the various dyes, a simple 20 mL glass vial was used to hold the appropriate electrodes and dye solution/electrolyte. Steps were taken to avoid

shorting and the electrochemistry was conducted inside a N_2 glovebox to prevent H_2O and O_2 contamination.

2.3 Electrochemistry

Electrochemistry played a critical role in the analysis of the films and a variety of techniques were used. The basic principles are outlined here, as are some of the more commonly used experimental parameters. However, due to the immense diversity of each experiment, more specific details are provided and discussed at the relevant sections.

2.3.1 Cyclic Voltammetry

Introduction

Cyclic voltammetry (CV) is perhaps the most commonly used electrochemical technique and is a useful method to gain insights into a wide variety of kinetic and thermodynamic parameters. Three electrodes are typically used to produce a cyclic voltammogram, the working electrode, reference electrode and counter electrode. The working electrode is where the electrochemical reactions in question take place and is the electrode on which the potential is controlled and the current is recorded. The reference electrode provides a known reference with which to bias the potential. Typically, they are made using well defined and stable redox systems such as the SCE or Ag/AgCl redox couples so that the applied potential on the working electrode (E_{we}) can be confidently and reliably reported against the reference electrode. Finally, the counter electrode is responsible for the reverse half cell reaction to balance those occurring on the working electrode; current is recorded between the working and counter electrodes. Common traits that make a good counter electrode include high surface area, good exchange current density and electrochemical stability.

To perform a CV, the potential of the working electrode is swept back and forth between two set potential limits at a predetermined scan rate. The current is recorded during this process and gives information on reactions that take place with respect to potential. Three main processes contribute to the current detected.

The first is capacitance which arises from changes in the double layer charges as they adsorb and desorb when E_{we} is changed; it is heavily influenced by scan rate. Capacitance is typically not desired as it reveals little about redox behaviour, however, it can provide useful information on film properties such as surface area and capacitance.

The second process that contributes to current comes about from the resistance in the working electrode or electrolyte and is apparent as a linear line in CV that follows Ohm's law. Resistance

is generally not desired and is minimised by selecting conductive substrates and the addition of a supporting electrolyte, though it is occasionally unavoidable due to the low conductivity of the sample. The effects of capacitance and resistance on the voltammogram is shown in Figure 2.6A and B.
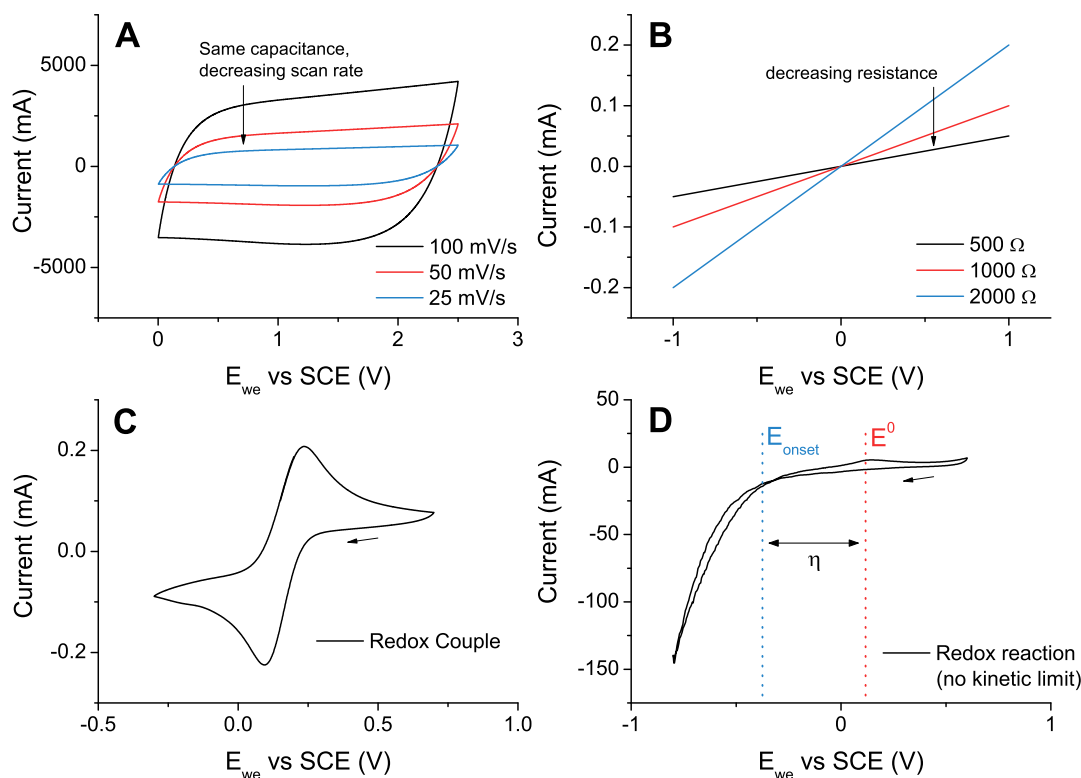
Figure 2.6: A series of voltammograms showing basic concepts in CV. (A) CV of a capacitor and how it is affected by scan rate, (B) how resistance ideally appears in a CV, (C) an ideal redox couple reaction (Fc/Fc^+) and (D) a reduction reaction where there are no diffusional limits as well as illustrating E^0, E_{onset} and η

The third and most important process to be observed in CVs are redox reactions. Every redox reaction has an inherent electrochemical potential at which it will take place, this is commonly known as E^0 and is based on the thermodynamics of the system. E^0 however, is based on theoretical ideal conditions and very often, extra potential – also known as an overpotential (η) – is required before the reaction can proceed on the working electrode. Once a sufficient overpotential is reached, the electrochemical reaction beings to take place and the point at which this happens is known as the onset potential (E_{onset}) ; these points can be observed in Figure 2.6D. As the potential continues past E_{onset}, the current grows until the point at which kinetic limitations such as diffusion begin to take hold. The result of this is a decrease in current and the appearance of an oxidation (positive current)/reduction (negative current) peak. Ideally, the oxidation and reduction peaks are reversible and form a characteristic "redox couple" pair as represented by Fc/Fc^+ in Figure 2.6C. However, there are many alternate redox

behaviours depending on the reversibility, kinetics and thermodynamics of the reaction. If the redox reaction is diffusion *independent*, as in the case of the HER where the electrolyte (H_2O) is the reactant, then there will be no kinetic limitations and no peak will form. Instead, a "tail" will be observed (Figure 2.6D) and is only stopped when the set potential limit of the CV is reached.

Standard Parameters

Each CV experiment was specifically tailored to the investigation, though a standard procedure was commonly used for the initial testing of each sample. Typically, the scan range used for the CV was 0.6 V to −0.8 V vs Ag/AgCl with a scan rate of $20\,\mathrm{mV\,s^{-1}}$ and performed under an inert atmosphere of either N_2 or Ar gas. The electrolyte was $0.1\,\mathrm{mol\,L^{-1}}$ PB at pH 7 while Ti mesh and Ag/AgCl made up the counter and reference electrodes respectively. Deviations from the standard are mentioned where appropriate.

2.3.2   Chronoamperometry

In Chronoamperometry (CA), a constant potential is applied to the working electrode and the resulting current is recorded as a function of time. Due to the constant E_{we}, CA is useful in probing long-term and equilibrium behaviours that are difficult to do in CV. As such, they are helpful in separating capacitance and true redox behaviour. In our experiments, CA was commonly used in conjunction with other analytical techniques such as gas chromatography, Raman spectroscopy *etc.* to trigger and maintain the photo-electrocatalytic reaction. CA was used to probe long-term catalysis performance and degradation of the film.

2.3.3   Electrochemical Impedance Spectroscopy

Introduction

Electrical impedance spectroscopy (EIS) is a powerful technique used to analyse a wide variety of electrochemical systems and have found extensive use in fields such as corrosion science, dye sensitised- and organic solar cells, battery development and photo-electrocatalysis. Simply put, EIS is the use of electronic circuitry components such as resistors and capacitors to develop a model with which to approximate electrochemical systems and their behaviour. The resulting model is known as the equivalent circuit and is able to reveal important information such as the charge transfer resistance, the diffusion rate, the number of active states and the time constants of different interactions. However, each system has their own equivalent circuit and some may even have multiple circuits that provide an empirically good fit but have different physical interpretations. Because of this, care must be taken when designing an equivalent

circuit. Ideally, each component should be assigned to a known system interaction. Obtaining a good fit for the sake of fitting can lead to extraneous components that have no real-world meaning.

To understand how an equivalent circuit is first fitted to EIS data, an understanding of impedance is required. In an ideal resistor, the resistance is given by Ohm's law in the relationship: $R = V/I$. However, this is not usually observed in electrochemical systems, thus a concept known as impedance is used to better describe resistive behaviour. Consider a pseudo-linear electrochemical system where a small sinusoidal potential input (E_t) is applied on top of the E_{we}. The resulting current response (I_t) will be sinusoidal in nature albeit with a phase shift (ϕ) due to the "resistance" of the system, see Figure 2.7.
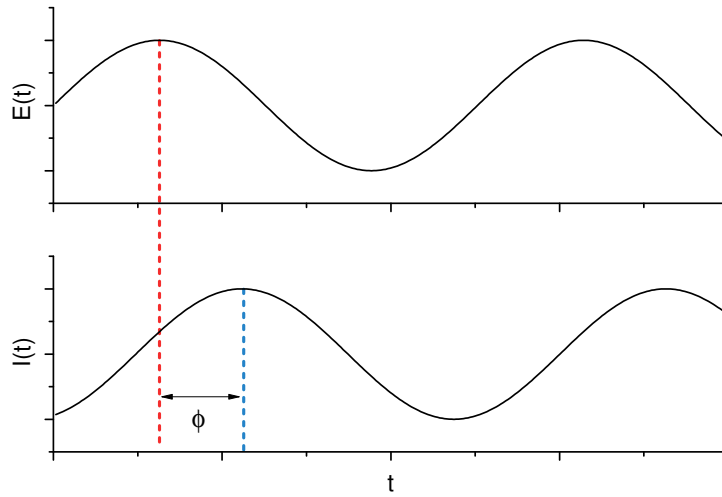
Figure 2.7: A graphical representation of the relationship between E_t, I_t and ϕ.

From this, E_t and I_t can be described by equations 2.1 and 2.2 respectively.

$$E_t = E_0 \sin(\omega t) \tag{2.1}$$

$$I_t = I_0 \sin(\omega t + \phi) \tag{2.2}$$

Where E_t and I_t is the input potential and output current at a given time respectively. E_0 and I_0 is the amplitude of the original signal and ω is the radial frequency ($\omega = 2\pi f$). From this, the impedance (Z) can be described using a relationship derived from Ohm's Law, eq 2.3. From this information, a Bode plot can be formed by plotting $|Z|$ and ϕ as a function of frequency (f) and is one of the common graphical methods with which to interpret EIS (shown in Figure 2.8).

$$Z = \frac{E_t}{I_t} = \frac{E_0 \sin(\omega t)}{I_0 \sin(\omega t + \phi)} = Z_0 \frac{\sin(\omega t)}{\sin(\omega t + \phi)} \tag{2.3}$$

Using Euler's relationship, eq 2.3 can also be represented as a complex number as shown in eq 2.4. The Nyquist plot, anothed method in which to represent EIS data, is made by plotting the real (Z_{Re}) and imaginary (Z_{Im}) impedance components on x- and y-axis respectively, see Figure 2.8.

$$Z(\omega) = Z_0(\cos \phi + j \sin \phi) \tag{2.4}$$

Using these relationships, it is then possible to describe a variety of electrical components such as resistors and capacitors in terms of impedance, see eq 2.5. When translated to Nyquist and Bode plots, resistors cause a shift in Z_{Re} and $|Z|$ respectively, while capacitors are observed in Bode plots as a linear section in $|Z|$ while ϕ trends towards 90°, see Figure 2.8. There are also phenomena such as diffusion that only exist in electrochemical systems, thus new descriptors are required to model their behaviour. Some of the more common electrochemical elements such as Warburg impedance and the constant phase element (CPE) are described in Eq 2.5.[6]

$$
\begin{aligned}
&\text{Resistor:} &&Z = R \\
&\text{Capacitor:} &&Z = \frac{1}{j\omega C} \\
&\text{Diffusion:} &&Z = \frac{1}{Y_0 \sqrt{j\omega}} \\
&\text{CPE:} &&Z = \frac{1}{Y_0(j\omega)^{-a}}
\end{aligned}
\tag{2.5}
$$

The Warburg impedance describes diffusion (assuming that the diffusion distance is infinite) and is critical when the redox reaction is dependent on the diffusion of reactants to, or products away from, the electrode. The Warburg impedance can be observed in EIS as a 45° tail in the Nyquist plot or a phase shift towards 45° in a Bode plot (Figure 2.8). A CPE element is a versatile component that can describe a wide range of behaviours due to its a exponent and can represent a capacitor ($a = 1$), resistor ($a = 0$) and Warburg element ($a = 0.5$). More importantly, the CPE allows the modelling of a range of "imperfect" elements that are often encountered in real-world systems. For example, a CPE where $a = 0.8 - 0.9$ is a good descriptor for the capacitance of a porous/uneven/imperfect surface while for $a = 0.1 - 0.2$, the CPE would describe a non-ideal resistor like behaviour.
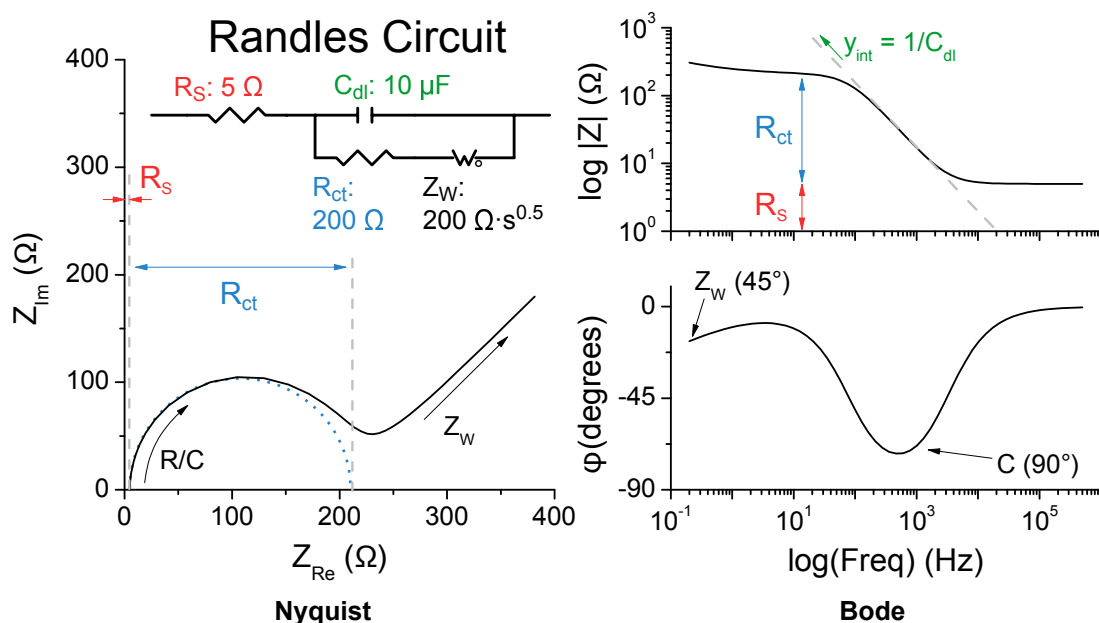
Figure 2.8: The Nyquist (Left) and Bode (Right) impedance plots of a sample Randles equivalent circuit. The values for each component is given for comparison with the graphical results.

Using the knowledge of these relationships and analysis of the Bode and Nyquist plots, it is possible to assign an equivalent circuit though this does becomes more difficult with complex systems. The Randles Circuit – shown in Figure 2.8 – is a good starting point for electrochemical reactions and incorporates many common phenomena such as solution resistance (R_S), charge transfer resistance (R_{ct}), double layer capacitance (C_{dl}) and diffusion (Z_W). Each system has their own distinct equivalent circuit and it is often useful to refer to literature for the initial template followed by further refinement. A χ^2 test is generally used to judge the accuracy of the proposed equivalent circuit though it is also important to relate each individual component to a real world process.

EIS parameters

All EIS measurements were conducted under an N_2 atmosphere in $0.1 \, mol \, L^{-1}$ phosphate buffer at pH 7 with a counter and reference electrode of glassy carbon and Ag/AgCl respectively. The samples were analysed over a frequency range from $100 \, kHz$ to $200 \, mHz$ with a sine wave perturbation of $10 \, mV$; illumination was supplied by a Leica KL 2500 halogen lamp source. Prior to EIS measurements, an initial CV was conducted to confirm the photo-electrocatalytic response of the film, followed by a CA measurement at -0.5 V vs Ag/AgCl to help remove residual O_2 and allow time for swelling of the film. EIS commenced once a stable photo-current of was reached, where Δphoto-current $<2 \, \mu A \, s^{-1}$ over a 15 min period.

2.4   Experiments and Methodologies

The following describes the key non-electrochemical experimental parameters. Techniques that were not common or details of very specific variations are provided in the relevant sections where required.

2.4.1   Gas Chromatography

Gas chromatography (GC) was performed with a SRI 310C gas chromatograph with a MS-5A column using a thermal conductivity detector and a carrier gas of Ar at 50 °C. This set-up was parametrised to enhance H_2 detection where the injection volume was 50 µL. Prior to injection, the gas chromatograph was left until a baseline equilibrium was reached. For a GC measurement, an injection of 10 s was done to completely flush the loading column followed by a 5 s wait before commencing the recording of GC data. Typically, H_2 eluted at 2 min, with trace amounts of O_2 and N_2 also being observed at 3.5 min and 6.5 min respectively.

To detect and quantify the catalytic production of H_2, the gas chromatograph was arranged in a flow-through set-up with the standard metal cell. The loading column for the GC was directly connected to the metal cell outlet so that each injection would sample the headspace of the cell, as shown in Figure 2.5A. Upon injection, the peaks of the gaseous products would be converted to a ratio with respect to the carrier Ar gas using a calibration curve. The flow rate of the carrier gas was critical in the determination of an accurate %H_2 and was set by a Brooks 5850 E Series Mass Flow Controller. Typically, a flow rate of 0.15 mL min^{-1} was used for low currents while better performing catalysts used a flow rate of 1 mL min^{-1} to improve the purging of air.

Calibration was performed by the injection of a known volumetric ratio of H_2:Ar; these samples were prepared underwater to prevent the escape of gas. The calibration graph was determined by the plot of the resulting peak height vs known %H_2 and spanned the ranges 0.02–1 %H_2.

2.4.2   UV-Vis Spectroscopy

The UV-Vis spectroscopy spectra were acquired using a Jasco V670 Spectrophotometer. Typically, a background correction was applied by subtracting the spectrum of the underlying substrate (e.g. glass slide). A typical scan range of 330–1500 nm was used for glass slide, FTO glass and plastic cuvettes while a range of 190–1500 nm was used for quartz cuvettes and quartz glass; quartz was typically used in dye characterisation.

In-situ UV-Vis Spectroscopy

To perform in-situ UV-Vis spectroscopy, a standard metal cell (see 2.5) was placed inside the sample chamber and the working electrode aligned with the UV-Vis beam. An FTO glass substrate was used due to the need for it to be both transparent and conductive. A CA would typically be used to apply the potential for the in-situ UV-Vis spectra. Once the current in dark had stabilised, UV-Vis analysis was taken of the film under the applied potential in both light and dark conditions. The light source was provided by a Leica KL2500 halogen lamp through a pinhole sized aperture which was formed by enclosing the lamp with a punctured foil sheet. Light leakage was minimised through shielding with metal foil.
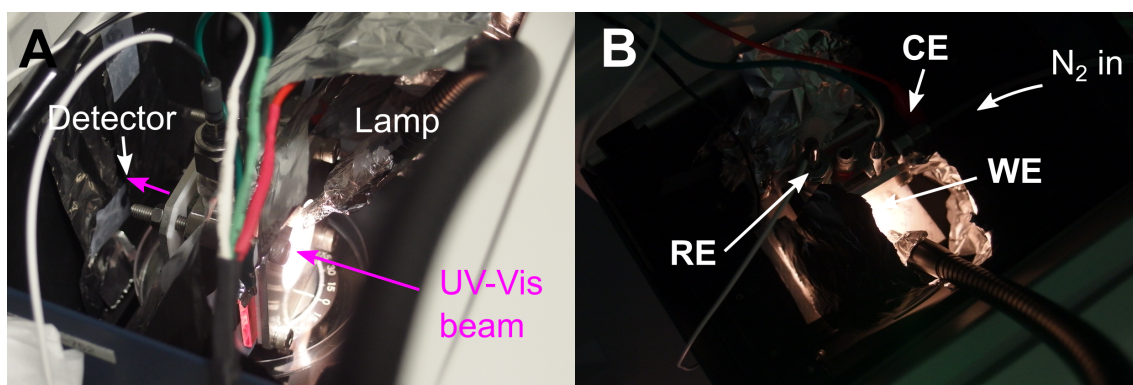
Figure 2.9: Pictures of the in-situ UV-Vis set-up. (A) The UV-Vis spectrometer showing the incoming UV-Vis beam and shielded detector; stray light is minimised by use of foil shielding. (B) The UV-Vis cell under experimental lighting conditions showing the electrochemical electrodes. The light from the lamp is brighter than in real life due to the heightened exposure of the photo to better reveal other features.

2.4.3 Fluorescence Spectroscopy

Fluorescence spectroscopy was used to characterise the photo-emission of various dyes and was conducted using a Horiba Fluoromax 4 spectrofluorometer. The dyes were typically diluted to a concentration of $10\,\mu\mathrm{mol\,L}^{-1}$ though higher concentrations were also used depending on the intensity of the fluorescence peak. The excitation wavelength was determined by the absorption data from UV-Vis spectroscopy.

2.4.4 Raman Spectroscopy

A Jobin-Yvon T64000 Raman system with a 488 nm blue diode laser was used for the majority of the Raman spectra. As the output of the diode laser was highly susceptible to temperature fluctuations, calibration would be done prior to every Raman test. An initial calibration was first performed with respect to a known mercury emission line from a fluorescent lamp (546.07 nm),

followed by confirmation of the laser output wavelength; ideally at 487.77 nm but could vary by ± 1 nm. Finally, calibration was conducted to the Raman line of a Si chip at 520.5 cm^{-1}. If the spectra deviated by more than 2 cm^{-1}, the calibration process would be repeated.

A normal Raman spectrum was performed by scanning between 200–3500 cm^{-1} in 500 cm^{-1} steps at a magnification of 100×. Each step comprised of 3 s acquisitions that were averaged over 5 takes. A 100% laser power (0.5 mW) was generally used, though this would be adjusted if the sample showed signs of degradation.

In-Situ Raman Spectroscopy

In-situ Raman was performed with two different systems; the Jobin-Yvon T64000 as described above and a Renishaw inVia Raman system with a 633 nm red HeNe laser. For the Renishaw Raman system, an accumulation time of 10 s repeated 3 times with 10% laser power was used. A 10× objective was used for all in-situ studies due to the need for a long working distance to keep it above the electrolyte. Raman was conducted after the electrochemical cell had reached equilibrium using the same parameters as listed in 2.4.4.
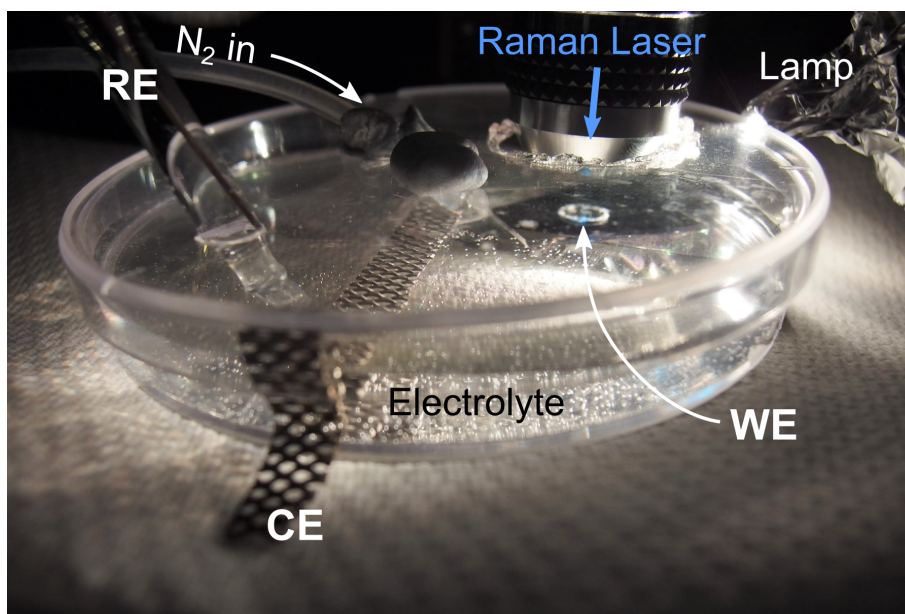
Figure 2.10: The in-situ Raman set-up showing the electrochemical electrodes and how the cell was arranged. N$_2$ was purged into the headspace above the electrolyte to remove as much air as possible.

For the electrochemical set-up, a 6 mm hole was cut into a petri-dish for the PBTh working electrode and attached by silicone tape. The petri dish was then filled with a thin layer of 0.1 mol L^{-1} PB electrolyte (pH 7) and the electrochemical set-up completed with the addition a Ag/AgCl RE and titanium mesh CE (Figure 2.10). The cell was purged continuously with N$_2$ throughout the test.

2.4.5 Scanning Electron Microscopy

For scanning electron microscopy (SEM), either a FEI Nova NanoSEM 450 or a JEOL 6300F field emission gun was used to acquire the various micrographs and energy dispersive X-ray (EDX) analysis. The machine used depended on their availability but for all intents and purposes they are comparable to each other. An accelerating voltage of 5 kV was typically used for all the samples due to the sensitive nature of the polymeric sample.

2.4.6 Light Dependency

Wavelength Dependency

A Spectra Physics arc-lamp housing (Model 66901) with a Xe bulb was used as the light source in conjuction with a Cornerstone 260 monochromator (Model 74100) for the wavelength depedency measurements. The wavelengths were manually selected in intervals of 20 nm from 800–600 nm and intervals of 10 nm from 600–300 nm. The photo-response was recorded after an illumination period of 30 s, the film was then allowed to rest for another 30 s in dark before the next photo-measurment. A calibration of the photo-intensity at each wavelength was conducted using a Si chip and the photo-response normalised to their respective intensities.

These measurements were conducted in-situ with a standard PBTh film on glassy carbon being held at a constant potential under N_2 in a $0.1 \, \mathrm{mol \, L^{-1}}$ PB solution. A standard metal cell set-up was used with a Ag/AgCl reference and Ti mesh counter electrode.

Intensity Dependency

The intensity dependence of the film was measured using a Newport Arc Lamp Housing (Model 67005) with a Xe bulb. An AM 1.5 spectral filter was used to model the solar spectrum while neutral density filters were used to adjust intensity. The light intensity was calibrated using a GaAs cell. A metal cell with a Ag/AgCl reference electrode and Ti mesh counter electrode was used, the working electrode was a standard PBTh film on glassy carbon and purged with N_2.

A constant voltage of $-0.5 \, \mathrm{V}$ vs Ag/AgCl was applied. The sample was allow to equilibrate in the dark for 20 min before the first photo-measurement began. Each measurement consisted of the application of light for 1 min followed by 1 min of darkness. The calculated photo-current is the current recorded at the end of the 1 min exposure subtracted by the dark current.

2.4.7   Mass Spectroscopy

Mass spectroscopy (MS) was used to analyse the purity of dyes. This was conducted on a Waters micromass ZQ quadrupole mass analyser using electospray ionisation with a cone voltage of 35 V. For some dyes, a hybrid technique of MS with high pressure liquid chromatography (HPLC) was used to extrapolate further information on purity. An Agilent 1200 series HPLC system with a flow rate of 300 μL min^{-1} (MeOH) was used for this MS-HPLC method.

2.5   Computational Chemistry

Computational chemistry uing density function theory (DFT) was performed to supplement experimental data. The 6-31+G* basis set[7–11] and the B3LYP hybrid functional[12–15] was used for all calculations unless otherwise stated. Generally, geometry optimisation, single point energy and solvation energy calculations were performed on the Monash Sun Grid (Monash University's high performance computing facility) while vibrational and time-depedent DFT (TD-DFT) calculations were performed locally where access to large amounts of memory was more readily available. All computations were run using NWChem[16] via the Extensible Computational Chemistry Environment (ECCE) .[17]

2.5.1   Thermodynamic Calculations of Dye Species

An initial geometry optimisation was carried out to determine the zero-point energy (ZPE), followed by a vibrational calculation to find the enthalpy (H_{corr}) and entropy (S) correction terms. Finally, a single point energy calculation using a COnductor-like Screening MOdel (COSMO)[18,19] was done to determine the solvation energy contribution; a solvation radius of 2.16 Å and a dielectric constant of 36.64 was used for acetonitrile. The overall free energy (G) for a dye species was determined by eq 2.6, where $T = 298$ K.

$$G = ZPE + H_{corr} - T \cdot S - G_{solv} \tag{2.6}$$

The free energy is also determined for the oxidised ($-e^-$) and reduced species ($+e^-$) and subtracted from the ground state to give the Gibbs free energy (ΔG) for each respective reaction. The $\Delta G_{red/ox}$ is converted to a electrochemical potential using eq 2.7 and then corrected to a potential vs Fc/Fc$^+$ using eq 2.8.

$$E(\text{eV}) = -\frac{\Delta G}{nF} \tag{2.7}$$

$$E(\text{vs Fc/Fc}^+) = -4.988 \text{ eV} - E(\text{eV}) \tag{2.8}$$

2.5.2 Investigating the Catalytic Mechanism of Polybithiophne

Computational calculations were also used to investigate the catalytic mechanism of PBTh using a 7-membered thiophene oligomer, see Figure 2.11. Initial thermodynamic calculations where conducted on this oligomer (referred to as PBTh) and it's protonated states (at the sulphur and α-Carbon atom) using a geometry optimisation, followed by single point energy and vibrational energy calculations using B3LYP/6-31++G**.

For analysis of the HOMO/LUMO molecular orbitals, the PBTh analogue was protonated at various sites (as shown in Figure 2.11) by forcing the proton to a distance of 1 Å then allowing for geometry relaxation. These initial preliminary computational studies were conducted with B3LYP/6-31+G* and analysed the HOMO and LUMO molecular orbitals via a single point energy calculation of the geometrically relaxed PBTh/protonated-PBTh sample with a COSMO solvation model (solvation radius = 0.5 Å, dielectric constant = 78.4 for H_2O).
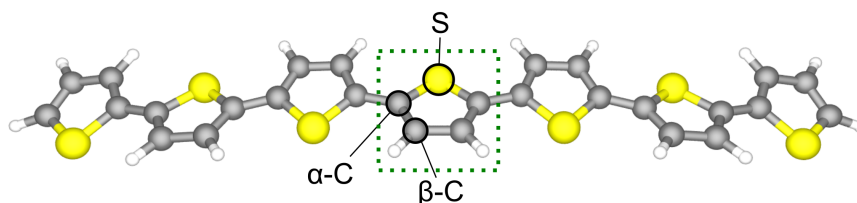
Figure 2.11: The 7-membered thiophene oligomer used as the analogue for PBTh in computational calculations. The various investigated protonation sites are indicated and situated on the central thiophene unit which is highlighted in green.

Further in-depth studies using TD-DFT with CAM-B3LYP/6-31+G*[20] were used to determine the ground to excited state transitions; number of roots (nroot) = 12. The ground and excited state orbitals corresponding to the most intense transition were then presented as the computationally determined ground and photo-excited state orbitals; this intensity is often several orders of magnitude larger then the other predicted transition.

The electrostatic potential (ESP) calculations were conducted on a geometry optimised PBTh/PBTh(S-H)$^+$ species using the NWChem ESP module.

Triplet state calculations were done by assigning a spin state of 1 to the PBTh/protonated PBTh analogue. A geometry optimisation was then performed, followed by a single point calculation to find the molecular orbital of the ground triplet state.

Bibliography

[1] O. Winther-Jensen, K. Chatjaroenporn, B. Winther-Jensen and D. R. MacFarlane. "Towards hydrogen production using a breathable electrode structure to directly separate gases in the water splitting reaction". *Int. J. Hydrogen Energy*, 2012. **37**, 10, 8185–8189.

[2] Z. Ademovic, J. Wei, B. Winther-Jensen, X. Hou and P. Kingshott. "Surface Modification of PET Films Using Pulsed AC Plasma Polymerisation Aimed at Preventing Protein Adsorption". *Plasma Process. Polym.*, 2005. **2**, 1, 53–63.

[3] B. Winther-Jensen and K. West. "Vapor-Phase Polymerization of 3,4-Ethylenedioxythiophene: A Route to Highly Conducting Polymer Surface Layers". *Macromolecules*, 2004. **37**, 12, 4538–4543.

[4] B. Winther-Jensen, J. Chen, K. West and G. Wallace. "Vapor phase polymerization of pyrrole and thiophene using iron(III) sulfonates as oxidizing agents". *Macromolecules*, 2004. **37**, 16, 5930–5935.

[5] A. Wexler and S. Hasegawa. "Relative humidity-temperature relationships of some saturated salt solutions in the temperature range 0 to 50C". *J. Res. Natl. Bur. Stand. (1934).*, 1954. **53**, 1, 19–26.

[6] Gamry Instruments. "Basics of Electrochemical Impedance Spectroscopy", 2015.

[7] W. J. Hehre, R. Ditchfield and J. A. Pople. "Self-Consistent Molecular Orbital Methods. XII. Further Extensions of Gaussian-Type Basis Sets for Use in Molecular Orbital Studies of Organic Molecules". *J. Chem. Phys.*, 1972. **56**, 5, 2257–2261.

[8] M. M. Francl, W. J. Pietro, W. J. Hehre, J. S. Binkley, M. S. Gordon, D. J. DeFrees and J. A. Pople. "Self-consistent molecular orbital methods. XXIII. A polarization-type basis set for second-row elements". *J. Chem. Phys.*, 1982. **77**, 7, 3654–3665.

[9] T. Clark, J. Chandrasekhar, G. W. Spitznagel and P. V. R. Schleyer. "Efficient diffuse function-augmented basis sets for anion calculations. III. The 3-21+G basis set for first-row elements, Li-F". *J. Comput. Chem.*, 1983. **4**, 3, 294–301.

[10] P. Hariharan and J. Pople. "The influence of polarization functions on molecular orbital hydrogenation energies". *Theor. Chim. Acta*, 1973. **28**, 3, 213–222.

[11] J. Slater and K. Johnson. "Self-consistent-field Xα cluster method for polyatomic molecules and solids". *Phys. Rev. B*, 1972. **5**, 3, 844–853.

[12] A. Becke. "Density-functional exchange-energy approximation with correct asymptotic behavior". *Phys. Rev. A*, 1988. **38**, 6, 3098–3100.

[13] S. H. Vosko, L. Wilk and M. Nusair. "Accurate spin-dependent electron liquid correlation energies for local spin density calculations: a critical analysis". *Can. J. Phys.*, 1980. **58**, 8, 1200–1211.

[14] C. Lee, W. Yang and R. Parr. "Development of the Colle-Salvetti correlation-energy formula into a functional of the electron density". *Phys. Rev. B*, 1988. **37**, 2, 785–789.

[15] P. Stephens, F. J. Devlin, C. F. Chabalowski and M. J. Frisch. "Ab-Initio Calculation of Vibrational Absorption and Circular-Dichroism Spectra Using Density-Functional Force-Fields". *J. Phys. Chem.*, 1994. **98**, 45, 11623–11627.

[16] M. Valiev, E. Bylaska, N. Govind, K. Kowalski, T. Straatsma, H. van Dam, D. Wang, J. Nieplocha, E. Apra, T. Windus and W. de Jong. "NWChem: a comprehensive and scalable open-source solution for large scale molecular simulations". *Comput. Phys. Commun.*, 2010. **181**, 1477.

[17] G. Black, S. Karen, D. Gracio and B. Palmer. "The Extensible Computational Chemistry Environment: A Problem Solving Environment for High Performance Theoretical Chemistry". In "Comput. Sci. - ICCS", Berlin, pp. 122–131.

[18] A. Klamt and G. Schüürmann. "COSMO: a new approach to dielectric screening in solvents with explicit expressions for the screening energy and its gradient". *J. Chem. Soc., Perkin Trans.*, 1993. **2**, 799–805.

[19] D. York and M. Karplus. "A smooth solvation potential based on the conductor-like screening model". *J. Phys. Chem. A*, 1999. **103**, 11060–11079.

[20] T. Yanai, D. P. Tew and N. C. Handy. "A new hybrid exchange-correlation functional using the Coulomb-attenuating method (CAM-B3LYP)". *Chem. Phys. Lett.*, 2004. **393**, 1-3, 51–57.

Chapter 3

Investigation of the Photo-electrochemical Properties of Dyes and Conducting Polymers

PART B: Declaration for Thesis Chapter 3

Declaration by candidate

In the case of Chapter 3, Publication 1, the nature and extent of my contribution to the work was the following:

Nature of contribution	Extent of Contribution
Initiation of work	100 %

The following co-authors also contributed to the work. If co-authors are students at Monash University, the extent of their contribution in percentage terms must be stated.

Name	Nature of contribution	Extent of Contribution
C. André Ohlin	Set-up and instruction on computational work	NA
Bjorn Winther-Jensen	Key ideas, proof reading, drafting	NA

The undersigned hereby certify that the above declaration correctly reflects the nature and extent of the candidate's and co-authors' contributions to this work*.

Candidate's Signature   **Supervisor's Signature**

Date: Date:

*Note: Where the responsible author is not the candidate's main supervisor, the main supervisor should consult with the responsible author to agree on the respective contributions of the authors.

3.1 Introduction and Initial PEDOT Studies

The use of ICPs (such as PEDOT) for catalysis stemmed from various studies by the Winther-Jensen group that achieved promising results for reactions such as O_2 reduction[1] and H_2O oxidation.[2] The most influential of these studies was the discovery of a PEDOT-PEG blend on Ti foil as an efficient catalyst for the HER[3] and served as the basis for the PhD project. Initial studies focused on the development of this PEDOT based catalyst to a photo-enhanced system with the inclusion of dyes and other light harvesters, similar to that of a dye sensitised solar cell. The envisioned energetic diagram and thermodynamic basis of this concept is shown in Figure 3.1, where the photo-excitation of the dye allows for the reduction of H^+ while the ICP serves as a conductive substrate to provide charge separation and dye regeneration.
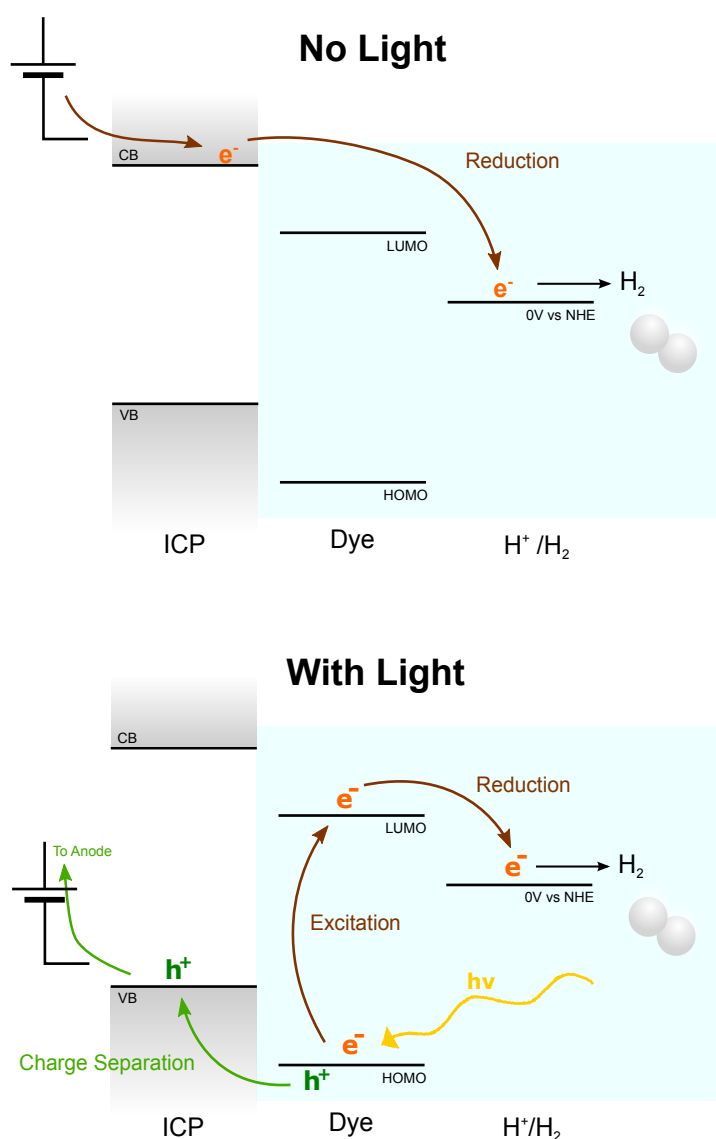

Figure 3.1: The working principle of the envisioned ICP/dye blend for the HER.

For this chapter, all electrochemical tests were conducted in the preliminary plastic cell with a
Ti mesh counter electrode and an SCE reference electrode, see Figure 2.4A.

3.1.1   PEDOT:Brilliant Blue

The first dye to be blended with PEDOT was Coomassie Brilliant Blue G250 (Brilliant Blue) and
was chosen due to its strong photo-absorbance, commercial availability, non-toxic nature and
large molecular structure which aided in its entrapment within the film. The chemical structure
of Brilliant Blue and PEDOT are shown in Figure 3.2. The blend was made by dissolving
Brilliant Blue into the precursor Fe(III)PTS solution prior to VPP; both Brilliant Blue and the
EDOT monomer were obtained from Sigma Aldrich and used without further purification.
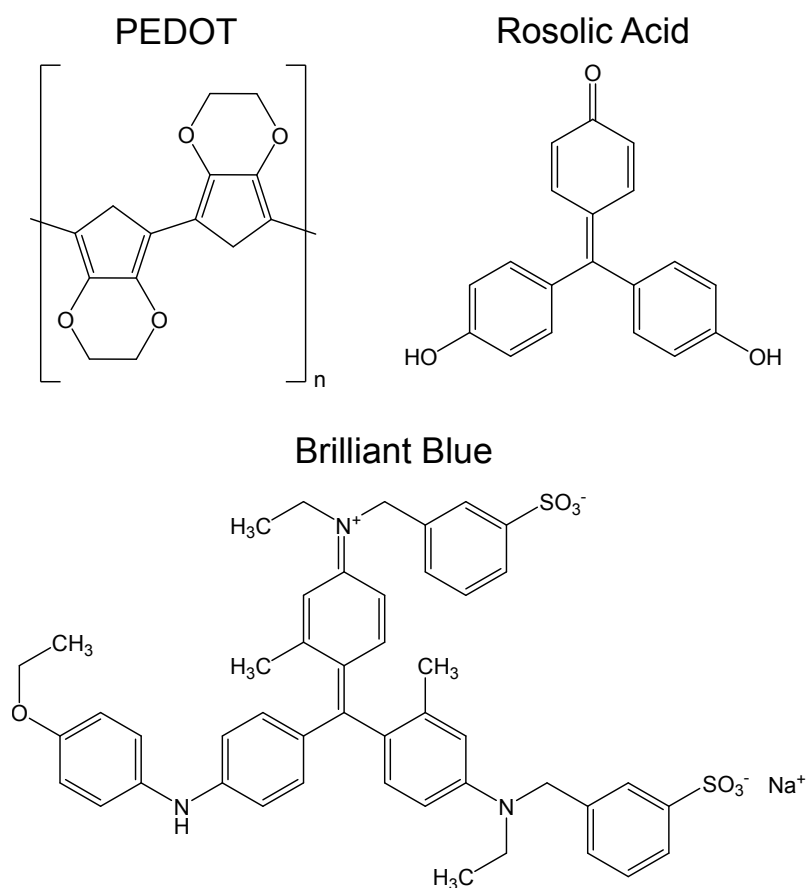
Figure 3.2: The chemical structure of PEDOT and the dyes, Rosolic Acid and Brilliant Blue.

Several different blends with varying ratios (v:v%) of PEDOT:Brilliant Blue (and one film of
PEDOT:PEG:Brilliant Blue 1:1:1) were made and characterised. The resulting conductivity
of each film is presented in Table 3.1 and showed good levels of conductivity. As expected,
the conductivity of the film drops with increasing amounts of Brilliant Blue. Interestingly,
conductivity was highest with blended PEG despite it being non-conductive.

Table 3.1: The conductivity of PEDOT:Brilliant Blue films on glass slide as measured using a Jandel RM3 4-point probe.

Sample	Conductivity (S/cm)	Standrd Deviation (S/cm)
PEDOT:PEG:Brilliant Blue 1:1:1	185	8
PEDOT:Brilliant Blue 1:1	155	27
PEDOT:Brilliant Blue 1:2	87	32
PEDOT:Brilliant Blue 1:3	63	19
PEDOT:Brilliant Blue 1:4	41	17

Characterisation of these films were also done via UV-Vis spectroscopy and the results are shown in Figure 3.3, along with that of PEDOT:PEG and Brilliant Blue for comparison. Since each film has a slightly different thickness and PEDOT content, each spectra (except for Brilliant Blue) was normalised to their respective PEDOT content by using the absorbance at 1000 nm (where Brilliant Blue is non-absorbing). The observed increase in the Brilliant Blue absorption peak at 630 nm reflects the trend of their ideal PEDOT:Brilliant Blue composition and confirmed the successful incorporation of the dye in the desired ratio.
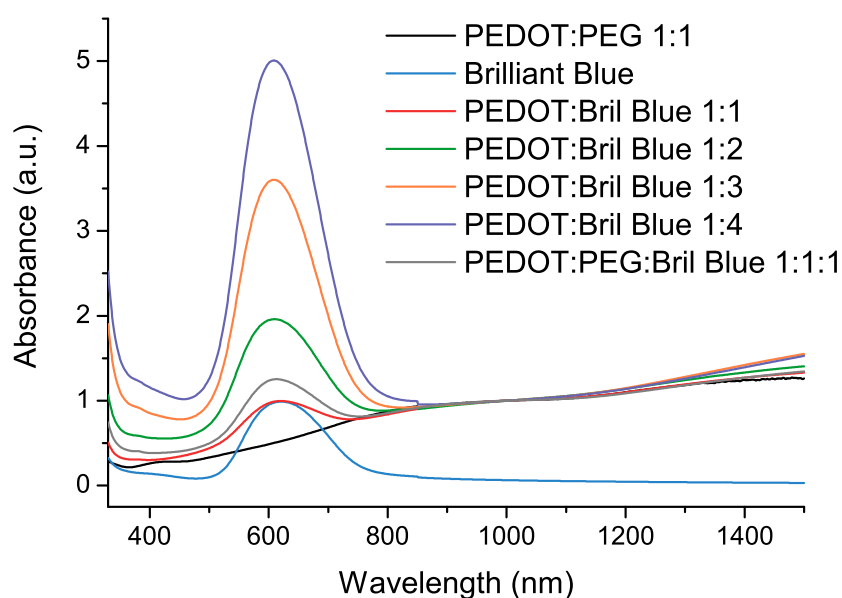
Figure 3.3: The UV-Vis spectra of various PEDOT:Brilliant Blue films on glass slides as well as that of PEDOT:PEG and pure Brilliant Blue.

The first electrochemical tests were conducted on a PEDOT:PEG:Brilliant Blue film in a 1:1:1 volume ratio on gold mylar. It was tested via CV in both $1 \, \text{mmol} \, \text{L}^{-1}$ H_2SO_4 (pH 3) and $0.1 \, \text{mol} \, \text{L}^{-1}$ PB (pH 7) at a scan rate of $5 \, \text{mV} \, \text{s}^{-1}$ under N_2 gas, Figure 3.4.
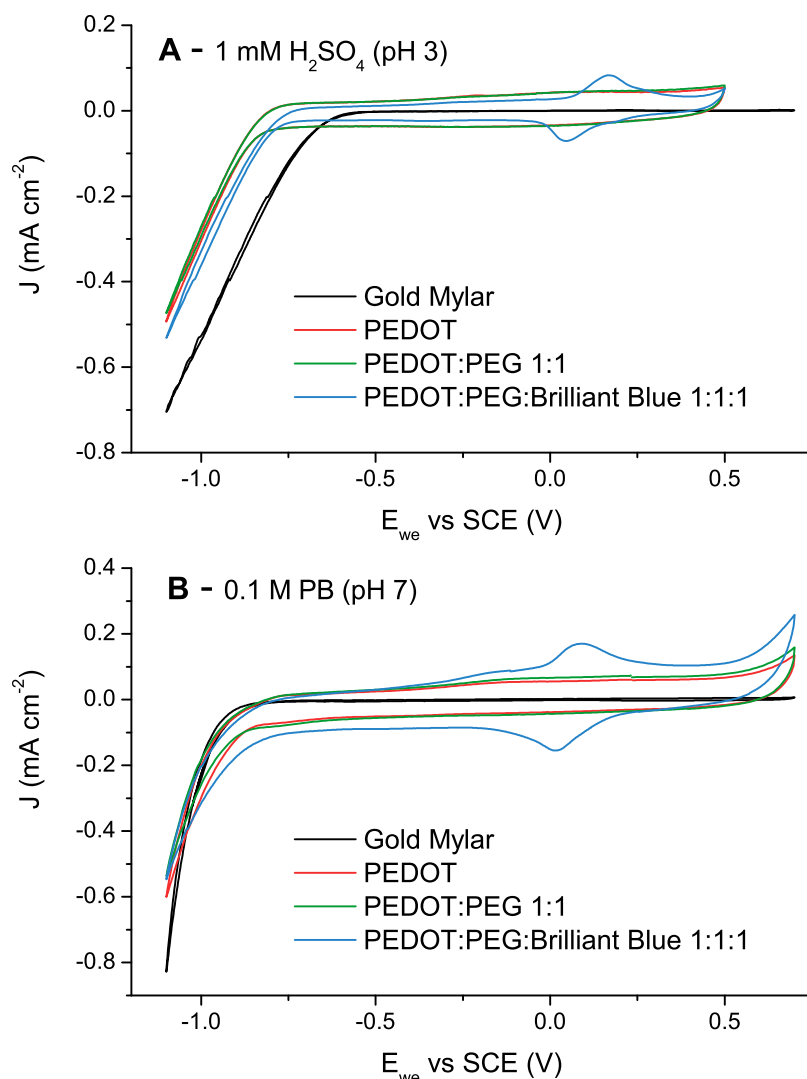
Figure 3.4: Initial CV tests on PEDOT:PEG:Brilliant Blue films as compared to PEDOT, PE-DOT:PEG and the gold mylar substrate. Conducted under bubbled N_2, CE was Ti mesh. **A:** The films in $1\,\mathrm{mmol\,L^{-1}}$ H_2SO_4 (pH 3) and **B:** $0.1\,\mathrm{mol\,L^{-1}}$ PB (pH 7)

The presence of a Brilliant Blue redox couple at $\approx 0.1\,\mathrm{V}$ vs SCE in Figure 3.4 indicated successful electronic interaction between the PEDOT film and Brilliant Blue dye. However, from the same set of results, it was quickly realised that gold mylar – in both electrolytes – was unsuitable as a substrate due to its catalytic activity towards the HER. As a result, the true electrochemical catalytic performance of the PEDOT:PEG:Brilliant Blue blend remained unknown. Furthermore, the use of PEG in the films resulted in inconsistent data as swelling from the uptake of H_2O altered catalytic performance. Because of this, PEG was omitted from future ICP:dye blends.

In light of the interference from gold, it was decided to investigate the catalytic properties of the PEDOT:Brilliant Blue film via photo-enhancement. Since gold is not photo-active, any
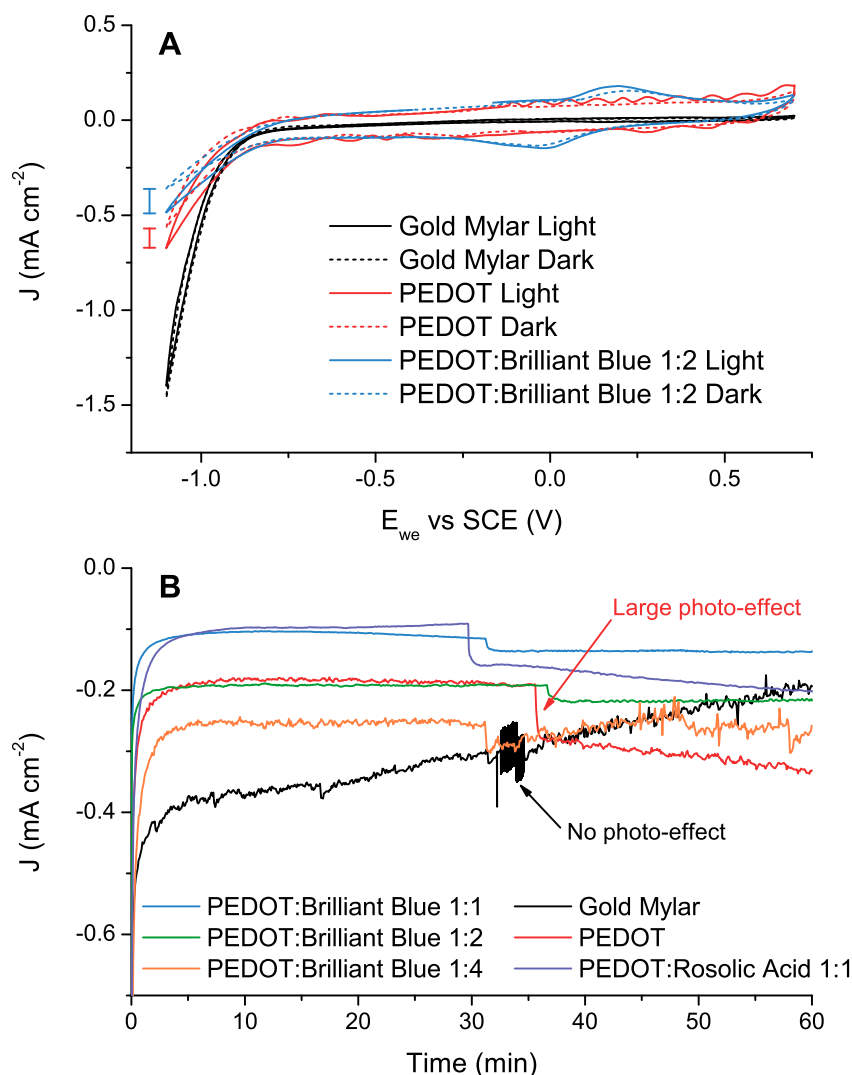
Figure 3.5: Photo-investigation of PEDOT:dye films in $0.1\,\text{mol}\,\text{L}^{-1}$ PB (pH 7). **A:** Shows the CV trace of the PEDOT:Brilliant Blue blend as compared to PEDOT and gold mylar. **B:** CA trace of the different films whilst held at $-1\,\text{V}$ vs SCE, the light was switched on $\approx 35\,\text{min}$. The photo-response of the gold mylar (black) and PEDOT (red) is highlighted.

photo-electrocatalytic contribution towards the HER would be from the blended film. A variety of PEDOT:Brilliant Blue ratios were investigated, from 1:1 to 1:4, to see if the increased ratio of Brilliant Blue would influence the detected photo-response. The CV response of the best performing film (PEDOT:Brilliant Blue 1:2) is presented in Figure 3.5A (blue) and showed a small but distinct increase in photo-current when illuminated. However, this effect was also exhibited by a plain PEDOT film (red) and threw into doubt the effectiveness of the Brilliant Blue dye.

The dye's effectiveness was further challenged by subsequent CA experiments over a period of 1 h (Figure 3.5B). Light was switched on at 35 min ±5 min and while all PEDOT:Brilliant Blue films exhibited a noticeable photo-current increase, the largest photo-response was from the pure PEDOT film (red trace). An alternative dye – Rosolic Acid – was also trialled to see if it could enhance the photo-effect; its structure is shown in Figure 3.2. While PEDOT:Rosolic Acid (1:1) showed a detectable photo-response (Figure 3.5B, purple trace), it was insignificant when compared to that of PEDOT. This confirmed that the observed photo-enhancement effect was not due to the dyes but an inherent property of the PEDOT film.
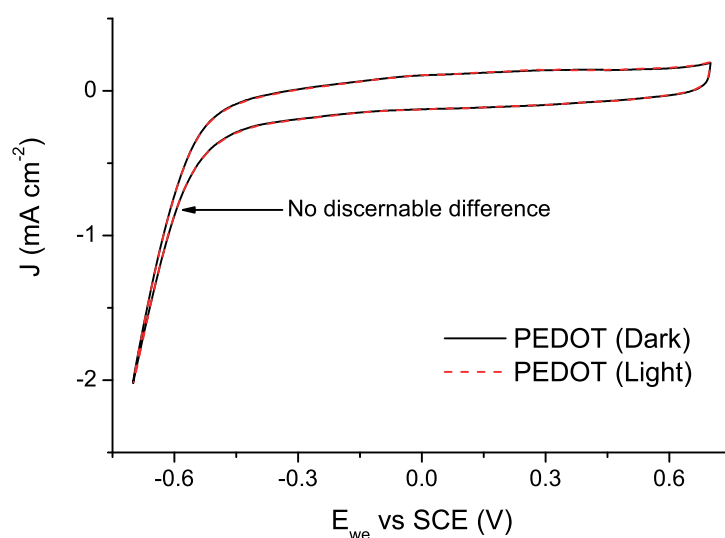
Figure 3.6: Light and Dark CV traces of PEDOT on Goretex (no gold), there is no observable photo-enhancement; the tests were conducted in $1\,\mathrm{mol\,L^{-1}}$ H_2SO_4, pH 0.

The photo-effect of PEDOT was unexpected and warranted further investigation. Studies were then undertaken on pure PEDOT films with Goretex substrates to avoid any catalytic effect from gold. As can be seen in Figure 3.6, these pure PEDOT films on Goretex did not exhibit any photo-enhancement in the absence of gold. This implied that the previously observed photo-response for the HER was due to a combination of the gold's catalytic abilities with PEDOT's inherent photo-absorbance.

Alternate substrates such as Ti film and FTO glass were also tried though they revealed no photo-response. The PEDOT and PEDOT:Brilliant Blue films were also ineffective as photo-catalysts towards other electrochemical reactions such as the reduction of Cu^{2+} to Cu or the reduction of $FcPF_6$; see Appendix C Figure S2 & S1. Moreover, the underlying catalytic concept of the ICP/dye was not realised and a redesign of the catalytic system was required. Several considerations were identified to aid in this, the most important of which was the correct characterisation and subsequent matching of energy band positions of the ICP and dye pair.

3.2 Exploration of Dye and Polymer Properties

A comprehensive analysis was undertaken for a wide variety of triarylmethane dyes as well as various ICPs from the polythiophene family, namely poly(2,2'-bithiophene) (PBTh), poly(2,2':5',2"-terthiophene) (PTTh) and PEDOT. The triarylmethane dye family was selected chiefly for their ability to remain stable in the precursor oxidant solution during the VPP process. Other common dye families like the azo- and phenazine- dyes were found to breakdown in the acidic oxidant solution and high temperatures of VPP. Characterisation was done via three main methods, electrochemistry, UV-Vis/fluorescence spectroscopy and computational chemistry.

Priority was given to electrochemical results as they were able to reveal the absolute HOMO (oxidation) and LUMO (reduction) levels. Optical spectroscopy and computational calculations reveal the HOMO/LUMO band gap and their predicted positions respectively but they were mainly intended to provide supporting data for the electrochemical results. By using the accumulated database of electrochemical and photo-excitation behaviour, it was hoped that an appropriate energy pairing of dye and conducting polymer could be made.

3.2.1 Electrochemistry

Characterisation was initially conducted using dichloromethane (DCM) but the small electrochemical window ($\approx 2\,\text{V}$) quickly precluded many dyes, where the reduction and oxidation of DCM obscures the dye peaks (Figure 3.7). This was a particularly noticeable problem with dyes that had large band gaps, as their oxidation and reduction positions were far apart.

Another electrolyte that was tried was propylene carbonate as it had a larger electrochemical window, however, it was not able to clearly resolve many dye peaks. An example of this can be observed in Figure 3.7 where the Rosolic Acid reduction couple at $-1\,\text{V}$ vs Fc/Fc^+ is absent in PC (red) but clearly observable in acetonitrile (blue). It was thus decided to conduct electrochemical characterisation of the dyes – at a concentration of $0.5\,\text{mmol}\,\text{L}^{-1}$ – in acetonitrile. The observed oxidation (E_{ox}) and reduction (E_{red}) redox couples were assigned as the HOMO and LUMO positions respectively and the difference between them as the electrochemical "band gap" (ΔE_{CV}) . These results and their discussion are presented in Publication 1 and its supplementary information in Appendix A.

3.2.2 Optical Spectroscopy

The band gap of the dye is an important piece of information that is able to reveal photo-excitation behaviour as well as provide support for electrochemical characterisation.[4] The use of UV-Vis and fluorescence spectroscopy is a common method with which to determine the dye's
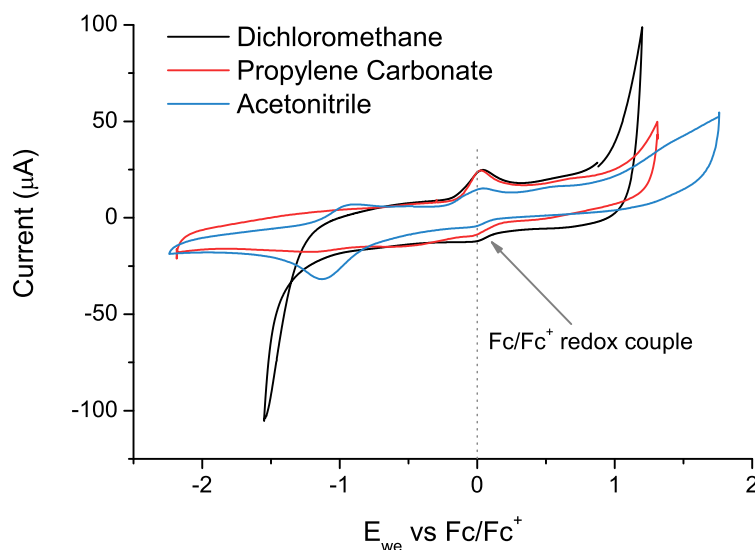
Figure 3.7: Characterisation of $0.5\,\mathrm{mmol\,L^{-1}}$ Rosolic Acid using various electrolytes with a $0.1\,\mathrm{mol\,L^{-1}}$ [TBA][PF$_6$] supporting electrolyte. $\mathrm{E_{we}}$ was normalised to a Fc/Fc$^+$ internal reference. Acetonitrile is ideal for its good peak resolution and large electrochemical window.

optical band gap ($\Delta\mathrm{E_{opt}}$) and is achieved by finding the intersection of the photo-absorbance (UV-Vis) and emission (fluorescence) spectra.[5]

To perform this, the dye solutions used in the electrochemical investigations were diluted to a concentration of $30\,\mathrm{\mu mol\,L^{-1}}$ and $10\,\mathrm{\mu mol\,L^{-1}}$ and analysed via UV-Vis and fluorescence spectroscopy respectively. The results of these studies are given in Publication 1.

3.2.3   Computational Calculations

Finally, as Publication 1 also will discuss, the determination of clear redox potentials for the HOMO and LUMO energies and well resolved photo-absorption and emission spectra for $\Delta\mathrm{E_{opt}}$ was not trivial. Computational chemistry was thus used to further aid in the characterisation of the dye. Thermodynamic parameters were calculated and used to find the free energy of the ground, oxidised and reduced species for each dye. From this, a Gibbs free energy for the redox reactions ($\Delta\mathrm{G_{ox/red}}$) and hence, $\mathrm{E_{ox}}$ and $\mathrm{E_{red}}$ could be calculated and compared with electrochemical results. Again, further details and discussion are presented in Publication 1.

3.3 Publication 1: Characterisation of a series of triarylmethane dyes as light harvesters for photo-electrochemical systems

The following paper details our experimental results and discussion with regards to the characterisation of triarylmethane dyes for use in future photo-electrocatalytic systems. Further information and the complete set of raw data used for this study can be found in Appendix A.

Characterisation of a series of triarylmethane dyes as light harvesters for photo-electrochemical systems

Chun Hin Ng [a, *], C. André Ohlin [b], Bjorn Winther-Jensen [a]

[a] Department of Materials Engineering, Monash University, Clayton 3800, Victoria, Australia
[b] School of Chemistry, Monash University, Clayton 3800, Victoria, Australia

ABSTRACT

A series of commercially available dyes were characterised by electrochemical, spectroscopic and computational methods. Several dyes, including Fuchsin Basic and Malachite Green were found to have properties that make them potential candidates for use in photo-electrochemical systems. The risks of combining different characterisation methods are also highlighted, namely the combination of thermodynamic reactions (electrochemical redox reactions), electronic transitions (optical spectroscopy) and the use of computational techniques to describe them.

© 2014 Elsevier Ltd. All rights reserved.

1. Introduction

The role of dyes as a functional component in electrochemical systems is a rapidly expanding field of which dye sensitised solar cells (DSSC) is perhaps the most prominent example [1–4]. Many of these devices utilise metal-based dyes that require expensive or toxic rare-earth elements [5], or custom synthesis of donor-acceptor type organic dyes [6], There are however, several low cost and commercially available dye families — such as those based on the *azo* and triarylmethane functionalities — that may show potential in these applications, many of which are non-toxic and produced annually on a large industrial scale [7,8].

Of particular interest to our research is the use of dyes in electrochemical systems as light harvesters [9], catalysts [10], and as substrate materials [11,12]. These applications take advantage of the inherent ability of the dye to absorb light and its electrochemical properties in order to create a photosensitive system. For the efficient design of a device it is thus imperative for a proper characterisation of both the photo- and electro-chemical properties [13–15].

We here investigate a series of triarylmethane dyes (Fig. 1) that are used as staining agents in microscopy (**1c**), pH indicators

(**4a, 4b**), anti-microbial agents (**2a, 2b**) as well as for colouring (**1b**) [16–18]. More importantly, triaryl dyes are known to be compatible with intrinsically conducting polymers [19], and present unique opportunities for developing novel organic dye sensitised systems. Yet, despite their advantages and commercial availability, the use of triaryl dyes as low-cost light harvesters in photo-electrochemical systems has thus far been limited.

To analyse these dyes, we explore several methods of characterisation. One of the most common is the use of cyclic voltammetry (CV) for the determination of the reduction (E_{red}) and oxidation (E_{ox}) potentials [20,21]. This method allows for the determination of the absolute energy levels, as opposed to relative energy levels, and is important in the understanding of the overall electron flow in the system. Another common technique is the combination of UV−Vis and fluorescence spectroscopy to identify the optical electronic transition energy (ΔE_{opt}) between the HOMO and LUMO energy levels [22,23]. Supplemented by CV data, ΔE_{opt} can be used to approximate the gap between reduction and oxidation potentials [24,25]. Additionally, computational methods are used to predict thermodynamic reduction and oxidation potentials. This last technique offers the possibility of exploring the properties of arbitrary dye structures, but requires a precise knowledge of the structures of the reactants and products. Here we are inspired by the DFT-based method of Speelman et al. [26,27] which are computationally affordable even in cases where access to high performance computing facilities is limited.

* Corresponding author. ▆▆▆▆▆▆▆
▆▆▆▆▆▆▆▆▆▆▆▆▆▆▆▆
▆▆▆▆▆▆▆▆▆▆▆▆
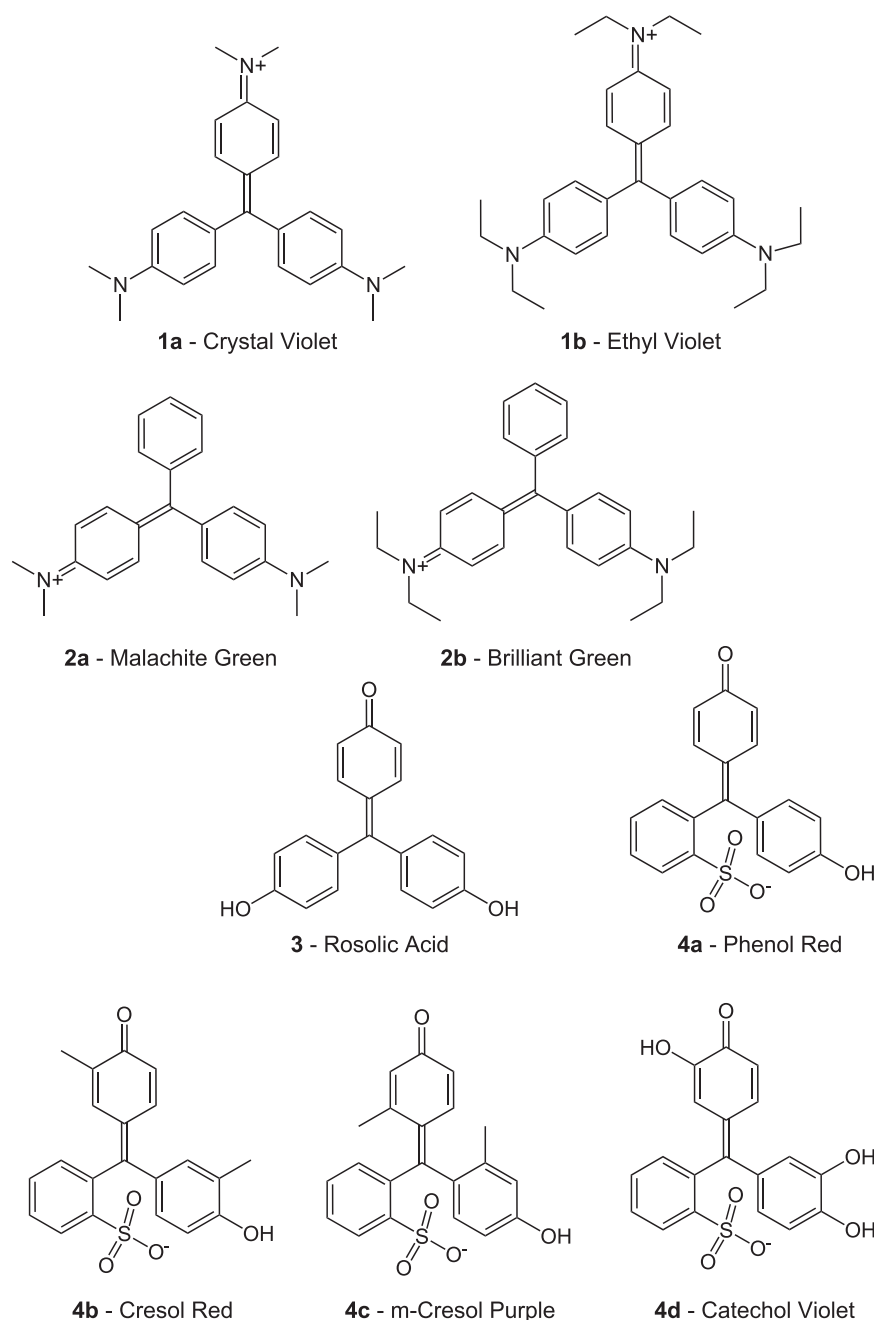
Fig. 1. Structures of the triarylmethane dyes in this study. Sub-groups 1 and 2 contain the nitrogen-based dyes: **1a**, **1b** for tri-amine dyes, **2a** and **2b** for di-amine dyes. Sub-groups 3−5 contain the oxygen based dyes which include the phenol type dyes **3** and the sulfonphthalein dyes **4a**, **4b**, **4c** and **4d**.

Importantly, by comparison and analysis of the varying techniques, the inherent short-comings of common literature methodologies are brought to light. These include, though is not limited to, the interchanging of the optically and electrochemically determined band gaps and the corresponding HOMO and LUMO energies. As this study and past studies support [28,29], significant deviations may result from its casual use.

2. Materials and methods

Ethyl Violet (**1b**), Malachite Green (**2a**), Brilliant Green (**2b**), p-Rosolic Acid (**3**), ferrocene (Fc) and tetrabutylammonium

hexafluorophosphate ([TBA][PF$_6$]) were obtained from Sigma Aldrich. Crystal Violet (**1a**), Cresol Red (**4b**) and Catechol Violet (**4d**) were obtained from the British Drug House, m-Cresol Purple (**4c**) from May & Baker, and Phenol Red (**4a**) from Fluka AG. Anhydrous acetonitrile from Sigma Aldrich was dried over freshly prepared 4 Å molecular sieves and stored in a nitrogen atmosphere. All other chemicals were used as received and verified using UV−Vis spectroscopy and mass spectroscopy, see ESI† (Table S1 and Figures S19−S27). The dye structures are shown in Fig. 1.

Dye solutions were prepared under a nitrogen atmosphere in a glove box using oven-dried (70 °C, 30 min) reagents. All dye

solutions were made to a concentration of 0.5 mmol L^{-1} in acetonitrile with 50 mmol L^{-1} [TBA][PF6] as the supporting electrolyte.

Cyclic voltammetry was performed using a high surface area titanium mesh [30,31] as the counter electrode and platinum wire as both reference and working electrodes. Data was acquired under a nitrogen atmosphere in a glove box at a scan rate of 20 mV s^{-1}. A ferrocene/ferrocenium (Fc/Fc$^+$) couple was used as an internal reference. [32].

The solutions used in the electrochemical study were then further diluted in acetonitrile to a concentration of 30 μmol L^{-1} and used for UV–Vis spectroscopy. Spectra were acquired between 190 and 1000 nm using quartz cuvettes. The wavelength of the maximum absorption in the visible region was assigned λ_{abs}. Fluorescence spectra of 10 μmol L^{-1} dye solutions in acetonitrile were acquired using λ_{abs} as the excitation wavelength and the resulting emission peak recorded as λ_{em}. For particularly noisy or low fluorescing dyes, the concentration was gradually increased from 10 μmol L^{-1} until a clear fluorescence emission peak λ_{em} was obtained.

Thermodynamic cycles were used to calculate the free energy changes for the oxidation and reduction of the ground state; where oxidised and reduced state were defined as the removal and addition of an electron from the ground state respectively. Calculations were done using a similar level of theory as was used by Speelman et al., see ESI† for further details. Briefly, the geometry of all species were optimised at the B3LYP/6-31 + G* [33–40] level of Kohn-Sham density functional theory while solvent effects were approximated using the COnductor-like Screening Model [41,42] (COSMO) with a solvent radius of 2.16 Å and dielectric constant of 36.64. Enthalpy and entropy values were determined via vibrational calculations on the optimised structure. Thermodynamic parameters from these normal mode analyses were used to calculate the reduction and oxidation potentials using a thermochemical cycle. The tabulated computational data can be found in the ESI†, Table S2. All computations were carried out using NWChem 6.4 [43], and managed by ECCE 7.0 [44].

The electrochemical, spectroscopic and computational data are tabulated in Table 1. Full cyclic voltammograms of the dyes before and after the addition of Fc/Fc$^+$ (Figures S1—S9) and optical spectra (Figures S10—S18) are available in the ESI†. All dyes, owing to their similar chemical structures, showed reduction, oxidation and optical activity in similar ranges.

3. Results and discussion

3.1. Electrochemical characterisation

There were a few principal challenges in characterising some of the dyes by cyclic voltammetry. These included weak redox reactions that led to broad or indistinct peaks (see Fig. 2B) as well as the presence of multiple redox processes which made it difficult to assign peaks to a specific process. Furthermore, some of the redox processes were irreversible and prevented the calculation of $E_{1/2}$. In these cases, E_{ox} and E_{red} were defined as the potential corresponding to the oxidation and reduction peak respectively (E_{peak}). As the peak potential is an overestimation of $E_{1/2}$, an empirically determined correction factor of 0.3 V has been included for positions determined using E_{peak} and can be observed in Fig. 4C. Typically, nitrogen based dyes such as Ethyl Violet **1b**, showed strong reversible redox processes (Fig. 2A) while oxygen based dyes such as Cresol Red **4b** (Fig. 2B) were more problematic and exhibited many of the aforementioned issues.

3.2. Optical spectroscopy characterisation

The combination of UV–Vis and fluorescence spectra was used to calculate ΔE_{opt} (Fig. 3) [28,45,46]. ΔE_{opt} was determined as the lowest energy intersect (λ_{int}) of the emission/excitation spectra. The variability in concentration between absorbance and fluorescence is assumed to affect λ_{int} with an empirically approximated symmetrical error of 0.04 eV.

3.3. Computational results

Computationally derived oxidation and reduction potentials were in most cases of the same order of magnitude as the experimentally derived electrochemical data (Fig. 4). This is particularly satisfying given that a relatively small basis set had to be used to yield manageable computational times owing to the large size of the organic molecules in this study. The large size of the dyes also rules out the use of more accurate post-Hartree-Fock methods *e.g.* Moeller-Plesset perturbation theory or coupled-cluster approaches. A significant weakness was also the inherent poor accuracy of implicit solvation models, which precludes the attainment of chemical accuracy.

Table 1
Tabulated data from electrochemical, computational and spectroscopic experiments.

Dye	Cyclic voltammetry			Computational (B3LYP/6-31 + G*)			Optical spectroscopy			
	E_{ox} (eV)[a]	E_{red} (eV)[a]	ΔE_{CV} (eV)[b]	E_{ox} (eV)[c]	E_{red} (eV)[c]	ΔE_{calc} (eV)	λ_{abs} (nm)[d]	λ_{em} (nm)[e]	λ_{int} (nm)	ΔE_{opt} (eV)[f]
1a	−5.70	−3.79	1.91	−5.42	−3.35	2.07	588	638	612	2.03
1b	−5.67	−3.78	1.88	−5.64	−3.35	2.28	592	639	616	2.02
2a	−5.66	−4.04	1.61	−5.68	−3.63	2.05	618	669	643	1.93
2b	−5.65	−4.06	1.60	−5.78	−3.62	2.16	626	678	648	1.92
3	−5.53	−4.01	1.51	−5.64	−3.16	2.47	420	547	500	2.48
4a	−5.63	−4.14	1.49	−6.89	−3.87	3.02	390	516	461	2.69
4b	−5.53	−4.07	1.46	−5.00	−2.84	2.16	394	553	465	2.67
4c	−5.56	−4.19	1.37	−5.48	−3.13	2.35	388	534	461	2.69
4d	−6.08	−4.18	1.90	−5.75	−3.56	2.19	420	544	472	2.63

[a] Assigned as the first clearly identifiable redox couple ($E_{1/2}$) on the respective oxidation and reduction sides. Converted to absolute energies by the relationship: eV = $E^+_{Fc/Fc}$ − $E_{ox/red}$, where $E^+_{Fc/Fc}$ = −4.988 eV [53].
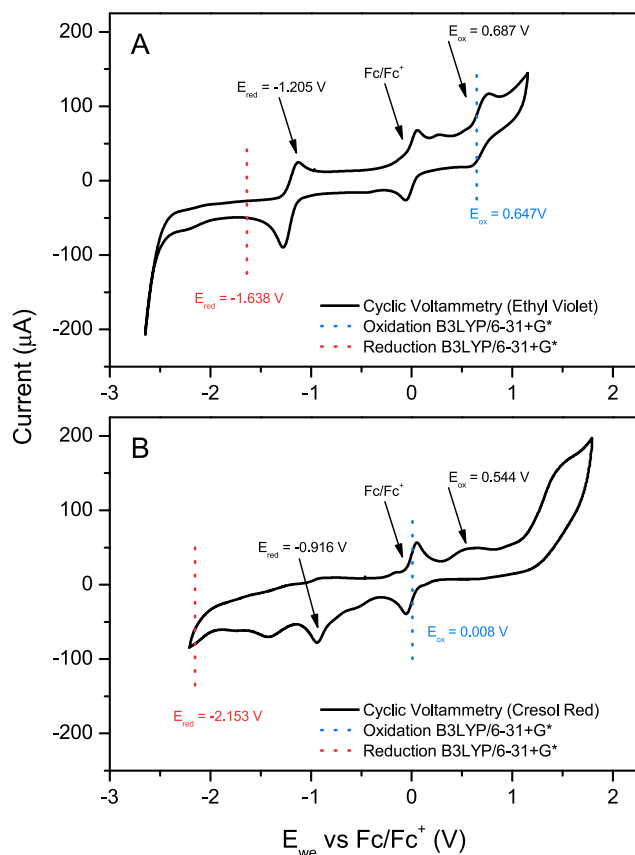[b] The difference between E_{ox} and E_{red}.
[c] ΔG is obtained from the calculations and converted to a potential ($E_{ox/red}$) via the relationship: ΔG = −nFE, full details in ESI†.
[d] λ_{max} from UV–Vis absorbance spectrum.
[e] λ_{max} from fluorescence emission spectrum.
[f] The intersect between the UV–Vis and fluorescence spectra.

Fig. 2. Cyclic voltammograms of 0.5 mmol L^{-1} solutions of Ethyl violet (**A**) and Cresol Red (**B**) in acetonitrile with 50 mmol L^{-1} [TBA][PF$_6$] at a scan rate of 20 mV/s. Computed reduction and oxidation potentials are indicated in blue and red, respectively. (For interpretation of the references to colour in this figure legend, the reader is referred to the web version of this article.)
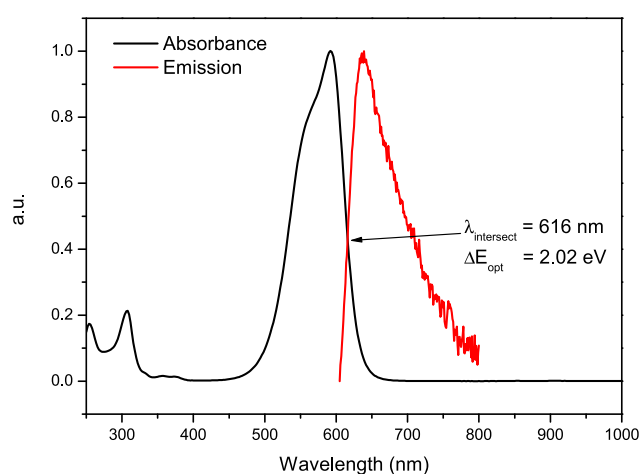
Fig. 3. Normalised UV—Vis absorbance (black) and fluorescence emission (red) spectra of Ethyl Violet in acetonitrile (30 μM and 10 μM, respectively). The λ$_{intersect}$ that corresponds to ΔE$_{opt}$ is shown. (For interpretation of the references to colour in this figure legend, the reader is referred to the web version of this article.)

3.4. Comparison between characterisation techniques

There was overall poor correlation between either the electrochemical and spectroscopic data, or the electrochemical and computational data. A detailed analysis shows that while the computational method quite accurately predicts the oxidation potential for some dyes, and fails spectacularly for others, it systematically overestimates the reduction potential, leading to the overall poor correlation between ΔE$_{CV}$ and ΔE$_{calc}$ (Fig. 4B). There were some notable exceptions, however, and these include Ethyl Violet and other members of the nitrogen based dyes (dyes **1a-b** and **2a-b**) which underwent reversible redox reactions. In either case the magnitude of non-systematic errors and the limited data range precluded the establishment of a simple linear correlation between the computed and experimentally determined data such as that described by Speelman et al. to better link computational and experimental data.

The qualitative correlation between the computational (ΔE$_{calc}$) and spectroscopic (ΔE$_{opt}$) data was somewhat better. According to the Franck-Condon principle, optical excitation is rapid and generally not accompanied by structural or chemical changes and instead constitutes a vertical electronic excitation. This was an implicit assumption present in the computational method — in that no chemical changes were accounted for — and may explain the relatively good correlation between ΔE$_{calc}$ and ΔE$_{opt}$ (Fig. 4A). However, this isn't necessarily the case for thermodynamic processes such as electrochemical reduction and oxidation where the species can undergo subsequent reactions, ranging from protonation/deprotonation and reorganisation [47—49]. The generally poor agreement between ΔE$_{opt}$ and ΔE$_{CV}$ (Fig. 4D) and much better agreement between ΔE$_{opt}$ and ΔE$_{calc}$ suggests that most of the dyes undergo at least some structural rearrangement. This is further supported by the observation where dyes that underwent reversible redox processes and exhibited clear redox waves — *e.g.* nitrogen based dyes — showed a closer agreement between the different methods. The reversibility indicates that they underwent minimal rearrangement, while dyes that were irreversibly reduced or oxidised, or showed diffuse peaks in the CV spectrum — such as the oxygen based dyes — showed a much poorer agreement, most likely due to redox induced structural and chemical changes. These irreversible processes strongly indicate that they can no longer be represented by a simple single electron addition/removal from the conjugated π system as is done in the computational method, and similarly, are not suitable targets for optical spectroscopy approximations that rely on vertical HOMO-LUMO transitions.

This is an important point to note due to the prevalence in the current literature that makes use of such approximations i.e., the determination of the LUMO (reduction) position by the addition of an optically determined band gap to an electrochemically determined HOMO (oxidation) level [50—52]. While the simplicity of this process is attractive, the present work is a strong reminder that not all species conform to this approximation; in particular, species that undergo conformational or chemical changes (*i.e.* pH dependent species). The lack of structural relaxation in the case of electronic transitions, as determined by the optical methods, means that these methods should yield a larger ΔE than the electrochemical method, which is a thermodynamic process.

Though the combination of optical and electrochemical methods is not empirically incorrect, it is important to be aware of the fundamental issues associated with combining a slow thermodynamic process (redox reactions) with a rapid electronic process (optical transitions) without proper consideration of the system.
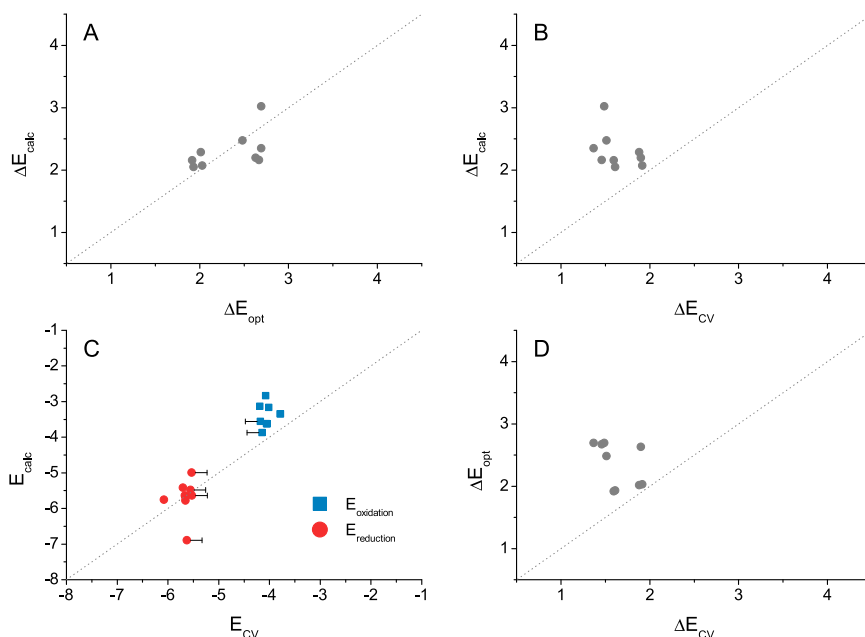
Fig. 4. Comparison between the different data sets. Values that lie on or close to the dotted line is indicative of good correlation between the methods.

4. Conclusions

We have compared electrochemical, spectroscopic and computational techniques as probes for the selection of triarylmethane dyes as low-cost light harvesters in electrochemical systems. We find that while there is some correlation between the methods for narrow classes of dyes, overall neither the optical or computational methods can predict the suitability of a dye for inclusion in photo-electrochemical devices as they do not reflect the presence of irreversible redox processes, nor do they provide a good quantitative indication of where these processes will occur.

The nitrogen based dyes (**1a-b, 2a-b**) showed promising features such as redox reversibility and strong light absorbance making them potential candidates for inclusion in photo-electrochemical systems. In contrast, the oxygen based dyes (**3, 4a-d**) revealed chemically unstable redox states and weak light absorption and as such, are unlikely candidates for light harvesters. However, these characteristics may lend themselves to applications as sensors.

Because the correlation between the different methods explored was low, the findings highlight the potential issues with characterisation methods currently employed for functional dyes: restricting the characterisation to a single or partial method is insufficient in providing a full and accurate picture of the dye's behaviour in photo-electrochemical systems.

Appendix A. Supplementary data

Supplementary data related to this article can be found at http://dx.doi.org/10.1016/j.dyepig.2014.12.016.

References

[1] Chatterjee D. Effect of excited state redox properties of dye sensitizers on hydrogen production through photo-splitting of water over TiO_2 photocatalyst. Catal Commun 2010;11:336–9.
[2] Maia DLS, Pepe I, Ferreia da Silva A, Silva LA. Visible-light-driven photocatalytic hydrogen production over dye-sensitized β-$BiTaO_4$. J Photochem Photobiol A 2012;243:61–4.
[3] Kanaparthi RK, Kandhadi J, Giribabu L. Metal-free organic dyes for dye-sensitized solar cells: recent advances. Tetrahedron 2012;68:8383–93.
[4] Kosa T, Sukhomlinova L, Su L, Taheri B, White TJ, Bunning TJ. Light-induced liquid crystallinity. Nature 2012;485:347–9.
[5] Mishra A, Fischer MKR, Bäuerle P. Metal-free organic dyes for dye-sensitized solar cells: from structure: property relationships to design rules. Angew Chem Int Ed 2009;48:2474–99.
[6] Lin L-Y, Chen Y-H, Huang Z-Y, Lin H-W, Chou S-H, Lin F, et al. A low-energy-gap organic dye for high-performance small-molecule organic solar cells. J Am Chem Soc 2011;133:15822–5.
[7] Ogugbue CJ, Sawidis T. Bioremediation and detoxification of synthetic wastewater containing triarylmethane dyes by Aeromonas hydrophila Isolated from industrial effluent. Biotechnol Res Int 2011;2011:967925.
[8] Silveira E, Marques PP, Macedo a. C, Mazzola PG, Porto a. LF, Tambourgi EB. Decolorization of industrial azo dye in an anoxic reactor by PUF immobilized Pseudomonas oleovorans. J Water Reuse Desalin 2011;1:18.
[9] O'Regan B, Grätzel M. A low-cost, high-efficiency solar cell based on dye-sensitized colloidal TiO_2 films. Nature 1991;353:737–40.
[10] Bi Z, Tien HT. Photoproduction of hydrogen by dye-sensitized systems. Int J Hydrogen Energy 1984;9:717–22.
[11] Ghica ME, Brett CMA. Poly(brilliant cresyl blue) modified glassy carbon electrodes: electrosynthesis, characterisation and application in biosensors. J Electroanal Chem 2009;629:35–42.
[12] Barsan MM, Pinto EM, Brett CMA. Methylene blue and neutral red electro-polymerisation on AuQCM and on modified AuQCM electrodes: an electrochemical and gravimetric study. Phys Chem Chem Phys 2011;13:5462–71.
[13] Barsan MM, Pinto EM, Brett CMA. Electrosynthesis and electrochemical characterisation of phenazine polymers for application in biosensors. Electrochim Acta 2008;53:3973–82.
[14] Pauliukaite R, Ghica ME, Barsan MM, Brett CMA. Phenazines and Poly-phenazines in electrochemical sensors and biosensors. Anal Lett 2010;43:1588–608.
[15] Kushwaha S, Bahadur L. Characterization of some metal-free organic dyes as photosensitizer for nanocrystalline ZnO-based dye sensitized solar cells. Int J Hydrogen Energy 2011;36:11620–7.
[16] Sabnis RW. Handbook of biological dyes and stains. New Jersey: John Wiley & Sons Ltd; 2010.
[17] Sabnis R. Handbook of acid-base indicators. Boca Raton: CRC Press; 2008.
[18] Cha C, Doerge DR, Cerniglia CE. Biotransformation of malachite green by the fungus Cunninghamella elegans biotransformation of malachite green by the fungus Cunninghamella elegans. Appl Environ Microbiol 2001;67:4358–60.

[19] Winther-Jensen B, Clark NB. Controlled release of dyes from chemically polymerised conducting polymers. React Funct Polym 2008;68:742—50.

[20] Mori S, Yanagida S. TiO$_2$-Based dye-sensitized solar cells. In: Soga T, editor. Nanostructured materials for solar energy conversion. Elsevier; 2006.

[21] Hara K, Wang Z-S, Sato T, Furube A, Katoh R, Sugihara H, et al. Oligothiophene-containing coumarin dyes for efficient dye-sensitized solar cells. J Phys Chem B 2005;109:15476—82.

[22] Seo KD, Song HM, Lee MJ, Pastore M, Anselmi C, De Angelis F, et al. Coumarin dyes containing low-band-gap chromophores for dye-sensitised solar cells. Dye Pigment 2011;90:304—10.

[23] Shen P, Liu X, Jiang S, Wang L, Yi L, Ye D, et al. Synthesis of new N, N-diphenylhydrazone dyes for solar cells: effects of thiophene-derived π-conjugated bridge. Dye Pigment 2012;92:1042—51.

[24] Kitamura T, Ikeda M, Shigaki K, Inoue T, Anderson NA, Ai X, et al. Phenyl-conjugated oligoene sensitizers for TiO$_2$ solar cells. Chem Mater 2004;16: 1806—12.

[25] Zhou H, Xue P, Zhang Y, Zhao X, Jia J, Zhang X, et al. Fluorenylvinylenes bridged triphenylamine-based dyes with enhanced performance in dye-sensitized solar cells. Tetrahedron 2011;67:8477—83.

[26] Speelman AL, Gillmore JG. Efficient computational methods for accurately predicting reduction potentials of organic molecules. J Phys Chem A 2008;112:5684—90.

[27] Lynch E, Speelman A. Testing a computational method for predicting the ground state reduction potentials of organic molecules on the basis of empirical correlation to experiment. J Org Chem 2012;77:6423—30.

[28] Djurovich PI, Mayo EI, Forrest SR, Thompson ME. Measurement of the lowest unoccupied molecular orbital energies of molecular organic semiconductors. Org Electron 2009;10:515—20.

[29] Al-Ibrahim M, Konkin A, Roth H-K, Egbe D a M, Klemm E, Zhokhavets U, et al. Phenylene-ethynylene/phenylene-vinylene hybrid polymers: optical and electrochemical characterization, comparison with poly[2-methoxy-5-(3′,7′-dimethyloctyloxy)-1,4-phenylene vinylene] and application in flexible polymer solar cells. Thin Solid Films 2005;474:201—10.

[30] Howlett PC, Zhang S, MacFarlane DR, Forsyth M. An investigation of a phosphinate-based Ionic liquid for corrosion protection of magnesium Alloy AZ31. Aust J Chem 2007;60:43.

[31] Hilder M, Winther-Jensen O, Winther-Jensen B, MacFarlane DR. Graphene/zinc nano-composites by electrochemical co-deposition. Phys Chem Chem Phys 2012;14:14034—40.

[32] Gritzner G, Kuta J. Recommendations on reporting electrode potentials in nonaqueous solvents. Electrochim Acta 1984;29:869—73.

[33] Hehre WJ, Ditchfield R, Pople JA. Self—consistent molecular orbital methods. XII. further extensions of gaussian—Type basis sets for use in molecular orbital studies of organic molecules. J Chem Phys 1972;56:2257.

[34] Francl MM, Pietro WJ, Hehre WJ, Binkley JS, Gordon MS, DeFrees DJ, et al. Self-consistent molecular orbital methods. XXIII. A polarization-type basis set for second-row elements. J Chem Phys 1982;77:3654.

[35] Clark T, Chandrasekhar J, Spitznagel GW, Schleyer PVR. Efficient diffuse function-augmented basis sets for anion calculations. III. The 3-21+G basis set for first-row elements, Li-F. J Comput Chem 1983;4:294—301.

[36] Hariharan P, Pople J. The influence of polarization functions on molecular orbital hydrogenation energies. Theor Chim Acta 1973;28:213—22.

[37] Slater J, Johnson K. Self-consistent-field Xα cluster method for polyatomic molecules and solids. Phys Rev B 1972;5:844—53.

[38] Becke A. Density-functional exchange-energy approximation with correct asymptotic behavior. Phys Rev A 1988;38:3098—100.

[39] Vosko SH, Wilk L, Nusair M. Accurate spin-dependent electron liquid correlation energies for local spin density calculations: a critical analysis. Can J Phys 1980;58:1200—11.

[40] Lee C, Yang W, Parr R. Development of the Colle-Salvetti correlation-energy formula into a functional of the electron density. Phys Rev B 1988;37:785—9.

[41] Klamt A, Schuurmann G, Schüürmann G. COSMO: a new approach to dielectric screening in solvents with explicit expressions for the screening energy and its gradient. J Chem Soc Perkin Trans 1993;2:799—805.

[42] York D, Karplus M. A smooth solvation potential based on the conductor-like screening model. J Phys Chem A 1999;103:11060—79.

[43] Valiev M, Bylaska EJ, Govind N, Kowalski K, Straatsma TP, Dam HJJ van, et al. NWChem: a comprehensive and scalable open-source solution for large scale molecular simulations. Comput Phys Commun 2010;181:1477.

[44] Black G, Karen S, Gracio D, Palmer B. The Extensible computational chemistry Environment: a problem solving environment for high performance theoretical chemistry. Berlin: Comput. Sci. - ICCS; 2003. p. 122—31.

[45] Egbe D, Cornelia B, Nowotny J, Gunther W, Klemm E. Investigation of the photophysical and electrochemical properties of alkoxy-substituted arylene-ethynylene/arylene-vinylene hybrid polymers. Macromolecules 2003;36:5459—69.

[46] Wilson J, Windscheif P, Evans U, Myrick ML, Bunz UHF. Band gap engineering of poly (p-phenyleneethynylene) s: cross-conjugated PPE-PPV hybrids. Macromolecules 2002;35:8681—3.

[47] Patsavas MC, Byrne RH, Liu X. Physical—chemical characterization of purified cresol red for spectrophotometric pH measurements in seawater. Mar Chem 2013;155:158—64.

[48] Clayton TD, Byrne RH. Spectrophotometric seawater pH measurements: total hydrogen ion concentration scale calibration of m-cresol purple and at-sea results. 1 Deep Sea Res 1993;40:2115—29.

[49] Byrne L, Lau KT, Diamond D. Monitoring of headspace total volatile basic nitrogen from selected fish species using reflectance spectroscopic measurements of pH sensitive films. Analyst 2002;127:1338—41.

[50] Baheti A, Singh P, Lee C-P, Thomas KRJ, Ho K-C. 2,7-diaminofluorene-based organic dyes for dye-sensitized solar cells: effect of auxiliary donor on optical and electrochemical properties. J Org Chem 2011;76:4910—20.

[51] Mike JF, Nalwa K, Makowski AJ, Putnam D, Tomlinson AL, Chaudhary S, et al. Synthesis, characterization and photovoltaic properties of poly (thiophenevinylene-alt-benzobisoxazole)s. Phys Chem Chem Phys 2011;13: 1338—44.

[52] Wu W, Zhang J, Yang H, Jin B, Hu Y, Hua J, et al. Narrowing band gap of platinum acetylide dye-sensitized solar cell sensitizers with thiophene π-bridges. J Mater Chem 2012;22:5382.

[53] Namazian M, Lin CY, Coote ML. Benchmark calculations of absolute reduction potential of ferricinium/ferrocene couple in nonaqueous solutions. J Chem Theory Comput 2010;6:2721—5.

3.4   Refined Polymer and Dye Blends

Using the data from Publication 1 and the previous electrochemical characterisation of ICP films – as performed by group members and presented in Table 3.2[6] – it was possible to explain the failings of the initial PEDOT:Brilliant Blue/Rosolic Acid films. Specifically, the band energy structure of PEDOT was inappropriate for the envisioned ICP/dye system.

Table 3.2: The valence (E_{ox}) and conduction band (E_{red}) – vs vacuum – of various ICPs as determined by cyclic voltammetry. The difference between them (ΔE_{CV}) is the electrochemical band gap and analogous to E_g.[7]

ICP	E_{ox} (eV)	E_{red} (eV)	ΔE_{CV} (eV)
PEDOT	-4.32	-2.84	1.48
PBTh	-5.48	-2.74	2.74
PTTh	-5.17	-2.74	2.43

The valence band energy of -4.32 eV in PEDOT is too high to effectively regenerate the dye species. Without this transfer, charge separation becomes difficult and the dye initiated photo-system fails. The close proximity of the PEDOT valence band and the H^+ reduction potential is also problematic as this bypasses the dye's role as light harvester. On the other hand, it may explain why PEDOT was photo-catalytic towards the HER when combined with gold, where some of the excited state electrons were transferred to Au with sufficient energy to perform the HER. These issues are better highlighted in Figure 3.8 and reveal that the initial ICP/dye pairings were not ideal for our envisioned photo-system (described in Figure 3.1). An alternative ICP candidate is PBTh, where the much lower valence band energy of -5.48 eV enables it to regenerate and thus pair well with a variety of dyes.
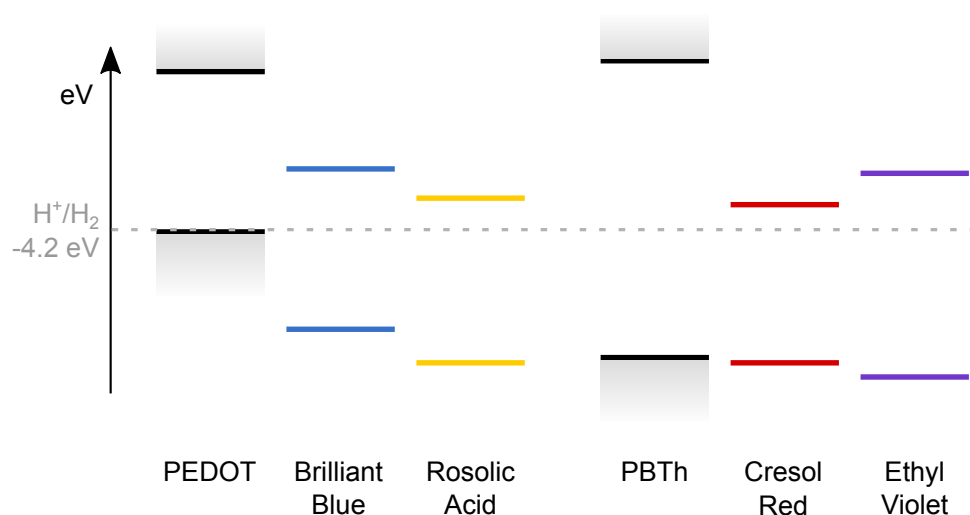

Figure 3.8: The determined band energies in acetonitrile for the initial ICP/dye combinations (PEDOT:Brilliant Blue/Rosolic Acid), and the new ICP/dye combination after characterisation (PBTh:Cresol Red/Ethyl Violet).

3.4.1 Polybithiophene:Dye Blends

The characterisations revealed numerous new pairings, amongst which was PBTh with the dyes Cresol Red and Ethyl Violet, where their energy levels were ideally suited for the photo-system. PBTh is of sufficient energy and close proximity for charge separation/dye regeneration and the dye's respective LUMO bands are at an appropriate level to to reduce H^+ (Figure 3.8). As a result, blends of PBTh:Cresol Red and PBTh:Ethyl Violet were made in a ratio of 1:1 to investigate their catalytic performance under illumination. Glassy Carbon was chosen as the substrate for its inertness over a wide range of potentials and served as a much better alternative to the catalytically active gold mylar.

The initial CV performance of the films in $1\,mol\,L^{-1}$ H_2SO_4 (pH 0) under N_2 is revealed in Figure 3.9A. The PBTh:Ethyl Violet film exhibited increased noise with the application of light but did not show any distinguishable photo-electrocatalytic response; experiments using CA at various potentials revealed the same inert behaviour. This suggests that despite the correct thermodynamic energy requirements, the photo-system is ineffective due to kinetic limitations and/or other phenomenon. A variety of mechanisms come to mind and include: fast recombination rates of the exciton, slow diffusion of H^+ to the active site, difficult charge transfer from the dye to H^+ and bad electronic interaction between PBTh and Ethyl Violet.
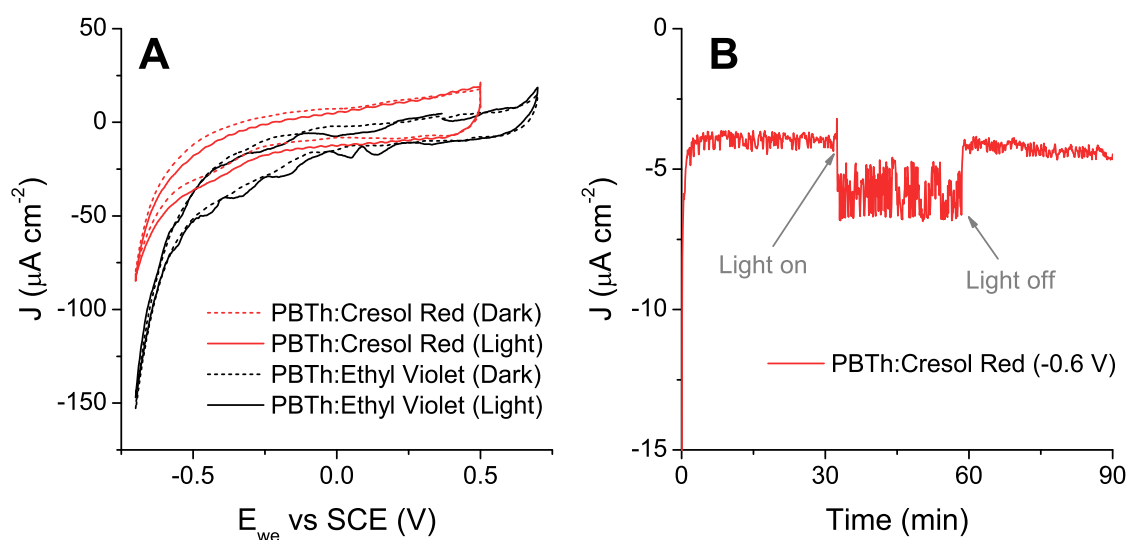
Figure 3.9: The photo-response of the newly paired PBTh:Dye films (1:1) conducted in $1\,mol\,L^{-1}$ H_2SO_4 at pH 0 with bubbled N_2. **A:** CV of PBTh:Cresol Red and PBTh:Ethyl Violet comparing light and dark response (scan rate $= 10\,mV\,s^{-1}$). **B:** CA of PBTh:Cresol Red whilst held at $-0.6\,V$ vs SCE.

A different story was observed for the PBTh:Cresol Red film where a small but noticeable photo-enhancement was consistently observed over a large number of CV cycles (Figure 3.9A, red). Further investigation using CA at $-0.6\,V$ vs SCE showed a distinct and rapid increase in the reduction current when light was applied at 30 min, which was then reversed when the light

was turned off at 60 min (Figure 3.9B). The effect was even more compelling when considering the inert glassy carbon substrate as this photo-current and catalytic response is solely provided by the PBTh:Cresol Red film. These factors confirmed that a photo-electrocatalytic response was occurring on the PBTh:Cresol Red film, though further confirmation was required to determine the exact nature of the reaction.

3.5   Conclusion

Many initial failings were revealed with the PEDOT:Brilliant Blue films, the most critical of which was the use of catalytically active gold mylar as the substrate material. It resulted in many experiments revealing false positives such as PEDOT's photo-electrocatalytic response. While this was novel, more thorough investigations revealed that the underlying mechanism was dependent on gold. This fact, combined with the relatively modest photo-enhancement, meant that pursuit of PEDOT based films were not ideal.

These findings thus catalysed the in-depth characterisation studies which helped shed light on the limitations of the initial PEDOT:dye films. More importantly, the breadth of the studies allowed the identification of alternate triarylmethane dyes for use as light harvesters. The promising PBTh:Cresol Red film was discovered in the subsequent studies and displayed photo-electrocatalytic behaviour in acidic conditions. This conducting polymer:dye combination showed immense potential for further investigations and seeded the discovery of a successful conducting polymer-based photo-electrocatalyst for the HER, as will be discussed in the following chapter.

Bibliography

[1] B. Winther-Jensen, O. Winther-Jensen, M. Forsyth and D. R. Macfarlane. "High rates of oxygen reduction over a vapor phase-polymerized PEDOT electrode." *Science*, 2008. **321**, 5889, 671–4.

[2] O. Winther-Jensen, B. Winther-Jensen and D. R. MacFarlane. "Photostimulated electrocatalysis of water oxidation by conjugated polymers". *Electrochem. commun.*, 2011. **13**, 4, 307–309.

[3] B. Winther-Jensen, K. Fraser, C. Ong, M. Forsyth and D. R. MacFarlane. "Conducting polymer composite materials for hydrogen generation." *Adv. Mater.*, 2010. **22**, 15, 1727–1730.

[4] I. Kaur, W. Jia, R. P. Kopreski, S. Selvarasah, M. R. Dokmeci, C. Pramanik, N. E. McGruer and G. P. Miller. "Substituent effects in pentacenes: gaining control over HOMO-LUMO gaps and photooxidative resistances." *J. Am. Chem. Soc.*, 2008. **130**, 48, 16274–86.

[5] T. Kitamura, M. Ikeda, K. Shigaki, T. Inoue, N. A. Anderson, X. Ai, T. Lian and S. Yanagida. "Phenyl-conjugated oligoene sensitizers for TiO2 solar cells". *Chem. Mater.*, 2004. **16**, 1806–1812.

[6] B. Kolodziejczyk, D. Mayevsky and B. Winther-Jensen. "Enhanced absorption spectra of conducting polymers co-polymerised from thiophene derivatives". *RSC Adv.*, 2013. **3**, 14, 4568–4573.

[7] A. J. Bard and L. R. Faulkner. *Electrochemical methods: fundamentals and applications*. John Wiley & Sons, Inc, New York, 2001.

Chapter 4

Photo-electrochemical Catalysis of the Hydrogen Evolution Reaction

PART B: Declaration for Thesis Chapter 4

Declaration by candidate

In the case of Chapter 4, Publication 2, the nature and extent of my contribution to the work was the following:

Nature of contribution	Extent of Contribution
Initiation of work	95 %

The following co-authors also contributed to the work. If co-authors are students at Monash University, the extent of their contribution in percentage terms must be stated.

Name	Nature of contribution	Extent of Contribution
Orawan Winther-Jensen	SEM microscopy, proof reading	NA
Bartlomiej Kolodziejczyk	Calibration of light source, advice on technical drawings, initiation of work	5%
C. André Ohlin	Proof reading, drafting	NA
Bjorn Winther-Jensen	Key ideas, proof reading, drafting	NA

The undersigned hereby certify that the above declaration correctly reflects the nature and extent of the candidate's and co-authors' contributions to this work*.

Candidate's Signature   **Supervisor's Signature**

Date: Date:

*Note: Where the responsible author is not the candidate's main supervisor, the main supervisor should consult with the responsible author to agree on the respective contributions of the authors.

4.1 Introduction

The characterisation of the dye and conducting polymer films represented a large step in the right direction towards the development of a HER catalyst. From this, the identification and testing of the PBTh:Cresol Red blend in the previous chapter showed promising hints of photo-activity. However, the confirmation of the HER was not trivial and required numerous steps in order to confirm the successful production of H_2. The following chapter thus describes the process in which the HER was isolated, confirmed and H_2 detected as well as presenting the paper in which this finding is described. Unless otherwise stated, glassy carbon was the substrate used throughout the following chapter due to its inertness towards the HER.[1]

4.1.1 Continued Studies on PBTh:Cresol Red

The discovery of a successful photo-electrocatalytic reaction with PBTh:Cresol Red represented an important step in the development of ICP/dye blends. Nevertheless, the exact nature of the reaction needed to be determined, particularly as the dark baseline of the PBTh:Cresol Red – observed in Figure 3.9 as $4\,\mu A\,cm^{-2}$ – was not negligible. A key concern was that the non-zero baseline could represent the oxygen reduction reaction (ORR) as shown in Eq 4.1, and is a competing reaction to the HER. Furthermore, earlier studies from the group have shown PBTh and PEDOT to be photo-electrocatalytically active towards O_2 reduction[2,3] and it was possible that the previously observed photo-response was due to the ORR.

$$O_2 + 4H^+ + 4e^- \longrightarrow 2H_2O \qquad (4.1)$$

To investigate further, plain PBTh and the blended PBTh:Cresol Red (1:1) film were analysed using CV under bubbled air, Figure 4.1A. From this, it was clearly evident that both PBTh and PBTh:Cresol Red were cataltyic towards the ORR with an impressive $0.55\,V$ reduction in onset potential (light vs dark). As an aside, PBTh:Cresol Red had a slightly earlier ORR E_{onset} than PBTh which might be attributed to the dye, however, the difference is small and Cresol Red was not as effective as originally intended.

The results presented in Figure 4.1A threw doubt on the promising photo-electrocatalytic results presented in the previous chapter (Figure 3.9). In hindsight, the lower bubbling rate of N_2 and use of the plastic (non-air tight) preliminary cell would have easily allowed the ingress of residual O_2. Further evidence is provided by the high dark currents of the CA experiment in Figure 3.9B which indicated the presence of a reduction reaction which was independent of photo-excitation.

Contamination with O_2 and the subsequent ORR was an issue that needed to be resolved and a complete purging using N_2 was attempted. This was done by sealing all open gaps on the
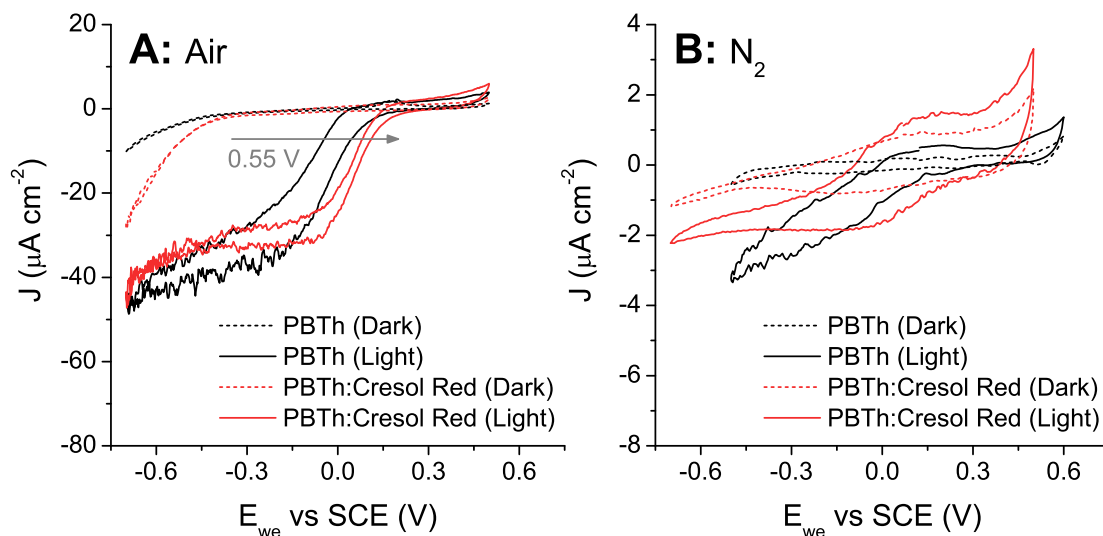
Figure 4.1: Analysis of the PBTh and PBTh:Cresol Red (1:1) films on glassy carbon for their photo-electrocatalytic response under bubbled **A:** air and **B:** N_2. These were conducted in the preliminary plastic cell in $0.1\,mol\,L^{-1}$ PB at pH 7 with a scan rate of $5\,mV\,s^{-1}$.

plastic cell with Blu-tack and substantially increasing the bubbling rate of N_2 gas; the cell was then left to purge overnight. CV was then conducted on the PBTh and PBTh:Cresol Red films in $0.1\,mol\,L^{-1}$ PB pH 7 and are presented in Figure 4.1B. When first examined, the obtained CV currents were significantly lower (as compared to Figure 4.1A) and indicated that a significant portion of the initial photo-response was due to O_2. Nevertheless, a reduction reaction could be observed with the application of light and although small, it was clear and distinguishable and clearly present over many cycles. This provided the first indications that an alternate reduction reaction beside the ORR was occurring, presumably the HER.

4.1.2   Initial Discovery

The discovery that PBTh and PBTh:Cresol Red was photo-active towards a reduction reaction under a N_2 atmosphere was important, though the danger of residual oxygen was still a concern in the preliminary plastic cell. To investigate, a longer term CA experiment was run with a potential of $-0.2\,V$ vs SCE; a region where PBTh and PBTh:Cresol Red was shown to be active (from Figure 4.1B). The light was turned on at t $= 30\,min$ for a period of $2\,h$ before being turned off and left to run in the dark again for another $30\,min$. The results for this experiment is presented in Figure 4.2 and showed that the photo-electrocatalytic response was immediate, and more importantly, was sustained over the $2\,h$ illumination period. As such, it points to a reactant that is abundant in the system. This was most likely not related to O_2 reduction since the continued intense bubbling of N_2 would result in a gradual decay over time as residual O_2 was used up. Similarly, the stable current suggests that the reduction of the PBTh film or Cresol Red dye – other potential reactants – was unlikely.
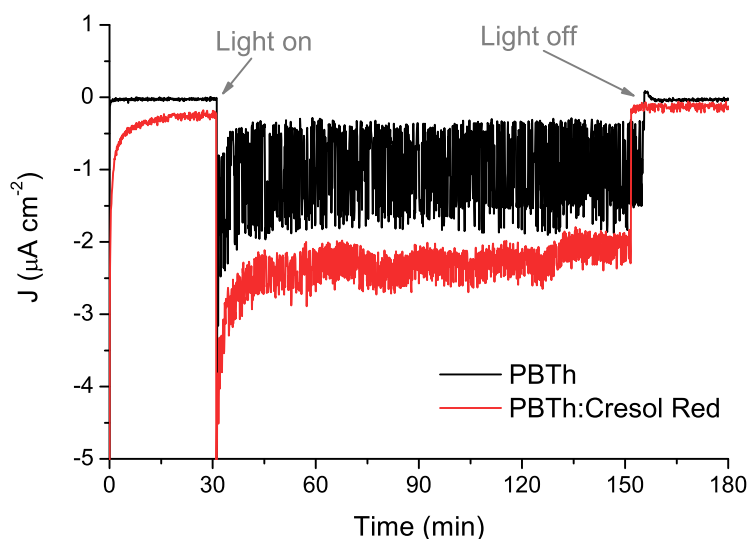
Figure 4.2: CA trace of PBTh and PBTh:Cresol Red on glassy carbon in $0.1\,mol\,L^{-1}$ PB, pH 7 at an applied potential of $-0.2\,V$ vs SCE. The photo-electrocatalytic current remains stable throughout. Also note the zero baseline current when in the dark.

The long term sustainability of the reaction was particularly surprising as the applied potential of $-0.2\,V$ was well below the theoretical onset of the HER at pH 7, where $E^0 = -0.65\,V$ vs SCE. This factor originally ruled out the HER and it was reasoned that reduction of the PO_4^{3-} of the phosphate buffer was taking place. Hence, experiments were undertaken using more inert electrolytes, namely $0.1\,mol\,L^{-1}$ NaCl with added $0.25\,mmol\,L^{-1}$ HCl (pH 3) to promote the HER. The electrolyte was continually purged with N_2 whilst numerous CV experiments were conducted over a period of 6 days. On the 7th day, a final CV was performed followed by long-term CA experiments on the PBTh film and the results are presented in Figure 4.3. Only the results for PBTh are presented as the PBTh:Cresol Red film showed signs of delamination and was stopped due to the significant decrease in film characteristics and an increase in ohmic resistance.

The CV in Figure 4.3A confirmed a photo-response despite prolonged testing and showed good stability of the film. Perhaps more critical to the investigation, higher photo-electrocatalytic currents and a lower onset potential was recorded at pH 3 (compared to pH 7 in Figure 4.1B) and follows the expected Nernstian behaviour for the HER.

The long-term results from the CA experiment, conducted over 24 h at $-0.7\,V$ vs SCE is shown in Figure 4.3B and highlight the photo-dependency of the PBTh system. Moreover, the remarkable stability of PBTh's photo-response over the 24 h period clearly rules out reduction of the conducting polymer. At the same time, the use of inert NaCl and HCl in the solution eliminates the possibility of reducing the supporting electrolyte salts (such as PO_4^{3-}). Most convincingly perhaps, was the evolution of bubbles when running the CA under illumination (Figure 4.3D)

but not when in dark (Figure 4.3C). Thus, the combined evidence points to the HER as the only viable candidate for the observed reduction reaction.
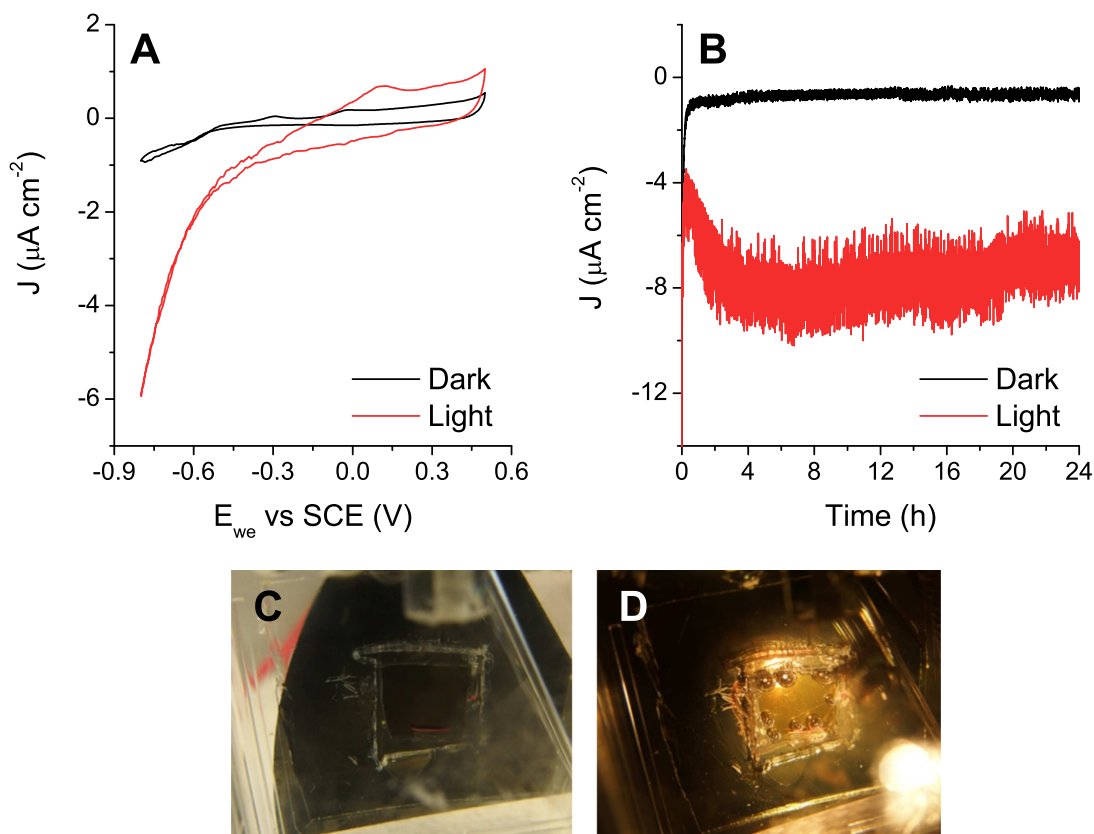
Figure 4.3: Electrochemical tests on PBTh (glassy carbon substrate) in $0.1\,mol\,L^{-1}$ NaCl, $0.25\,mmol\,L^{-1}$ HCl (pH 3) whilst bubbling under N_2 in the preliminary plastic cell. **A:** CV in light and dark at $5\,mV\,s^{-1}$. **B:** CA at $-0.7\,V$ vs SCE for a period of 24 h in light and dark. The PBTh film after CA in **C** dark and **D:** light.

4.1.3 Detection of H_2

From the above experiments, the evidence of H_2 production was compelling though direct detection was not yet achieved. It was realised at this point that another electrochemical cell set-up was required as the preliminary plastic cell lacked the gas tightness and appropriate points of attachment for a GC detection system. The preliminary lab *metal* cell was thus trialled (Figure 2.4B) and it was hoped that the metal fittings would prevent gas escape and O_2 ingress. Unfortunately, due to design limitations of the sample holder, the preferred glassy carbon substrates were too thick to be used. Many alternative substrates were trialled but they were plagued by bad electrical connections – short circuiting and noise were major issues – and difficulty in reproducing the photo-electrocatalytic reaction, see Figure 4.4.
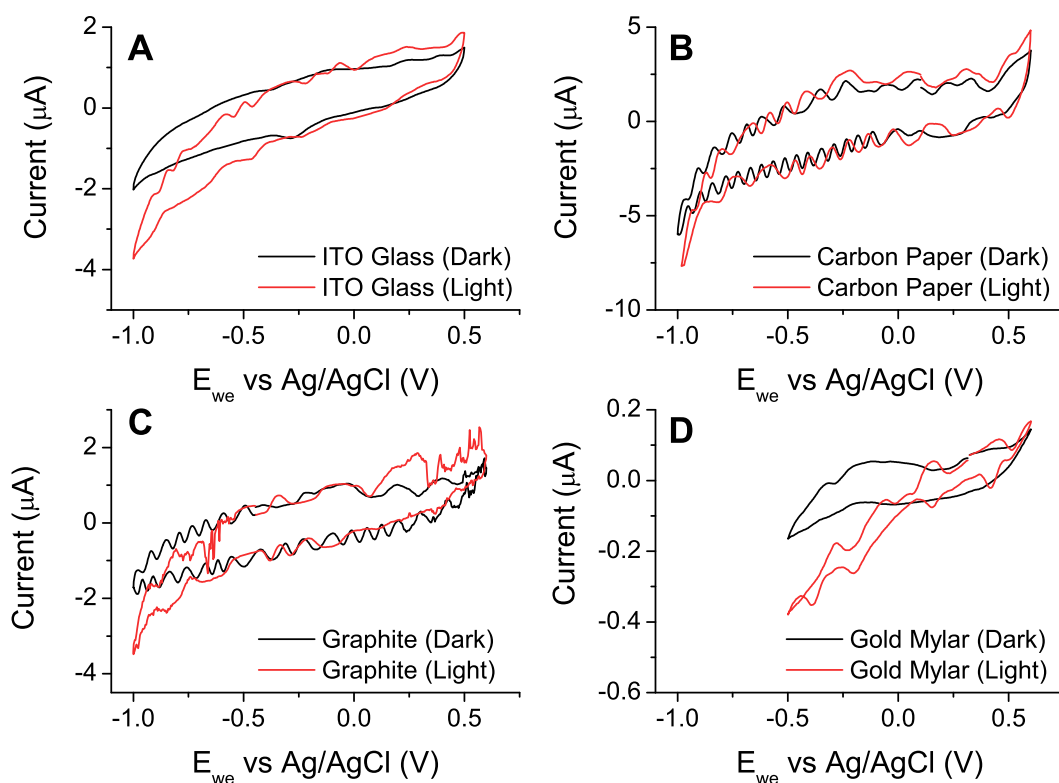
Figure 4.4: PBTh coated on various substrates for use in the preliminary lab metal cell scan rate of 5 mV s^{-1}, electrode area was not recorded. **A:** ITO glass, **B:** carbon paper, **C:** Graphite and **D:** Gold mylar (the potential range on gold mylar was limited to avoid catalytic activity from gold). In general, these films were limited by the sample holder and poor electrical contact.

It should be noted that studies on PBTh:Cresol Red ceased at this point after further difficulties in obtaining a stable film. Numerous samples of PBTh:Cresol Red also exhibited catalytic performances that were inferior to those of pure PBTh and threw into question the effectiveness of the dye as a light-harvester (Figure 4.5A). A possible explanation was that the hydrophilic nature of Cresol Red promoted the ingress of H$_2$O to swell the film. Initially, this could promote catalytic activity but over time, this swelling would lead to delamination; thus reducing electrical contact and coherence of the PBTh:Cresol Red film and leading to poor catalytic performance (Figure 4.5B). Despite the small improvements observed on certain PBTh:Cresol Red films, further studies of the dye blend was postponed. Moreover, the removal of the dye aided the simplification of the PBTh catalyst system so that a better understanding of this novel photo-system could be made.

In a final attempt to use the preliminary lab metal cell, the glassy carbon substrate was attached to the very back of the cylindrical cell using silicon tape, bypassing the small sample holder. This allowed the use of the thicker and preferred glassy carbon substrate but meant that the PBTh film was obstructed by the reference and counter electrodes and positioned far away from
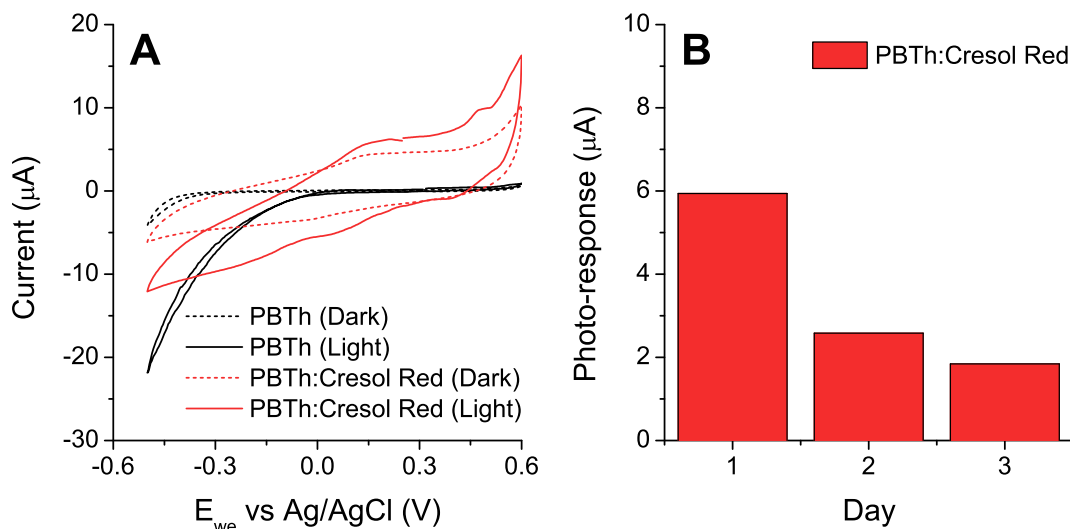
Figure 4.5: Comparison between the performance of pure PBTh vs the PBTh:Cresol Red blend; done in the preliminary plastic cell in $0.1\,mol\,L^{-1}$ PB, pH 7 under N_2. **A:** The initial CV trace of the two films at $5\,mV\,s^{-1}$, the area of the electrode $\approx 1\,cm^2$, PBTh shows a higher catalytic response. **B:** The photo-response of PBTh:Cresol Red over a period of 3 days showing gradual degradation.

the light source. The use of silicon tape was also a concern as it has a higher H_2 permeability and represents a potential point of escape for H_2 gas. This set-up was not ideal but it was the only cell that was available at the time.

Due to size limitations of the cell, the electrochemical/GC experiments were conducted using a Ag/AgCl reference electrode and stainless steel counter electrode; instead of the SCE RE and Ti mesh CE. A $0.1\,mol\,L^{-1}$ PB electrolyte was also used at pH 7 with bubbled Ar gas (to match the GC carrier gas). Phosphate Buffer at pH 7 was chosen for several reasons, the first being that it was much better than NaCl solutions at maintaining a consistent pH, particularly over longer term experiments. It was also deemed safe to use as the results from Figure 4.3 had shown that phosphate was not responsible for the observed photo-currents. Finally, a pH of 7 was chosen since catalysis of the HER at this neutral pH is much more compelling and novel than in acidic media; particularly as preliminary data had suggested catalysis at pH 7 to be possible (Figure 4.2).

Initial CV tests on the PBTh film in the preliminary lab metal cell (Figure 4.6A) showed a strong reduction reaction when illuminated and begins well below the E^0 of the HER ($E^0 = -0.63\,V$ vs Ag/AgCl). The catalytic response was also higher as a result of more experience in the fabrication of the PBTh film; as later studies will reveal, transfer speeds and exposure to air and humidity has a large effect on the performance of the film. Using this CV data, a potential of $-0.5\,V$ vs Ag/AgCl was chosen for the subsequent CA experiment, primarily
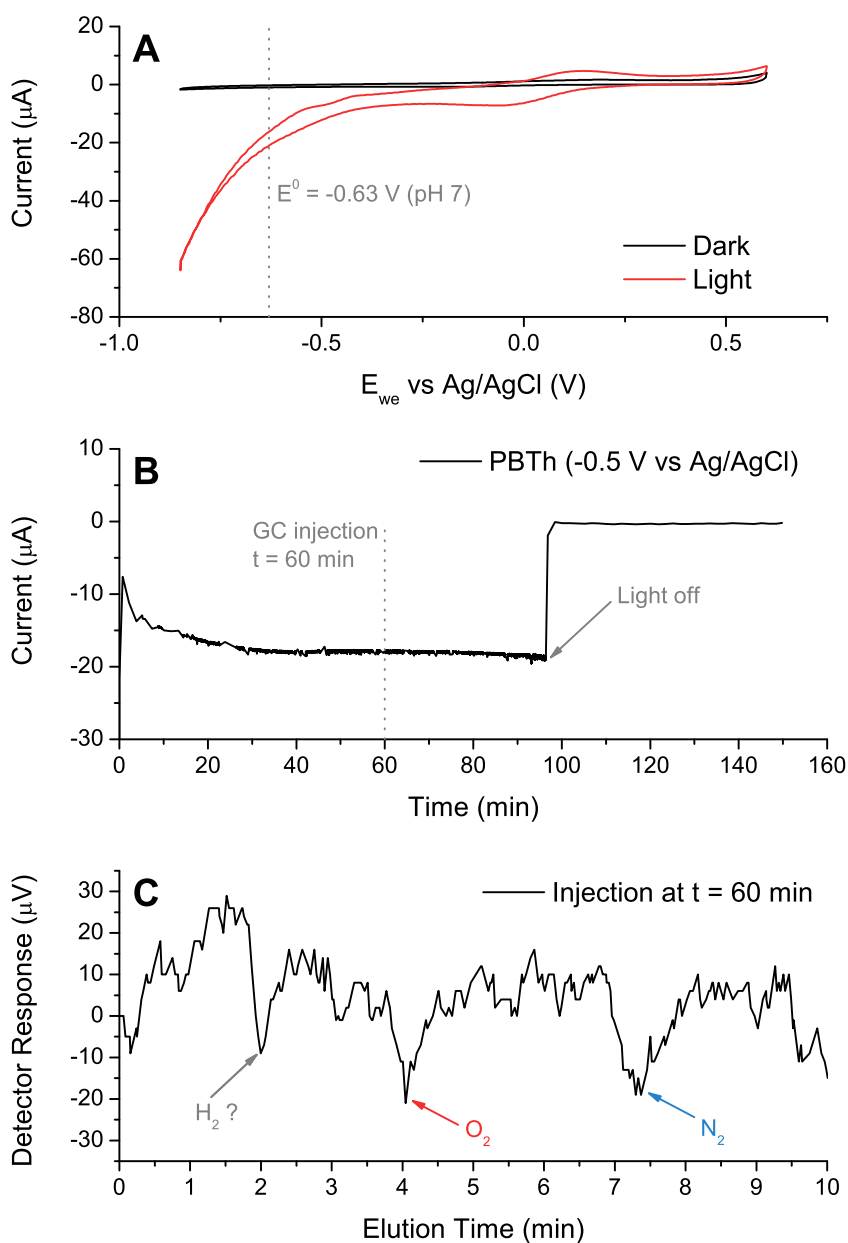
Figure 4.6: Tests on the PBTh film on glassy carbon in the preliminary lab metal cell, done in $0.1\,\text{mol}\,\text{L}^{-1}$ PB at pH 7 with bubbled Ar. (**A**) The CV of the film in light and dark, $5\,\text{mV}\,\text{s}^{-1}$; the E^0 of the HER is also shown. (**B**) The CA trace performed at $-0.5\,\text{V}$ vs Ag/AgCl. (**C**) The GC trace of the injection done at $t = 60\,\text{min}$ of the CA experiment showing a hint of H_2.

because the film was significantly photo-active at this potential, but also because it would be note-worthy to show the evolution of H_2 at an energy lower than that of E^0.

The CA experiment commenced with illumination and presented decent photo-currents of $\approx 15\,\mu\text{A}$ that was maintained until the light was switched off at 95 min; whereby the reduction

current immediately dropped to zero (Figure 4.6B). During the CA, GC injections were made at 30, 60 and 90 min though only the GC injection at 60 min is shown, see Figure 4.6C. This GC injection was particularly exciting as it revealed the first signs of a H_2 peak at the expected 2 min elution time, see Appendix C Figure S8. Unfortunately, the small size of the peak was not significantly above the noise threshold to be convincing. Furthermore, the injections at 30 and 90 min did not reveal a clear H_2 peak. These results suggested that leaks were still occurring and was supported by the presence of air peaks (O_2/N_2) and further compounded by the fact that the set-up was not ideal for the glassy carbon substrate. It was thus decided to design and commission a new electrochemical set-up, culminating in the custom test cells shown in Figure 2.5; details of studies using this custom cell is presented in Publication 2 (Section 4.2).

4.2   Publication 2: Photo-electrocatalytic H_2 evolution on poly(2,2'-bithiophene) at neutral pH

The first signs of H_2 gas in the preliminary lab metal cell was encouraging but a different set-up was required in order to realise a more convincing conclusion. The attached paper thus describes the results and investigations using the custom designed metal cell and the eventual detection of evolved H_2 from the PBTh film.

Supplementary information relating to this publication is attached in Appendix B.

Available online at www.sciencedirect.com

ScienceDirect

journal homepage: www.elsevier.com/locate/he
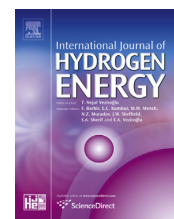
Short Communication

Photo-electrocatalytic H$_2$ evolution on poly(2,2′-bithiophene) at neutral pH

Chun Hin Ng [a,*], *Orawan Winther-Jensen* [a], *Bartlomiej Kolodziejczyk* [a], *C. André Ohlin* [b], *Bjorn Winther-Jensen* [a]

[a] *Department of Materials Engineering, Monash University, Clayton, 3800 Victoria, Australia*
[b] *School of Chemistry, Monash University, Clayton, Victoria 3800, Australia*

ARTICLE INFO

ABSTRACT

Vapour phase polymerised (VPP) polybithiophene (PBTh) on glassy carbon is revealed to be an efficient photo-electrocatalytic electrode for the hydrogen evolution reaction (HER). An onset potential of −0.03 V vs SCE for the HER is observed on illumination using visible light in 0.1 mol L^{-1} phosphate buffer at pH 6.9, 600 mV lower in energy than E^0. Hydrogen evolution is confirmed using gas chromatography with a calculated faradaic efficiency of 34% when holding at a potential of −0.5 V. Importantly, this process occurs without platinum and under neutral aqueous conditions thus revealing a significant but overlooked application for PBTh: a potential low-cost cathode material for the splitting of water.

Introduction

The latest Intergovernmental Panel on Climate Change report considers the warming of our planet as "unequivocal", with the move away from fossil fuels ever more crucial in order to limit the impact of climate change [1]. Hydrogen has been long proposed as a sustainable replacement energy medium but is hindered by current industry practices which rely on fossil fuels while alternative renewable methods have been difficult to commercialise [2–4]. In the case of electrolysis, an electrochemical technique that converts water to H$_2$ and O$_2$, commercialisation has been difficult due to its reliance on harsh chemical environments, expensive catalyst materials, and large energy requirements [5]. We here propose an alternative cathodic electrode material for electrolysis using poly (2,2′-bithiophene) (PBTh), a low-cost intrinsically conducting polymer (ICP).

Previous studies on the hydrogen evolution reaction (HER), which occurs at the cathode, have focused on the use of metal complexes [6,7], biological enzymes [8,9], and inorganic materials such as MoS$_2$ [10] and WS$_2$ [11] as catalysts. However, the use of ICPs such as PBTh remains relatively unexplored in spite of their advantages which include chemical stability in a

Fig. 1 − Custom designed metal electrochemical cell with in-situ gas chromatography; RE, CE and WE refers to the reference, counter and working electrode respectively. Initial cyclic voltammetry measurements were conducted inside a plastic cell Fig. S3.

polymer's reduction and oxidation potential at −1.54 V [16] and 1.24 V [17] vs SHE respectively, which is of sufficient energy to photo-catalyse the HER. This direct use of a single semi-conductor for both light harvesting and catalysis is uncommon, and with the exception of TiO_2 [18], has often been unsuccessful. Thus despite PBTh being a relatively known and studied material, our use of PBTh represents a unique and novel application which has, to our knowledge, never previously been attempted.

Material and methods

The overall low conductivity and difficulty in processing PBTh means that it is often overlooked in favour of more exotic derivatives. To overcome these inherent obstacles, a technique known as vapour phase polymerisation (VPP) was utilised [19]. Briefly, an Fe(III) oxidant was spin-coated onto a glassy carbon substrate, quickly transferred to a VPP chamber containing evaporated 2,2′-bithiophene monomer and left to polymerise for 1 h at 70 °C. The film was then washed in 1 mmol L^{-1} p-toluenesulphonic acid to remove residual Fe oxidant, a known contaminant from the VPP process; further details are provided in Supporting information†.

The resulting thin film (thickness ca 300−400 nm) on the conductive glassy carbon substrate helps negate the low conductivity of PBTh while the use of VPP helps provide a dense and uniform film which is free of the globules and loosely connected structures commonly seen on electrochemically polymerised conducting polymers [20,21]. Characterisation of the PBTh film was conducted via UV−Vis (see Fig. S1†) and Raman (Fig. S2†) spectroscopy. In brief, the film's characteristic $\pi \rightarrow \pi^*$ UV−Vis absorption at ca 480 nm corresponds to a band gap of 2.6 eV and is in close agreement with literature λ_{max} values [14,22−24] as well as our group's studies of VPP PBTh that revealed an electrochemical band gap of 2.7 eV [16]. Strong Raman peaks at 1505 cm^{-1}

wide range of environments, ease of manufacture, low-cost, and the ability for their properties and morphology to be tuned through the use of different polymerisation techniques. Furthermore, polymer chains inherently allow for the entrapment and diffusion of species within and throughout the ICP. These characteristics are invaluable to optimising catalysis performance.

We have demonstrated in the past the use of ICPs as catalytic electrodes in processes such as oxygen reduction [12,13], water oxidation [14], and hydrogen production [15]. We here further explore this novel use of ICPs by harnessing the inherent optical and electrochemical properties of PBTh to photo-electrically catalyse the HER and reduce the overall energy required to split water. Important properties of PBTh that lend themselves to this application include its visible light absorption band gap (480 nm) and the position of the

Fig. 2 − Cyclic voltammogram of the PBTh films in 0.1 mol L^{-1} phosphate buffer (pH = 6.9) at a scan rate of 5 mV s^{-1}. (A) Smooth PBTh in dark and under illumination compared with the glassy carbon substrate while bubbling with Ar; the reduction reaction only occurs under illumination. (B) Comparison of the performance of a smooth and rough PBTh film while bubbling with N_2; the rough film has an E_{onset} that is lower in energy with a much higher current. (C) SEM images of a smooth film and (D) a rough film with a R_a value of 26.21 nm and 44.52 nm respectively (refer to Fig. S5† for more details on roughness and SEM measurements). The pore size of the rough film is approximately 500 nm.

(conjugated coordinate mode), 1463 cm^{-1} (C=C symmetric stretching) and 1225 cm^{-1} (C–C stretch) were also observed and are typical for PBTh [22,25]. The washed films were then placed inside a test cell and sealed for electrochemical and in-situ gas chromatography measurements (Fig. 1). Light was provided by a Leica KL 2500 LCD halogen lamp with a visible light emission centred at 600 nm. See the Supporting information for additional experimental and characterisation information.

Results and discussion

Cyclic Voltammetry (CV) experiments were first conducted to deduce the effect of light, if any, on the electrochemical interactions of the system. Initial CV measurements in 0.1 mol L^{-1} phosphate buffer (pH 6.9) on a rough PBTh film revealed a photo-electrocatalysed HER with an onset potential of −0.03 V vs the standard calomel electrode (SCE, Fig. 2B). This onset is more than 600 mV lower in energy than the theoretical HER potential at pH 6.9 (E^0 = −0.65 V vs SCE) and indicates the generation of a photo-voltage on par with those observed in bulk heterojunction solar cells; where the open circuit voltage ranges from 0.5 to 1.0 V [26]. Moreover, subsequent voltammograms on smooth films acquired in the dark down to a potential of −1.1 V vs SCE (Fig. 2A) shows no indication of the HER, hinting at the generation of a significantly higher photo-voltage, or the presence of an alternative reaction pathway for the HER upon illumination. Further investigation to more negative potentials were not conducted to avoid degradation of the sample, although more detailed mechanistic studies are currently underway.

We also found that surface area was a major contributing factor to the performance of the film. Comparing smooth and rough films, where the rough film was produced by alternative templating using crystallised Fe(III) oxidant, the rough film achieved a current five times higher at −0.5 V vs SCE (see Fig. 2B) and an E_{onset} that is 0.24 V lower in energy. Importantly, these results were generated using the relatively simple polythiophene backbone which operated as a single semiconductor in neutral pH without requiring additional photo-active components, rare-earth elements or sacrificial additives [27,28].

Subsequent studies were undertaken in order to rule out possible side reactions and to confirm the production of hydrogen. Chronoamperometry (CA) on a smooth PBTh film at a potential of −0.7 V vs SCE under illumination revealed a sustained reduction current of 5 μA for over 8 h (see Fig. S6†) and indicates an abundant reactant species which is unlikely to be a contaminant. Furthermore, this sustained current demonstrates the stability of PBTh during the reduction reaction under illumination and applied potential. The absence of a contaminating species is supported by EDX measurements and is shown in Fig. S7† where main elemental composition was shown to be carbon and sulphur. The sustained current also rules out reduction of the film itself since this would be evident as a decline in current over time due to the reduction and dedoping of PBTh. Additionally, the reduction of oxygen was discounted

due to the lack of an oxygen reduction wave in the CV trace acquired in the dark; the presence of oxygen would have been apparent as a large reduction tail beginning at E_{we} = −0.1 V vs SCE in dark (Fig. S4†). Taken together, this leaves the HER as the only remaining candidate. The reduction of protons to gaseous hydrogen was further supported by the presence of bubbles on the film after longer periods of sustained testing (Fig. 3A), while the photo-electrocatalytic mechanism is clearly illustrated in the same figure by the instantaneous increase in reduction current when illuminated.

Final confirmation of hydrogen production was provided by gas chromatography (SRI 310C, TCD, MS-5A column, Ar carrier). A distinctive peak corresponding to H$_2$ at an elution time of 2 min is generated on the illuminated sample with an equivalent volume percentage of 0.053% H$_2$ (see Fig. 3B). This equates to a hydrogen production rate of 0.19 μmol h^{-1} and a faradaic efficiency of 34%. A major limitation and contributing factor to this evolution rate and low faradaic efficiency
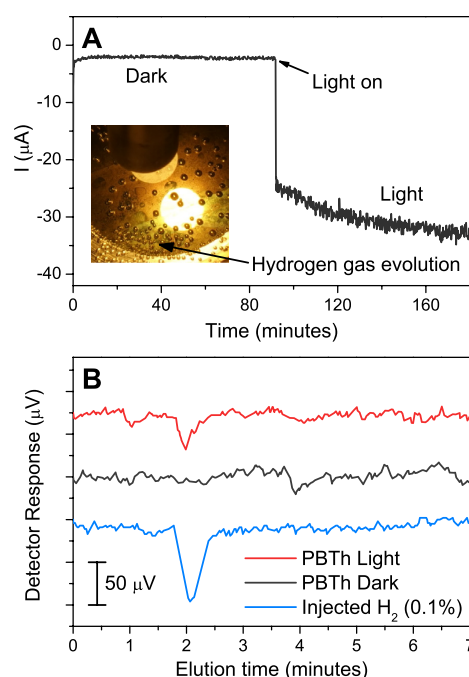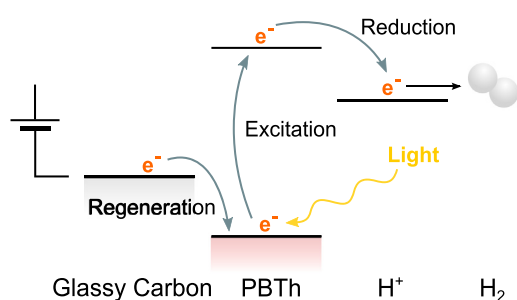

Fig. 3 – **Measurements on a smooth PBTh film on glassy carbon mounted in a metal cell with bubbled Ar (0.15 mL min^{-1}) while holding at −0.5 V vs Ag/AgCl (−0.52 V vs SCE) in 0.1 mol L^{-1} phosphate buffer (pH 6.9). (A) Recorded CA current on the PBTh film during the dark and illuminated phase. Light was applied using a Leica KL 2500 LCD halogen lamp (1.6 suns); spectral information of the lamp is provided in Supporting information Fig. S1†. Insert: The evolution of bubbles on the PBTh film during the experiments. (B) GC trace of the PBTh film after 90 min in the dark and under illumination respectively. A chromatogram of injected 0.1% H$_2$ is also shown for reference.**

is crossover reactions of products between anode and cathode in the frit-less cell. This issue was observed and addressed in studies by Winther-Jensen et al. where the separation of the gaseous product from the counter electrode resulted in an increase of faradaic efficiency from 61% to 92% [29]. In light of this, a redesign on the electrode setup is currently underway. No hydrogen peak was observed in the absence of light.

The following mechanism for the PBTh film system is proposed (see Fig. 4). On illumination by light, electrons from the valence band of PBTh are excited into the conduction band and injected into the surrounding protons, thus catalysing their reduction to H_2. The PBTh is regenerated by receiving an electron from the glassy carbon electrode. Thermodynamically, this proposed mechanism does not present any significant challenges; however, the ability of the system to satisfy the kinetic requirements to achieve charge separation is unexpected. This requires either a rapid injection of electrons from either PBTh to H^+ (to form H_2) or from the glassy carbon to PBTh. Identification of the responsible injection is currently ongoing and will be fundamental to the understanding of this system and improving the design and performance of future ICP based electrodes.

The enhanced performance on the rough film suggests that (currently) the surface area of the film is the limiting factor on performance, and not an inherent property of the system's mechanism such as excessive charge recombination or a deficiency in the photo-absorbance. The importance of the surface area is likely explained by the hydrophobic nature of the PBTh which limits the diffusion of water into the polymer network; the contact angle of PBTh in its reduced state (below 0.4 V vs Ag/AgCl, the region in which we operate) has been determined to be 180° [30]. As it stands, the low H_2 production rates currently obtained from the PBTh films is a manifestation of mainly morphological restraints and does not represent a threshold on the capabilities of the PBTh films. Thus there is substantial scope for improvement in performance through for example, the incorporation of hydrophilic components (e.g. poly(ethylene glycol)) and gelatin which had been shown to improve the performance of other ICPs [15,31], as well as increasing the porosity and roughness of the film and the use of mesoporous conducting substrates.

Conclusions

Our findings reveal a new and effective method for generating hydrogen using PBTh, a low-cost polymer, via a simple vapour deposition technique. The photo-enhanced onset potential represents the generation of a substantial photo-potential and enabled the photo-electrocatalytic generation of H_2 at 0.6 V below E^0. More significantly, this was achieved under aqueous conditions in a neutral pH of 6.9. Despite our initial scepticism of the production of H_2 from a basic thiophene structure, these notable results have been reproduced and substantiated with over half a dozen PBTh films, each generating detectable amounts of H_2. However, questions into PBTh's long-term stability and catalytic activity will need to be addressed through further studies. The preliminary findings presented thus far are promising and show a sustained current, albeit small, for a period of 8 h with little indication of degradation. In spite of the low hydrogen evolution rates, the flexibility of PBTh allows for significant modifications and improvements in performance. Coupled with the relatively low-cost of PBTh in comparison to platinum, this study on PBTh presents a novel and exciting organic based opportunity in which to dramatically increase the competitiveness of hydrogen as a new sustainable energy carrier.

Acknowledgements

Appendix A. Supplementary data

Supplementary data related to this article can be found at http://dx.doi.org/10.1016/j.ijhydene.2014.09.003.

Fig. 4 – Schematic diagram of the overall light-enhanced catalysis of the HER using PBTh on a glassy carbon substrate.

REFERENCES

[1] Stocker TF, Qin D, Plattner GK, Tignor M, Allen KK, Boschung J, et al. IPCC, 2013: summary for policymakers. In: Climate change 2013: the physical science basis. Contribution of working group I to the fifth assessment report of the intergovernmental panel on climate change; 2013. Cambridge, United Kingdom and New York, NY, USA.

[2] Turner J. Sustainable hydrogen production. Science 2004;305:972–4.

[3] Riis T, Hagen EF, Vie PJS, Ulleberg O, Sandrock G. Hydrogen production and storage R&D priorities and gaps. Paris, France. 2006.

[4] Merki D, Hu X. Recent developments of molybdenum and tungsten sulfides as hydrogen evolution catalysts. Energy Environ Sci 2011;4:3878–88.

[5] Guo JH, Chen XB. Hydrogen generation: electrochemistry and photoelectrolysis 1. Solar hydrogen generation: transition metal oxides in water photoelectrolysis. McGraw Hill; 2011.

[6] Jaramillo T, Bonde J, Zhang J. Hydrogen evolution on supported incomplete cubane-type $[Mo_3S_4]^{4+}$ electrocatalysts. J Phys Chem C 2008;112:17492–8.

[7] Karunadasa HI, Chang CJ, Long JR. A molecular molybdenum-oxo catalyst for generating hydrogen from water. Nature 2010;464:1329–33.

[8] Lamle S, Vincent K, Halliwell L. Hydrogenase on an electrode: a remarkable heterogeneous catalyst. Dalt Trans 2003:4152–7.

[9] Morozov S, Vignais P, Cournac L. Bioelectrocatalytic hydrogen production by hydrogenase electrodes. Int J Hydrogen Energy 2002;27:1501–5.

[10] Hinnemann B, Moses PG, Bonde J, Jørgensen KP, Nielsen JH, Horch S, et al. Biomimetic hydrogen evolution: MoS_2 nanoparticles as catalyst for hydrogen evolution. J Am Chem Soc 2005;127:5308–9.

[11] Chen TY, Chang YH, Hsu CL, Wei KH, Chiang CY, Li LJ. Comparative study on MoS_2 and WS_2 for electrocatalytic water splitting. Int J Hydrogen Energy 2013;38:12302–9.

[12] Kolodziejczyk B, Winther-Jensen O, MacFarlane DR, Winther-Jensen B. Conducting polymer alloys for photo-enhanced electro-catalytic oxygen reduction. J Mater Chem 2012;22:10821–6.

[13] Winther-Jensen B, Winther-Jensen O, Forsyth M, Macfarlane DR. High rates of oxygen reduction over a vapor phase-polymerized PEDOT electrode. Science 2008;321:671–4.

[14] Winther-Jensen O, Winther-Jensen B, MacFarlane DR. Photostimulated electrocatalysis of water oxidation by conjugated polymers. Electrochem Commun 2011;13:307–9.

[15] Winther-Jensen B, Fraser K, Ong C, Forsyth M, MacFarlane DR. Conducting polymer composite materials for hydrogen generation. Adv Mater 2010;22:1727–30.

[16] Kolodziejczyk B, Mayevsky D, Winther-Jensen B. Enhanced absorption spectra of conducting polymers co-polymerised from thiophene derivatives. RSC Adv 2013;3:4568–73.

[17] Waltman R, Bargon J, Diaz A. Electrochemical studies of some conducting polythiophene films. J Phys Chem 1983;2:1459–63.

[18] Fujishima A, Honda K. Electrochemical photolysis of water at a semiconductor electrode. Nature 1972;238:37–8.

[19] Winther-Jensen B, West K. Vapor-phase polymerization of 3,4-ethylenedioxythiophene: a route to highly conducting polymer surface layers. Macromolecules 2004;37:4538–43.

[20] Pringle JM, Armel V, MacFarlane DR. Electrodeposited PEDOT-on-plastic cathodes for dye-sensitized solar cells. Chem Commun 2010;46:5367–9.

[21] Zhou C, Liu Z, Du X, Ringer SP. Electrodeposited PEDOT films on ITO with a flower-like hierarchical structure. Synth Met 2010;160:1636–41.

[22] Zhang D, Xue G. Evolutions of structure of a thin polybithiophene film upon doping and cycling studied by in situ SERS technique. Synth Met 1998;95:185–90.

[23] Cutler CA, Burrell AK, Officer DL, Too CO, Wallace GG. Effect of electron withdrawing or donating substituents on the photovoltaic performance of polythiophenes. Synth Met 2002;128:35–42.

[24] Pekmez NÖ, Abacı E, Cınkıllı K, Yağan A. Polybithiophene and its bilayers with polyaniline coatings on stainless steel by electropolymerization in aqueous medium. Prog Org Coat 2009;65:462–8.

[25] Baibarac M, Baltog I, Lefrant S. Raman spectroscopic evidence for interfacial interactions in poly (bithiophene)/single-walled carbon nanotube composites. Carbon 2009;47:1389–98.

[26] Schlenker CW, Thompson ME. The molecular nature of photovoltage losses in organic solar cells. Chem Commun 2011;47:3702–16.

[27] Patsoura A, Kondarides DI, Verykios XE. Enhancement of photoinduced hydrogen production from irradiated Pt/TiO_2 suspensions with simultaneous degradation of azo-dyes. Appl Catal B Environ 2006;64:171–9.

[28] Maia DLS, Pepe I, Ferreira da Silva A, Silva LA. Visible-light-driven photocatalytic hydrogen production over dye-sensitized β-$BiTaO_4$. J Photochem Photobiol A 2012;243:61–4.

[29] Winther-Jensen O, Chatjaroenporn K, Winther-Jensen B, MacFarlane DR. Towards hydrogen production using a breathable electrode structure to directly separate gases in the water splitting reaction. Int J Hydrogen Energy 2012;37:8185–9.

[30] Kossmehl G, Niemitz M. Preparation and controlled wettability of poly (2,2′-bithienyl-5,5′-diyl) layers. Synth Met 1991;43:1065–71.

[31] Stavrinidou E, Winther-Jensen O, Shekibi BS, Armel V, Rivnay J, Ismailova E, et al. Engineering hydrophilic conducting composites with enhanced ion mobility. Phys Chem Chem Phys 2014;16:2275–9.

4.3   Conclusion

The initial studies using PBTh:Cresol Red led to the discovery of an unknown photo-electrocatalytic reduction reaction. Systematic studies were then undertaken to elucidate the nature of this reduction reaction and began with the prevention of the competing ORR. This was followed by the use of inert electrolytes and long-term analysis which eventually lead to the formation of gaseous bubbles. During these tests, it was found that the presence of Cresol Red was not critical to the successful operation of the photo-electrocatalytic system and as a result, studies were redirected to focus on neat PBTh films.

An optimisation of the electrochemical cell was undertaken in order to minimise gas leaks and allow for the use of in-situ GC detection. This culminated in the first hints of H_2 from the PBTh film using the preliminary lab metal cell followed by a much more definitive evidence using the customised metal cell. Publication 2 summarises the key initial findings of the PBTh photo-system.

The confirmation of H_2 evolution is particularly noteworthy due to the low potential at which it occurs, potentially up to 600 mV *below* E^0. Furthermore, this was all achieved under a neutal pH of 7 and in an aqueous environment without the need for a sacrificial oxidant. As a result, PBTh presents a huge potential for further optimisation and improvement which is further explored in Chapter 4.

Bibliography

[1] R. L. Mccreery. "Advanced Carbon Electrode Materials for Molecular Electrochemistry". *Chem. Rev.*, 2008. **108**, 2646–2687.

[2] B. Kolodziejczyk, O. Winther-Jensen, D. R. MacFarlane and B. Winther-Jensen. "Conducting polymer alloys for photo-enhanced electro-catalytic oxygen reduction". *J. Mater. Chem.*, 2012. **22**, 21, 10821–10826.

[3] R. Kerr, C. Pozo-Gonzalo, M. Forsyth and B. Winther-Jensen. "Influence of the Polymerization Method on the Oxygen Reduction Reaction Pathway on PEDOT". *ECS Electrochem. Lett.*, 2013. **2**, 3, F29–F31.

Chapter 5

Optimisation of Polybithiophene films for the Hydrogen Evolution Reaction

PART B: Declaration for Thesis Chapter 5

Declaration by candidate

In the case of Chapter 5, Publication 3, the nature and extent of my contribution to the work was the following:

Nature of contribution	Extent of Contribution
Initiation of work	100 %

The following co-authors also contributed to the work. If co-authors are students at Monash University, the extent of their contribution in percentage terms must be stated.

Name	Nature of contribution	Extent of Contribution
Orawan Winther-Jensen	Proof reading, SEM and EDX microscopy	NA
C. André Ohlin	Consultation of ideas, proof reading	NA
Bjorn Winther-Jensen	Key ideas, proof reading, drafting	NA

The undersigned hereby certify that the above declaration correctly reflects the nature and extent of the candidate's and co-authors' contributions to this work*.

Candidate's Signature   **Supervisor's Signature**

Date: Date:

*Note: Where the responsible author is not the candidate's main supervisor, the main supervisor should consult with the responsible author to agree on the respective contributions of the authors.

5.1   Introduction

The realisation of PBTh as a successful HER photo-electrocatalyst was a vital breakthrough and opened up a wide range of research directions. Some possible ideas included the re-introduction of dyes into PBTh for photo-enhancement, the blending of the film with other ICPs and the deposition of known catalytic particles/compounds into the photo-system to further increase catalytic activity. However, despite these exciting directions, it was deemed more prudent and necessary to further characterise and investigate the properties of the PBTh film prior to the addition of extra components.

These exploration studies of PBTh was particularly important considering the early stage of development. This chapter thus describes in detail the various parameters that were investigated, chief of which include the faradaic efficiency of the film, its long-term stability and performance under various pH. These are mostly presented in Publication 3 (Section 5.2) though additional studies on altering the microstructure of PBTh is presented in Section 5.4.1.

5.2   Publication 3: Exploration and optimisation of Poly(2,2'-bithiophene) as a Stable Photo-electrocatalyst for Hydrogen Production

The key findings from our exploration and optimisation studies are presented in Publication 3 and show a number of impressive properties. These include the remarkable longevity (12 days) and stability of the PBTh film and the ability to catalyse the HER in alkaline environments (pH 11).

The supplementary information for publication 3 is provided within this chapter – instead of at the appendix – due to the significant portion of relevant work presented within. This includes much of the original raw data, calculations and further elaboration on several key results. As a result, a full appreciation of the results and findings may require a little more alternating between the publication and supplementary information than expected.

Journal of Materials Chemistry A

Exploration and optimisation of poly(2,2′-bithiophene) as a stable photo-electrocatalyst for hydrogen production†

Chun Hin Ng,*[a] Orawan Winther-Jensen,[a] C. André Ohlin[b] and Bjorn Winther-Jensen[a]

An organic photo-electrochemical catalyst for the hydrogen evolution reaction (HER) based on the conducting polymer, poly(2,2′-bithiophene) (PBTh), is further explored. Long-term stability testing shows the successful operation of the catalyst over a period of 12 days at neutral pH with corresponding turnover numbers exceeding 6×10^4. Experimental parameters such as substrate type, electrolyte, pH and thickness of the film are explored and their subsequent effects on catalytic behaviour and performance discussed. Significant findings include the four-fold increase in performance by the reduction of thickness to better facilitate charge transfer and the successful photo-catalysis of the HER at pH 11, with an onset that is 0.14 V below E^0. Faradaic efficiency was also determined with a maximum recorded efficiency of 80% despite known losses such as crossover reactions and H_2 escape from within the system.

Introduction

The potential consequences of anthropogenic climate change have been known for some time, but the dependence of the world economy on fossil fuel based technologies has hindered the transition to renewable based processes. The rate at which the world is diverging from fossil fuels is further influenced by factors such as economics, availability of natural resources and politics, but the absence of a truly breakthrough energy technology has severely limited the attraction and feasibility of moving to a sustainable energy economy.[1–4] Commercially available renewable energy platforms such as solar and wind can provide renewable energy but their intermittent nature necessitates the use of a storage medium such as batteries or hydrogen.

Hydrogen has numerous advantages as an energy medium, key of which being that it is completely clean burning, with only H_2O as a by-product. Its ability to provide fuel for both electricity generation and transportation – which account for over 45% of our energy consumption[5] – is also invaluable. To make hydrogen a viable alternative however, sustainable production methods that are capable of H_2 generation at an industrial scale are needed. A promising solution is the use of solar or wind power in combination with water electrolysis. However,

cheaper, more robust and energy efficient alternatives than the currently used Pt-based electrode catalysts must first be found. Potential solutions include using biological and bio-mimetic approaches,[6,7] improved use of noble metals such as RuO_2 or reducing Pt loading,[8] as well as the development of new hetero- and homogeneous catalysts;[9] unfortunately, a large energy input is still often required. A common technique to reduce electrolysis energy requirements is the development of photo-driven/assisted water splitting catalysts and systems (photolysis),[10,11] and is an approach that is harnessed in this body of work.

A key hurdle in the development of a water splitting system is to design one that is conducive to both the cathodic hydrogen evolution reaction (HER) – typically acidic – and the anodic oxygen evolution reaction (OER) – typically alkaline. The studies herein continue the development of electrolysis electrodes with a focus directed at the cathodic HER process, which is currently heavily dependent on Pt.[12] Promising alternative HER catalysts have harnessed biological enzymes such as hydrogenase,[13] synthetic bio-mimics and complexes,[14–16] and inorganic particle catalysts such as MoS_2;[17] often with the incorporation of a photo-active component in an attempt to lower energy requirements.[18–20] However, difficulties such as stabilising complex bio-catalyst centres, continued use of acidic or non-aqueous environments, and a requirement for large over-potentials remain key obstacles.

Previous studies have shown the potential of intrinsically conducting polymers (ICPs) in overcoming some of these issues.[21,22] While the use of organic ICPs is a break from the more traditional catalytic materials, the photo-active,

[a]*Department of Materials Engineering, Monash University, Clayton, 3800 Victoria, Australia.* ▮

[b]*School of Chemistry, Monash University, Clayton, 3800 Victoria, Australia*

conductive and stable nature of these materials[23] – particularly of the polythiophene family – lends themselves well to catalysis. Such successful uses of ICPs include the oxygen reduction reaction for fuel cell applications,[24–26] the reduction of nitrite to ammonia for waste treatment[27] and the water oxidation[28,29] and proton reduction[30] reactions of the electrolysis process.

More recently, our group has reported the ability of poly(2,2′-bithiophene) (PBTh) to photo-electrocatalytically produce H_2 from a neutral (pH 7.0) aqueous phosphate buffer solution.[31] Although the faradaic efficiency was low, the system demonstrated an onset potential that was significantly lower than that of the theoretical reduction potential (E^0) when illuminated. These promising preliminary results have prompted us to further investigate the effect of pH, substrate materials, electrolyte and film characteristics such as thickness on hydrogen evolution using PBTh.

Results and discussion

All PBTh films tested, with the exception of those used for thickness measurements, were prepared in the same manner *via* a vapour phase polymerisation (VPP) technique using a Fe(III) oxidant solution as described in the Experimental section, see ESI† for further experimental details. This preparation method results in what is referred to below as the standard PBTh film.

Determination of faradaic efficiency and cell optimisation

Ideally, the operation of the PBTh film should yield a 100% faradaic conversion of electrons to hydrogen gas (with a molar ratio of $2 : 1$ e$^-$: H_2); however, the initial published findings showed a faradaic efficiency of only 34%.[31] Therefore, it is important to determine the origin of this efficiency loss, be it *via* competing reduction reactions or the escape of produced hydrogen gas or other means. Moreover, it would be beneficial to establish a correlation between observed current and detected hydrogen gas so that we can use the observed current to determine the rate of H_2 evolution. To this end, a special cell was designed.

A key goal was to minimise cross-over reactions, whereby oxygen produced at the counter electrode diffuses towards the working electrode to reduce in a competing oxygen reduction reaction and *vice versa*. These parasitic currents adversely affect the generation and measurement of H_2 and is a key contributor to the low initial faradaic efficiency of 34% observed in our initial work.[31] To improve upon this, the counter electrode was moved away from the main chamber into a separate tube angled in such a way that the generated O_2 gas is directed away from the main cell into a separate head space, Fig. S1.† Earlier designs had also placed the PBTh film within a recessed edge which was found to trap bubbles and affect the detected amount of H_2. The cell thus was further modified so that any gases generated from the film were allowed to escape directly into the head space. Lastly, great care was taken to seal the cell from leakage, both from egress of H_2 and ingress of O_2 from the surrounding air.

A standard glassy carbon supported PBTh film was utilised for the testing. Periodic injections of head space samples into the gas chromatograph were conducted, from 75 to 275 min while the film was held at a potential of −0.8 V *vs.* Ag/AgCl in 1.0 mol L^{-1} phosphate buffer (pH 7.0) under an illumination of 1.6 suns. The corresponding peak height of H_2 was converted to a molar amount *via* a calibration curve Fig. S2.† In agreement with earlier findings from our group,[31] the response of the photo-system to light consists of a rapid initial increase in reduction current (with a speed that is comparable to that of inorganic semiconductors[32,33]) followed by a more gradual growth in current. This growth is attributed to the gradual swelling of the film and the subsequent exposure of more catalyst centres to the electrolyte, this behaviour can be more clearly observed in Fig. S8.† With the termination of light, the reduction reaction current rapidly returns to zero, see Fig. 1 and 2.

The results from Fig. 1 show an increased faradaic efficiency of up to 80% and demonstrates the effectiveness of our techniques. Nonetheless, leakage of hydrogen remains an issue due the ease by which it is able to diffuse through the remaining polymer parts of the setup (such as O-rings and tubing). Moreover, the detection of trace amounts of O_2 and N_2, which elute after *ca.* 3.5 and 6.5 min respectively (Fig. S3b†) indicates the presence of air and thus, the competing oxygen reduction reaction. Finally, dissolved oxygen and hydrogen in the electrolyte remains liable to diffuse between the chambers and cause small amounts of parasitic current despite the steps taken to separate the electrodes.

Nevertheless a faradaic efficiency of up to 80% is still indicative of an efficient electrocatalysis process, especially considering that the attainment of a 100% faradaic efficiency is not trivial.[34] This high faradaic efficiency also justifies the use of the recorded electrochemical current on the PBTh electrode as an accurate proxy indicator for produced hydrogen. Thus, in the proceeding results and discussion, current is used as a measure of H_2 evolution.
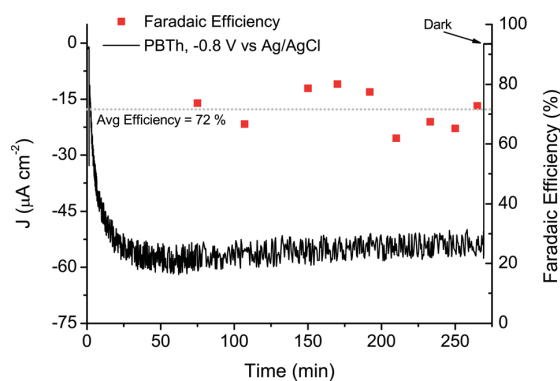

Fig. 1 Faradaic Efficiency of PBTh on Glassy Carbon. Each point represents the calculated faradaic efficiency from the detected amounts of H_2 from each GC injection. Peak efficiency was recorded as 80% at an injection time of 170 min; the overall average efficiency was 72%. The corresponding chromatograms are presented in Fig. S3a.†
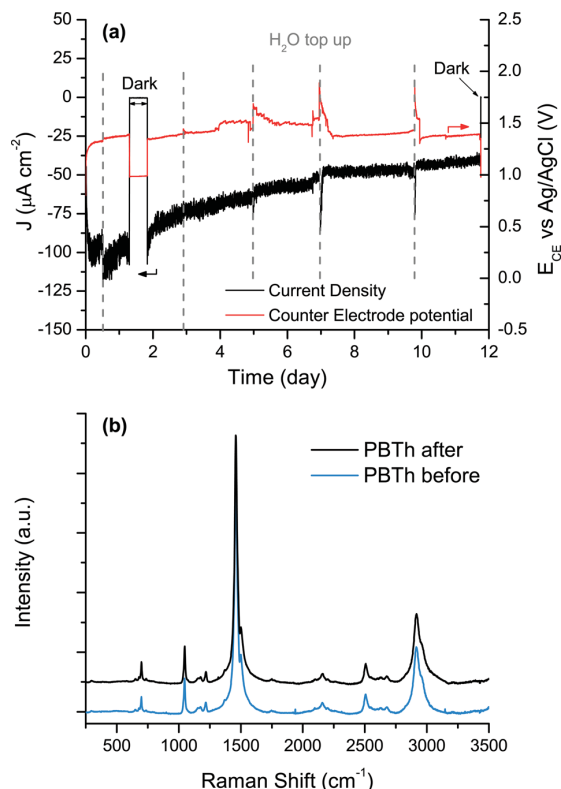
Fig. 2 (a) Long-term testing of a standard PBTh film on glassy carbon over a period of 12 days at an applied potential of -0.5 V vs. Ag/AgCl, in 1.0 M PB (pH 7.0) under constant illumination of 1.6 suns. (b) Raman spectroscopic analysis of the film after long-term testing over 12 days. No discernible differences can be observed.

Stability testing

For any catalyst the long-term stability is crucial for the performance and indeed for gaining any commercial interest. We thus probed the long term stability of the PBTh film to determine this important criterion. This was tested *via* chronoamperometry (CA), where a standard PBTh film was held at -0.5 V vs. Ag/AgCl at neutral pH 7.0 (0.13 V less than E^0) under illumination over a period of 12 days and the current recorded (see Fig. 2a). Occasional top ups of water was necessary due to the need of an open cell setup and the continuous purging with N_2 gas; these top up points are marked in Fig. 2a. Inspection of the CA trace shows a gradual decrease in recorded photocurrent over time. This is partly accounted for by a gradual decrease in the light intensity from the halogen light bulb which was recorded between days 4–12 and account for over 70% of the recorded decrease in photocurrent between these days; see Fig. S4 and ESI† for further details. The stability of the PBTh film is also supported by the Raman spectroscopy results which show no discernible differences in the Raman spectrum of the film before and after testing (Fig. 2b) and confirms that the chemical structure of PBTh has not been altered.

Nonetheless, a noticeable decrease in performance can be observed despite corrections for the lamp's output. Probing *via* SEM and EDX reveals the presence of Cu and Fe which would reduce the number of available catalytic sites and are likely culprits for the gradual drop in photo-current. The magnitude of this deposition and subsequent degradation of the photo-current was much lessened by the use of a mixed oxide Ti mesh counter electrode when compared to stainless steel and platinum wire counter electrodes but not fully prevented (see Fig. S5–S7†). Migration of dissolved ions from the counter electrode and the surrounding metal casing to the working electrode consequently leads to their deposition onto the PBTh film; although slow, the long duration of these tests compounds this adverse effect. Alternative inert counter electrode and cell materials such as glassy carbon and glass respectively would aid in minimising deposition as would increasing the area of the counter electrode to reduce its oxidation potential. It is worth noting that this occurrence of competitive deposition on the working electrode is a general issue for the field, not specific for the PBTh catalyst.

In light of these findings, it is important to remark that the photocurrent was maintained over a period of 12 days; in comparison, lifetimes for contemporary catalysts for the HER are reported on the timescale of hours.[14,35] Moreover, this was achieved under neutral conditions at a potential that is 0.13 V below E^0 and the reaction was stopped before the exhaustion of catalytic activity. Given the lack of chemical degradation as determined by Raman spectroscopy, it is highly probable that the long term photo-catalytic activity of PBTh is significantly higher. Maintenance of this catalytic performance is also likely to be further improved upon with the removal of metal ions from the electrochemical system. Assuming that one bithiophene unit is equivalent to one catalytic site (a lower bound estimate), the turnover number (TON) for the complete 12 day period was calculated to be 6.7×10^4, where the density of PBTh film is 1.52 g cm^{-3}[36] see ESI.† Alternatively, if a more realistic catalytic site comprising of a 13 membered thiophene oligomer is used instead – the span of an average polaron site[37] – the TON is 4.4×10^5. It should be noted however, that the true size of the active site is still currently under investigation.

Substrate

Investigations on the substrates were conducted to determine if alternate, low-cost substrates were suitable for pairing with the PBTh films for catalysis. In spite of the chemical inertness, high conductivity and promising preliminary results on glassy carbon, it is an inherently expensive and non-transparent material that may hinder implementation if scaled to industrial capacities. It is thus prudent to investigate alternative substrate options as a precursor to further development. For substrate testing, a standard film of PBTh was polymerised atop the substrate and tested *via* cyclic voltammetry (CV). An aqueous 1.0 M NaCl (pH 6.0) electrolyte was used for all substrates.

The resulting CVs in Fig. 3 show that despite the capability of PBTh for HER catalysis, the selection of substrates play an important role in the overall system. The work function of the
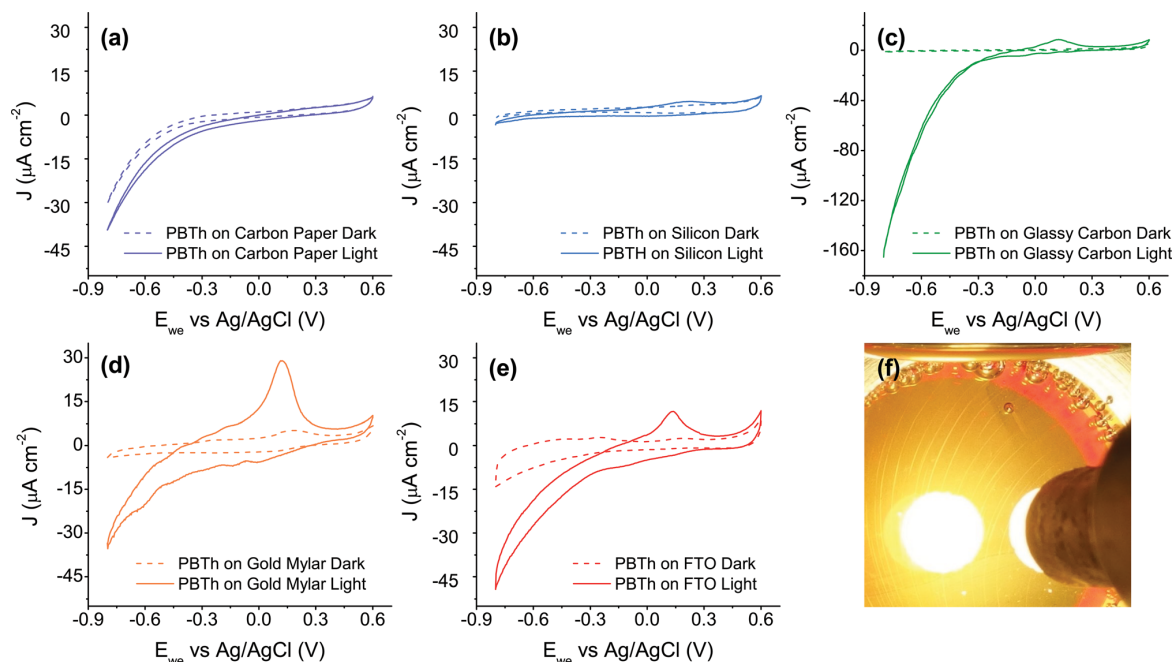
Fig. 3 CV showing the performance of PBTh on various substrates; 1 M NaCl pH 5.98, 20 mV s^{-1}. (a) Carbon paper, (b) silicon, (c) glassy carbon for comparison, (d) gold mylar and (e) FTO glass. (f) The evolution of H$_2$ bubbles from the FTO/PBTh film trapped on the top edge of the cell. The oxidation peak present in (c−e), corresponds to the oxidation of adsorbed H$_2$.

substrate is a key consideration in any photo/electrochemical system; however, the selected materials all possess sufficient energy to regenerate the PBTh HOMO band (5.3 eV [38]): glassy carbon 4.5 eV,[39] silicon 4.8 eV,[40] gold 4.8 eV [39] and FTO glass 5.0 eV.[41] Thus the limitation to successful catalysis is beyond a simple work function requirement. Good adhesion of film, inertness of the substrate and facile electron transport between substrate and PBTh are other key parameters to consider as discussed below; however studies to quantify them are currently beyond the scope of this work.

Analysis of Fig. 3 shows the failure of PBTh on carbon paper to be photoactive even though it is a carbon based substrate. It is possible that residual air trapped within the fibres or impurities/degradation of the electrode is leading to a competing reduction reaction. Residual O$_2$ is likely to arise given the hydrophobicity of the carbon paper (which would also adversely affect the performance of the film). However, the limited photo-effect suggests the issue is not O$_2$ related as PBTh has been known to show strong photo-electrocatalytic behaviour towards oxygen reduction.[31] Degradation of the carbon paper is more difficult to address and, together with the limited photoactivity, precludes carbon paper as a viable option. The inactivity of silicon conversely is likely due to its limited ability to transfer electrons effectively to the deposited PBTh film. This is supported by the negligible currents, capacitive and faradaic, recorded in both light and dark conditions, and is most likely the result of the presence of the SiO$_2$ layer that reduces good electron conductivity.

On the other hand, we do observe successful catalysis from the gold coated mylar and FTO glass substrates. While not comparable to the currents obtained from glassy carbon, both exhibit substantial photo-electrocatalytic behaviour and the successful activation of the H$_2$O/PBTh/substrate photosystem. The success of gold mylar is unremarkable given its inherently high conductivity and the affinity of sulphur to gold, however, it is not an ideal substitute due to its high cost and relatively low performance. The success of the FTO glass as a substrate for PBTh in the HER is of more commercial interest due to its low-cost, chemical inertness and transparency; characteristics which help allow it to better compensate for its lower catalytic performance as compared to glassy carbon.

It should be noted that for the rest of this work, glassy carbon remained the substrate of choice due to its superior performance. For this seminal work, it is more critical that the maximum potential of the film is recognised and harnessed. Nonetheless, the identification of alternative substrates remains significant.

The effect of electrolyte

A key interest in the operation and performance of the PBTh film is the role that the electrolyte plays in the overall mechanism, in particular whether the use of phosphate buffer (PB) was critical to successful operation of the PBTh photo-electrocatalytic system[31] or if it can be replaced with simple salts such as NaCl. To this end, PB and sodium chloride solutions (pH 7.0) were investigated, at 0.1 and 1.0 mol L^{-1} concentrations.
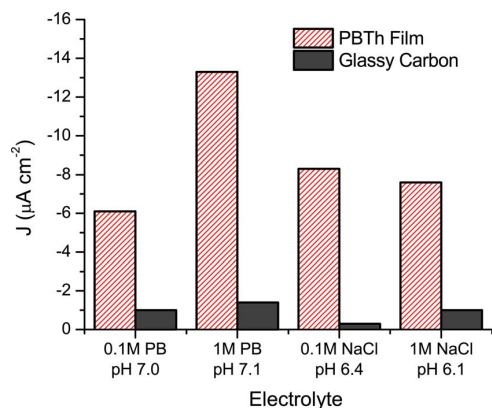
Fig. 4 Comparison of the PBTh current density in aqueous PB and NaCl electrolytes at concentrations of 0.1 and 1.0 mol L^{-1}, see Fig. S8† for CA traces.

A potential of -0.5 V *vs.* Ag/AgCl was applied to the immersed PBTh film while under illumination and the current recorded after a period of 60 min. The resulting comparison between PB and NaCl at the concentrations of 0.1 and 1.0 mol L^{-1} is presented in Fig. 4.

The significant photocurrents recorded in the NaCl solution is evidence that a mono- or di-hydrogen-phosphate containing electrolyte is not crucial and that H$_2$O is capable of acting as a source of protons for the HER. This finding is particularly noteworthy as only very few systems are able to photo-electro-catalytically reduce H$_2$O directly to H$_2$ without sacrificial additives such as methanol[42] at neutral pH and is a crucial step to the realisation of an effective HER catalyst. The observed doubling in current when increasing the concentration of PB indicates that the introduction of phosphate ions has a positive effect on the amount of available protons for the HER. It is unlikely that the improvement in photocurrent in the PB solutions was due to an increase in ionic strength due to the concentration independence shown by the (0.1 and 1.0 mol L^{-1}) NaCl solutions. Thus this suggests that the performance of the overall system can be improved by the addition of protonating species such as H$_2$PO$_4^-$ (pK_a 7.2 [43]). Currently, this has only been demonstrated in relation to PB but it would be of particular interest to see which other species and are able to interact and enhance the PBTh system and further, the extent to which performance can be improved by increasing the concentration of proton donating species. For comparison, the results from using bare glassy carbon substrate are also shown in Fig. 4; the small detected currents (*ca.* 0.5–1.5 µA cm^{-2}) is attributed to the presence of trace amounts of residual O$_2$.

The effect of pH

The pH dependence of the system was also investigated owing to the important role it plays in understanding the limitations of a particular HER catalyst. Given the ability of PBTh to perform this photo-electrocatalytic function at a neutral pH, it is appealing to review its capabilities at either end of the pH
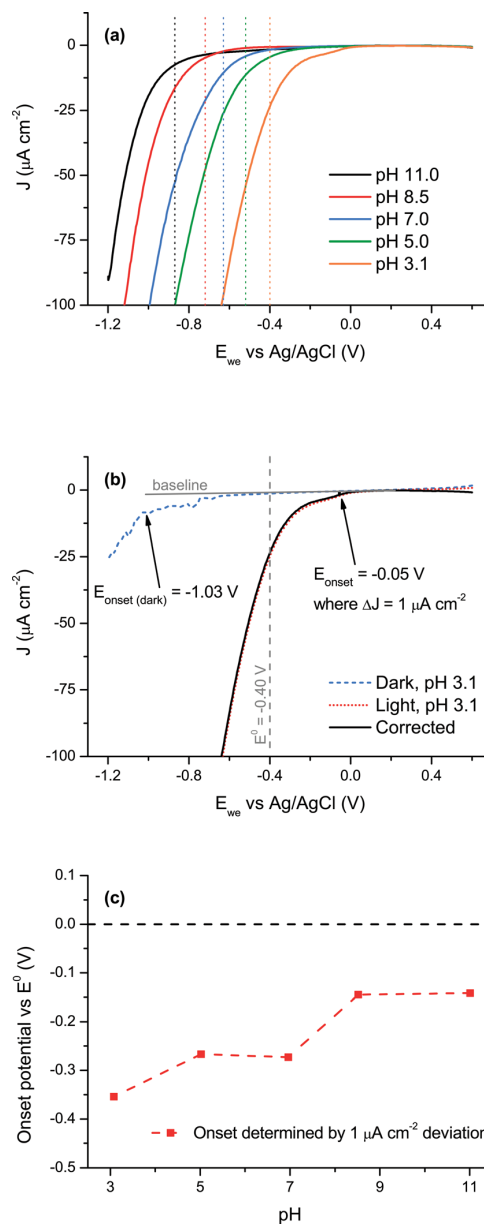
Fig. 5 Comparison of PBTh performance and onset potential for the HER under illumination as pH is varied from 3.1 to 11.0. (a) The CV reduction sweep comparing PBTh catalytic activity at different pH. The theoretical E^0 of each pH is indicated by the dotted line. (b) Determination of the onset potential at pH 3.1. The estimated onset potential in dark is also presented. CVs of the remaining pH tests are presented in the ESI, Fig. S9.† (c) Comparison of the pH onset potential, potential has been normalised to E^0 of the respective pH where a negative overpotential indicates an onset that is below E^0.

spectrum. PB (0.1 mol L^{-1}) was used as the electrolyte and the pH was varied from 3 to 11.

The onset potential of the film was used to characterise the pH performance and was determined *via* CV. A slow scan rate of

0.1 mV s^{-1} was utilised to minimise electrical double layer and diffusional effects. The pH of the electrolytes before and after each run was recorded and showed that pH was maintained throughout the experiment (see Table S1†). The resulting voltammograms (Fig. 5a) exhibited reduction onset potentials that moved steadily to more negative potentials with increasing pH, as expected from the stoichiometry of the HER which invokes H$^+$ as a reactant.

For a more rigorous comparison it is necessary for the onset potentials to be normalised with respect to the E^0 at each pH. E^0 was determined using the Nernst equation and corrected for the Ag/AgCl reference electrode (0.222 V *vs.* SHE). With respect to the onset potential, the trace obtained in the dark was subtracted from the trace collected in the light to correct for O$_2$ contamination; this corrected trace was then used to determine the subsequent onset potential (see the solid black trace in Fig. 5b). The onset potential was defined as the point where the corrected reduction current deviates from the baseline by a value of more than 1.0 µA cm^{-2}. The resulting onset potentials *vs.* E^0 is presented in Fig. 5c.

The low onset potential at pH 3.1 is noteworthy because it represents the generation of a photovoltage of *ca.* 1.0 V, which is obtained by subtracting the estimated E_{onset} in dark (-1.03 V) and the E_{onset} in light (-0.05 V), see Fig. 5b. This highlights the generation of high energy photo-electrons by PBTh for hydrogen production. A slight increase in onset potential is also observed as pH increases – from -0.35 V *vs.* E^0 at pH 3.1 to -0.14 V *vs.* E^0 at pH 11.0 (see Fig. 5c) – and represents the increase in activation energy of the HER as the equilibrium shifts from high H$^+$ concentrations at pH 3.0 to high OH$^-$ concentrations at pH 11.0. Despite this, PBTh has demonstrated the ability to catalyse the HER at the highly alkaline environment of pH 11.0, which is particularly noteworthy given the implications for overall water splitting process. As stated before, for effective electrolysis both the HER and its conjugate reaction (the OER) must proceed readily. A low pH aids H$_2$ production but this acidic environment drives up the energy required for the OER. Conversely, an alkaline electrolyte aids in the OER but is detrimental to the energetics of the HER in most catalytic systems. Thus, the discovery that PBTh remains an effective photo-electrocatalyst at pH 11 with an onset potential that is 0.14 V below E^0 is a key finding in the progress towards a viable commercial water splitting device.

Interaction between light and PBTh

The effect of the PBTh film thickness on the HER performance was investigated. As the catalysis process is dependent on light to generate an active excited state, the more light absorbed the more potential catalytic events. Equally, good conductivity of holes is a prerequisite for the effective charge separation/regeneration of the film. Therefore, the PBTh photo-electrocatalytic system requires an ideal balance of light absorption *vs.* charge transport from the active site to the supporting electrode; in the case of the poorly conducting PBTh, this balance becomes even more important. To investigate this, the thickness of the PBTh film is varied and the resulting performance is
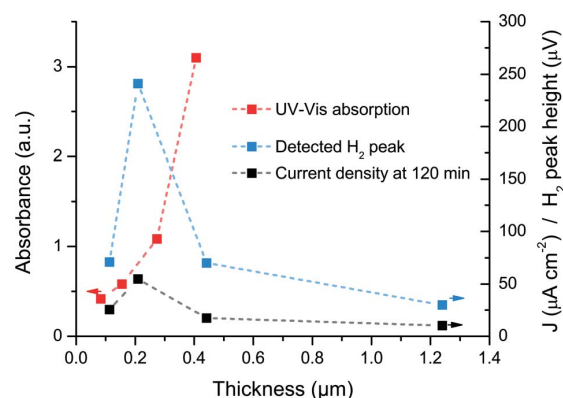

Fig. 6 Comparison of PBTh as thickness is varied. Three parameters are presented, the UV-Vis absorbance, the detected H$_2$ peak (in µV) at 120 min and the current sustained at the end of 120 min under illumination and an applied potential of -0.5 V *vs.* Ag/AgCl. The UV-Vis absorbance was measured on PBTh on glass slide (Fig. S10†). See Fig. S11 and S12† for the corresponding CA trace and gas chromatogram respectively.

compared against the measured absorbance of PBTh on a glass slide. Four different thicknesses were prepared – 0.11, 0.21, 0.44 and 1.24 µm – where the standard film is represented by the thickness of 0.44 µm, the thickness of each film was measured *via* profilometry.

Fig. 6 highlights the importance of the balance between conductivity and light absorbance. The thicker films at 0.44 and 1.24 µm has a dramatically increased absorbance – to the point where the saturation of UV-Vis detector was reached for the 1.24 µm film; however, the higher resistance through the thicker films considerably reduces the ability for efficient charge separation. As a result, a large portion of the generated excitons recombine as they are unable to move and separate, thus causing a decline in the overall photo-electrocatalytic ability. Conversely, by having a thin film, there is facile mobility of the charges from substrate to the catalytic site at the PBTh-water interface but the absorbance of the film suffers. As a result, fewer excitons are generated and the number of possible catalytic events decreases. An optimum balance between these two factors is achieved by the film at a thickness of 0.21 µm and is evident by the recorded current and detected hydrogen which represents a threefold increase in performance when compared to the 0.44 µm film (standard film).

By utilising the limitations discovered in these investigations, it is also possible to infer several details with respect to the catalytic mechanism of the system. The dependence on thickness – and hence, resistance with regard to hole conduction and possible recombination – suggests that the kinetic driving force of the system operates *via* the conduction of the photo-generated holes away from the catalytic site, thus achieving charge separation. Had charge separation occurred *via* the fast injection of the photo-electron into H$^+$, thickness should have had little effect on the measured photocurrent; save for a slight voltage drop from internal resistance. Due to the hydrophobic nature of PBTh in its reduced form[44] we
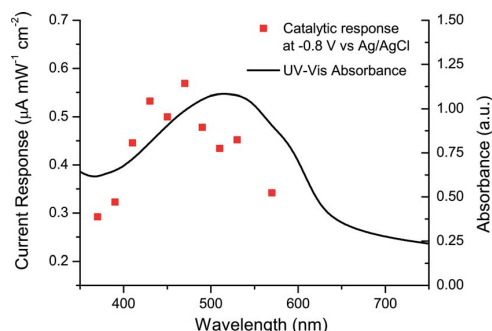
Fig. 7 The wavelength of PBTh's catalytic performance with respect to the incident photon wavelength with an applied potential of −0.8 V *vs.* Ag/AgCl; the raw current response is shown in Fig. S13.† The UV–Vis absorption spectrum of PBTh is also shown for comparison.

assume that the active catalytic area of the film remains confined to the interfacial layers and is independent of the thickness of the PBTh film. Direct empirical evidence would be required to support these arguments though it is encouraging to note that the deductions made thus far are able to account much of the current observations.

The wavelength dependency was also probed to determine if the excitation photon energy and subsequent photo-electro-chemical response corresponded well to the absorbance spectrum of PBTh. This is similar in purpose as the commonly reported incident photon-to-current efficiency (IPCE) measurement used for solar-cells and highlights PBTh's photo-response for a given wavelength. For our purposes, the dependency of PBTh's catalytic response (reported in μA mW^{-1} cm^{-2}) is compared against the wavelength of the incident photons to illustrate their relationship; no IPCE in its conventional sense is calculated due to the need for an applied potential.

A PBTh film on glassy carbon with a relatively high reduction potential of −0.8 V *vs.* Ag/AgCl was chosen to yield a better photo response. A high intensity Xe lamp was used for the photo-dependency measurements to allow for a wider spectral window. The reported results in Fig. 7 show a strong match up to the absorbance of PBTh though there is a slight blue shift in the response. This is not surprising considering that the energetics of the two-electron catalysis reaction will be more demanding than a conventional singlet excitation process. Importantly, the results show that it is the $\pi \rightarrow \pi^*$ transition in the visible spectrum (between 400 to 550 nm) that is responsible for the photo-electrochemical catalysis of the HER.

Conclusion

The investigation into various system parameters have resulted in a substantial increase in performance on the PBTh film with respect to the HER. Importantly, it has revealed the significant potential of PBTh as a commercially viable catalyst for the HER and exhibits key characteristics such as high faradaic efficiency and long term stability. Furthermore, PBTh's high pH performance and low onset potential provides an ideal condition for

the water oxidation reaction and presents a very compelling material for the water splitting system.

The use of a conducting polymer as a photo-electrochemical catalyst brings further novelty in its implications for future catalyst designs, not solely for HER. The ease in which polymers can be polymerised, blended, patterned and manipulated brings about a flexibility not often observed with traditional catalyst materials. As a result there remains significant scope with which the PBTh system can be modified and investigated. Future studies into combinations of various polymerisation parameters *e.g.* humidity, polymerisation time and polymeri-sation temperature and/or into engineering aspect of the substrate morphology and cell design will thus further aid in determining the true potential of the PBTh system.

Experimental

The standard PBTh film was polymerised using a 40 w/v% Fe(III) *p*-toluenesulfonate in butanol as the oxidant solution. Approx-imately 0.5 mL of this solution was spin-coated onto a glassy carbon substrate (polished to a mirror finish) at 1500 rpm for 30 s. The deposited sample was then placed in a pre-heated VPP chamber with 2,2′-bithiophene monomer (from Sigma Aldrich) and left to heat and polymerise in the oven at a temperature of 70 °C for 1 h. The sample was then taken out and washed and left to soak overnight in ethanol. After soaking the sample was rinsed once more and left to dry in air. Unless otherwise stated, the counter and reference electrodes used was stainless steel wire and Ag/AgCl respectively. An initial CV scan was performed for all samples prior to testing to confirm photo-electrocatalytic behaviour. Illumination was provided by a Leica KL 2500 LCD lamp with an equivalent power of 1.6 suns.

Efficiency

A standard PBTh film was used for testing efficiency but a modified metal cell was utilised for better sealing and separation of the counter electrode (Ti mesh[45]), see Fig. S1.† An initial CV was performed to check photo-electrocatalysis. Main investigations proceeded *via* a CA measurement. Regular gas chromatography (GC) injections into the gas chromatograph (SRI 310C, TCD, MS-5A column, Ar carrier) was performed and the resulting hydrogen peak at 1.96 min recorded. Conversion to a hydrogen : Ar ratio was done using the calibration curve as shown in Fig. S2† and the rate of hydrogen production was calculated (Ar flow rate 2 mL min^{-1}) for conversion to faradaic efficiency.

Stability testing

A standard film was used for long-term tests and was continually purged with N_2 to remove O_2, a titanium mesh was used as the counter electrode. The CA test was left to run over a period of 12 days with sporadic top ups with distilled H_2O to replace evaporated and consumed H_2O.

Substrates

Each substrate was sonicated in a 50 : 50 mixture of ethanol and H_2O for 1 h and rinsed in acetone prior to polymerisation. Polymerisation was conducted as per before save glassy carbon was replaced with the appropriate substrate. Testing proceeded after an initial purge using Ar gas and consisted of a CV run at 20 mV s^{-1}.

Electrolyte

The NaCl and PB solutions used in the electrolyte testing was made up using NaCl and NaH_2PO_4/Na_2HPO_4 salts from Merck respectively. The pH of each electrolyte solution was tested prior to the studies using a Mettler Toledo pH meter; the NaCl solutions were adjusted to approach pH 7.0 using small amounts of 0.1 mol L^{-1} HCl and NaOH. Testing was conducted on the same PBTh film but a new area was utilised for each electrolyte. N_2 was bubbled through the cell for 20 min prior to commencement, followed by the main CA test.

pH

The 0.1 mol L^{-1} PB pH solutions were made up using varying ratios of NaH_2PO_4 and Na_2HPO_4 and dissolved in water. At pH 9, the solution was almost entirely Na_2HPO_4 and for pH 11, *ca.* 4 mL of 0.1 mol L^{-1} NaOH was added to increase alkalinity. A standard PBTh film was used for testing with each pH run performed on a different area; this helps to minimise variations due to differences between films. The cell was purged with Ar prior to the main pH testing; CV at a scan rate of 0.1 mV s^{-1}. The pH before and after each run was recorded and is presented in Table S1.†

Interaction between light and PBTh

Thickness. For the preparation of the thin PBTh films the oxidant solution (40% Fe(III) PTS in butanol) was diluted with butanol to a concentration of 20 w/v% and 10 w/v% Fe(III) PTS for the 0.21 μm and 0.11 μm film respectively. Polymerisation then occurred *via* the standard technique. The 0.44 μm film was prepared in the same manner as the standard film. The 1.24 μm film was prepared using two depositions of the oxidant solution; after an initial first polymerisation of the standard film (but before the wash step), another layer of the oxidant solution was deposited *via* spin coater and the VPP process repeated. The resulting double layer of PBTh was then washed as per usual in ethanol to produce the thick 1.24 μm film. Polymerisation of each thickness was conducted on both glassy carbon substrates and glass slides.

CV and CA measurements on the glassy carbon PBTh films were run under Ar (0.15 mL min^{-1}) to assess the performance of the film. CA measurements were conducted by applying a potential of −0.5 V *vs.* Ag/AgCl over a period of 120 min under illumination. GC measurements were conducted concurrent to CA and the resulting H_2 peak height at 120 min is shown in Fig. S12.† UV-Vis spectroscopy of the PBTh films polymerised on glass slides were conducted on a Jasco V670 Spectrophotometer to determine the absorbance.

Wavelength dependency. A thin film of 0.21 μm was prepared as described in the thickness measurements, on glassy carbon. An initial CV was conducted followed by a CA run held at −0.8 V *vs.* Ag/AgCl reference electrode, Ti mesh and 1 mol L^{-1} PB at pH 7 were used as the counter electrode and electrolyte respectively. The light source was provided by a high intensity Xe lamp (Rofin Polilight PL6) and the wavelengths selected using the respective bandpass filter (Newport 10BPF10-XXX series). The PBTh film was placed under illumination for a period of 10 min and the average current recorded as the catalytic response; a 5 min dark interval separated each wavelength measurement. Intensity was determined using a Si solar cell and converted with the approximation that 1 sun is equivalent to 100 mW cm^{-2}. Ar was used to purge the cell throughout the experiment at a rate of 10 mL min^{-1}.

References

1 J. Turner, *Science*, 2004, **305**, 972–974.
2 M. Bowker, *Green Chem.*, 2011, **13**, 2235–2246.
3 R. Kleijn and E. van der Voet, *Renewable Sustainable Energy Rev.*, 2010, **14**, 2784–2795.
4 T. Abbasi and S. A. Abbasi, *Renewable Sustainable Energy Rev.*, 2011, **15**, 3034–3040.
5 The International Energy Agency, *Key World Energy Statistics*, Paris, 2014.
6 P. D. Tran, V. Artero and M. Fontecave, *Energy Environ. Sci.*, 2010, **3**, 727–747.
7 T. W. Woolerton, S. Sheard, Y. S. Chaudhary and F. A. Armstrong, *Energy Environ. Sci.*, 2012, **5**, 7470–7490.
8 M. Carmo, D. L. Fritz, J. Mergel and D. Stolten, *Int. J. Hydrogen Energy*, 2013, **38**, 4901–4934.
9 K. S. Joya and H. J. M. de Groot, *Int. J. Hydrogen Energy*, 2012, **37**, 8787–8799.
10 S. Esiner, H. van Eersel, M. M. Wienk and R. A. J. Janssen, *Adv. Mater.*, 2013, 2932–2936.
11 M. G. Walter, E. L. Warren, J. R. McKone, S. W. Boettcher, Q. Mi, E. A. Santori and N. S. Lewis, *Chem. Rev.*, 2010, **110**, 6446–6473.
12 P. D. Tran and J. Barber, *Phys. Chem. Chem. Phys.*, 2012, **14**, 13772–13784.
13 A. Le Goff, V. Artero, B. Jousselme, P. D. Tran, N. Guillet, R. Métayé, A. Fihri, S. Palacin and M. Fontecave, *Science*, 2009, **326**, 1384–1387.
14 H. I. Karunadasa, E. Montalvo, Y. Sun, M. Majda, J. R. Long and C. J. Chang, *Science*, 2012, **335**, 698–702.
15 M. Wang, Y. Na, M. Gorlov and L. Sun, *Dalton Trans.*, 2009, 6458–6467.

16 A. Magnuson, M. Anderlund, O. Johansson, P. Lindblad, R. Lomoth, T. Polivka, S. Ott, K. Stensjö, S. Styring, V. Sundström and L. Hammarström, *Acc. Chem. Res.*, 2009, **42**, 1899–1909.

17 B. Hinnemann, P. G. Moses, J. Bonde, K. P. Jørgensen, J. H. Nielsen, S. Horch, I. Chorkendorff and J. K. Nørskov, *J. Am. Chem. Soc.*, 2005, **127**, 5308–5309.

18 Y. Sun, J. Sun, J. R. Long, P. Yang and C. J. Chang, *Chem. Sci.*, 2013, **4**, 118–124.

19 X. Zong, G. Wu, H. Yan, G. Ma and J. Shi, *J. Phys. Chem. C*, 2010, **114**, 1963–1968.

20 Y. Hou, B. L. Abrams, P. C. K. Vesborg, M. E. Björketun, K. Herbst, L. Bech, A. M. Setti, C. D. Damsgaard, T. Pedersen, O. Hansen, J. Rossmeisl, S. Dahl, J. K. Nørskov and I. Chorkendorff, *Nat. Mater.*, 2011, **10**, 434–438.

21 E. Lanzarini, M. R. Antognazza, M. Biso, A. Ansaldo, L. Laudato, P. Bruno, P. Metrangolo, G. Resnati, D. Ricci and G. Lanzani, *J. Phys. Chem. C*, 2012, **116**, 10944–10949.

22 M. P. Gustafson, N. Clark, B. Winther-Jensen and D. R. MacFarlane, *Electrochim. Acta*, 2014, **140**, 309–313.

23 A. J. Heeger, *J. Phys. Chem. B*, 2001, **105**, 8475–8491.

24 B. Kolodziejczyk, O. Winther-Jensen, D. R. MacFarlane and B. Winther-Jensen, *J. Mater. Chem.*, 2012, **22**, 10821–10826.

25 R. Kerr, C. Pozo-Gonzalo, M. Forsyth and B. Winther-Jensen, *ECS Electrochem. Lett.*, 2013, **2**, F29–F31.

26 B. Winther-Jensen, O. Winther-Jensen, M. Forsyth and D. R. Macfarlane, *Science*, 2008, **321**, 671–674.

27 O. Winther-Jensen and B. Winther-Jensen, *Electrochem. Commun.*, 2014, **43**, 98–101.

28 O. Winther-Jensen, B. Winther-Jensen and D. R. MacFarlane, *Electrochem. Commun.*, 2011, **13**, 307–309.

29 M. P. Gustafson, K. Matsumoto, D. R. MacFarlane and B. Winther-Jensen, *Electrochim. Acta*, 2014, **122**, 166–172.

30 B. Winther-Jensen, K. Fraser, C. Ong, M. Forsyth and D. R. MacFarlane, *Adv. Mater.*, 2010, **22**, 1727–1730.

31 C. H. Ng, O. Winther-Jensen, B. Kolodziejczyk, C. A. Ohlin and B. Winther-Jensen, *Int. J. Hydrogen Energy*, 2014, **39**, 18230–18234.

32 Y. Zhang, N. Zhang, Z.-R. Tang and Y.-J. Xu, *Phys. Chem. Chem. Phys.*, 2012, **14**, 9167–9175.

33 W. Teng, X. Li, Q. Zhao and G. Chen, *J. Mater. Chem. A*, 2013, **1**, 9060–9068.

34 O. Winther-Jensen, K. Chatjaroenporn, B. Winther-Jensen and D. R. MacFarlane, *Int. J. Hydrogen Energy*, 2012, **37**, 8185–8189.

35 J. Luo, J. H. Im, M. T. Mayer, M. Schreier, M. K. Nazeeruddin, N.-G. Park, S. D. Tilley, H. J. Fan and M. Grätzel, *Science*, 2014, **345**, 1593–1596.

36 S. Hotta, T. Hosaka and W. Shimotsuma, *Synth. Met.*, 1983, **6**, 69–71.

37 A. Aguirre, P. Gast, S. Orlinskii, I. Akimoto, E. J. J. Groenen, H. El Mkami, E. Goovaerts and S. Van Doorslaer, *Phys. Chem. Chem. Phys.*, 2008, **10**, 7129–7138.

38 B. Kolodziejczyk, D. Mayevsky and B. Winther-Jensen, *RSC Adv.*, 2013, **3**, 4568–4573.

39 S. S. Moganty, R. E. Baltus and D. Roy, *Chem. Phys. Lett.*, 2009, **483**, 90–94.

40 F. G. Allen and G. W. Gobeli, *Phys. Rev.*, 1962, **127**, 150–158.

41 M. G. Helander, M. T. Greiner, Z. B. Wang, W. M. Tang and Z. H. Lu, *J. Vac. Sci. Technol., A*, 2011, **29**, 011019.

42 D. Merki and X. Hu, *Energy Environ. Sci.*, 2011, **4**, 3878–3888.

43 P. Y. Bruice, *Organic Chemistry*, Pearson Eduction Inc., Upper Saddle River, NJ, 5th edn, 2007.

44 G. Kossmehl and M. Niemitz, *Synth. Met.*, 1991, **43**, 1065–1071.

45 M. Hilder, O. Winther-Jensen, B. Winther-Jensen and D. R. MacFarlane, *Phys. Chem. Chem. Phys.*, 2012, **14**, 14034–14040.

5.3 Supplementary Information for Publication 3: Exploration and optimisation of Poly(2,2'-bithiophene) as a Stable Photo-electrocatalyst for Hydrogen Production

Supporting Information

Efficiency

A new cell setup was procured with an improved layout for gas detection and determination of faradaic efficiency.


Fig. S1: New cell setup in metal cell with separated counter electrode compartment, direct access to headspace and improved sealing. Area of the film is determined to be 6.79 cm^2

Calibration of the gas chromatograph with % H$_2$ (in Ar) to detector response (in μV) was conducted and presented in Fig. S2. The molar evolution of H$_2$ per second is determined using the known flow rate of Ar (2 mL min^{-1}), the calculated % H$_2$ and the molar volume of gas (24.5 L mol^{-1}).
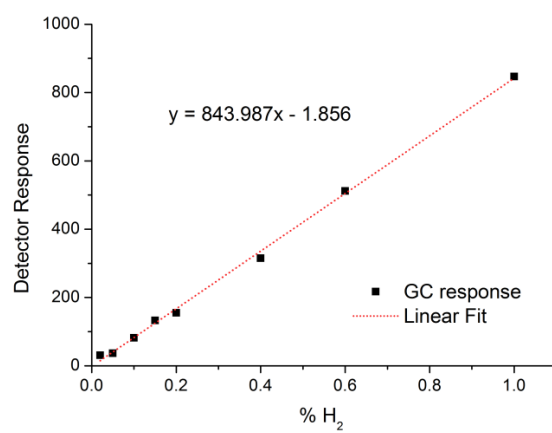
Fig. S2: Calibration curve relating GC detector response and % H_2
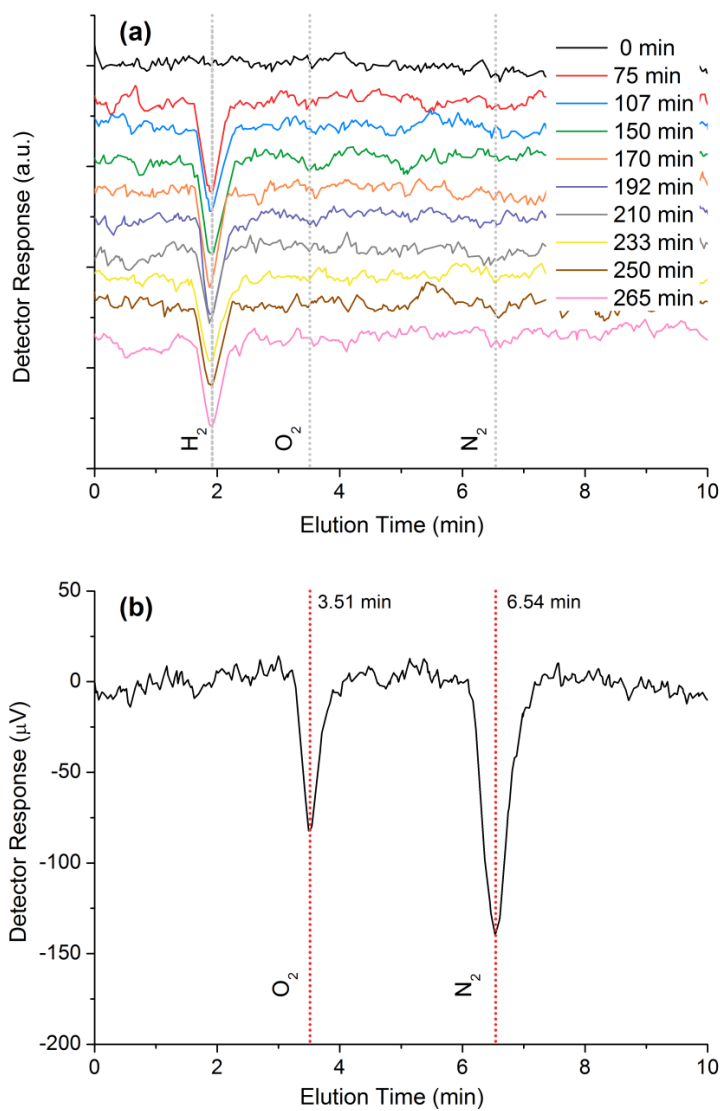
Fig. S3: (a) GC of injected headspace showing detected H$_2$ for the determination of faradaic efficiency, Ar flow = 2 mL min^{-1}. **(b)** GC injection of air showing its characteristic O$_2$ and N$_2$ peak at 3.51 min and 6.54 min respectively, Ar flow = 0.15 mL min^{-1}.

Stability Testing

Full stability CA

Correction of Light Intensity

The correction for the lamp intensity was done utilising an Edmund Optics LaserCheck power meter (model 54-018) with a silicon cell; the power measurement was conducted at a wavelength of 488 nm. An initial power reading (in mW) was taken at 3.9 days and used as the baseline power (100% lamp intensity). Subsequent readings were converted to a percentage based on this initial reading and compared with the photocurrent. Once the decrease in light output is accounted for, the decrease in photocurrent from day 4 to day 12 is *ca*. 80%; as compared to *ca*. 60% without the correction.
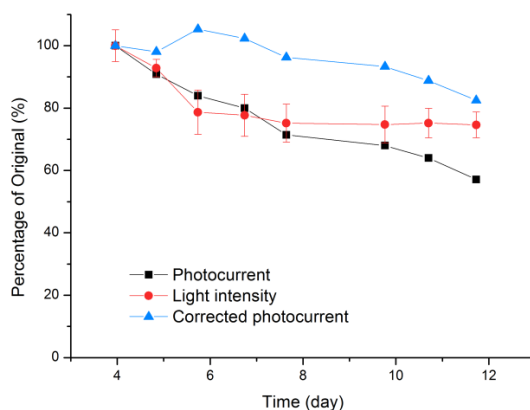
Fig. S4 Longterm percentage decrease from day 4 to 12. The —▲— trace shows the corrected decrease in photocurrent when the decrease in light intensity is accounted for.

Counter Electrodes

Initial tests utilising a stainless steel and platinum wire as counter electrodes resulted in a dramatic decrease in photocurrent over time. The comparison between these counter electrodes is shown in Fig. S5 where Ti mesh (black trace) is shown to retain the best long term performance.
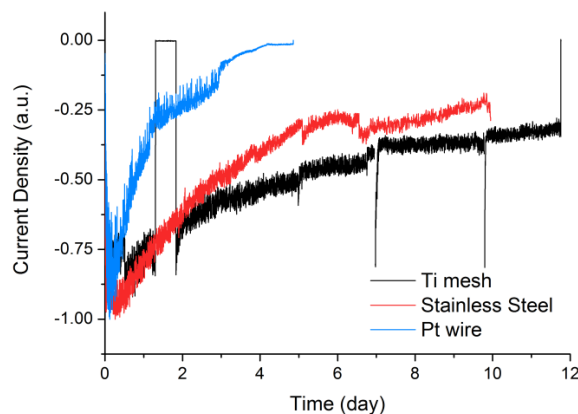
Fig. S5 Comparison of the CA trace of each counter electrode material, all were conducted on the standard PBTh film at -0.5 V vs Ag/AgCl in 1 mol L^{-1} phosphate buffer. They have been normalised to their maximum reduction current for better comparison of their degradation over time.

Subsequent studies using SEM and EDX shows the presence of deposited precipitates of various metal ions, refer to Fig. S6 and Fig. S7 respectively. Different counter electrode materials exhibited slightly behaviour with stainless steel showing substantially higher depositions of metal. This is unsurprising due to the relative reactiveness of stainless steel which would oxidise at higher rates than that of Pt or the mixed metal oxide layer on the Ti mesh electrode. Nonetheless, despite a higher resistance to oxidation, all samples exhibit noticeable metal deposits.
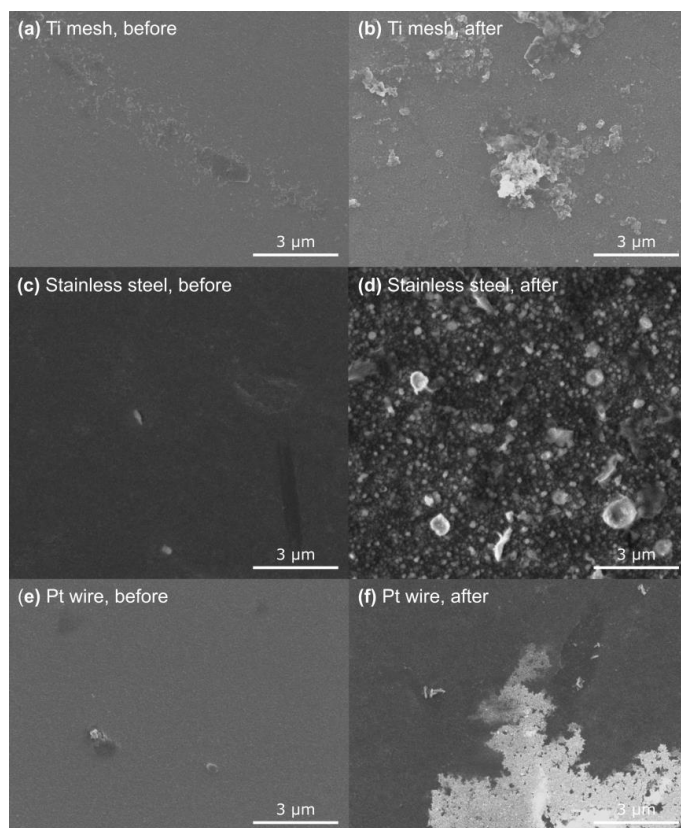
Fig. S6 SEM showing the PBTh film, before and after lonterm stability testing with different counter electrodes. The deposition of precipitates are observed throughout all samples.
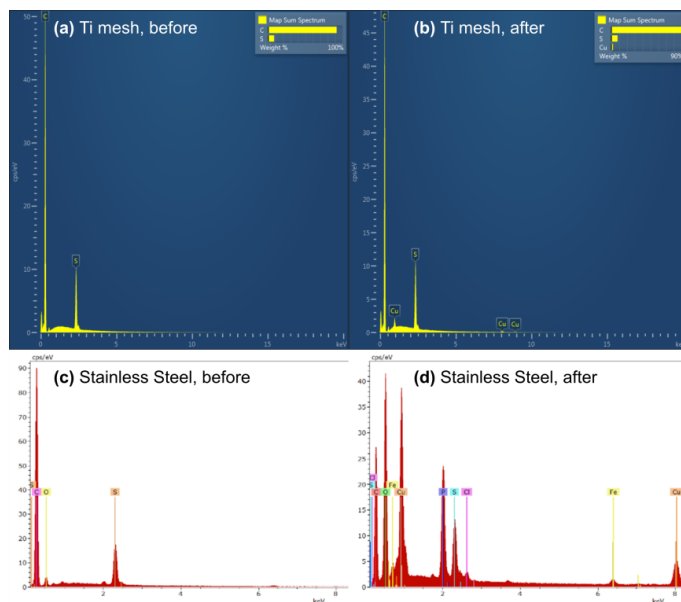
Fig. S7 EDX showing the significant presence of metals after stability testing, prior to testing, all films only exhibited the expected C and S peaks associated with PBTh. The stainless steel electrode resulted in a significantly higher amount of deposition and is reflected in the EDX spectra (d). Pt wire showed an EDX spectra similar to that of Ti mesh.

Calculation of turn over number (TON)

To calculate the total amount of hydrogen produced (assuming faradaic efficiency is 100%) integration of the current density (A/cm^2) over time (s) over the 12 day period was done to determine the total amount of charge. This resulted in a value of 60.1 C/cm^2. Converting to an amount of H_2 gas:

$$No.\,of\,e^- = 60.1 \times 6.241 \times 10^{18} = 3.75 \times 10^{20}\ e^-/cm^2$$
$$No.\,of\,H_2 = 3.75 \times 10^{20}\ \div 2 = 1.88 \times 10^{20}\ H_2/cm^2$$

To determine the number of catalytic sites, given the hydrophobicity of PBTh, we assume that only the first 5 nm of the material is permeable to H_2O and catalytically active.   Thus:

$$Volume\ PBTh\ reacting = 1\ cm^2 \times 5 \times 10^{-7} cm = 5 \times 10^{-7} cm^3$$

Density of PBTh = 1.52 g/cm^3

$$m(PBTh\ reacting) = 1.52\ g/cm^3 \times 5 \times 10^{-7} cm^3 = 7.6 \times 10^{-7} g$$

Assuming one catalytic site is one unit of polymerised bithiophene, M_r(catalytic site) = 164.2 g/mol

$$mol(catalytic\ sites) = 7.6 \times 10^{-7} g \div 164.2\ g/mol = 4.63 \times 10^{-9} mol$$
$$No.\,of\,catalytic\ sites = 4.63 \times 10^{-9} \times 6.022 \times 10^{23} = 2.79 \times 10^{15} sites$$

$$\therefore TON = \frac{1.88 \times 10^{20}}{2.38 \times 10^{15}} = \mathbf{6.7 \times 10^4}\ per\ cm^2 of\ PBTh$$

Electrolyte
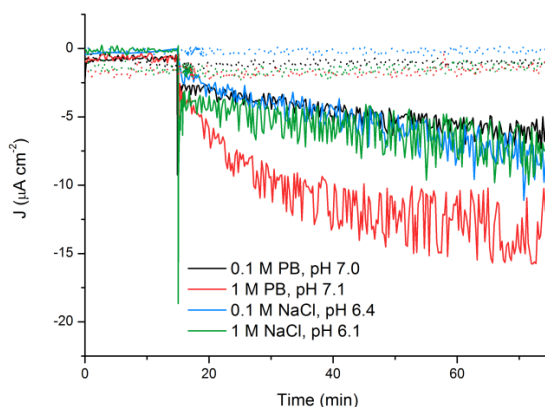
Fig. S8 CA trace at a potential of -0.5 V vs Ag/AgCl in different electrolytes under bubbled N_2. Solid traces represent PBTh films, dotted traces represent glassy carbon under the same conditions. Light was switched on at 15 min, current was recorded at 75 min (after 60 min of illumination).

pH

The pH of the electrolyte was recorded before and after each CV test to ensure that pH had been maintained; this is presented in Table S1.

Table S1: The pH of each solution measured before and after the experiment.

pH Test	pH before	pH after
3	3.1	3.2
5	5.0	5.2
7	7.0	6.9
9	8.5	8.9
11	11.0	10.9

Fig. S9 shows the CV traces in light, dark and the corrected trace showing the determined onset potential and E^0 at various pH.
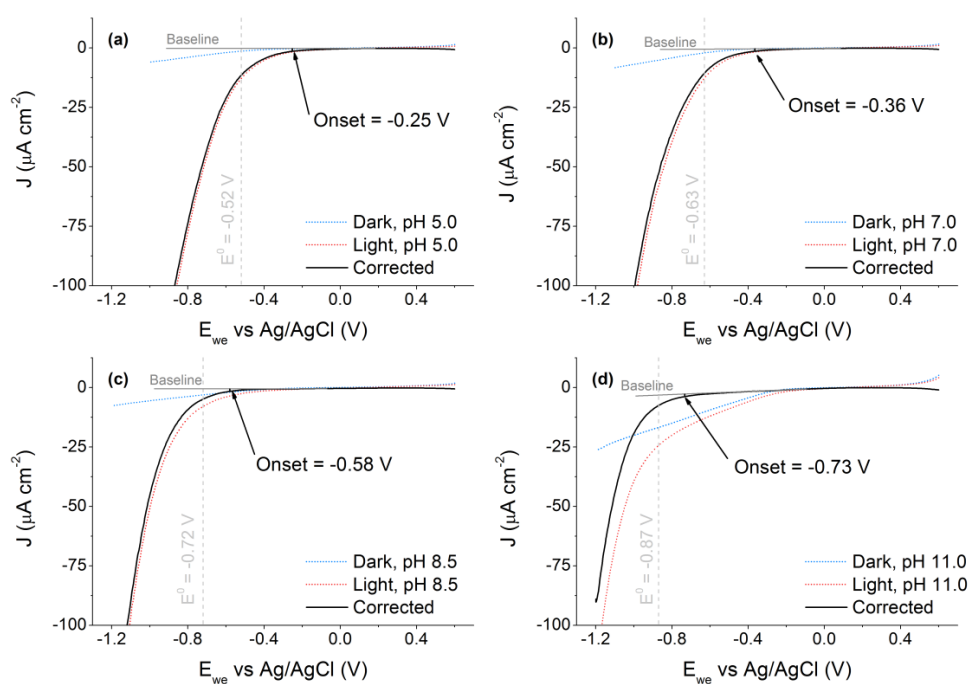
Fig. S9 CV of the PBTh film at different pH showing the determined onset potential, E^0 at the specified pH, the original dark and light traces and the corrected trace. (a) pH 5.0, (b) pH 7.0, (c) pH 8.5, (d) pH 11.0. pH 3.1 is shown in the main manuscript.

Thickness
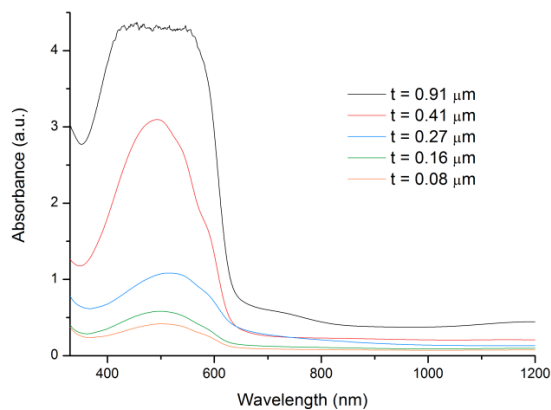
Fig. S10 UV-Vis absorption spectra of various PBTh film thicknesses on glass slide. The absorbance of the 0.91 μm film resulted in saturation of the detector and is not presented in the main manuscript, Fig. 6
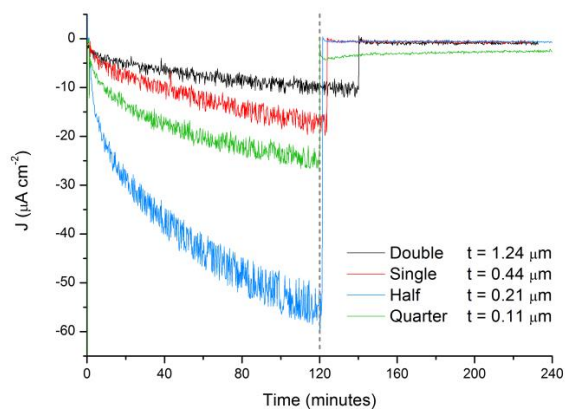
Fig. S11 CA measurement of different thickness with an applied potential of -0.5 V vs Ag/AgCl. The current is recorded at 120 min for comparison (dotted grey line) in Fig. 6. The measured thickness of each film is also shown in the legend.
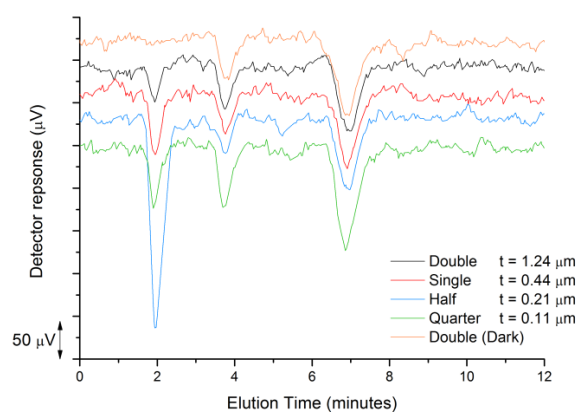
Fig. S12 Gas chromatograms of the injected headspace at 120 min and the recorded H_2 peak at 2 min. Ar bubbling rate was 0.15 mL min^{-1}; O_2 and N_2 can also be observed. The measured thickness of each film is also shown in the legend.

Wavelength dependency
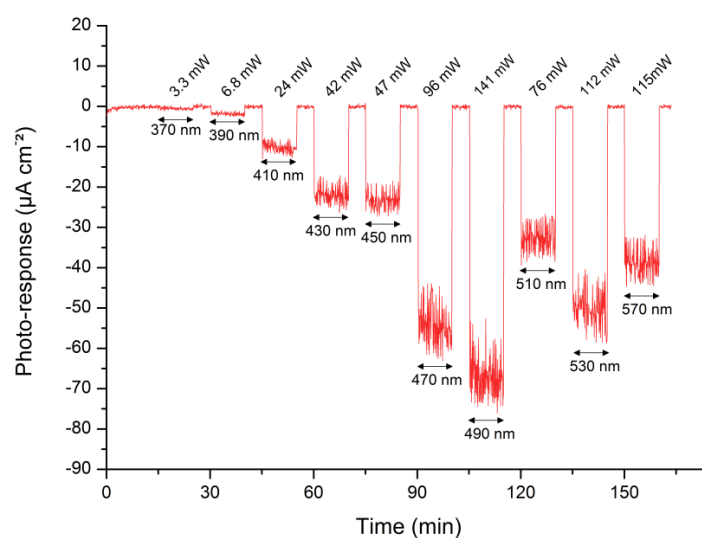
Fig. S13 CA measurement at -0.8 V vs Ag/AgCl in 1 mol L^{-1} phosphate buffer (pH 7) for wavelength dependence measurements; $E_0(HER)$ = -0.63 V vs Ag/AgCl. The photo response is the average current over the 10 min interval with light. The wavelength and corresponding intensity of each band pass filter is also provided.

5.4   Influence of Morphology on Catalytic Performance

In Publication 2, it was hinted that higher roughness significantly enhanced catalytic activity and was attributed to the increased surface area as well as the improved penetration of the electrolyte. From this result, we attempted a more in-depth look into how the performance of PBTh can be improved by altering the film's morphology. Numerous methods were proposed and included the use of pre-roughened substrates, mesoporous structures, porous foams, incorporation of hydrophilic components (like PEG), and laser etching. However, to maintain consistency, (flat) glassy carbon was retained as the substrate while the PBTh films were altered. This modification to PBTh was done via two main – albeit related – methods, exposure of the Fe(III)PTS oxidant to humidity prior to polymerisation and the exposure of a $FeCl_3$ oxidant to humidity prior to polymerisation.

5.4.1   Modification of Morphology using Humidity

Exposure of the precursor oxidant solution to high levels of humidity is not typically desired in the VPP process as it leads to the formation of iron crystallites which disrupts the smooth ordering of the conducting polymer. This in turn can result in rough films with adverse effects to conductivity; a common indicator for conducting polymer quality. However, it was discovered during the testing of a rough film – formed unintentionally by exposure to air on a particularly humid day – that it exhibited significantly improved photo-catalytic responses. This interesting effect was thus further investigated, though due to issues with obtaining consistent results, these findings were not included in Publication 3.
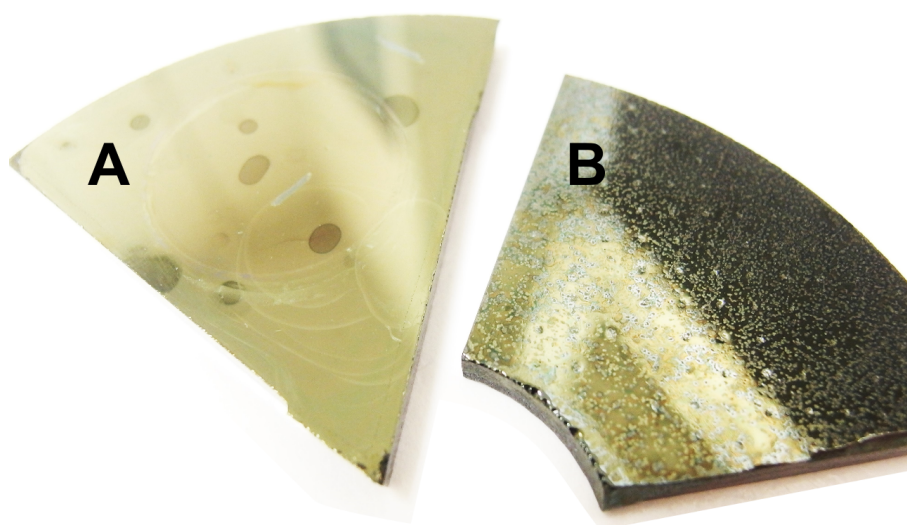
Figure 5.1: Comparison of a smooth and rough PBTh film made using the humidity chamber. **A:** A smooth film, 0 min in humidity chamber (some blemishes can be seen due to evaporated electrolyte and residual salt) and **B:** a rough film, 2 min in humidity chamber.

A variety of films were produced by varying exposures to humidity and tested via electrochemistry. Initial tests used a humidity chamber, a glass dessicator that was filled with a saturated aqueous NaCl solution so that a constant humidity of $\approx 75\%$ was obtained.[1] The spin coated oxidant solution was placed in this humidity chamber for 1 and 2 min prior to VPP so that small amounts of iron crystallites could form. The PBTh films were then allowed to undergo VPP as per normal, followed by washing in $1\,\mathrm{mmol\,L^{-1}}$ PTSa and left to dry; the resulting smooth and rough films are shown in Figure 5.1.

CA testing of these initial humidity films (held at $-0.5\,\mathrm{V}$ vs Ag/AgCl) showed promising performances (Figure 5.2). The currents and the recorded H_2 peaks obtained for the "rough" films (1 and 2 min) were much higher than the "smooth" film (0 min sample) and presented a compelling case as a method for enhancing photo-electrocatalysis. At the same time, the use of the humidity chamber was problematic as the transfer time from the spin-coater to the humidity chamber and then to the VPP chamber was difficult to keep consistent. Moreover, it exposed the film to atmospheric humidity and made samples which were prepared on different days difficult to compare. A humidity and temperature controlled glovebox with an internal spin coater and oven would be more ideal for reproducibility, though this was not available to us at the time.
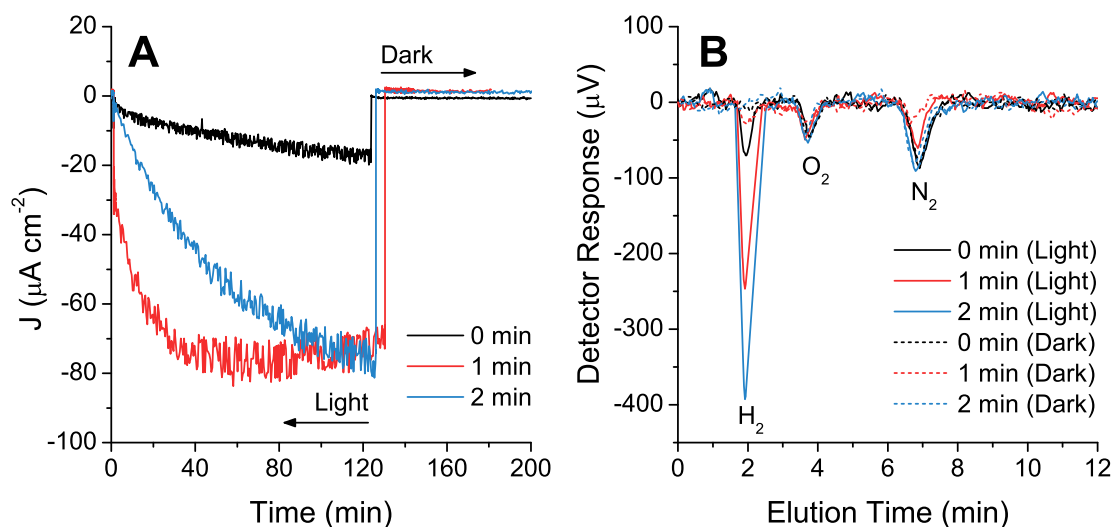
Figure 5.2: Comparison of the rough films after varying exposures to 74% humidity in the humidity chamber. Testing was conducted in the 1st generation metal cell in $1\,\mathrm{mol\,L^{-1}}$ NaCl electrolyte (pH 6), and bubbling at Ar $= 0.15\,\mathrm{mL\,min^{-1}}$. **A:** CA trace of the PBTh film held at $-0.5\,\mathrm{V}$ vs Ag/AgCl for 120 min in light, then for $\approx 60\,\mathrm{min}$ in dark. **B:** GC trace of the headspace during the CA experiment, conducted at t $= 120\,\mathrm{min}$ (Light) and t $= 180\,\mathrm{min}$ (Dark). Trace amounts of O_2 and N_2 can also be observed.

In order to bypass the transfer times and associated humidity swings of using the humidity chamber, it was decided to simply expose the film to atmospheric humidity. This would isolate exposure time as the only experimental variable – given the same atmospheric conditions – and

would allow for a more consistent humidity exposure and hence, degree of roughness. The samples were exposed to air (humidity = 47%, 21 °C) for 0, 4, 10, 20 and 30 min after spin coating then placed into the VPP for polymerisation. They were washed in ethanol and tested in $0.1 \, mol \, L^{-1}$ PB (pH 7); PB was used to better maintain pH at these higher currents.

The results of these air exposed films is shown in Figure 5.3 and reveal a surprising trend. Contrary to previous findings, the smooth film with 0 min exposure – the one transferred directly from spin coater to VPP chamber – had the highest performance by far. This was particularly surprising since it was prepared in the same manner as previous films. One proposed explanation was the use of the 2nd generation metal cell for the humidity tests, whereas the initial experiments on smooth films (eg: in Figure 5.2) utilised the 1st generation metal cell and older designs. The 2nd generation cell was designed to isolate the products (O_2) produced at the counter electrode which would then limit cross-over reactions and increase HER activity. As a result, the 0 min sample in Figure 5.3 was able to exhibit much higher catalytic activities. Furthermore, care was taken to avoid the introduction of metal ions and other contaminants into the main chamber of the newly acquired 2nd generation cell. Whereas in the 1st generation metal cell, studies using a variety of reactive counter electrodes such as graphite and stainless steel resulted in trace contaminants which could adversely affect performance.

Another possible explanation is that through the encounter of favourable atmospheric/synthesis conditions, this particular PBTh film was much more active. This is not surprising considering the large variation in PBTh performance that has been observed throughout our studies. The exact cause is unknown but it is strongly influenced by atmospheric humidity, temperature, speed of transfer from spin coater to VPP chamber *etc.*

Analysis of the rough films showed a peak current of $75 \, \mu A \, cm^{-2}$ at 120 min and was on par with previous rough films made using the humidity chamber. However, they did not vary much between themselves and no trend between humidity exposure and catalytic performance could be inferred. This suggests at a saturation of the iron crystallite formation and its subsequent roughness effect. In hindsight, it would have been more apt to investigate films with exposure times between 0 and 4 min. At the time, it was thought that the lower atmospheric humidity – 47% vs 75% of the humidity chamber – would require a longer exposure times to compensate. This was reinforced by visual inspection where the originally planned exposure times of 1, 2 and 4 min failed to show the texture previously observed for a rough film. As a result, the exposure times were extended to >4 min.

The failure of the (rough) air exposed films to generate improved catalytic performance was in direct conflict with earlier results and demanded further studies. Furthermore, no information was gained regarding the trend between roughness and catalytic activity as a result of the long exposure times. Quantification of the roughness/porosity was also not undertaken which made
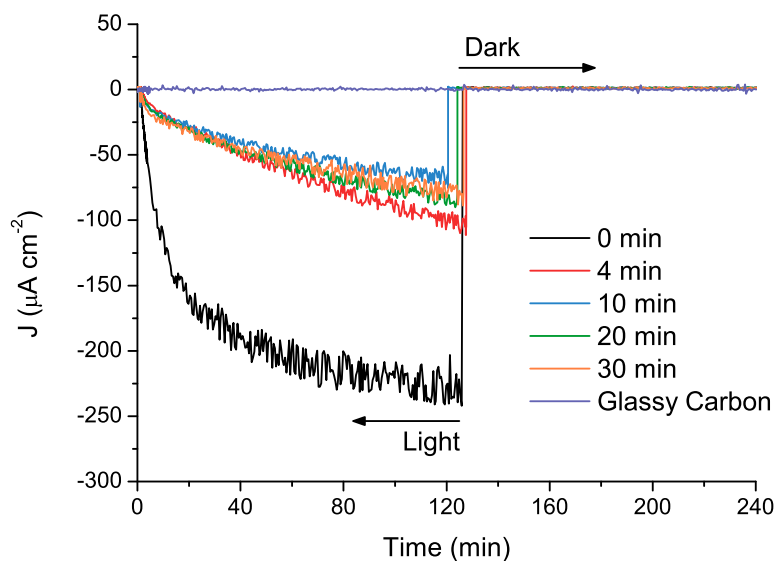
Figure 5.3: The performance of smooth PBTh and glassy carbon electrodes compared to rough PBTh samples made by exposure to atmospheric humidity (47% at 21 °C). Conducted in the 2nd generation metal cell in $0.1 \, \mathrm{mol \, L^{-1}}$ PB (pH 7) with bubbled Ar.

analysis of the samples difficult. In an attempt to address these points, a final investigation using $FeCl_3$ was conducted.

5.4.2   Modification of Morphology using $FeCl_3$

A key contributing factor to the difficulties of producing rough films was the use of Fe(III)PTS which was originally selected for the VPP process due to its resistance to crystallite formation.[2] However, in order to produce a rough film, the formation of iron crystallites *is* desired and thus, $FeCl_3$ was chosen as a replacement oxidant. $FeCl_3$ has been described in literature both for its ability to perform VPP on polythiophenes[3] and formation of crystallites.[4]

A 40% $FeCl_3$ oxidant solution in butanol was made up, spin coated onto glassy carbon substrates and exposed to air (Humidity 40±2 %, 22±0.5 °C) for 0, 1, 2 and 4 min before undergoing VPP. The resulting films were washed in ethanol and appeared much rougher with the presence of pockmarks, high surface texture, and dull (non-reflective) films which indicate scattering and increased surface roughness. This increase in roughness is particularly apparent when compared with films prepared using Fe(III)PTS, see Figure 5.4. Unfortunately, due to the ease in which crystallites were formed with $FeCl_3$, even the 0 min film exhibited some surface roughness (Figure 5.4C). The films were characterised for their catalytic performance via CA and GC, as well as roughness and morphology using profilometry and SEM respectively.
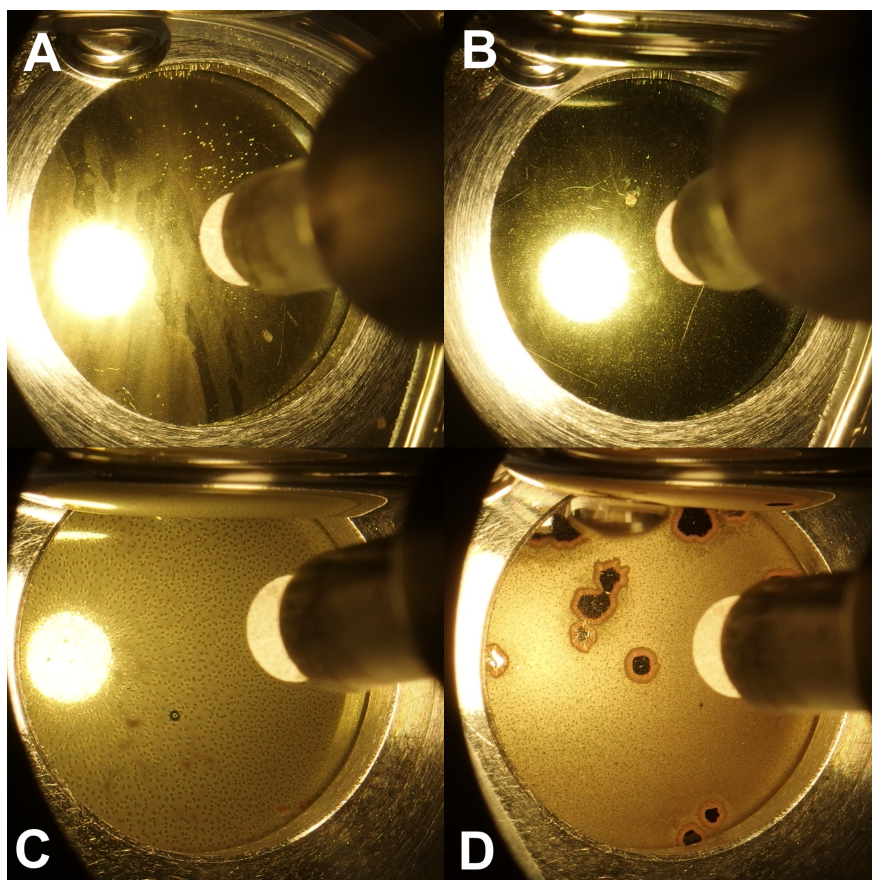
Figure 5.4: Photographs of various smooth and rough films made by exposure to atmospheric humidity. These were prepared using Fe(III)PTS (**A:** 0 min, **B:** 4 min) and FeCl$_3$ (**C:** 0 min, **D:** 4 min). In general, rougher films have more diffuse surfaces and pockmarks.

The CA and GC results are presented in Figure 5.5 and confirm the benefits of rougher films, where an exposure time of 0 min resulted in the lowest photo-response and H$_2$ signal. The peak CA current occurs with the 2 min film (blue trace) but it is interesting to note that the photo-current trend of the 0 and 4 min film remains growing whilst the other films have plateaued. The result is significant as the films were prepared on two different days, the 0 and 4 min film on one (38%, 22 °C) and the 1 and 2 min film on the other (41%, 22 °C). This reveals that even small variations in atmospheric conditions can have a significant impact on the resulting film and emphasises the importance of humidity/temperature control.

The different CA behaviour makes it difficult to directly compare the films but it is not surprising that the 4 min sample shows a slightly decreased catalytic behaviour (when compared to that of 2 min). The formation of too many crystallites would likely hinder the VPP process and lead to poor cohesion and electrical contact between the polymer chains. It is likely that a balance is required between the use of crystallites to increase roughness/surface area and maintaining good electrical properties within the bulk film.
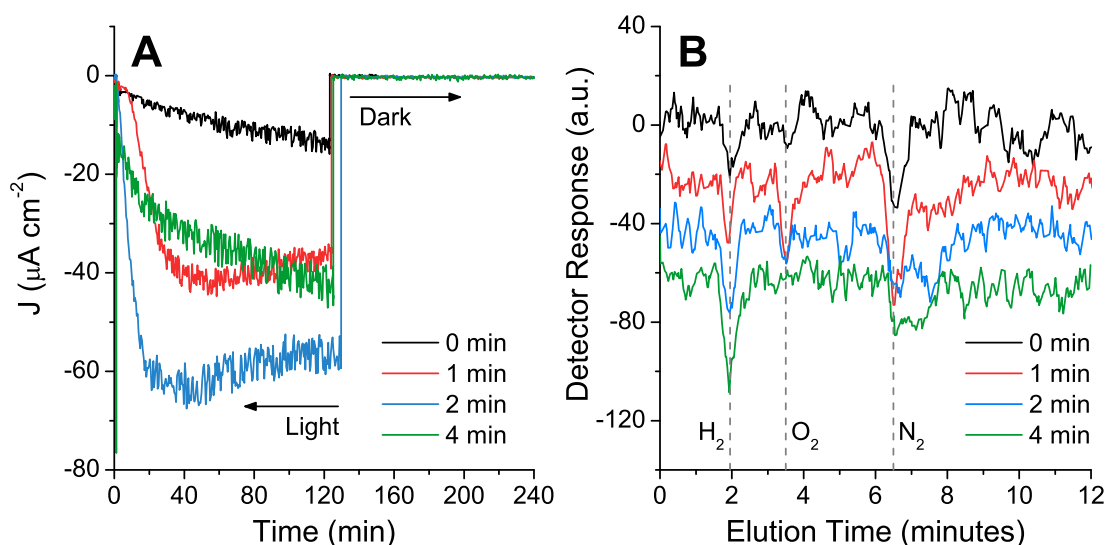
Figure 5.5: Photo-electrocatalytic performance of the films in $0.1\,\mathrm{mol\,L^{-1}}$ PB, pH 7 with bubbled Ar ($1\,\mathrm{mL\,min^{-1}}$). **A:** CA at $-0.5\,\mathrm{V}$ vs Ag/AgCl, **B:** GC results with injection at $120\,\mathrm{min}$.

The GC results of the headspace during the CA (at t = $120\,\mathrm{min}$) are shown in 5.5B, all films show a clear hydrogen peak though there is a trace presence of air. The chromatograms reveal a similar finding to the CA where the film with 0 min exposure shows the lowest H_2 signal though the difference between the rough films (1–4 min) are not as noticeable. Nevertheless, analysis of the CA and GC results show that increasing roughness by the formation of crystallites is a viable technique for improving catalytic response.

The next part of the studies involved the quantification of the film's roughness and this was undertaken using profilometry with a Dektak 150 Profilometer. The calculated values of roughness are given in Table 5.1 though the values vary depending on the formulation used. In brief R_a (Eq 5.1, where $Z(x)$ describes the height profile) gives the arithmetic average deviation from the mean and is a common parameter to quantify roughness; however it does have drawbacks and tends to under-represent large peaks in an otherwise smooth surface. R_q is a better parameter to account for these occasional spikes and represents the root-mean-square average of the film, its formulation is described in Eq 5.2. The last measurement used to calculate roughness was R_p which is simply the maximum peak height (Eq 5.3).

$$R_a = \frac{1}{L}\int_0^L |Z(x)|\,dx \tag{5.1}$$

$$R_q = \left[\frac{1}{L}\int_0^L Z(x)^2\,dx\right]^{\frac{1}{2}} \tag{5.2}$$

$$R_p = \max Z(x) \tag{5.3}$$

Table 5.1: Calculated roughness parameters from profilometry

Sample	R_a (µm)	R_q (µm)	R_p (µm)
0 min	0.31	0.39	0.87
1 min	0.35	0.48	1.85
2 min	0.16	0.34	1.68
4 min	0.59	0.99	4.07

The calculated roughness parameters confirm the expected trends with longer exposure times leading to increased roughness. One exception is the 2 min sample though this depends on the roughness parameter used. A clearer idea of each profile can be observed in Figure 5.6 and helps explain the major discrepancies. The 0 min film has significant texture – not surprising considering the rapid rate at which crystallites form with $FeCl_3$ – thus explaining its high R_a value. The rough films also have small amounts of texture but they are interspersed with large plateau features that correspond to polymerisation around a crystallite. As a result, R_q and R_p values are more appropriate parameters for the rough films as they can better account for fewer but larger surface features.
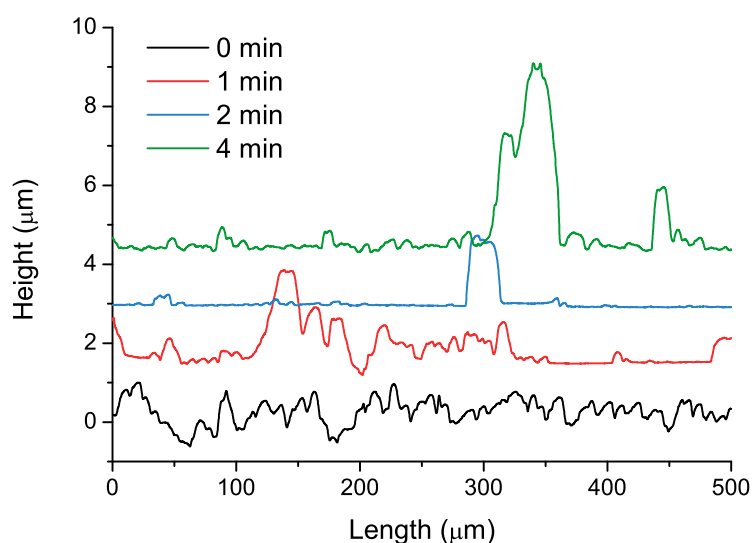
Figure 5.6: The profilograph of the films as prepared using $FeCl_3$ with varying exposure times to air. The traces have been offset from each other for easier comparison.

A longer length-scale and multiple profilographs would have been preferable for a better average roughness and the determination of a standard deviation. Unfortunately, at the time, the profilometer was chiefly used for the measurement of film thickness and only a single profilogram was saved. Furthermore, the films were destroyed shortly after SEM for the preparation of new films as the glassy carbon substrate was in limited supply, and no further data could be gathered.

SEM was the last experiment performed on the films and presents a much clearer picture of the film morphology (Figure 5.7). At a magnification of $100\times$ (1st column) the 0 min sample shows a relatively featureless film whilst the air exposed films show much more distinct features. This is particularly obvious in the 1 and 2 min films where numerous disk like features have formed and accounts for the large plateau regions observed in their profilogram (Figure 5.6). On the 4 min sample, more dendritic like features are observed and can explain the lower recorded catalytic response (from CA, Figure 5.5A). Although the dendrites increase surface area, it would be more difficult to conduct charge to and away from the dendrite tips, thus rendering them inactive in the catalytic reaction. On the other hand, the plate like structures of the 1 and 2 min samples form a much more coherent structure which would likely aid in charge transport.
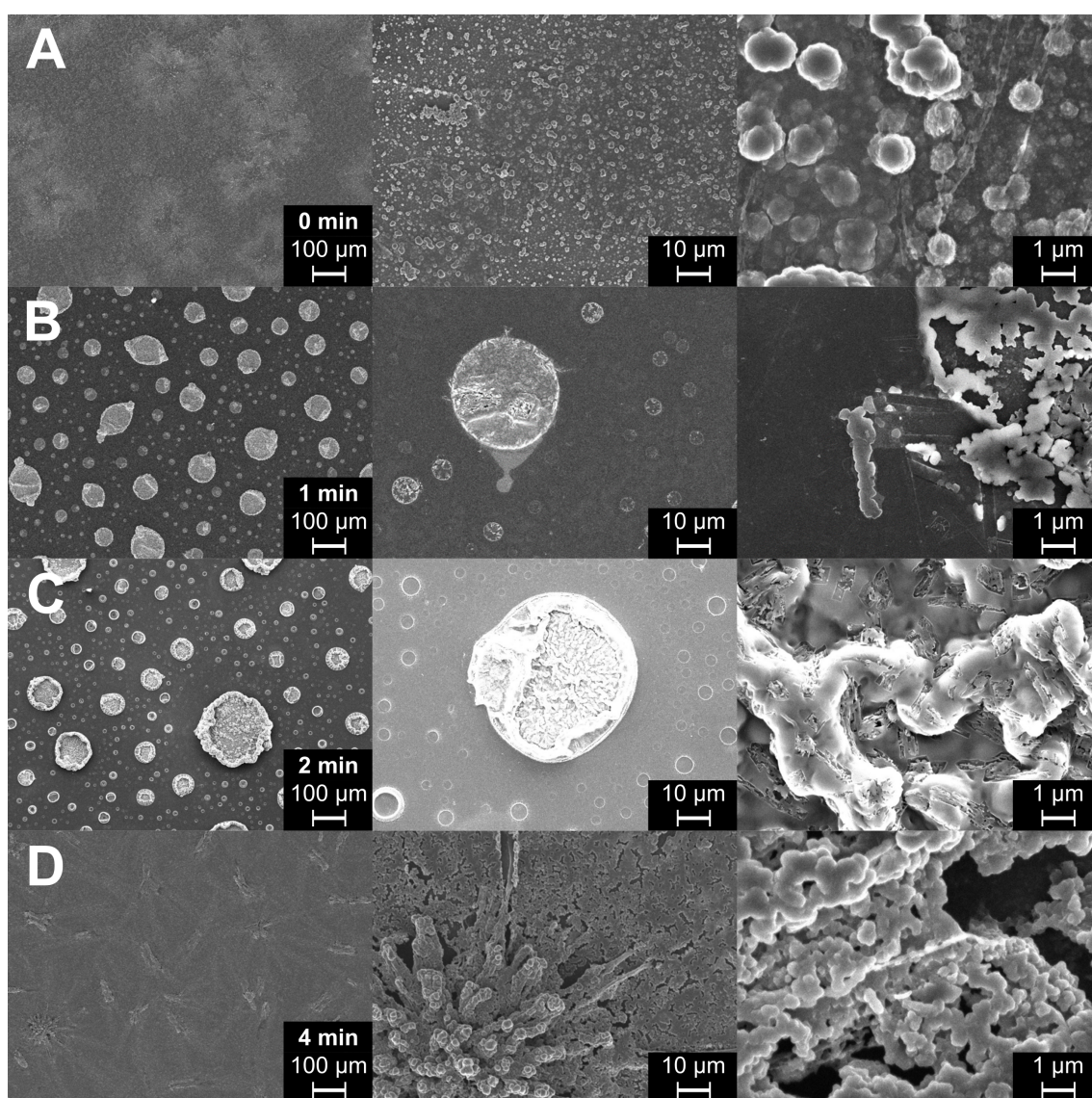
Figure 5.7: SEM micrographs (5 kV) of the $FeCl_3$ prepared PBTh films investigating their morphology at $100\times$, $1000\times$ and $10000\times$ in the 1st, 2nd and 3rd column respectively. **A:** 0 min film, **B:** 1 min film, **C:** 2 min film and **D:** 4 min film.

The 10000× magnification (3rd column) provides a more in-depth view of the films' microstructure. Small particles can be observed on the 0 min sample and explains the film's textured profilograph, however overall, the film is fairly flat and homogeneous. The surface roughness grows noticeably as the exposure time is increased, beginning from flat and slightly dendritic textured disks at 1 min, to much larger and more textured structures at 2 min. At 4 min, significant voids can be observed on the sample and suggests at a porous structure.

These SEM results confirm the formation of rougher surfaces with longer air exposure times though the actual microstructure varies substantially between each sample. It is unknown whether this is an effect of the polymerisation on different days or the natural progression of surface morphology with increasing exposure to air. Further testing in more controlled environments and with smaller time intervals would be required.

5.5   Conclusion

The analysis of various experimental parameters of PBTh revealed important information on the photosystem as well as many surprising capabilities. The high faradaic efficiency and long term stability rule out alternative reduction reactions with significant scope for further improvements and even commercial development. Continuous operation over a 12 day period with good chemical stability is rare and even more noteworthy given that it was arbitrarily stopped. At the same time, the successful operation of PBTh on low-cost substrates like FTO glass help support the case for potential commercialisation.

The low currents observed with the PBTh system is a particular concern and is perhaps the biggest short-coming of this system. Typically, a photo-response on the order of 10–100 $\mu A\,cm^{-2}$ is observed for the PBTh films, compared to the $mA\,cm^{-2}$ range commonly reported in other HER systems. However, it has been discovered from the studies on film thickness and roughness, that small alterations in the film's structure can lead to significantly higher photo-responses (up to 200 $\mu A\,cm^{-2}$). Future investigations with film optimisation in a more controlled synthesis environment would no doubt lead to further improvements.

Lastly, the studies on pH and electrolyte were able to reveal important details on the nature of the reduction mechanism. Successful photo-electrocatalysis of the HER at a pH of 11 shows that the photo-system is not reliant on H$^+$ as a reactant and can reduce H$_2$O directly. This is further supported by the operation of the photo-system in NaCl solutions, whereby the absence of phosphate ions forces the film to obtain the proton directly from H$_2$O (for the HER).

Taken together, these studies present a very compelling case for the use of PBTh as a HER catalyst. However, up to this point, the operational mechanism of the film is still very much unknown. With this in mind, we focus our attention to understanding how this unique photo-electrocatalytic system works.

Bibliography

[1] A. Wexler and S. Hasegawa. "Relative humidity-temperature relationships of some saturated salt solutions in the temperature range 0 to 50C". *J. Res. Natl. Bur. Stand. (1934).*, 1954. **53**, 1, 19–26.

[2] D. de Leeuw, P. Kraakman, P. Bongaerts, C. Mutsaers and D. Klaassen. "Electroplating of conductive polymers for the metallization of insulators". *Synth. Met.*, 1994. **66**, 3, 263–273.

[3] J. Kim, E. Kim, Y. Won, H. Lee and K. Suh. "The preparation and characteristics of conductive poly(3,4-ethylenedioxythiophene) thin film by vapor-phase polymerization". *Synth. Met.*, 2003. **139**, 2, 485–489.

[4] B. Winther-Jensen, J. Chen, K. West and G. Wallace. "Vapor phase polymerization of pyrrole and thiophene using iron(III) sulfonates as oxidizing agents". *Macromolecules*, 2004. **37**, 16, 5930–5935.

Chapter 6

Investigations Into the Mechanism for the Photo-electrochemical Catalysis Process on Polybithiophene

6.1   Introduction

The realisation of an organic photo-electrocatalyst for the HER that is stable, operable at high pH and able to achieve an onset that is below E^0 is a landmark breakthrough.[1] Despite the relatively low initial reaction rate, there has been significant improvements of over an order of magnitude by the simple variation in thickness and surface morphology. Further improvements could no doubt be gained through the exploration of aspects such as substrate morphology, hydrophobicity and addition of light harvesters *etc.* Nonetheless, in this last chapter we eschew the logical continuation of increasing catalytic performance to tackle a more fundamentally important question: how does this unique catalyst work? The work detailed herein is our attempt to reveal the operating mechanisms of the PBTh catalyst and in doing so, we try to explore details which may aid in the further development of PBTh; and potentially, a family of PBTh-like catalysts.

6.2   Results and Discussion

6.2.1   Iron dependency

A key concern that needed to be addressed was the issue of residual Fe^{2+}/Fe^{3+} oxidant after the ethanol wash step. It has been recognised that trace amounts of metal calatyst particles have been able to bring about a significant catalytic response despite being in the concentrations of ppm.[2] Thus it became critical to determine whether our photo-electrocatalytic activity was an inherent property of PBTh or if it was a result of trace Fe particles (or a combination of the two).

For the investigation, four films of PBTh were washed in different solutions after polymerisation with the aim to discern differences in performance according to the effectiveness of Fe^{3+} removal. The initial wash solutions were: H_2O, Ethanol, $0.1\,mol\,L^{-1}$ PTSa in H_2O (pH $= 0.9$) and $0.1\,mol\,L^{-1}$ PTSa in Ethanol. It was assumed that the hydrophobic nature of PBTh[3] would reduce the penetration of aqueous media, thus ethanol would be more effective at removing Fe species than H_2O. At the same time, Fe^{2+}/Fe^{3+} species are more soluble in acidic media,[4] hence the acidic $0.1\,mol\,L^{-1}$ PTSa solutions should remove more Fe than their neutral counterparts.

After the initial wash, each film was tested via CA (at $-0.8\,V$ vs Ag/AgCl) in $0.1\,mol\,L^{-1}$ PB (pH 7) to compare their photo-electrocatalytic performance (Figure 6.1A). A cursory analysis of this result shows significantly higher photo-currents from the acidic wash solutions, however a proper quantification of the Fe in the films was required. To this end, the four films were then washed in $0.1\,mol\,L^{-1}$ PTSa in H_2O after CA testing, and the resulting wash solution collected. Peroxide was added to each film's wash solution to convert Fe^{2+} to Fe^{3+}, followed by KSCN to form the $FeSCN^{2-}$ complex. The Fe^{3+} content of each of the four wash solutions was then

determined by analysing the UV-Vis absorption peak of the resulting $FeSCN^{2-}$ ion at 460 nm. This analysis is referred to as the "initial wash"; please refer to the supplementary information at the end of this chapter for additional details.

The calculated Fe^{3+} concentration from each sample (of the initial wash) is presented in Figure 6.1A as the • markers and show an inverse relationship between the amount of residual iron and catalytic performance (photocurrent). This supports our case that iron does not play a role in the catalysis process and in fact, it seems that having more residual iron in the system is detrimental to catalytic performance.
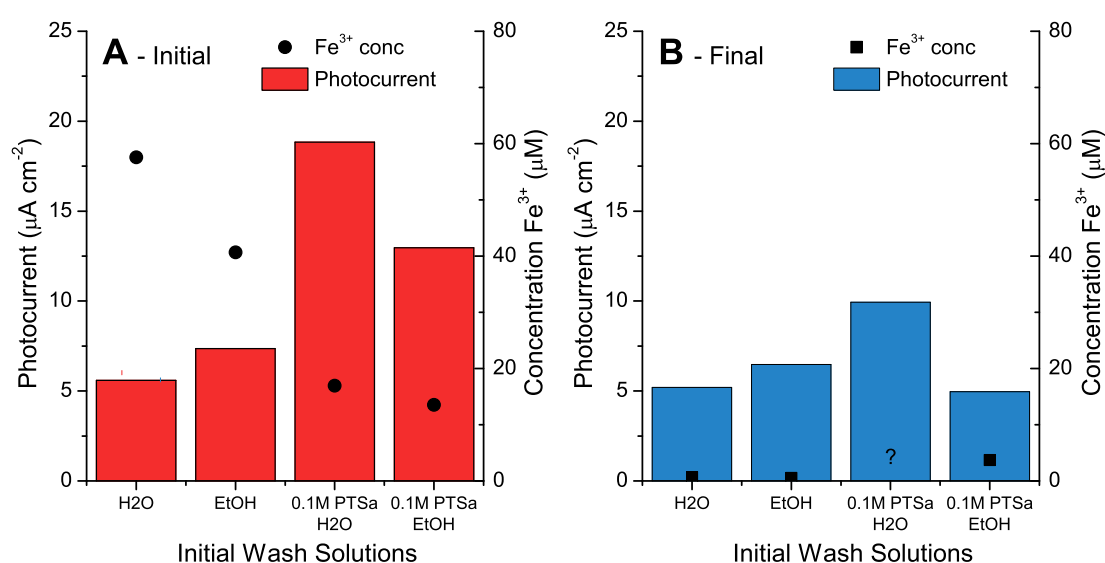
Figure 6.1: Comparison of the photocurrent obtained via CA at -0.8 V vs Ag/AgCl **A:** after the initial wash, and **B:** after the 6 acid washes to remove Fe^{3+}. The detected Fe^{3+} concentration in the wash solution (0.1 mol L^{-1} PTSa in H_2O) after each test is also shown (in black). The Fe^{3+} concentration of the 0.1M PTSa H_2O in the final wash was not detectable.

In an attempt to completely remove any traces of Fe, the four films were subjected to a series of washes in 0.1 mol L^{-1} PTSa in H_2O and Ethanol. At each step, the wash solution for each film was collected and analysed for their iron content which showed a reduction in Fe concentration of up to three orders of magnitude from the initial wash to wash 7, Figure 6.2. Washes 5 and 6 had a higher concentration of Fe^{3+} though this can be explained by the use of ethanol; where the enhanced penetration of ethanol into the bulk film enabled the release of previously trapped Fe species. The final wash back in the aqueous 0.1 mol L^{-1} PTSa solution revealed that the Fe concentration had indeed further decreased.

After wash 6, the films were tested again for their photo-electrochemical performance and showed photocurrents that were on par with that of the initial tests, despite having significantly lower concentrations of Fe, see Figure 6.1B. There are decreases in catalytic performance for all samples after the six wash steps, however, this is more likely to be caused by delamination of the
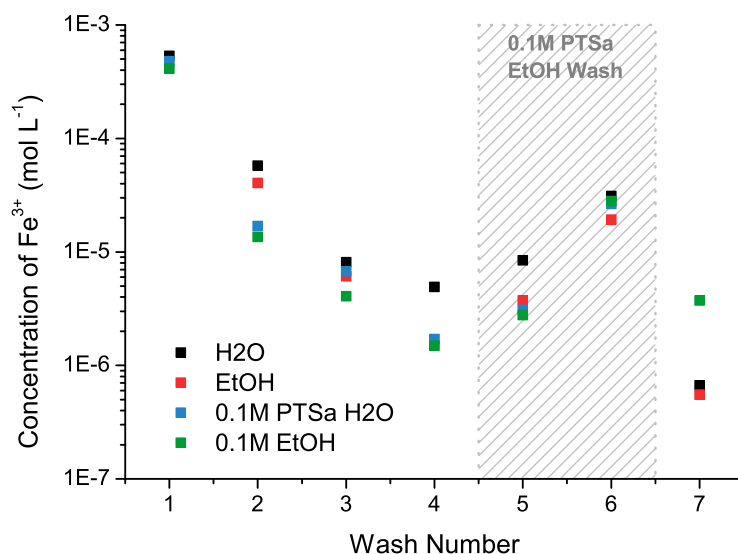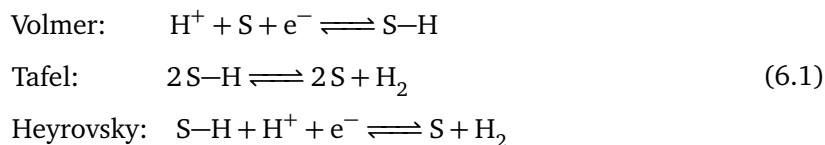
Figure 6.2: The detected concentration of Fe^{3+} from UV-Vis spectroscopy after each successive wash step. Wash 1 utilised the initial varying wash solutions; thereafter, wash 2-4 and wash 7 used 0.1 M PTSa in H_2O and wash 5-6 used 0.1 M PTSa in EtOH. Certain data points were unavailable due to saturation of the UV-Vis detector or difficulty in resolving the $FeSCN_2^-$ peak.

film from the FTO substrate and mechanical damage from the successive swelling and drying processes involved in each wash step rather than from the difference in iron concentration. This is especially apparent when considering the PBTh sample that was initially washed with H_2O. The catalytic performance is almost completely unaffected despite the three order of magnitude decrease in Fe concentration (from $534\,\mu mol\,L^{-1}$ at the initial wash to $0.7\,\mu mol\,L^{-1}$ at the 7th wash). This provides compelling evidence that catalytic behaviour is not dependent on entrapped iron particles and thus, we focus our attention on elucidating a mechanism pathway based on the PBTh film.

6.2.2   Proposed Mechanism

An initial mechanism was proposed based on our knowledge of the system at the time and some preliminary computational modelling. It was understood that at neutral pH, the PBTh film could catalyse the HER but only with the application of light and thus, consideration of excited states became critical. Furthermore the photo-current had been shown to remain stable over extended periods of time which indicates the regeneration of the catalyst site. Assuming that the reaction proceeds via the standard Volmer, Tafel, Heyrovsky type mechanisms for the HER,[5] a protonation of the PBTh chain is required; Eq 6.1 shows the respective mechanisms in acidic conditions where S is the catalyst surface.[6] It should also be noted that since PBTh is able to catalyse the HER in basic conditions, it is foreseeable that the alkaline forms of the

Volmer, Tafel and Heyrovsky reactions are also valid. Nevertheless, for simplicity, Eq 6.1 and protonation in acidic condictions remain the point of consideration.

$$
\begin{aligned}
\text{Volmer:} \quad & H^+ + S + e^- \rightleftharpoons S{-}H \\
\text{Tafel:} \quad & 2\,S{-}H \rightleftharpoons 2\,S + H_2 \\
\text{Heyrovsky:} \quad & S{-}H + H^+ + e^- \rightleftharpoons S + H_2
\end{aligned}
\tag{6.1}
$$

The high electronegativity of the sulphur atom is a likely site for the initial interaction with protons in solution and a potential site for the photo-activated protonation. Moreover, the positive and $\delta-$ charges of the proton and sulphur respectively would result in a close interatomic distance. This would facilitate the rapid catalytic response when illuminated, as opposed to a much more gradual build up of reacting species. This is particularly of note considering that excitation of thiophenes can promote electron density into the sulphur lone pair orbitals,[7] and a likely region in which H^+ would reside. This is supported in our initial DFT modelling using B3LYP/6-31+G* where the LUMO of PBTh – as modelled by a geometrically relaxed 7-membered thiophene oligomer – adopts a quinoidal structure with a significant electron density over the sulphur atom (Figure 6.3B); this is also in agreement with literature HOMO/LUMO calculations on polythiophene.[8] From these results, it is expected that protonation of the PBTh chain would occur on the sulphur atom.

To further investigate the protonation idea via computational modelling, a proton was placed at a distance of $1\,\text{Å}$ from the central sulphur and the structure allowed to relax. The proton stabilised at a distance of $1.36\,\text{Å}$ (Figure 6.3C) without the breakup of the PBTh structure and thus is good agreement with the known stability of the PBTh film. Interestingly, when the LUMO state of this sulphur protonated PBTh (PBTh(S-H)$^+$) is calculated, the electron density becomes concentrated over the introduced proton, see Figure 6.3D. Should free protons be in close proximity, the LUMO (photo-excited) orbital of PBTh(S-H)$^+$ represents a particularly desirable site for a Heyrovsky type release mechanism. It should be noted that this proposed Heyrovsky reaction would require a second photo-excitation as the ground state of PBTh(S-H)$^+$ does not show orbitals that are conducive to interactions with protons (Figure 6.3C). However, the ground state PBTh(S-H)$^+$ may undergo a Tafel type release if there is a photo-excited PBTh(S-H)$^+$ nearby; the large electron density of the photo-excited state may overlap sufficiently to form a chemical bond and release H_2.

Protonation at the α- and β-carbons are alternative protonation sites though the resulting sp^3 carbon would break the conjugated structure (Figure S2). Furthermore this reaction is likely difficult to reverse and does not fit well with PBTh's known long term stability and high turn over numbers (as presented in Publication 3).

Utilising the gathered computation data, the resulting mechanism detailed in Figure 6.4 is proposed. The mechanism is by no means conclusive, especially without further experimental

A - PBTh HOMO
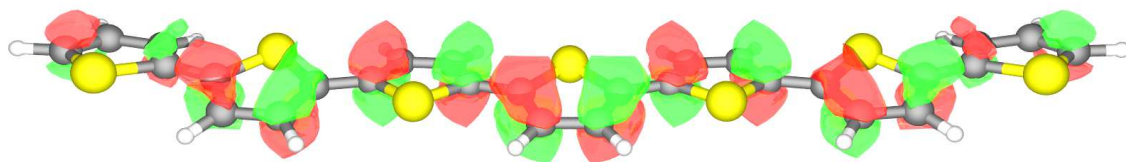
B - PBTh LUMO
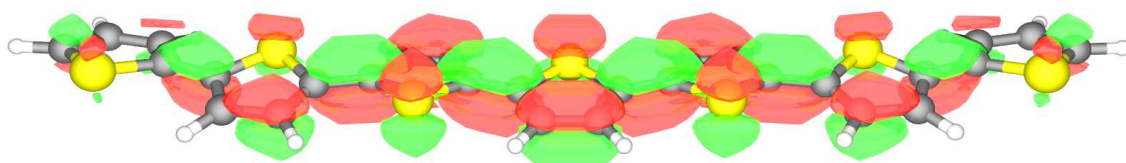
C - PBTh(S-H)$^+$ HOMO
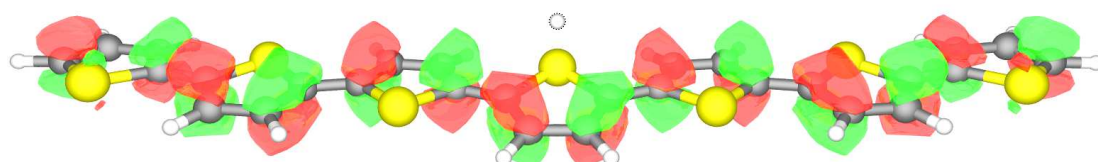
D - PBTh(S-H)$^+$ LUMO
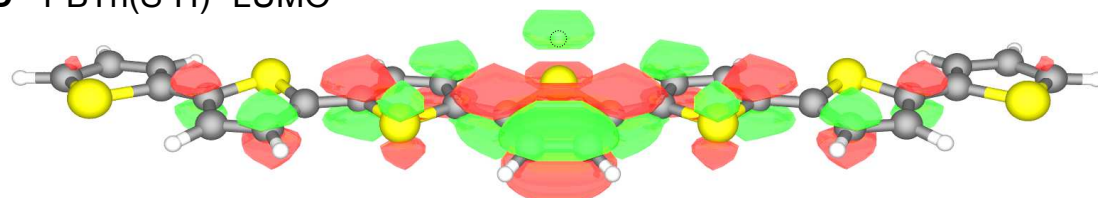
Figure 6.3: The approximated HOMO (ground) and LUMO (photo-excited) molecular orbitals of the PBTh and sulphur protonated PBTh (PBTh(S-H)$^+$) species; as calculated by DFT methods using B3LYP/6-31+G*.

data but it accounts for many of our previously observed behaviours which include rapid photo-responses, high catalyst stability and heavy dependence on photo-excitation. As a result, protonation at the sulphur site forms the template of our experimental mechanistic studies. Alternative mechanisms such as reaction sites at the carbon atoms, or a hybrid mechanism involving different protonation sites are also possible but the DFT calculations of these intermediate species reveal less compelling scenarios, see Figure S2.
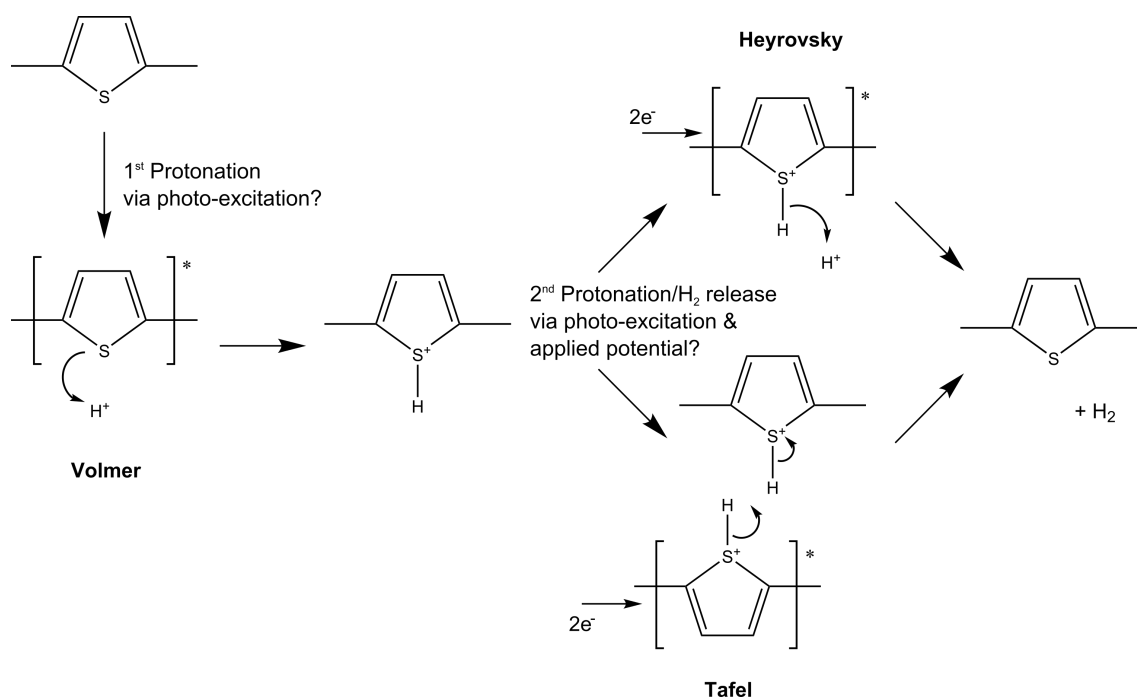
Figure 6.4: Proposed mechanism of the HER on PBTh showing the initial Volmer-like protonation, followed by a Tafel- or Heyrovsky-like mechanism to form and release H_2. It should be mentioned that at this point, these processes are speculative and that roles of photo-excitation/applied potential/electron injection remain highly contested.

6.2.3 Extended Cyclic Voltammetry of PBTh

It was anticipated that in-situ measurements of PBTh in its active would be difficult where the need to apply electrochemical potential and photo-illumination complicates many typical analytical methods. Techniques such as UV-Vis, Raman and transient absorption spectroscopy can reveal changes in conjugation, bond formation and charge lifetimes respectively but they are all adversely affected by external light sources. In recognition of this, an attempt was made to activate the HER catalysis via electrochemical potential alone. Up until now, the majority of the CVs performed on the PBTh film only went to a potential of $-0.8\,\mathrm{V}$ vs Ag/AgCl, an overpotential of approximately $0.15\,\mathrm{V}$ in pH 7 and insufficient to drive the HER in dark. An extended CV of PBTh was thus performed with a potential range up to $-1.8\,\mathrm{V}$ vs Ag/AgCl and is shown in Figure 6.5. The figure shows PBTh's catalytic performance in light and dark, in $0.1\,\mathrm{mol\,L^{-1}}$ PB (pH 7) as well as its self oxidation and reduction reactions in anhydrous propylene carbonate (PC).

As expected, the application of light triggered the photo-electrocatalytic response from PBTh in the aqueous electrolyte, but a strong reduction tail is also observed on PBTh in dark with an onset of $\approx -1.5\,\mathrm{V}$ vs Ag/AgCl. While originally assigned as electrochemically driven HER, comparison with the PBTh CV in PC shows that this reduction reaction overlaps exactly with the n-doping region of PBTh. As a result, we are unable to study the HER reduction on PBTh
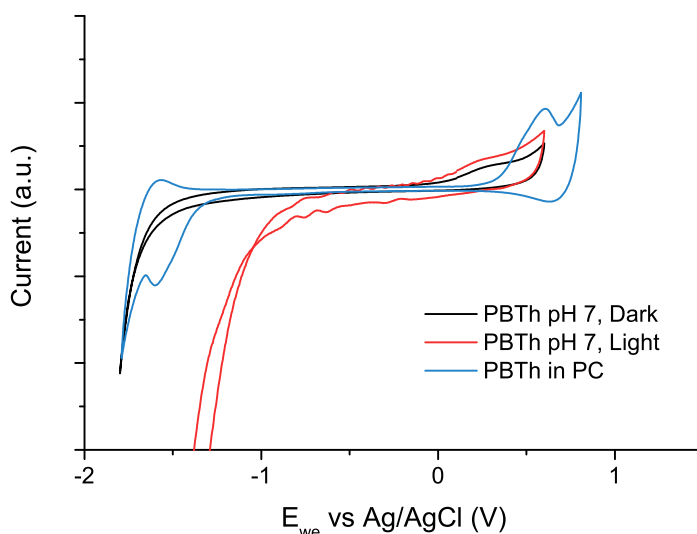
Figure 6.5: An extended CV of the PBTh film showing its electrochemical behaviour in aqueous 0.1 mol L^{-1} PB at pH 7 and in anhydrous PC (0.1 mol/LTBAPF$_6$) whilst under N$_2$; no discernible differences were observed for light and dark in PC. The recorded current is presented in arbitrary units due to the scaling for easier comparison; a per cm^2 correction was not sufficient, likely due to the vastly different interactions of PBTh in PC and in aqueous environments.

in the dark as it becomes severely obscured by the n-doping region of the polymer. This was unfortunate as it meant the continued reliance on external light sources and it ruled out more sensitive spectroscopy methods such as transient absorption and severely complicated other techniques such as UV-Vis and Raman spectroscopy. However, it was hoped that interference from the light source could be minimised with careful cell set-up and appropriate shielding of the detectors.

Regardless, it is clear that the photo-excitation of PBTh creates substantially different thermo-dynamic conditions that allows for the catalysis of the HER. Moreover, the catalytic conditions cannot be easily replicated by the simple application of electrochemical potential.

6.2.4   Photo-dependency

Photo-intensity

Analysis of the photo-response of PBTh is an important early step in establishing a relationship between photons, charge carriers and the catalysis process. In the first study, PBTh's response to light intensity was probed using a Xe lamp with an AM 1.5 spectra filter, the intensity was varied from 0.03 to 2.2 suns using ND filters whilst under an applied potential of -0.5 V vs
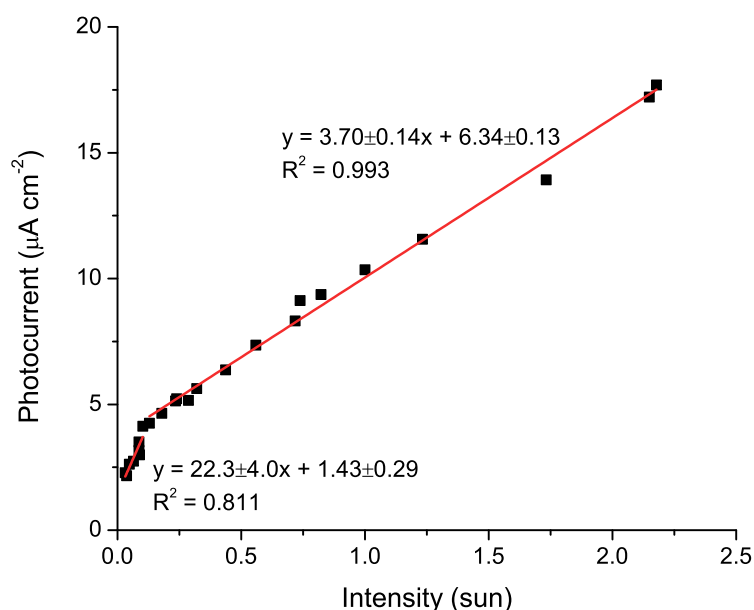
Figure 6.6: Photo-electrochemical current response as photo-intensity of a Xe lamp (with an AM 1.5 spectral filter) is varied, where E_{we} = -0.5 V vs Ag/AgCl in 0.1 M PB, pH 7 under N_2.

Ag/AgCl, further experiment details can be found in section 2.4.6. The photo-current at each intensity was recorded after a 1 min exposure and the results are shown in Figure 6.6.

Two distinct linear regions that transition at $\approx$ 0.1 sun can be observed. The low light intensity region has a much higher gradient and photo-response, perhaps representing the first protonation step (Volmer reaction). At higher intensities, this step becomes saturated as all of the available sites have reacted, thus the second stage – likely Heyrovsky/Tafel reactions – begin to dominate. The lower photo-response gradient indicates that the 2nd reacting step has slower kinetics and is kinetically limiting. This is unsurprising considering that once the first protonation occurs, sulphur's initial electronegativity would be countered by repulsion from introduced $\delta+$ charge of the attached hydrogen. To complete the HER, the active site then requires a further photo-excitation to push electron density into the attached hydrogen (see Figure 6.3D) to form a $\delta-$ charge, thereby attracting nearby protons in solution. Given the relatively short lifetime of excited states, the rate of this reaction would be slow as is reflected in the lower gradient. However, this issue is likely to be mitigated somewhat by the abundance of protons/H_2O in solution as well as mechanisms that promote excited state lifetimes such as the intersystem crossing to triplet states or charge separation.

It is also important to note that from Figure 6.6, there does not appear to be a threshold photo-intensity for catalysis to start; the linear fit of the low intensity mode trends towards unity. This can potentially indicate the generation of hydrogen even from very low light, however,
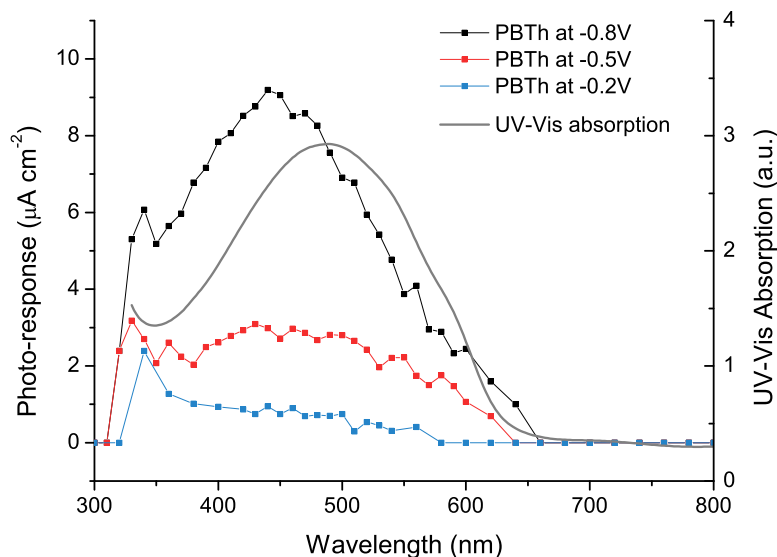
Figure 6.7: Photo-response of PBTh while held at -0.2, -0.5 and -0.8 V vs Ag/AgCl as the wavelength is varied; conducted in 0.1 M PB at pH 7. The UV-Vis absorbance spectrum of PBTh on glass slide is also shown for comparison. The photo-intensity at each wavelength was measured using a Si chip and the photo-response normalised to the respective intensities.

if our earlier analysis holds true, this section mainly corresponds to the first protonation of the PBTh. Further information to be gained from the photo-intensity response shows that the linear regions extends up to 2.2 suns without reaching a plateau. Additional data on higher photo-intensities (and the use of better performing films) would be desirable to truly understand the capabilities of the film. As it stands, the photo limit of PBTh has yet to be observed and is likely to be significantly higher; the use of 10 suns would be interesting to truly test the capabilities of PBTh.

Wavelength Dependence

The wavelength dependence of the PBTh system is another important consideration where true photo-electrocatalysis should have a photo-response that matches closely to its absorption spectrum. A similar experiment had been reported in our earlier paper[1] but it is prudent to further examine the wavelength dependence in detail. A Xe lamp was used as the light source in conjunction with a monochromator to select the individual wavelengths whilst a range of potentials ($-0.2\,\mathrm{V}$, $-0.5\,\mathrm{V}$ and $-0.8\,\mathrm{V}$ vs Ag/AgCl) were applied to the film. The corresponding photo-response was then measured and the results are presented in Figure 6.7 along with the UV-Vis absorbance of PBTh.

At an applied potential of $-0.8\,\mathrm{V}$ vs Ag/AgCl, there is a very good agreement between PBTh's photo-response and its $\pi - \pi^*$ UV-Vis absosorption peak at 490 nm (Figure 6.7). However, at lower reduction potentials – while the catalysis still lies within the $\pi - \pi^*$ absorption region of PBTh – the overall photo-response profile is different and dramatically lowered. The decrease in magnitude is not too surprising given the lower electrochemical driving force and corresponding decrease in reaction kinetics. On the other hand, the change in the shape of the profile was unexpected given that the population of excited states in PBTh is still highest at 490 nm, regardless of the applied potential.

The photo-response profile at $-0.2\,\mathrm{V}$ is particularly different with the requirement of higher energy photons for the same catalysis reaction. This behaviour is revealing in that the catalysis of the HER on PBTh is very much a photo- and electro- dependent process and requires both to generate H_2. The simple absorption of photons by PBTh is not enough for catalysis, it must also be of sufficient energy to drive the catalysis and this required energy is heavily dependent on the applied potential.
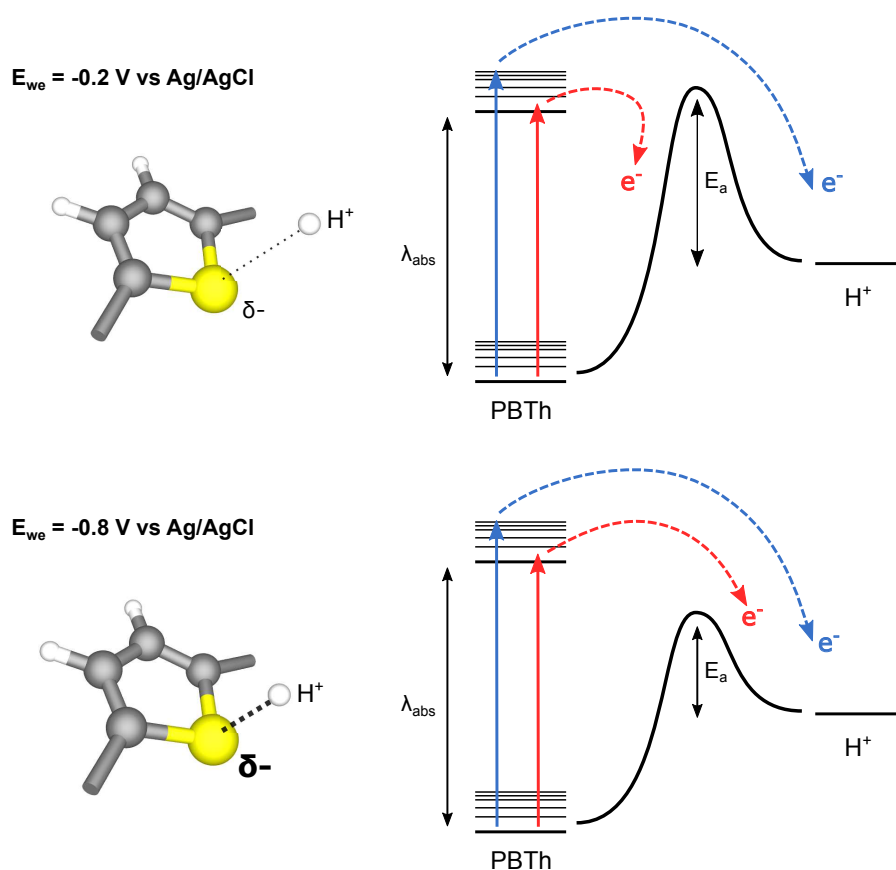
Figure 6.8: Energy diagram showing how an applied potential can alter the sulphur/H$^+$ interaction and the subsequent change in activation energy and wavelength dependence. However, it is not yet sure whether this effects the initial protonation, the charge transfer, the H_2 release or a combination of these stages. The red and blue represents excitation from low energy ($>550\,\mathrm{nm}$) and high energy photons ($<550\,\mathrm{nm}$) respectively.

It is possible that at more positive potentials ($-0.2\,\text{V}$) the low energy photons ($>500\,\text{nm}$) – despite being absorbed by PBTh – do not have sufficient energy to overcome the reaction energy barrier and the generated exciton is unable to proceed with the protonation/charge transfer reaction (Figure 6.8). Higher energy photons are thus required to overcome the weaker S—H interaction by excitation to higher energy vibrational states. Conversely, at $-0.8\,\text{V}$, the strong negative potential enhances the electronegativity of sulphur and creates a much stronger charge interaction with H^+ in solution. As a result, even photo-excitation with low energy photons are able to overcome the energy barrier and initiate the charge transfer process.

This energy model is presented in Figure 6.8 and more clearly demonstrates how the H_2 evolution mechanism is limited thermodynamically; either for the first protonation, or the secondary charge transfer/H_2 release, or both. Hence, it requires a combination of electrochemical potential and photo-energy to overcome the activation energy. A strong negative potential would be beneficial in increasing the population of strong S—H interactions and charge transfer to the point that PBTh's photo-absorption becomes the sole limiting factor. This explains why the photo-response at $-0.8\,\text{V}$ is much improved and why it closely follows the absorption spectra of PBTh. It also accounts for the different photo-response profiles at each potential, something that is not expected for a purely photo-excitation dependent process.

### 6.2.5   Impedance spectroscopy

Electrical impedance spectroscopy (EIS) is a powerful technique with which to study the system's electrical interactions such as those between the film and electrolyte, between the film and electrode and even within the film itself. Given its inherently in-situ nature, we are able to probe how these electrical interactions change as the PBTh film moves from a non-catalytic to catalytic state and the effect of applied potential and light. For more information on EIS and experimental details, please refer to section 2.3.3.

The resulting Bode plot from the EIS is shown in Figure 6.9 where several observations can be made. Looking at the $\log|Z|\,vs\,\log(\text{freq})$ plot (Figure 6.9A), there is a dominant Warburg diffusion type behaviour $<10^1\,\text{Hz}$ – as shown by the $-\frac{1}{2}$ gradient – and is particularly noticeable at oxidative potentials ($0.6\,\text{V}$). However, at more negative potentials, this Warburg diffusion behaviour changes and a distinct difference appears between the light and dark impedance plots. In dark, the straight Warburg like behaviour is still observed (particularly below $1\,\text{Hz}$), but when under illumination, the Warburg tail flattens out to a more resistor like behaviour.

This trend is particularly evident in the Bode phase plot (Figure 6.9B) where the phase changes in light and in dark (at -0.4 and $-0.8\,\text{V}$) is particularly noticeable. This is in agreement with the expected photo-catalytic behaviour, in the dark, the HER reaction cannot occur and the Bode plots show a more diffusion/capacitance behaviour; where ϕ approaches $90°$. On the other hand, under illumination, charge is able to flow from the film to perform the HER, thus a

more resistor like behaviour is observed. Since the kinetics of the chemical HER reaction is slow – as compared to the fast electron transport within the film – these changes occur in the low frequency region (<10 Hz).

The Bode phase plot also shows a significant phase shift which suggests the presence of a capacitance like behaviour around 10^5, 10^3 Hz and 10^1 Hz. while the former two is in agreement with the $|Z|$ results, the latter is in direct contradiction to the previously assigned Warburg behaviour. Herein lies an issue with the Bode plot, where the complexity of the system and the overlap of multiple components can create difficulties in ascribing elements and producing meaningful models. As a result, the Nyquist plot is also analysed for a fuller picture of the appropriate equivalent circuit.
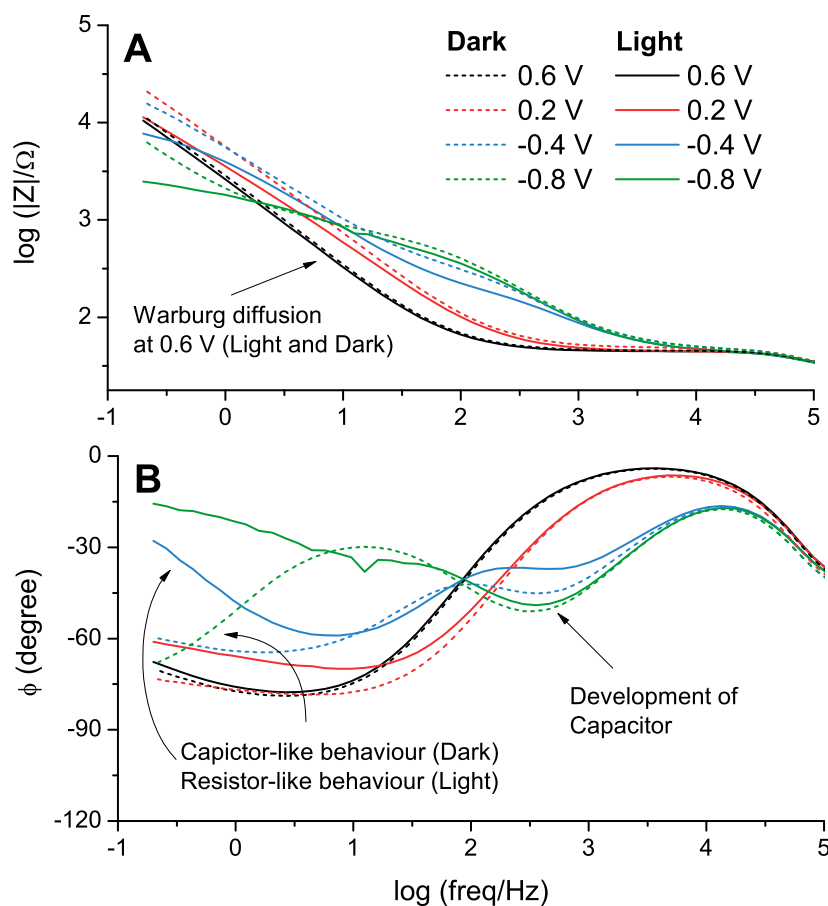
Figure 6.9: The Bode plot of the PBTh photo-system at various potentials in light (solid lines) and in dark (dashed lines). **A:** The $\log|Z|$ vs log(freq) plot and **B:** the phase shift (ϕ) vs log(freq) plot. These graphs are plotted on separate axes for better clarity.

The obtained Nyquist plots of the impedance spectra are shown in Figure 6.10 where they correspond to in-situ studies of changes in potential under dark and light conditions. A cursory observation of Figure 6.10 shows a decrease in resistance and a change in capacitative behaviour as the film shifts from a non-catalytic state (dark and/or oxidative potentials) to a catalytic state.

As conditions become favourable for the HER, the straight Warburg like diffusion behaviour observed at 0.6 V gives way to a more semi-circular shape which suggests a parallel RC element and the presence of an electrochemical reaction. This transition is only observed for illuminated samples, for the dark traces, despite a high negative potential of -0.8 V, the straight lines of the impedance spectra shows that it is still governed by a diffusion/capacitance type behaviour.
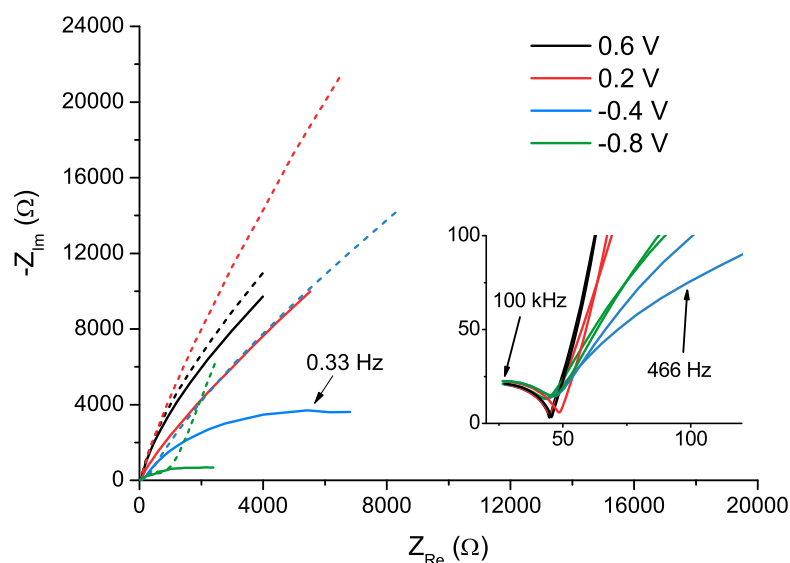
Figure 6.10: The Nyquist plot of PBTh from 100 kHz to 200 mHz at various applied voltages (vs Ag/AgCl) in 0.1 M PB at pH 7, when illuminated (solid lines) and when in dark (dotted lines); the insert shows a close up of the film's behaviour at higher frequencies.

From these observations and previous literature, an equivalent circuit was ascribed to the PBTh system. A well fitting equivalent circuit can lead to many insights into the electrochemical system while a poorly fitted or badly assigned model reveals very little. Initial models were based on literature polythiophene equivalent circuits but they yielded mixed results.[9–11] A significant source of deviation is likely to have come from the non-aqueous nature of the literature studies[10,12] and their analysis of purely oxidative behaviour.[9] As a result, the literature models could typically fit non-catalytic behaviour well but as the film approached reductive potentials and light was applied, large deviations would appear.

An effort was thus made to develop an alternative equivalent model with a higher emphasis placed on matching the equivalent circuit model to our obtained data. Using a Randles circuit (Figure 2.8) as the basis for the HER electrochemical reaction, two capacitor/resistor elements in parallel were added to describe the charge transfer behaviour through the PBTh film and between the electrode and PBTh. This model was also based on the Bode/Nyquist plots that suggest the presence of at least 3 capacitative elements via either a phase shift or the presence of semi-circles.

Initial fittings did not yield an acceptable χ^2 value, particularly in the transition from non-catalytic to catalytic behaviour and was attributed to the inflexibility of components such as capacitors and Warburg diffusion elements. While these descriptors are good analogues for set processes, they are unable to accurately account for the substantial changes in electrical behaviour when moving between catalytic and non-catalytic states. For example, in a non-catalytic state, PBTh behaves like a capacitor with a build up of double layer charges, however in a catalytic state, PBTh much more resembles a resistor where R is governed by the charge transfer resistance. A constant phase element (CPE) is much more suited to this change in electrical behaviour and is described by the equation:

$$Z_{CPE}(\omega) = \frac{1}{Q}(j\omega)^{-a} \tag{6.2}$$

Where $j = \sqrt{-1}$, $0 < a < 1$ and Q is a constant with the dimensions of $F \cdot s^{a-1}$. The varying exponent "a" can describe a spectrum of different behaviours from a pure capacitor ($a = 1$) to a pure resistor ($a = 0$) to a Warburg diffusion ($a = 0.5$)[13, 14] and the states in-between. The flexibility of a CPE helps to account for imperfections commonly observed with uneven, porous or inhomogeneous films. In this particular case, the use of the flexible CPE allows for a much better modelling of the film as it changes catalytic behaviour. CPEs were thus used for elements that were expected to change significantly when alternating between catalytic and non-catalytic behaviour. The resulting equivalent circuit is presented in Figure 6.11.
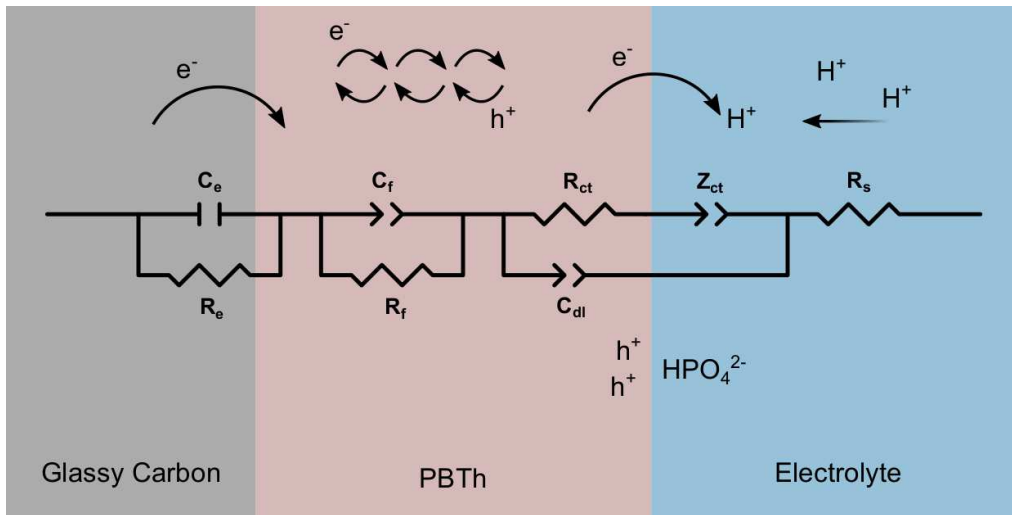
Figure 6.11: Equivalent circuit diagram and the approximate electrochemical interactions corresponding to each element. Where: C_e and R_e are the capacitor and resistor elements for the transfer of electrons from the glassy carbon electrode to the PBTh film, C_f and R_f corresponds to the film's internal capacitance and resistance respectively, C_{dl} is the film's double layer capacitance at the film/electrolyte interface, R_{ct} is the HER charge transfer resistance, R_s is the solvent resistance and Z_{ct} is a CPE that describes the charge transfer interactions from PBTh to the electrolyte; C_f and C_{dl} are also modelled by CPEs

The equivalent circuit presented in Figure 6.11 was used to fit the EIS data and modelled the transitions well with an average χ^2 value of 0.015. A smaller χ^2 could have been obtained by further expansion of the model with more electrical elements, but we have been unable to satisfactorily assign the role of these additional components to real-world electrical interactions. Without this information, the addition of extraneous elements was deemed to be inappropriate despite its ability to provide a better fit. Moreover, given the non-steady state, electrochemical environment of the PBTh system where swelling, diffusion, substitution of counter-ions and evolution of H_2 gas was constantly occurring, it is unsurprising that an impedance model with an extremely low χ^2 values is difficult to achieve.

The only capacitor used in our model was incorporated in the electrode to PBTh film transference as C_e and can be viewed as the build up of charge between the glassy carbon electrode and the PBTh film. Its parallel element, R_e represents the resistance of charge transfer from glassy carbon to PBTh. As expected from the highly conductive glassy carbon substrate, both C_e and R_e remain small and constant throughout the EIS at $\approx 14\,\mathrm{nF\,cm^{-2}}$ and $\approx 100\,\Omega\,\mathrm{cm^2}$ respectively. Similarly, due to high ionic conductivity, the resistance from the $0.1\,\mathrm{mol\,L^{-1}}$ PB solution (R_s) remains small, varying from $0\text{-}4\,\Omega$ throughout the in-situ EIS experiments.

The parallel RC element corresponding to the PBTh film shows a more significant variation with potential. From Figure 6.12A, a gradual increase in film resistance (R_f) is observed as PBTh moves from a doped (oxidised) region towards an undoped state. This behaviour is expected in a p-type semi-conductor such as PBTh but it is interesting to note that the resistance continues to increase even after PBTh has been fully dedoped (at $\approx 0.2\,\mathrm{V}$ vs Ag/AgCl). The underlying mechanism has not yet been identified though this could be due to a fitting artefact from the equivalent circuit. The overall resistance of the film is also lower with applied light. This drop in resistivity has been previously observed[15] and is likely due to the formation of polarons (formed from the HER) which are able to conduct charge.
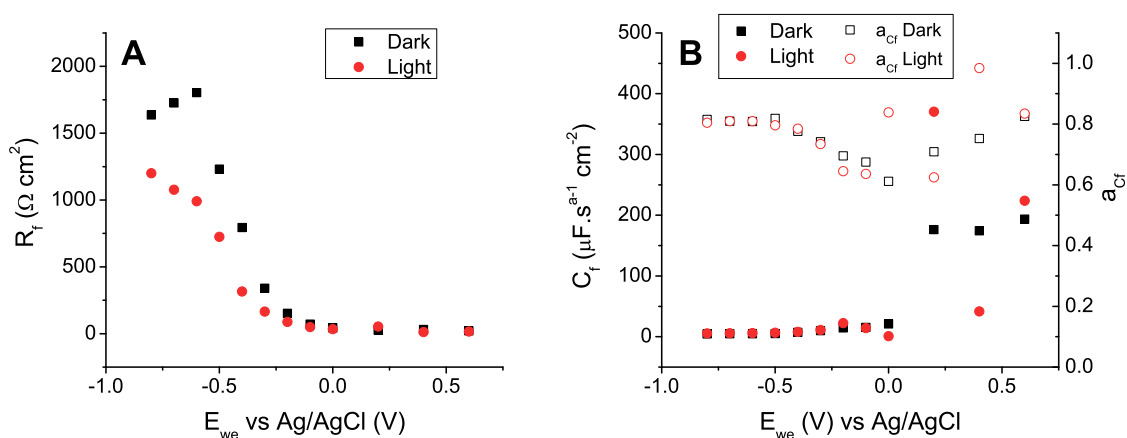
Figure 6.12: Fitted parameters of the film elements **A:** R_f and **B:** C_f from impedance measurements as it varies with potential.

The film capacitance (C_f) was modelled by a CPE and shows for the most part, a trend towards a capacitive behaviour with a ≈ 0.8 which is indicative of a porous/non-uniform film (Figure 6.12B). There is a significant change below 0.2 V vs Ag/AgCl where the capacitance drops from 200 nF cm^{-2} to ≈ 15 nF cm^{-2} (in dark). A possible cause of this is the loss of doped sites as the PBTh film is reduced to its neutral state; this expels the no longer required counter ions and drops the capacitance by an order of magnitude. This also helps account for the decrease in the "a" exponent where entrapped counter ions within the film require time to diffuse out, thus causing the trend toward a diffusion type process of 0.5 before recovering to its initial position at 0.8 when this process has completed. These trends are much more clearly articulated in the dark impedance fits, the overall trend also holds true whilst under illumination but it is interspersed with substantial outliers.

The elements corresponding to the PBTh/electrolyte junction show the highest amount of change as is expected for the components associated with the catalytically active states. Figure 6.13 highlights the variations of the three key elements, the charge transfer resistance (R_{ct}), the charge transfer behaviour (Z_{ct}) as modelled by a CPE , and the double layer capacitance of the film/electrolyte interface (C_{dl}). R_{ct} can be seen to decrease from ≈ 20 kΩ at -0.1 V to 5 kΩ in dark and 0 kΩ in light (read at -0.3 V vs Ag/AgCl). This trend highlights the decreasing resistance to the reduction reaction as the potential shifts towards higher overpotentials. More importantly, it highlights the drop in charge transfer resistance to almost zero when PBTh is illuminated.

The most significant deviation between light and dark can be observed in Z_{ct}, Figure 6.13B. At potentials more positive than 0.2 V vs Ag/AgCl, both light and dark samples result in similar capacitance values and behaviour where $a_{Zct} = 0.5$ and Z_{ct} describes a Warburg diffusion element. In effect, this describes the diffusion of charged species to/away from the double layer as the doping state of PBTh changes; note that at 0.6 V, a_{Zct} approaches 0 and is likely a reflection of the charge transfer behaviour as the film is oxidized. Below 0 V however, the behaviour of Z_{ct} in the dark trends towards a capacitive interaction and a_{Zct} approaches 1. This is a reflection of the full dedoping of PBTh and the absence of further ionic movement in the double layer.

Conversely, under illumination, a_{Zct} approaches 0 and becomes resistor-like; this happens in two distinct regions. The first region – between 0 to -0.2 V – shows a mix of resistor and diffusion-like behaviour where $a_{Zct} = 0.35$, suggesting that the reacting species is trending towards resistor like charge transfer while also remaining kinetically limited by diffusion. This could be partly due to the higher R_{ct} which only allows charge transfer under specific catalytic conditions such as the close interaction of H$^+$. The second region of a_{Zct} occurs below -0.4 V and shows a very resistor like behaviour ($0.1 < a_{Zct} < 0.2$), effectively removing the diffusional dependency of the charge transfer reaction. The lack of a diffusion element indicates that PBTh no longer require the diffusion of "ideal H$^+$" to its active sites for catalysis and that it is able to utilise the bulk of the surrounding H$^+$ in electrolyte. This phenomenon of how the applied
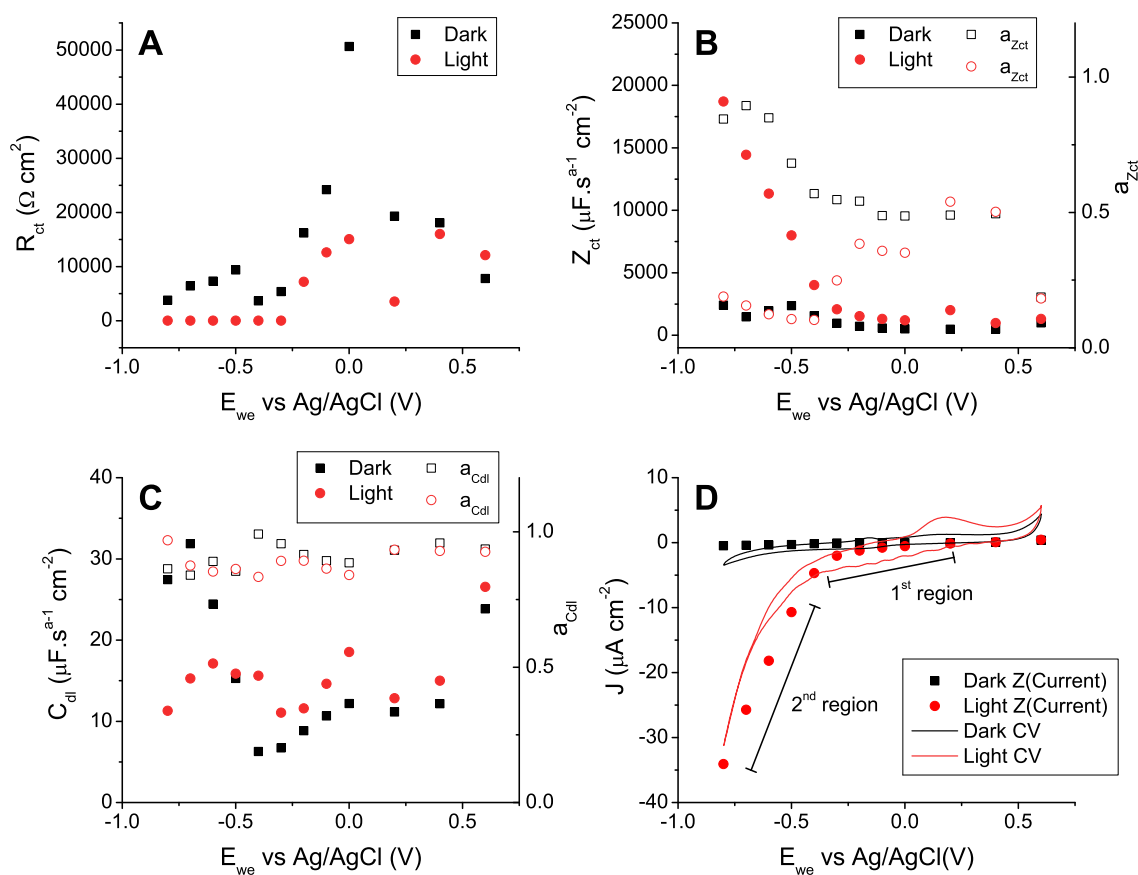
Figure 6.13: Fitted parameters of the PBTh/electrolyte interface as they vary with applied potential in light and dark: **A:** R_{ct}, **B:** Z_{ct} and a_{Zct}, **C:** C_{dl} and a_{Cdl}. **D:** The recorded current at each impedance measurement and the CV trace of a standard PBTh film is also presented.

potential heavily affects the catalytic activity (not just light) is supported by earlier observations from the wavelength dependency tests (Figure 6.8).

At the same time, the capacitance of Z_{ct} increases substantially with light but only at the region where both charge resistance (R_{ct}) and diffusion dependence (a_{Zct}) is low (<-0.3 V) and highlights the presence of a region with distinctly different electrical properties. This behaviour helps explain why the CV of photo-catalytic PBTh shows two distinct regions: an initial reduction with a kinetically (diffusion) limited current at an onset potential of ≈ 0.2 V vs Ag/AgCl, followed by a much more rapidly increasing catalysis region from ≈ -0.3 V as the kinetic limitation is removed (Figure 6.13D).

The element C_{dl} was used to model the double layer capacitance inherently present on PBTh, mainly as a result from surface area. As such, it is unsurprising that it displays mainly capacitive behaviours with $a_{Cdl} \approx 1$, Figure 6.13C. The capacitance values are also representative of the expected trend where slightly higher capacitance was recorded at the extremes of the applied

potential. In dark, this is a reflection of the stronger Stern layer potential at 0.6 V (positive charges) and below −0.5 V (negative charges). Under illumination, the value of C_{dl} is higher at 0.6 V but the capacitance remains steady despite more negative potentials, probably due to the ability for PBTh to lose charge by undergoing the catalysis reaction.

While impedance spectroscopy is unable to directly show the chemical reaction mechanism, much valuable information was gained from the modelled circuit. The key of which includes the identification of a two-stage step in the catalysis reaction that may reflect the traditional Volmer-Heyrovsky/Volmer-Tafel reaction schemes for the HER. The important role of the electrochemical potential in regards to the overall reaction kinetics is also reaffirmed. Furthermore, the electronic elements that were assigned in the photo-system was able to demonstrate good agreement with expected interactions and behaviours.

6.2.6 In-situ UV-Vis Spectroscopy

In-situ UV-Vis spectroscopy was used in an attempt to probe the changes in the electronic band structure which was thought to occur by the protonation of the PBTh chain and the subsequent change of the π-electron conjugation. This idea was supported through time-dependent density function theory (TD-DFT) calculations. TD-DFT is a computational technique that allows for the time-dependent relaxation of excited states and commonly used to determine their energies.[16,17] The CAM-B3LYP/6-31+G* basis set was used due to its increased accuracy at describing charge transfer excitation which are presumed to occur for our photo-electrocatalysis reaction.[18]
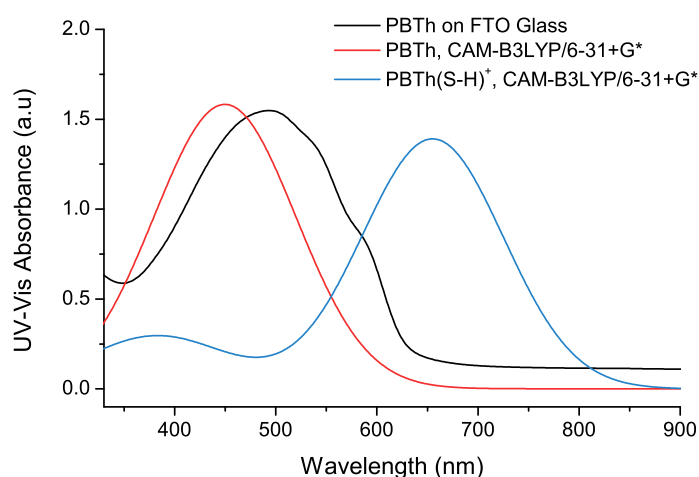
Figure 6.14: The predicted UV-Vis absorbance spectrum of PBTh and the expected PBTh(S-H)$^+$ intermediate as modelled by TD-DFT. The experimental UV-Vis absorption spectrum of PBTh is also presented.

From TD-DFT, it was observed that the protonation of a 7-membered thiophene oligomer to PBTh(S-H)$^+$ led to a substantial change in the overall absorption spectra, see Figure 6.14. Thus it was hoped that by probing the in-situ appearance and disappearance of the predicted PBTh(S-H)$^+$ absorbance peaks (at $\approx 650\,\text{nm}$), insight into the mechanism could be gained. For comparison, the TD-DFT predicted absorbance of a 7-membered thiophene oligomer as well as the experimental absorption spectrum of PBTh are also provided; the good correlation between the spectra provides support that our modelling methods are suitable.

For the in-situ measurements, a standard PBTh film was polymerised onto FTO glass and placed in the metal cell setup. UV-Vis absorption spectroscopy was conducted whilst applying potential in an electrolyte of $0.1\,\text{mol}\,\text{L}^{-1}$ PB, pH 7. The utmost care was taken to shield the detector from stray light but significant background scattering caused saturation of the UV-Vis spectrometer at all but the lower photo-intensities; examples can be seen in Figure S4. A more recognisable spectrum was obtained at the lower intensities of 0.05 and 0.03 sun and is shown in Figure 6.15A. While it avoids the saturation of the detector, there is negligible photo-effect and still considerable noise. The increase in absorbance at 850 nm and 350 nm is likely the result of scattering from the change in diffraction grating and absorption from the FTO substrate respectively. A Logitech R800 green laser pointer 522 nm was also used in an attempt to reduce interference but it was unable to sustain a consistent beam output.
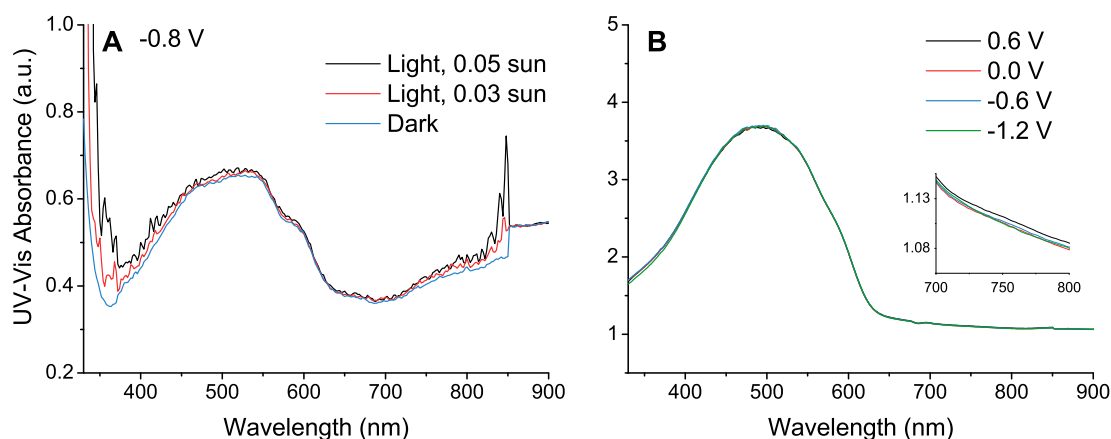
Figure 6.15: A: UV-Vis of the PBTh on FTO glass in dark and light (different intensities) whilst held at $-0.8\,\text{V}$ vs Ag/AgCl. **B:** UV-Vis absorbance spectra of PBTh under various applied potentials in $0.1\,\text{mol}\,\text{L}^{-1}$ PB (pH 7) (no light); the insert shows an enlarged area of the typical polaron region in PBTh.

The absence of the expected PBTh(S-H)$^+$ peak at $\approx 650\,\text{nm}$ suggests that these species are either short-lived, low in population, a combination of the two or are simply not formed. Given the difficulties in the effective photo-activation of the PBTh film however, their absence is not surprising and does not provide conclusive evidence without more reliable measurements.

As a consequence of the difficulties in providing photo-excitation, another attempt was made to use electrochemical potential to substitute the photo-effect, this time conducted in $1 \, \mathrm{mol \, L^{-1}}$ H_2SO_4 at pH = 0. The acid environment is not representative of the typical PBTh systems tested thus far, but it was hoped that the use of acid would induce the electrochemical potential driven HER before n-doping of the PBTh. The CV of PBTh in Figure S5 shows a strong reduction tail beginning $\approx -1 \, \mathrm{V}$ vs Ag/AgCl but this is also present (and much more prominent) on the plain FTO sample. This indicates that while a reduction reaction is occurring, it is inherent to FTO and not attributed to the HER on PBTh.

For completeness, the purely electrochemical driven in-situ UV-Vis spectroscopy was conducted in PB (pH 7) whilst being held at the potentials of 0.6 V, 0 V, −0.6 V and −1.2 V (in dark); Figure 6.15B. It was hoped that at a negative potential of −1.2 V, the HER could occur on the PBTh in dark, however this was not the case. Not surprisingly, there is negligible difference in the $\pi - \pi^*$ absorption peak at each potential, though the absence of light had rendered a much cleaner spectra. There is a slight polaron absorption when held at 0.6 V (see insert, Figure 6.15B), however this is typical for polythiophenes when oxidised[19,20] and does not reflect the changes from a catalysis mechanism.

6.2.7 In-situ Raman Spectroscopy

Following the difficulties in obtaining a relevant absorption spectra from in-situ UV-Vis spectroscopy, a further attempt with in-situ Raman spectroscopy was done to help provide information on the chemical mechanism. It was hoped that the use of this technique would allow the identification of a reaction intermediate and elucidation of the chemical bonds that would form (and break) during the catalysis process. Initial tests were conducted in $0.1 \, \mathrm{mol \, L^{-1}}$ PB at pH 7 with an illumination from a Leica KL 2500 lamp (≈ 0.4 sun). Two Raman systems were utilised for the measurements, the Jobin Yvon T64000 Raman system using a 488 nm diode laser and the Renishaw inVia Raman system using a HeNe laser, 633 nm.

Raman tests on the 488 nm Jobin Yvon system resulted in significant fluoresence above $3000 \, \mathrm{cm^{-1}}$ (Figure 6.16A) and was exacerbated by the appearance of strong OH water peaks when PB was added, Figure 6.16B (red trace). The use of an external lamp also created a noticeable background interference despite our best efforts to minimise it and the use of a baseline subtraction; nonetheless the key peaks of PBTh remain identifiable. Unfortunately, analysis of the spectra at different potentials in Figure 6.16A show very little difference in the position or intensity of the peaks and no change in the expected area for the thiol band (generally between 2540–$2600 \, \mathrm{cm^{-1}}$).[21] The observed peak at $2500 \, \mathrm{cm^{-1}}$ was not easily assigned and literature studies on PBTh do not go above $2000 \, \mathrm{cm^{-1}}$.[22–24] However, given its inertness to illumination, potential and electrolyte, it was assumed to be independent of the photo-electrocatalytic process; possibly an artefact of kinks in the PBTh chains. As a result, the only significant change was the increase in fluorescence (particularly $>2750 \, \mathrm{cm^{-1}}$) as E_{we}
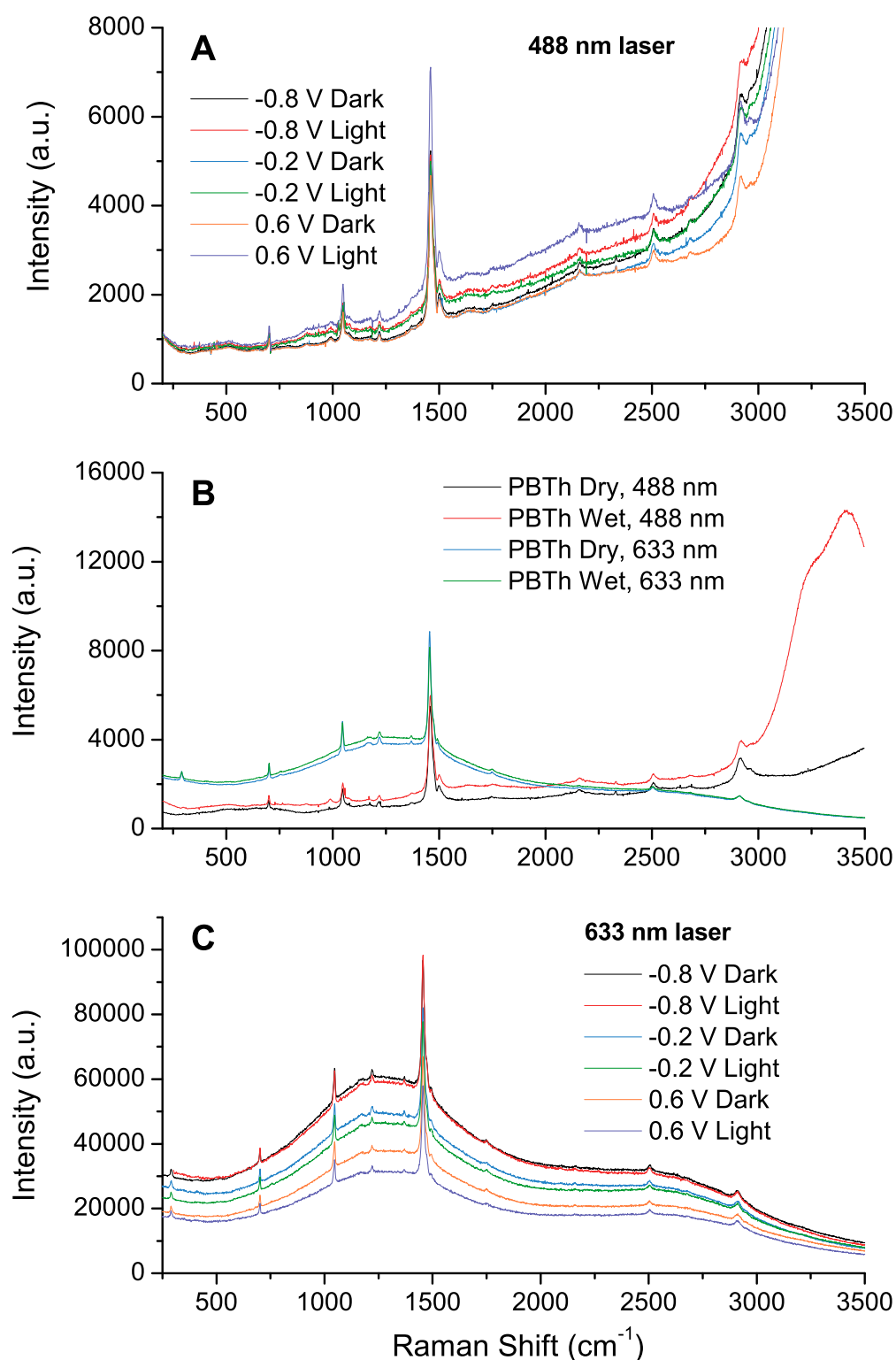
Figure 6.16: A: In-Situ Raman of PBTh in $0.1 \, mol \, L^{-1}$ PB, pH 7 using a 488 nm laser. **B:** Raman of the dry and wet ($0.1 \, mol \, L^{-1}$ PB) comparing the two lasers, with no applied potential. **C:** In-Situ Raman of PBTh using a 633 nm laser in $0.1 \, mol \, L^{-1}$ PB, pH 7.

was moved towards negative potentials. This may be explained by the increased ground state population as PBTh moves from a doped/oxidised state to a neutral/ground state.

There also persisted a major issue with the use of a 488 nm and that was the triggering of the photo-electrocatalysis process from the Raman laser itself. This rendered it impossible to have a truly dark baseline that represented the inactive film; as shown in Figure S6 where the measurement of the "dark" spectra at -0.8 V using the 488 nm laser is enough to trigger a substantial photo-current. In response to this, the Renishaw inVia Raman system with a red HeNe (633 nm) laser was used.

The in-situ Raman spectra obtained using the 633 nm laser shows a much cleaner signal that is absent of the strong OH peak and fluorescence above 2750 cm^{-1}. However a different fluorescence mechanism centred around 1250 cm^{-1} is now present (Figure 6.16C). This fluorescence is present regardless of electrolyte (Figure 6.16B) and is triggered by the red laser while dark and light measurements both show this fluorescence peak. Since the main Raman peaks again show little change, this fluorescence behaviour was analysed to provide some insight into our comparison between the PBTh film in light and dark.

In PBTh's oxidised state at 0.6 V, the use of light lowers the fluorescence intensity which is unexpected as fluorescence intensity is generally directly proportional to incident light intensity. Moreover, the relatively low overall intensity of the emission points to a spin forbidden energy transition such as phosphorescence or excimer fluorescence. It has previously been reported in numerous studies that phosphorescence is weak in several oligothiophenes,[25–28] particularly at ambient temperatures.[29] As a result, the broad peak at 1250 cm^{-1} was assigned to an excimer fluorescence, an effect that has been observed in polythiophenes at room temperature.[29,30] On this assumption, we attempt to ascertain information regarding mechanistic behaviour.

First and foremost, the excimer fluorescence (EF) peak trends toward higher intensities with more negative potential, showing that the formation of excimers is made more facile by negative potentials. This is unsurprising given that excimers can be thought of as short-lived charge transfer states[31] and that electrochemical potentials facilitate charge transfer. The important question to be considered here is the identity of this excimer. As yet, we have been unable to find direct spectroscopic evidence of its formation but given its presence even in the dry Raman spectra (Figure 6.16B, blue trace), it is likely due to a dimerisation of two adjacent PBTh units. This is interesting since a di-PBTh excimer can undergo singlet fission to yield two triplet states[32] which make compelling species for charge transfer due to their significantly longer excited state lifetimes; and of interest to the HER.

We also observe from Figure 6.16C that illumination of the PBTh causes a reduced EF peak, this can be explained if the excimer is a reaction intermediate. Assuming that the excimer is di-PBTh, then failure of this species to proceed with the next step of the HER – for example, singlet fission – results in its degradation and excimer fluorescence. Unfortunately, this explanation does not account for all the observed variations, chief of which include why this EF (representing the

failure of catalysis) grows with higher overpotentials. Another explanation is that application of a broad spectrum light instead of the narrow 633 nm laser causes a significant increase in the population of excited states, thus reducing the number of ground PBTh available for excimer formation and the overall intensity of EF falls. Furthermore, the change in the light source may affect the quantum yields, for example, increasing fluorescence when under broad spectrum illumination at the expense of excimer formation. However, neither of these explanations can fully explain our Raman spectra.

What is known is that as potential moves towards more negative values, the difference between light and dark becomes negligible and the EF intensity equalises. Analysis of this trend (see Figure 6.17) shows that the transition matches closely to that of the onset potential for the HER; where CA shows significant photo-current starting at 0 V while Δintensity of the EF peak at $1250\,\text{cm}^{-1}$ decreases to $\approx 0\%$ at -0.2 V. This close correlation suggests that the formation of excimers is closely related to the photo-catalysis of the HER, possibly by forming desirable excimer structures for the HER, or perhaps the singlet fission of excimers to photo-active triplet states. However without a more in-depth investigation using techniques such as transient absorption spectroscopy, it is difficult to infer further information on the catalysis mechanism from purely the variation in the EF peak.
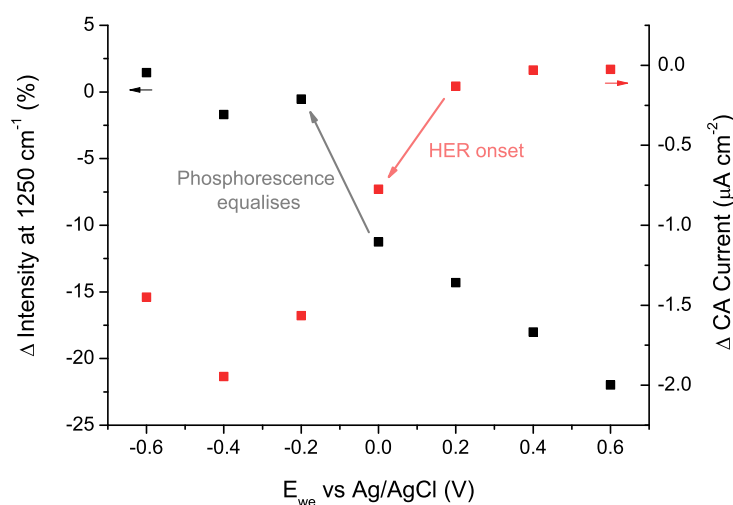
Figure 6.17: Comparison of in-situ Raman on PBTh in light and dark between the change in phosphorescence peak at $1250\,\text{cm}^{-1}$ and the obtained CA currents

Transient spectroscopy was considered but it was feared too difficult to probe a photo-electrochemical process whilst limiting noise to a reasonable level. Past experience from CA shows significant noise throughout the experiment, particularly with the application of light; examples of this can be seen in Figure S6. This noise could be attributed to the heterogeneous, photo-dependent and electrochemical nature of our setup and would become detrimental for sub-microsecond lifetime measurements. Further investigation with transient spectroscopy could be beneficial if

noise was sufficiently reduced, perhaps via film optimisation, increase of electrolyte strength, reducing counter and reference electrode distance *etc.* but due to time constraints, these steps are currently outside the scope of our study.

As an experiment to probe extreme reduction conditions, in-situ Raman was conducted in $1\,mol\,L^{-1}$ H_2SO_4 (pH 0) with the 488 nm laser. Only the applied electrochemical potential and the blue Raman laser was used to activate the reduction reaction in an attempt to limit background noise from external light sources. Two applied potentials were tested, 0.6 V and -1.2 V vs Ag/AgCl, the resulting spectra is shown in Figure 6.18 along with the H_2SO_4, dry PBTh and wet PBTh (E_{oc}) background spectra.
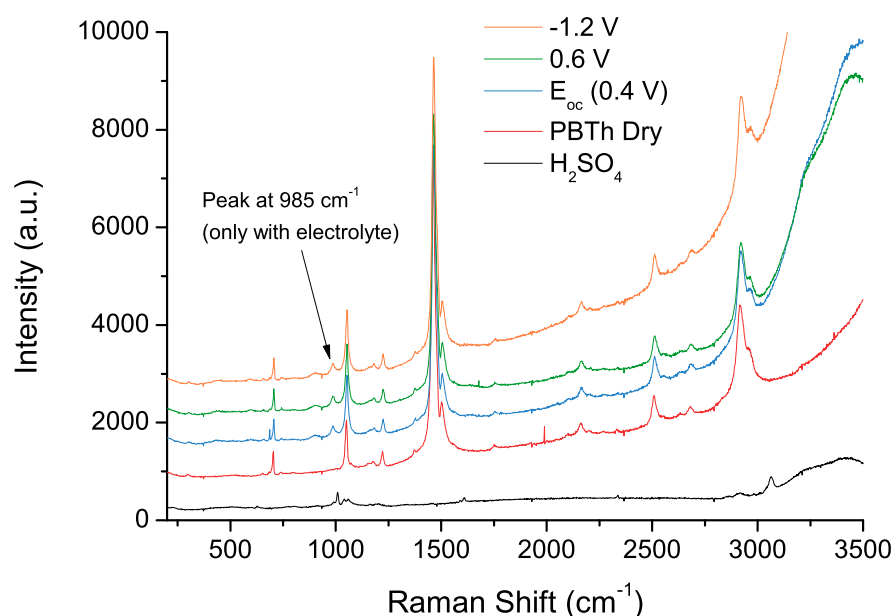
Figure 6.18: Raman of PBTh and tests using $1\,mol\,L^{-1}$ H_2SO_4 (pH 0) with the 488 nm laser (no external lamp). The Raman spectra is given at an applied potential of 0.6 V and -1.2 V; the baseline spectra of H_2SO_4, dry PBTh and wet PBTh at the open circuit potential ($E_{oc} = 0.4$ V) is also given for comparison.

At last, a significant change can be seen in the Raman signal with the evolution of a peak at $985\,cm^{-1}$. However, the difference was not observed between the 0.6 V and -1.2 V spectra as expected, but between the dry PBTh and the wet PBTh spectra (with electrolyte). This is especially surprising given that this peak is present regardless of the applied potential; and even in E_{oc} where *no* potential is applied. Initially, it was thought to be due to H_2SO_4 as its spectra shows weak bands around $1000\,cm^{-1}$ from the S=O interactions (Figure 6.18, black trace).[21] But when earlier spectra of PBTh in PB is analysed, the same phenomenon is observed when the PB electrolyte is added (Figure 6.16B, red trace).

The fact that the evolution of this peak is only brought on with the addition of aqueous electrolyte and photo-illumination (from the 488 nm laser) points to a photo-interaction between the PBTh and H_2O. Further support comes from literature studies which have shown S—H bending modes between 800–1000 cm^{-1},[21,33,34] thus revealing the first experimental indication of an S—H species on PBTh. The conditions under which this S—H band forms is surprising and brings up several readjustments to our model. The most important of which is perhaps the recognition that this S—H species is formed even without an applied potential. This indicates that the first protonation step is entirely photo-driven. Moreover, no current is observed at E_{oc} or at 0.6 V (see Figure S7), thus this first protonation to S—H occurs via the localised oxidation of the PBTh chain by the introduced proton. This would in turn lead to a charged intermediate species (PBTh(S-H)$^+$) and at the same time, suggests that electrochemical potential only plays a role in the second protonation/H_2 release stage.

It is interesting that the S—H peak is not observed with the 633 nm laser even with the external light source. However, this is likely due to the fact that the intensity of the peaks are simply not strong enough to be observed. This is further justified when considering the small size of the S—H peak even with the 488 nm Raman in spite of the strength of the blue laser, its close match to the λ_{max} of PBTh and the direct excitation of the sampling volume. In contrast, the external light source on the 633 nm Raman is placed further away, and faces significant shadowing from the objective lens, thus, the actual intensity of the S—H band would be much smaller. It is slightly harder to reconcile the lack of the S—H whilst still recording significant EF signals. But given the presence of the EF peak in both wet and dry conditions (Figure 6.16B), it is possible that we are observing the EF of the bulk PBTh; needless to say, further studies would be of great benefit.

These issues are also made worse by the hydrophobic nature of PBTh which limit catalytic activity to the thin electrolyte/PBTh interface. This is further exacerbated by the use of a 10× objective lens. The longer focal distance was required to keep the objective above the electrolyte, but the large focal plane meant that a considerable majority of the Raman signal originated from the bulk (inactive) PBTh.

It was unfortunate that identification of this promising band came so late in the candidature as further studies would undoubtedly reveal new details. For example, the use of different laser intensities would reveal photo-dependency effects while the use of different organic solvents could help probe the properties of the S—H band. Also, the use of an external blue laser as a light source could increase the population of the S—H bands so that it can be detected with the 633 nm Raman system; this is particularly important to establish a true dark and light Raman comparison. Finally, a confocal set-up or a higher magnification objective would reduce the inactive/bulk PBTh signal and help isolate the reacting surface species.

In summary, the Raman data shows the evolution of an S—H band at 985 cm^{-1} and the formation of PBTh(S-H)$^+$ when under illumination and in the presence of water. This first protonation

process is entirely photo-driven and does not require the presence of an applied potential. However, the intermediate alone is unable to yield H_2 as shown by the lack of a recorded current. While these observations do not confirm our overall mechanism, they reveal that the PBTh(S-H)$^+$ intermediate state is present and easily triggered under catalytic conditions, thus solidifying a crucial cornerstone of our proposed mechanism.

6.2.8 Density Functional Theory Study of Reaction Mechanics

Despite the success achieved by Raman spectroscopy at revealing the S—H intermediate, computational studies were conducted to help further identify and support important mechanistic processes. This was also done with the goal to identify characteristic signals so that future experimental studies could be more targeted. The initial computational investigation examined the thermodynamics of the system. Typically, the free energy (G) for each reaction intermediate was calculated with the geometrically relaxed zero-point energy and their respective vibrational contribution. These computations were conducted by our collaborators, Sun *et al.* at Monash University with a B3LYP/6-31++G** level of theory. The identification of intermediate states via kinetic studies were not attempted at this point as they are costly and highly variable depending on the assumptions of the system and hence, not suitable without more confident experimental data.

The basic PBTh analogue used was a 7-membered thiophene oligomer since the model had previously shown good accuracy in predicting the photo-absorbance properties in earlier TD-DFT studies (Figure 6.14). To this initial state, protonation was introduced on the central thiophene at the α-carbon (C_α) and sulphur positions, the resulting ΔG for the first protonation step is hence calculated and converted to eV via the relationship:

$$\Delta G = -nFE \tag{6.3}$$

The resulting thermodynamic data show that protonation of the C_α in PBTh (PBTh(C-H)$^+$) is more favourable compared to protonation at the sulphur (PBTh(S-H)$^+$) (Figure 6.19) and is surprising given the Raman data. Nevertheless, if PBTh(C-H)$^+$ is the dominant mode for protonation, the change from an sp^2 bonded carbon site to sp^3 would result in a dramatic shift of the π conjugated structure and an effect that could potentially be isolated for UV-Vis or Raman analysis. Subsequent investigation via vibrational and TD-DFT modelling of the PBTh(S-H)$^+$ species indicate a new C-H vibrational band occurring at 3050 cm^{-1} and a changed UV-Vis absorption peak to 520 nm. Unfortunately, reanalysis of the previous experimental data revealed none of the predicted changes for PBTh(C-H)$^+$ and give support to the S—H protonation pathway observed via Raman spectroscopy. Additionally, the photo-absorption of PBTh (λ_{max} = 480 nm = 2.6 eV) is sufficient to drive protonation at both the C_α and sulphur site.

PBTh

$\Delta G = 2.47$ eV $\Delta G = 0.80$ eV

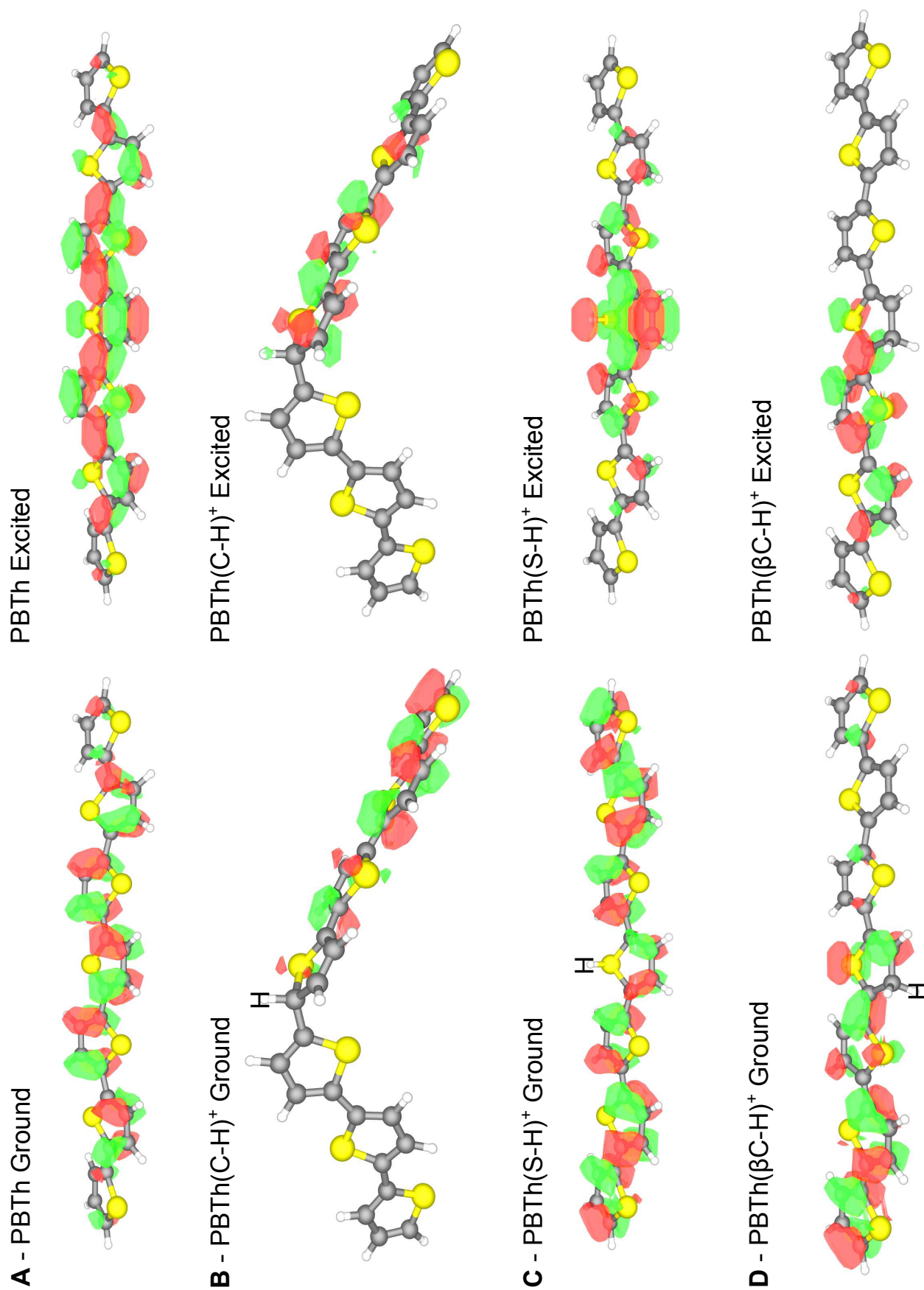**PBTh(S-H)**   **PBTh(C-H)**
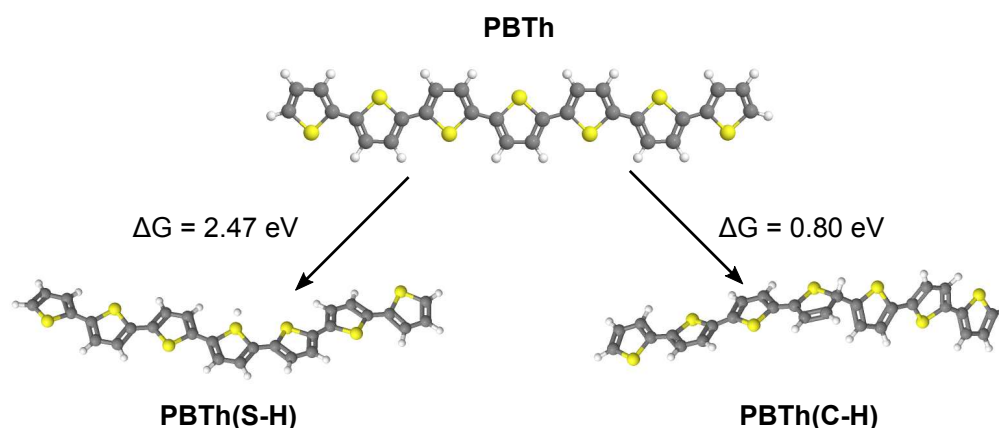
Figure 6.19: The PBTh analogues used for the computational calculations showing the initial sites for the first protonation (at the C_α and S) and the associated ΔG in eV.

Due to time constraints, our collaborators were unable to conduct further studies and we continued independently with our attempts to isolate a likely reaction site. Our computational investigations were directed towards the *qualitative* analysis of the reaction mechanism via the study of ground and excited state molecular orbitals; *not* quantitative studies. For this purpose, the low-cost and well established B3LYP/6-31+G* level of theory was deemed suitable.[8,35–37] That being said, we are aware of its limitations and given more time and expertise, the use of more advanced basis sets and computational techniques would no doubt bring improvements in accuracy for quantitative calculations.[38–40]

The calculation of the ground and excited state orbitals using TD-DFT (B3LYP/6-31+G*) were conducted for PBTh and its various protonated forms; presented in Figure 6.20. The excited PBTh orbitals (Figure 6.20A) show a variety of possible protonation sites with electron density spread across the whole chain, making it difficult to identify an obvious candidate; hence all potential protonation sites were examined. The earlier findings (Figure 6.19) showed PBTh(C-H)$^+$ to possess the lowest ΔG for protonation but when analysing the calculated ground/excited state orbitals of PBTh(C-H)$^+$, it shows minimal electron density on the attached proton (Figure 6.20B). This would make it difficult for PBTh(C-H)$^+$ to proceed to the second reduction reaction and helps explain the absence of experimental data.

Further TD-DFT analysis of the alternate PBTh protonation sites – at the sulphur (PBTh(S-H)$^+$) and the C_β (PBTh(C_β-H)$^+$) – were conducted to find their ground and excited state orbitals, Figure 6.20C, D. The molecular orbitals of PBTh(C_β-H)$^+$ reveal very unfavourable conditions for further reduction to H$_2$. On the other hand, PBTh(S-H)$^+$ is in many ways ideally primed for the evolution of H$_2$, whereby upon photo-excitation, a large portion of the electron density is pushed towards the attached proton, see Figure 6.20C. This would then aid further interaction with adjacent H$^+$/PBTh(S-H)$^+$ chains and facilitate charge transfer to form H$_2$. More importantly, it

Figure 6.20: Molecular orbitals for the most intense ground to excited state transitions in PBTh, PBTh(C-H)$^+$, PBTh(S-H)$^+$ and PBTh(C_β-H)$^+$ as calculated by TD-DFT using CAM-B3LYP/6-31+G*. The introduced proton is labelled "H"

confirms that the formation of PBTh(S-H)$^+$ is favourable to the photo-electrocatalysis of the HER and in agreement with the Raman data.

Protonation at the sulphur atom is further supported by the calculated electrostatic potential (ESP) charges of PBTh in its ground state (S$_0$), see Figure 6.21A. The most significant negative sites are at the sulphur and C_β, and indicate likely sites for interactions with protons in solution. Given the lack of free lone-electron pairs on the C_β, the interaction, photo-induced charge transfer and protonation of PBTh would much more readily occur at the sulphur atom.

Evidence from literature also points to sulphur as a key reaction site and include early studies on polythiophene which suggested at the interaction of O$_2$ or H$_2$O with the sulphur atom through its lone pairs.[41] More recent investigations have shown photo-degradation/oxidation mechanisms on the sulphur atom to sulphur oxides when polythiophenes are exposed to oxygen.[42,43] Finally, there are numerous studies which have revealed a propensity for the HER to occur on sulphur sites and include MoS$_2$[44] and its derivatives (WS$_2$, [Mo$_3$S$_4$]$^{4+}$ *etc.*).[45–47] These past studies, together with our computational data and the observed S−H Raman peak firmly confirm the sulphur atom as the first protonation site in the PBTh system.

Nonetheless, there remains the question of the second protonation/reduction to form H$_2$, be it via a Heyrovsky or Tafel like process. To this end, further computational studies were conducted. From Raman spectroscopy (Figure 6.16C), it was suggested that the formation of excimers is an important consideration for the photo-electrocatalysis of the HER. Regretfully, the direct modelling of excimer formation and their catalytic behaviour is currently outside the range of our computational expertise and resources. However, it was also proposed that the formation of excimers could lead to singlet fission and the creation of triplet states; states which *are* within our skills to model. The triplet state is of particular interest given their long lifetimes (18.7 µs for certain polythiophenes[48]), enabling more flexible reaction kinetics. Furthermore, the creation of triplet pairs on adjacent PBTh chains via singlet fission make for a compelling site for H$_2$ evolution via a Tafel-like reaction. Based on this idea, a study of PBTh's and PBTh(S-H)$^+$'s triplet state, ESP and molecular orbitals was conducted and presented in Figure 6.21; for comparison, their ground and excited singlet states are also shown.

Figure 6.21 shows a variety of interesting changes, the first being that the formation of triplet states form much more favourable reaction sites. In PBTh, the ESP charge on the sulphur atom drops to –0.22 (Figure 6.21B) and would present a stronger electrostatic attraction to H$^+$ in solution (and possibly even H$_2$O). Whether the formation of a PBTh triplet site is conducive to protonation is difficult to say, though the excited singlet state has a much more diffuse orbital which would aid in charge transfer (Figure 6.21C). Time limitations meant that we were unable to perform the calculation of ESP for excited states, thus we have no information on the charge distribution of the singlet excited PBTh. Nonetheless, given the inherent electrostatic attraction in the ground state (where ESP on $S = -0.09$), the presence of large, diffuse orbitals would likely play a much larger role in the success of protonation. This is supported by the Raman

A - PBTh S_0

B - PBTh T_1

C - PBTh S_1

D - PBTh(S-H)$^+$ S_0

E - PBTh(S-H)$^+$ T_1

F - PBTh(S-H)$^+$ S_1
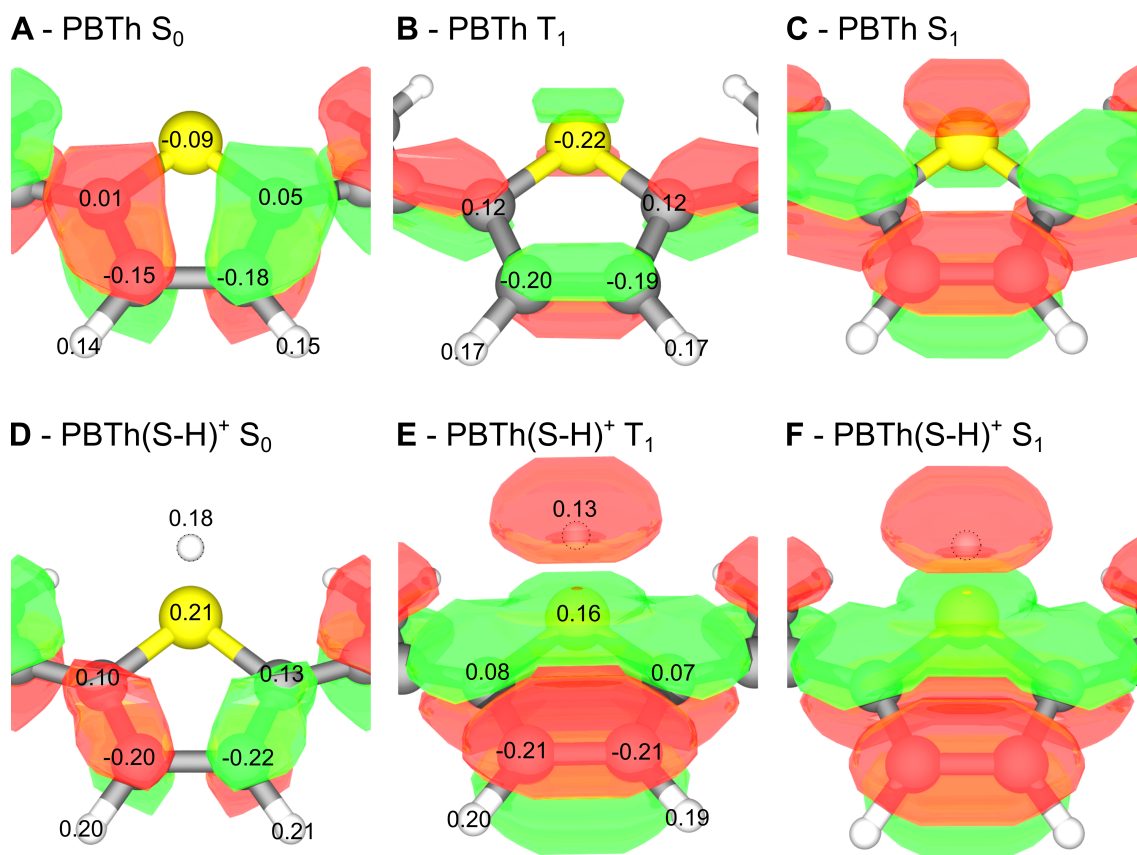
Figure 6.21: The calculated molecular orbitals and electrostatic potential (ESP) of the atoms in a 7-membered PBTh and PBTh(S-H)$^+$ at their central thiophene unit. **A,D** shows the ground singlet (S_0) state while **B,E** shows the ground triplet (T_1) states. **C,F** Show the excited singlet states (S_1) of PBTh and PBTh(S-H)$^+$ for comparison with their triplet counterparts.

results which show formation of the S—H bond at E_{oc}, indicating that the PBTh system does not require further electrostatic potential to enable the first protonation step (when illuminated). Hence we propose that the first protonation occurs via the singlet excitation of PBTh and subsequent localised charge transfer to H$^+$ at the sulphur site to form PBTh(S-H)$^+$. This is supported by literature findings that show the formation of polarons in P3HT via illumination,[49] in our case, the "polaron" is formed by "doping" with H$^+$.

Continuing on, the subsequent PBTh(S-H)$^+$ singlet ground state shows a significant positive ESP on the sulphur and attached proton (Figure 6.21D). The triplet state (Figure 6.21E) shows a more negative ESP – albeit still a positive charge – and represents a slightly more favourable scenario for the second reduction reaction to form H$_2$. Moreover, the molecular orbitals of the triplet state and excited singlet state (Figures 6.21E, F) present extremely favourable reaction sites; whereby large, diffuse electron orbitals envelop the introduced proton and form an ideal site for the HER. The triplet state is even more compelling given its extended lifetime plus the evidence of excimer formation and the possibility for singlet fission to produce two adjacent

triplet states. As a result, we propose that the second reduction to form H_2 begins with the photo-excitation of the ground PBTh(S-H)$^+$ to PBTh(S-H)$^+$ singlet*, followed by the excimer formation with an adjacent ground state PBTh(S-H)$^+$ which would then undergo singlet fission to form two adjacent PBTh(S-H)$^+$ triplet states and the rapid release of H_2.

6.3   Conclusion

The determination of the photo-electrocatalytic HER mechanism on PBTh was attempted. Key findings included the exclusion of iron from the overall reaction and the identification of a two stage catalysis mechanism, supported by photo-intensity measurements and electrical impedance spectroscopy. EIS also revealed various electronic attributes that are significantly altered when under illumination, chiefly, the reduction in charge transfer resistance and the trend towards resistor like behaviour. On the other hand, when in the dark, PBTh exhibited capacitor like behaviour (no charge transfer). While this did not reveal the chemical mechanism, it showed that the overall electrical behaviour of the PBTh film was drastically different with light and was attributed to the catalytic response.

Building on this, wavelength dependence measurements and extended CV were able to show that the overall process requires both photo and electrochemical stimulation for successful catalysis. One without the other is not able to drive the PBTh system and revealed the importance of the photo-excited state (and its associated orbitals) as well as the need for an applied potential.

Studies with in-situ Raman spectroscopy revealed excimer formation as an intermediate state via the observation of excimer fluorescence; the singlet fission to yield two triplet states is also proposed. Most importantly, Raman was able to show the evolution of an S—H band at $985\,\mathrm{cm}^{-1}$ whilst under illumination and in the presence of H_2O. Given these conditions, the appearance of this peak and its intensity was independent of electrochemical potential – present even at E_{oc} – and revealed that the formation of the PBTh(S-H)$^+$ intermediate is entirely photo-driven and rapid.

Lastly, computational studies were invaluable in revealing a variety of interactions that could not be determined experimentally. Briefly, this included the thermodynamic justification of the PBTh photo-system, confirmation of the first protonation at the sulphur atom via TD-DFT and the identification of favourable singlet and triplet molecular orbitals on the PBTh(S-H)$^+$ intermediate for the second reduction to H_2.
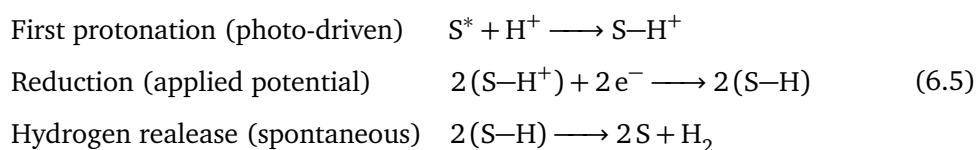
Combining this information, we propose the following mechanism (Figure 6.22) where: photo-excitation of PBTh in the presence of H_2O triggers the first protonation at the sulphur atom. Subsequent singlet excitation of PBTh(S-H)$^+$ and interaction with an adjacent ground states eventually leads to the formation of an excimer. This excimer then undergoes singlet fission to yield two adjacent triplet states which then release H_2 via a Tafel-like mechanism; the original

PBTh is then regenerated from the external circuit. The reaction equations are presented in Eq 6.4 and deviate slightly from the standard Volmer-Tafel equations.

$$
\begin{aligned}
\text{First protonation (photo-driven)} &\quad \text{S}^* + \text{H}^+ \longrightarrow \text{S–H}^+ \\
\text{Singlet fission (photo-driven)} &\quad (\text{S–H}^+)^* + \text{S–H}^+ \longrightarrow 2\,(\text{S–H}^+)^* \\
\text{Hydrogen release (spontaneous)} &\quad 2\,(\text{S–H}^+)^* \longrightarrow 2\,\text{S}^+ + \text{H}_2 \\
\text{Regeneration (applied potential)} &\quad 2\,\text{S}^+ + 2\,\text{e}^- \longrightarrow \text{S}
\end{aligned}
\tag{6.4}
$$
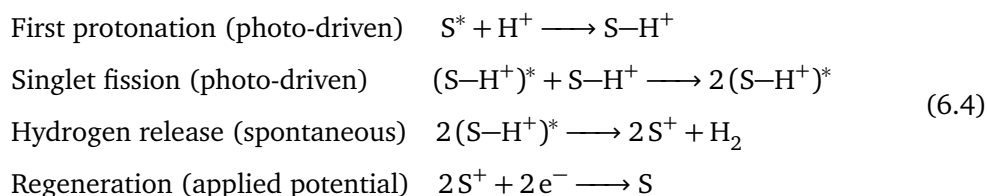
It must be mentioned that this proposed mechanism remains speculative given the limited direct experimental data and heavy reliance on computational models performed with limited experience. Because of this, several issues remain which include addressing the charge states of PBTh and movement of electrons, both within the PBTh/H^+ system and from the external circuit. Whether the PBTh remains charged after protonation is uncertain, for computational simplicity, we have included the positive charge in our models and descriptions (PBTh(S-H)$^+$). This is somewhat backed by our Raman data which showed the formation of S–H at E_{oc} and indicates that this protonation reaction does not require external electrons to neutralise PBTh once protonated. At the same time, external electrochemical potential is critical for driving the intermediate towards hydrogen evolution, though the role of this potential is not yet confirmed. Several options are open, one of which – as is currently presented – is the regeneration of the neutral PBTh ground state after the release of H_2 from the two triplet states. Another is the use of electrochemical potential to drive the second stage of the HER, in which case, the mechanism Eq 6.4 is replaced by Eq 6.5:

$$
\begin{aligned}
\text{First protonation (photo-driven)} &\quad \text{S}^* + \text{H}^+ \longrightarrow \text{S–H}^+ \\
\text{Reduction (applied potential)} &\quad 2\,(\text{S–H}^+) + 2\,\text{e}^- \longrightarrow 2\,(\text{S–H}) \\
\text{Hydrogen realease (spontaneous)} &\quad 2\,(\text{S–H}) \longrightarrow 2\,\text{S} + \text{H}_2
\end{aligned}
\tag{6.5}
$$

In this scenario, the PBTh(S-H)$^+$ species would be formed with photo-excitation and quickly followed by the electrochemical reduction to neutral PBTh(S-H). Assuming the neutral PBTh(S-H) is long-lived, hydrogen would then be evolved when two PBTh(S-H) are in close proximity. The formation of this neutral PBTh(S-H) also opens up the possibility for a Heyrovsky release mechanism though further studies on this species are required.

As it can be seen, the final mechanism remains highly contested. Regardless, from the data currently available to us, we propose the reaction mechanism as shown in Figure 6.22 which places a heavy emphasis on a photo-driven mechanism. For completeness, other possible pathways are also presented (greyed out) as they have not yet been conclusively ruled out. It is even possible that all the proposed mechanisms may be occurring simultaneously.
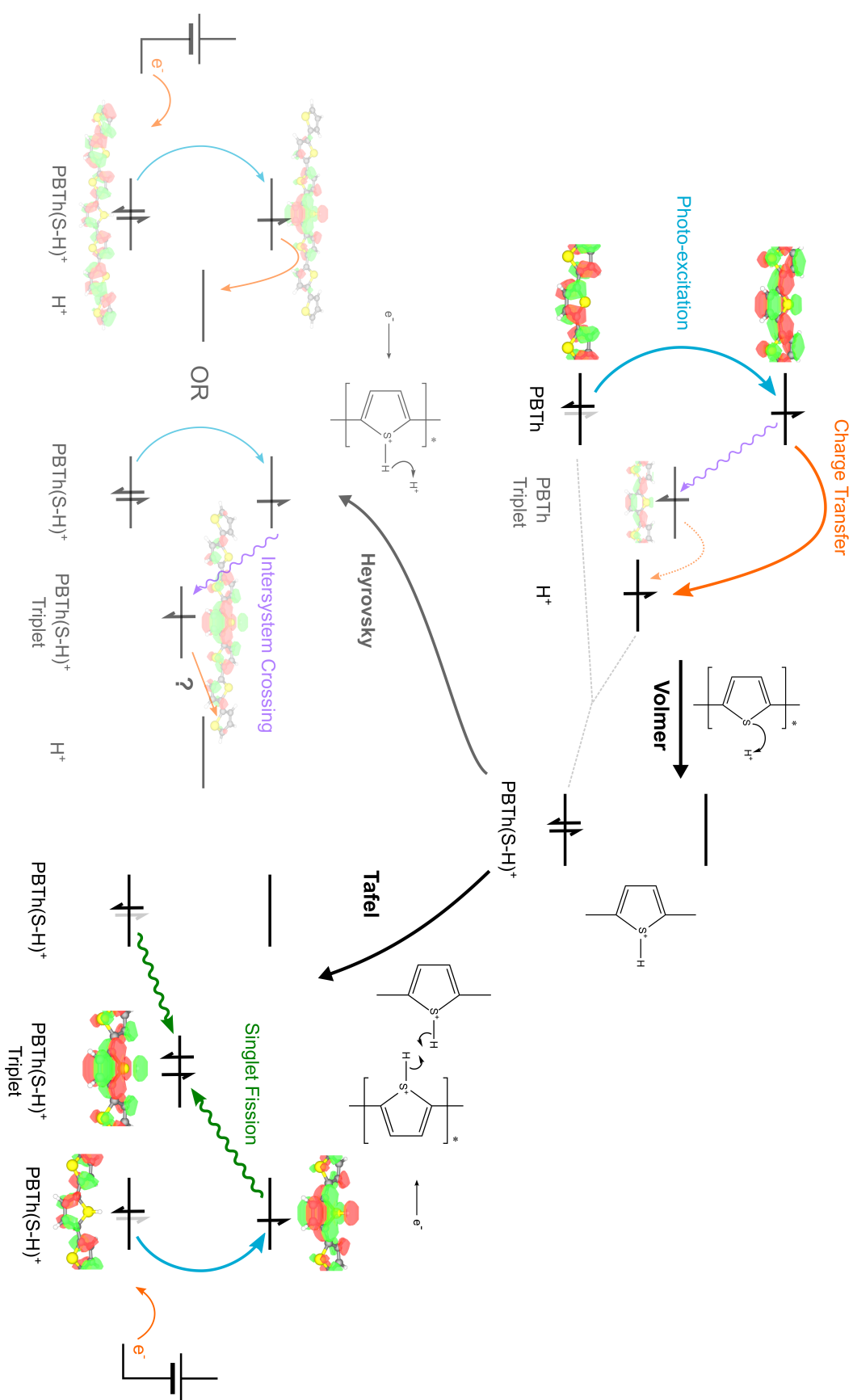
Figure 6.22: The proposed mechanism is presented (solid colours); the band positions are taken from single point energy calculations of the respective species. Although these energies are not quantitative, it gives a starting point for the relative positions and furthermore, show good thermodynamic agreement with the proposed scheme. Alternative reaction mechanisms are also presented but are greyed out. It should be noted, as discussed in the main text that this proposed mechanism is by no means confirmed but simply one possible explanation for observed data and trends.

In closing, despite the significant body of work presented, the study of PBTh as a photo-electrocatalyst is still in its infancy and time will no doubt bring new information on this novel and exciting photo-system.

6.4   Supporting Information

6.4.1   Experimental

A significant portion of the experimental details can be found in Chapter 2 under their relevant sections. However, some more specialised procedures are listed here for completeness.

Washing of Fe$_3^+$

The PBTh films were prepared on 3 cm by 3 cm FTO glass and polymerised as per standard procedures: spin coated 0.5 mL of Fe(III)PTS at 1500 RPM for 30 s, then placed in preheated PBTh VPP chamber for polymerisation at 70 °C for 1 h. The films were then taken out, rinsed with 2 mL of the respective wash solution, then left to soak overnight in 30 mL of their respective wash solution; H_2O, ethanol, $0.1\,mol\,L^{-1}$ PTSa in H_2O and $0.1\,mol\,L^{-1}$ PTSa in ethanol; ethanol was obtained from Merck Emplura (96%), p-toluenesulfonic acid monohydrate (PTSa) was obtained from Sigma Aldrich.

After the wash, the films on FTO were dried tested via CV and CA in a metal cell while the wash solutions were analysed for their Fe content. Excess KSCN $\approx$ were added to each solution along with peroxide to convert any Fe^{2+} species to Fe^{3+}. The UV-Vis spectra and λ_{max} of each wash solution was then taken and compared with the calibration graphs (Figure S1) to determine their iron content.

For the electrochemical tests, the cell was purged with Ar for 15 min at $8\,mL\,min^{-1}$ then CV was conducted from 0.6 V to -0.8 V vs Ag/AgCl reference in $0.1\,mol\,L^{-1}$ PB (pH 7) at $20\,mV\,s^{-1}$, first in light for 5 cycles, then in dark for another 5 cycles; the CV was conducted to confirm that successful photo-electrocatalysis was achieved. A CA was then run at -0.8 V first in dark until the current (from O_2 reduction) dropped below $2\,\mu A$, then the the Leica KL2500 halogen light ($\approx$0.4 sun) was switched on, the peak current recorded at 20 min under illumination is taken as the photocurrent of each film and presented in Figure 6.1.

After this initial test, each film was then washed in 30 ml of $0.1\,mol\,L^{-1}$ PTSa in H_2O and left to soak overnight. The individual wash solutions were then collected, made back up to 30 mL (if evaporation occurred) and $100\,\mu L$ of 30%peroxide (from Merck) was added to convert all Fe^{2+} to Fe^{3+}. Approximately 100 mg of KSCN was then added to form the $FeSCN^{2-}$ complex and the resulting blood red solution was analysed with UV-Vis spectroscopy to determine the iron content. $0.1\,mol\,L^{-1}$ PTSa in ethanol was also used instead of the aqueous solution during washes 5 and 6 to further remove residual Fe.

The electrochemical tests were repeated on the PBTh films after the 6th wash to investigate the effects on the photocurrent after iron removal.
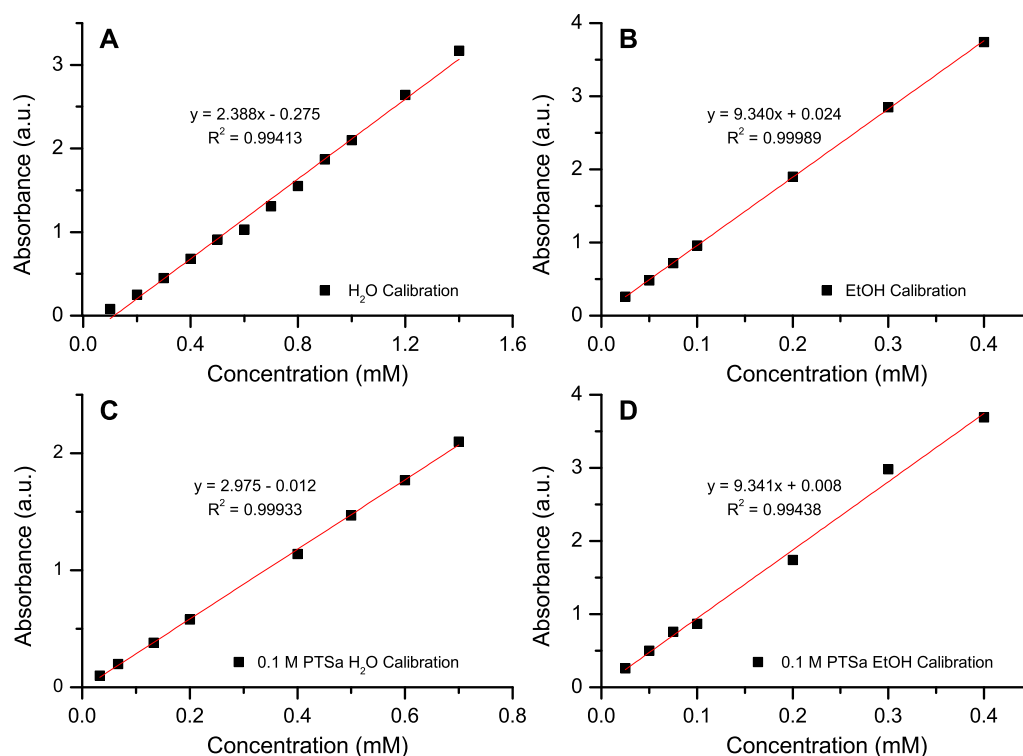
Figure S1: Fe^{3+} concentration calibration for the four different wash solutions, **A** H_2O, $\lambda_{max} = 470\,nm$, **B** Ethanol, $\lambda_{max} = 504\,nm$, **C** $0.1\,mol\,L^{-1}$ PTSa in H_2O, $\lambda_{max} = 472\,nm$ and **D** $0.1\,mol\,L^{-1}$ PTSa in Ethanol, $\lambda_{max} = 508\,nm$. The standard solution was made of $FeCl_3$ with excess KSCN dissolved in the respective solution

Extended CV of PBTh

The extended CV of PBTh was conducted on two separate PBTh films, one for aqueous $0.1\,mol\,L^{-1}$ PB (pH 7) and one in anhydrous propylene carbonate; PC from Sigma Aldrich and used as is. Both were polymerised on glassy carbon as per standard procedures and CV was conducted under N_2. The CV was extended gradually from the initial $-0.8\,V$ vs Ag/AgCl towards more electronegative potentials until a significant current was detected. Illumination was provided by the Leica KL 2500 lamp (≈ 0.4 sun).

6.4.2 Miscellaneous Supporting Data

A - PBTh(C-H)⁺ HOMO

PBTh(C-H)⁺ LUMO

B - PBTh(βC-H)⁺ HOMO
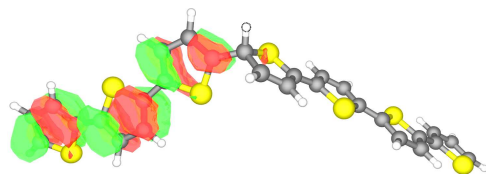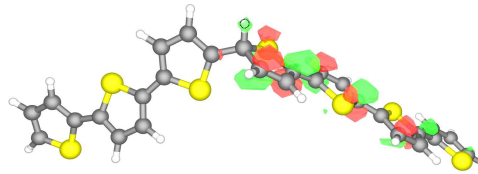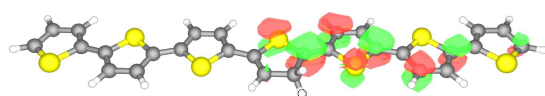
PBTh(βC-H)⁺ LUMO
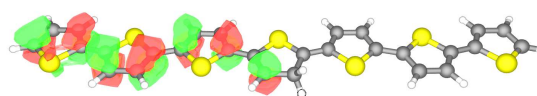
Figure S2: HOMO (ground) and LUMO (photo-excited) molecular orbitals of the PBTh and PBTh-H⁺ with protonation at alternative sites (C_α and C_β); as calculated by DFT methods using B3LYP/6-31+G(d)
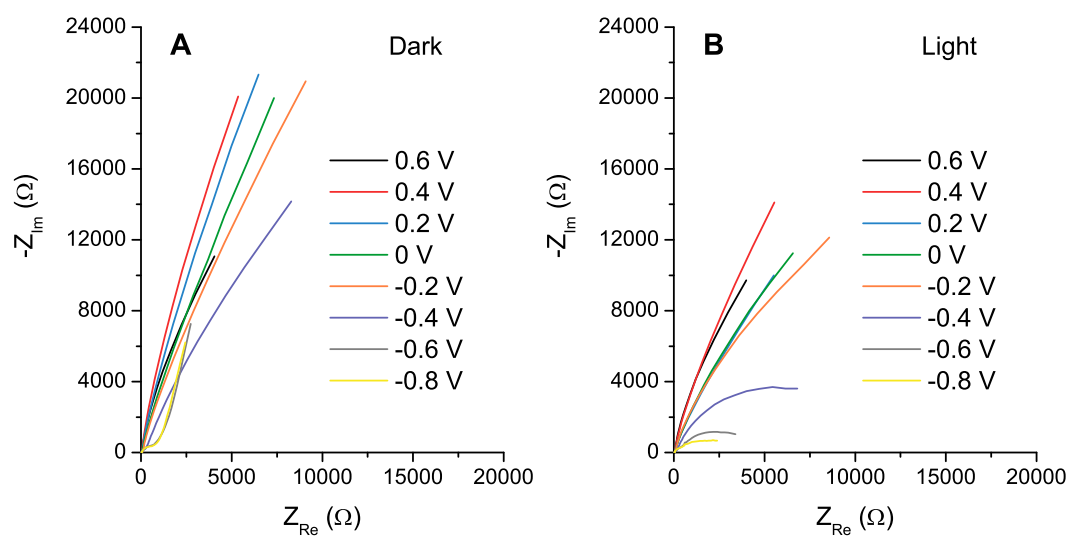
Figure S3: More Impedance measurements of the film.
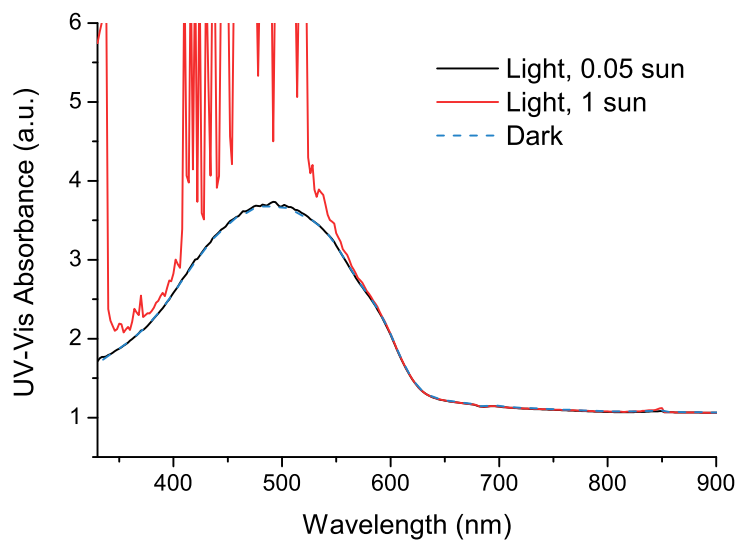
Figure S4: The UV-Vis spectra when light shone onto the film whilst holding at 0.6 V in 0.1 mol L^{-1} PB, pH 7; the dark absorption spectrum of PBTh is also included.
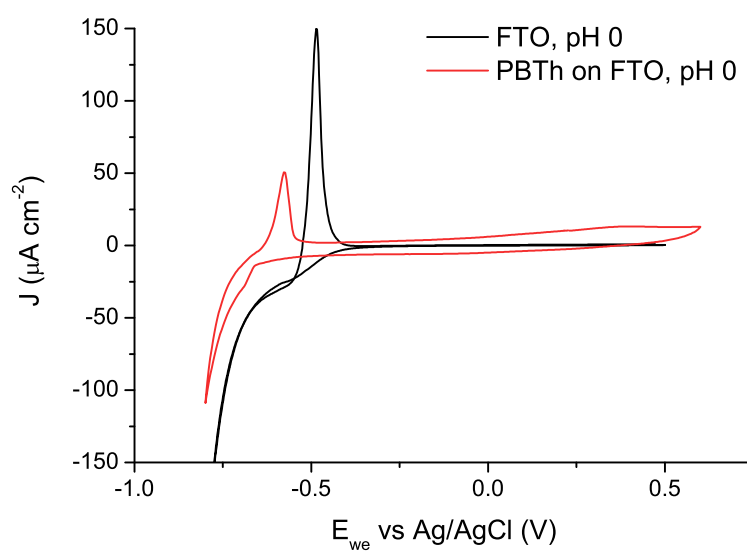
Figure S5: CV showing the strong reduction and re-oxidation of the FTO substrate in 1 mol L^{-1} H$_2$SO$_4$, pH 0
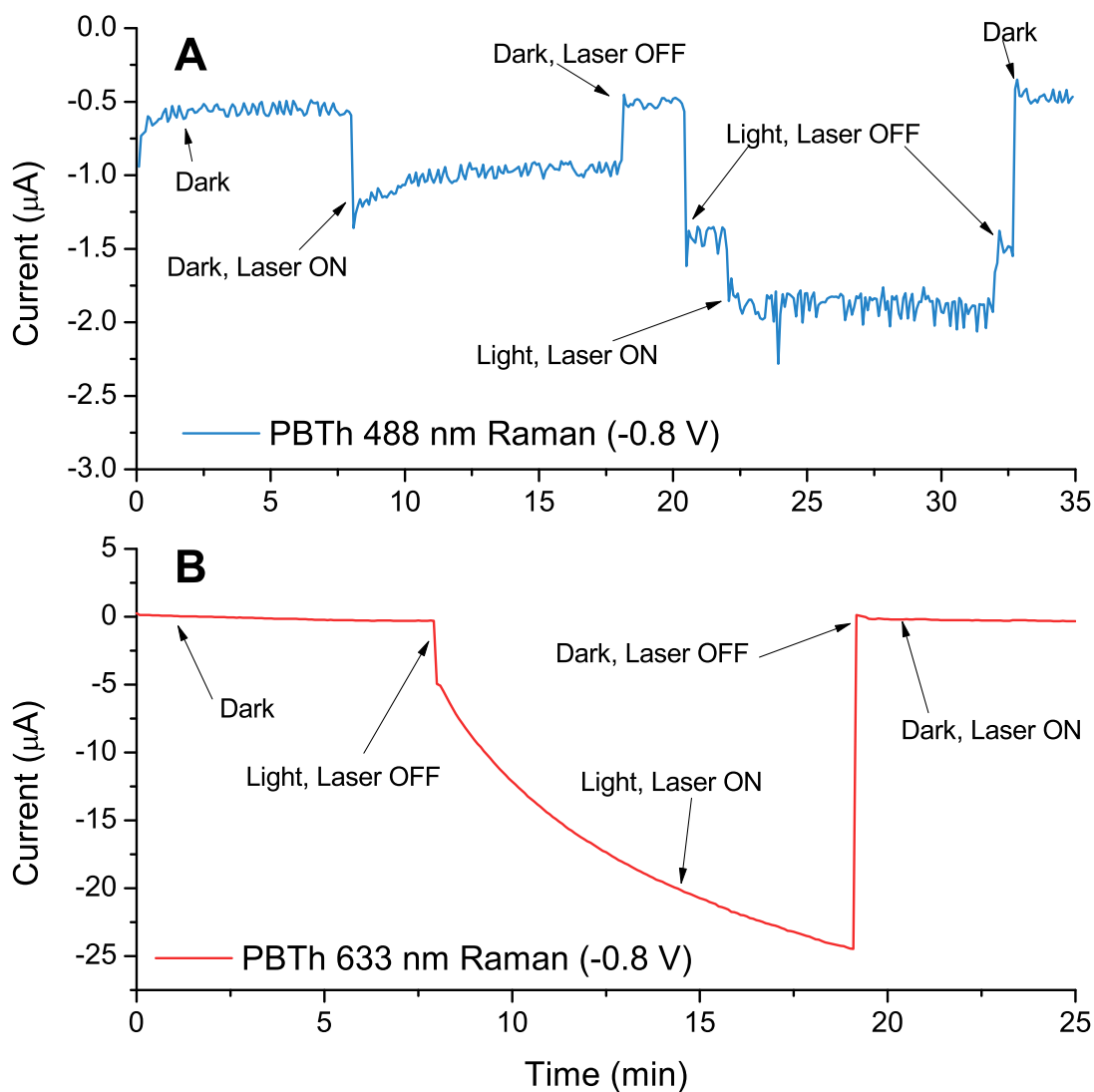
Figure S6: A: The CA trace of PBTh for in-situ Raman in the blue (488 nm) laser whilst held at $-0.8\,$V vs Ag/AgCl in $0.1\,$mol$\,$L^{-1} PB, pH 7. As the figure shows, the blue laser was sufficient to generate a substantial photo-catalytic response and makes determination of the "dark" PBTh Raman spectrum impossible. **B:** The CA trace of PBTh whilst running in-situ Raman with the 633 nm laser; photo-excitation is only triggered when the external light was switched on.
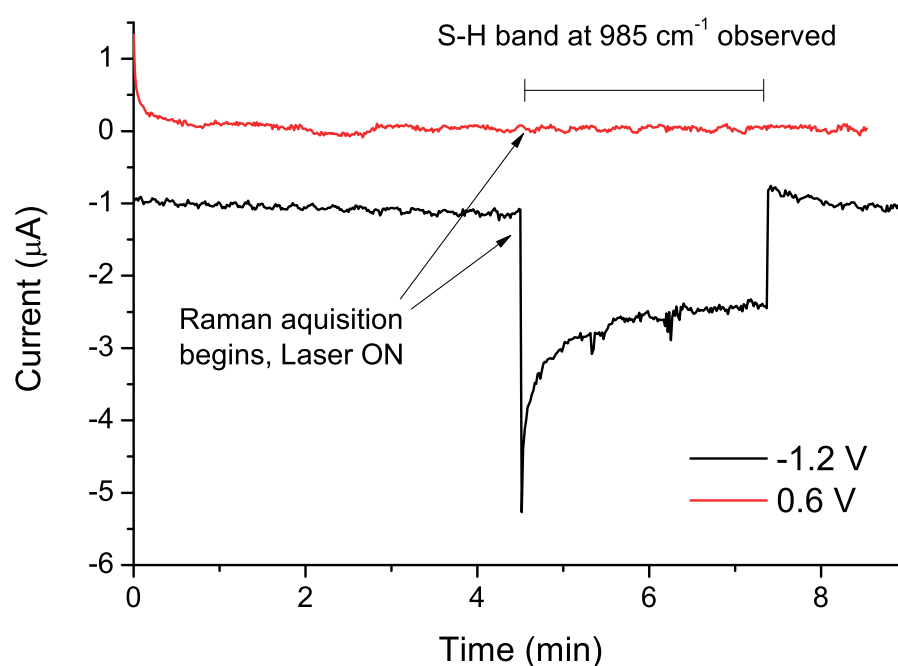
Figure S7: The CA trace of PBTh during in-situ Raman in $1\,mol\,L^{-1}$ H_2SO_4, pH 0 under N_2 at the applied potential of $-1.2\,V$ and $0.6\,V$ vs Ag/AgCl. The S$-$H peak was observed in the Raman trace of both potentials despite no current running at 0.6 V. The 488 nm laser was the only source of illumination.

Bibliography

[1] C. H. Ng, O. Winther-Jensen, C. A. Ohlin and B. Winther-Jensen. "Exploration and optimisation of poly(2,2'-bithiophene) as a stable photo-electrocatalyst for hydrogen production". *J. Mater. Chem. A*, 2015. **3**, 11358–11366.

[2] C. Gu, B. C. Norris, F.-R. F. Fan, C. W. Bielawski and A. J. Bard. "Is Base-Inhibited Vapor Phase Polymerized PEDOT an Electrocatalyst for the Hydrogen Evolution Reaction? Exploring Substrate Effects, Including Pt Contaminated Au". *ACS Catal.*, 2012. **2**, 5, 746–750.

[3] G. Kossmehl and M. Niemitz. "Preparation and controlled wettability of poly (2,2'-bithienyl-5, 5'-diyl) layers". *Synth. Met.*, 1991. **43**, 1065–1071.

[4] B. Beverskog and I. Puigdomenech. "Revised Pourbaix diagrams for iron at 25-300C". *Corros. Sci.*, 1996. **38**, 12, 2121–2135.

[5] J. Xie, J. Zhang, S. Li, F. Grote, X. Zhang, H. Zhang, R. Wang, Y. Lei, B. Pan and Y. Xie. "Controllable disorder engineering in oxygen-incorporated MoS2 ultrathin nanosheets for efficient hydrogen evolution". *J. Am. Chem. Soc.*, 2013. **135**, 47, 17881–17888.

[6] S. A. Vilekar, I. Fishtik and R. Datta. "Kinetics of the Hydrogen Electrode Reaction". *J. Electrochem. Soc.*, 2010. **157**, 7, B1040.

[7] C. Corminboeuf, A. Prlj and B. F. E. Curchod. "Excited State Dynamics of Thiophene and Bithiophene: New Insights into Theoretically Challenging Systems". *Phys. Chem. Chem. Phys.*, 2015. **17**, 14719–14730.

[8] S. S. Zade and M. Bendikov. "Twisting of conjugated oligomers and polymers: Case study of oligo- And polythiophene". *Chem. - A Eur. J.*, 2007. **13**, 13, 3688–3700.

[9] A. A. Diagne, M. Fall, M. Guène, M. M. Dieng, F. Deflorian, S. Rossi, P. Bonora and C. D. Volpe. "Electrochemical impedance spectroscopy of polybithiophene films in an aqueous LiClO4 solution". *Comptes Rendus Chim.*, 2007. **10**, 6, 558–563.

[10] F. c. Cebeci, E. Sezer and a. S. Sarac. "A novel EDOT-nonylbithiazole-EDOT based comonomer as an active electrode material for supercapacitor applications". *Electrochim. Acta*, 2009. **54**, 26, 6354–6360.

[11] M. Ates and a. S. Sarac. "Electrochemical Impedance Spectroscopic Study of Polythiophenes on Carbon Materials". *Polym. Plast. Technol. Eng.*, 2011. **50**, 11, 1130–1148.

[12] A. Galal, S. a. Darwish and R. a. Ahmed. "Hybrid organic/inorganic films of conducting polymers modified with phthalocyanines. II. EIS studies and film characterization". *J. Solid State Electrochem.*, 2007. **11**, 4, 531–542.

[13] J. Bisquert, G. Garcia-Belmonte, P. Bueno, E. Longo and L. Bulhões. "Impedance of constant phase element (CPE)-blocked diffusion in film electrodes". *J. Electroanal. Chem.*, 1998. **452**, 2, 229–234.

[14] J. F. Rubinson and Y. P. Kayinamura. "Charge transport in conducting polymers: insights from impedance spectroscopy." *Chem. Soc. Rev.*, 2009. **38**, 12, 3339–47.

[15] O. Winther-Jensen, B. Winther-Jensen and D. R. MacFarlane. "Photostimulated electrocatalysis of water oxidation by conjugated polymers". *Electrochem. commun.*, 2011. **13**, 4, 307–309.

[16] A. Dreuw and M. Head-Gordon. "Single-reference ab initio methods for the calculation of excited states of large molecules". *Chem. Rev.*, 2005. **105**, 11, 4009–4037.

[17] E. Runge and E. K. U. Gross. "Density-functional theory for time-dependent systems". *Phys. Rev. Lett.*, 1984. **52**, 12, 997–1000.

[18] T. Yanai, D. P. Tew and N. C. Handy. "A new hybrid exchange-correlation functional using the Coulomb-attenuating method (CAM-B3LYP)". *Chem. Phys. Lett.*, 2004. **393**, 1-3, 51–57.

[19] Z.-g. Xu and G. Horowitz. "From oligomers to polymer. An insight into the electrochemical doping-dedoping of polythiophene from electrochemical data on thiophene oligomers". *J. Electroanal. Chem.*, 1992. **335**, 123–134.

[20] G. Harbeke, D. Baeriswyl, H. Kiess, W. Kobe and W. Kobel. "Polarons and Bipolarons in Doped Polythiophenes". *Phys. Scr.*, 1986. **302**, 302–305.

[21] G. Socrates. *Infrared and Raman Characteristic Group Frequencies: Tables and Charts*. John Wiley & Sons Ltd, Chichester, UK, 3rd edition, 2001.

[22] D. Zhang and G. Xue. "Evolutions of structure of a thin polybithiophene film upon doping and cycling strudied by in situ SERS technique". *Synth. Met.*, 1998. **95**, 185–190.

[23] M. Baibarac, I. Baltog and S. Lefrant. "Raman spectroscopic evidence for interfacial interactions in poly(bithiophene)/single-walled carbon nanotube composites". *Carbon N. Y.*, 2009. **47**, 5, 1389–1398.

[24] Y. Furukawa, N. Yokonuma, M. Tasumi, M. Kuroda and J. Nakayama. "Raman Studies of Doped Polythiophene and the Radical Cation and Dication of Quinquethiophene". *Mol. Cryst. Liq. Cryst.*, 1994. **256**, 1, 113–120.

[25] G. Lanzani, G. Cerullo, S. Stagira and S. De Silvestri. "Excited state dynamics of oligothiophenes studied by transient pump-probe spectroscopy". *J. Photochem. Photobiol. A Chem.*, 2001. **144**, 1, 13–19.

[26] R. S. Becker, J. S. de Melo, a. L. Macanita and F. Elisei. "Comprehensive investigation of the solution photophysics and theoretical aspects of oligothiophenes of 1-7 rings". *Pure Appl. Chem.*, 1995. **67**, 1, 9–16.

[27] R. S. Becker, J. S. Demelo, a. L. Macanita and F. Elisei. "Comprehensive evaluation of the absorption, photophysical, energy transfer, structural, and theoretical properties of alpha-oligothiophenes with one to seven rings". *J. Phys. Chem.*, 1996. **100**, 48, 18683–18695.

[28] R. Weinkauf, L. Lehr, E. W. Schlag, S. Salzmann and C. M. Marian. "Ultrafast dynamics in thiophene investigated by femtosecond pump probe photoelectron spectroscopy and theory." *Phys. Chem. Chem. Phys.*, 2008. **10**, 3, 393–404.

[29] S. I. Hintschich, C. Rothe and A. P. Monkman. "Temperature dependence of long-lived photoexcitations in a polythiophene". *Synth. Met.*, 2003. **135-136**, 365–366.

[30] C. Rothe, S. Hintschich, A. P. Monkman, M. Svensson and M. R. Anderson. "Spectroscopic investigation of the different long-lived photoexcitations in a polythiophene". *J. Chem. Phys.*, 2002. **116**, 23, 10503–10507.

[31] M. A. Slifkin. "Charge Transfer and Eximer Formation". *Nature*, 1963. **200**, 766–767.

[32] B. J. Walker, A. J. Musser, D. Beljonne and R. H. Friend. "Singlet exciton fission in solution." *Nat. Chem.*, 2013. **5**, 12, 1019–24.

[33] R. L. Garrell, C. Szafranski and W. Tanner. "Surface-Enhanced Raman Spectroscopy of Thiols and Disulfides". *Technology*, 1990. **1336**, c, 264–271.

[34] V. S. Minkov and E. V. Boldyreva. "Weak hydrogen bonds formed by thiol groups in N-acetyl-l-cysteine and their response to the crystal structure distortion on increasing pressure". *J. Phys. Chem. B*, 2013. **117**, 46, 14247–14260.

[35] A. Baheti, P. Singh, C.-P. Lee, K. R. J. Thomas and K.-C. Ho. "2,7-Diaminofluorene-based organic dyes for dye-sensitized solar cells: effect of auxiliary donor on optical and electrochemical properties." *J. Org. Chem.*, 2011. **76**, 12, 4910–20.

[36] S. S. Zade and M. Bendikov. "Theoretical study of long oligothiophene dications: Bipolaron vs polaron pair vs triplet state". *J. Phys. Chem. B*, 2006. **110**, 15839–15846.

[37] S. Roy, S. K. S. Mazinani, T. L. Groy, L. Gan, P. Tarakeshwar, V. Mujica and A. K. Jones. "Catalytic Hydrogen Evolution by Fe(II) Carbonyls Featuring a Dithiolate and a Chelating Phosphine." *Inorg. Chem.*, 2014. **53**, 8919–8929.

[38] F. A. Evangelista, P. Shushkov and J. C. Tully. "Orthogonality Constrained Density Functional Theory for Electronic Excited States BT - The Journal of Physical Chemistry A". *J. Phys. Chem. A*, 2013. **117**, 7378–7392.

[39] T. Stein, L. Kronik and R. Baer. "Reliable prediction of charge transfer excitations in molecular complexes using time-dependent density functional theory." *J. Am. Chem. Soc.*, 2009. **131**, 8, 2818–2820.

[40] L. Goerigk and S. Grimme. "A thorough benchmark of density functional methods for general main group thermochemistry, kinetics, and noncovalent interactions." *Phys. Chem. Chem. Phys.*, 2011. **13**, 14, 6670–88.

[41] C. Wu, J. Nilsson, O. Inganas, W. Salaneck, J.-E. Österholm and J. Brédas. "Electronic Structure of Polythiophene". *Synth. Met.*, 1987. **21**, 197–202.

[42] Y. Aoyama, T. Yamanari, N. Koumura, H. Tachikawa, M. Nagai and Y. Yoshida. "Photo-induced oxidation of polythiophene derivatives: Dependence on side chain structure". *Polym. Degrad. Stab.*, 2013. **98**, 4, 899–903.

[43] M. Manceau, A. Rivaton, J. L. Gardette, S. Guillerez and N. Lemaître. "The mechanism of photo- and thermooxidation of poly(3-hexylthiophene) (P3HT) reconsidered". *Polym. Degrad. Stab.*, 2009. **94**, 6, 898–907.

[44] B. Hinnemann, P. G. Moses, J. Bonde, K. P. Jorgensen, J. H. Nielsen, S. Horch, I. Chorkendorff and J. K. Norskov. "Biomimetic hydrogen evolution: MoS2 nanoparticles as catalyst for hydrogen evolution." *J. Am. Chem. Soc.*, 2005. **127**, 15, 5308–5309.

[45] J. Kibsgaard, T. F. Jaramillo and F. Besenbacher. "Building an appropriate active-site motif into a hydrogen-evolution catalyst with thiomolybdate [Mo3S13]2- clusters." *Nat. Chem.*, 2014. **6**, 3, 248–53.

[46] D. Merki and X. Hu. "Recent developments of molybdenum and tungsten sulfides as hydrogen evolution catalysts". *Energy Environ. Sci.*, 2011. **4**, 10, 3878–3888.

[47] Y. Hou, B. L. Abrams, P. C. K. Vesborg, M. r. E. Björketun, K. Herbst, L. Bech, A. M. Setti, C. D. Damsgaard, T. Pedersen, O. Hansen, J. Rossmeisl, S. Dahl, J. K. Norskov and I. Chorkendorff. "Bioinspired molecular co-catalysts bonded to a silicon photocathode for solar hydrogen evolution." *Nat. Mater.*, 2011. **10**, 6, 434–438.

[48] M. Koch, R. Nicolaescu and P. V. Kamat. "Photodegradation of polythiophene-based polymers: Excited state properties and radical intermediates". *J. Phys. Chem. C*, 2009. **113**, 27, 11507–11513.

[49] S. Cook, A. Furube and R. Katoh. "Analysis of the excited states of regioregular polythiophene P3HT". *Energy Environ. Sci.*, 2008. **1**, 2, 294.

Chapter 7

Conclusions and Future Studies

Conclusions

Much has been achieved throughout the past three and a half years, and the original aims for *"the development of a photo-electrocatalyst for the hydrogen evolution reaction utilising blends of conducting polymers and organic dyes."* was more than realised. In the end, the envisioned light harvesting role of the dye was not required but the successful evolution of hydrogen from the PBTh film revealed a completely novel method in which to use polythiophene; generally considered as a fairly "uninteresting" material. This discovery is significant in the field of conducting polymers and HER catalysis, particularly given PBTh's longterm stability, onset below E^0 and successful operation up to pH 11. Moreover, the studies presented thus far represent only the beginning of the investigations with regards to PBTh and photo-catalysis and the full impact of this finding remains to be seen.

Literature Comparisons

In comparison to literature, our current findings fall short in terms of the typical catalytic activity of other electrocatalysis systems, where current densities in the order of mA cm^{-2} are commonly observed. However, the advantage of PBTh is the harnessing of light to photo-enhance the reduction reaction, allowing an onset potential *below* that of E^0; that is a claim that no electrocatalyst can make. In addition, our PBTh system does not require the synthesis of metal complexes (many of which are not trivial), or the use of unstable biological enzymes or bio-mimics. The simplicity of the system is particularly desirable and provides a versatile platform with which to make further improvements; often via very simple adjustments such as thickness. This is of particular benefit in terms of commercial development as it provides a large degree of flexibility and greatly aids scalability.

In comparison to traditional photo-catalysts, our system cannot achieve the photo-driven production of H_2. However, it is critical to note that photo-catalysts are often unstable with limited operational lifetimes and require the constant addition of sacrificial additives for their successful operation. Furthermore, many literature photo-systems – particularly the higher performing catalysts – are only operable with the use of rare-earth metals and/or under certain organic solvents which limits their viability for commercial applications. These issues in and of itself do not rule out the idea of photo-driven H_2 production, but it does create numerous issues that electrocatalysts do not face. Being a photo- *and* an electro-catalyst, PBTh is able to avoid many of these issues whilst still harnessing the advantages of photo-catalysis.

The unique property of the PBTh system is that it is able to bridge these two main classes of catalysts for the HER. Its inherent photo-activity allows it to produce H_2 at much lower potentials while the electrochemical set-up maintains charge balance and longevity of the film. Though the use of conducting polymers for electrochemical applications is not new, the photo-catalytic activity shown by PBTh was initially hard to reconcile. However, given the

expansive use of polythiophenes in organic photovoltaics, the photo-activity of PBTh is perhaps not so surprising; though it remains to be seen if others in the polythiophene family are capable of this behaviour.

There are certainly more catalytically active, better photo-enhanced and cheaper catalysts for the HER than PBTh. However, the strength of the PBTh catalyst lies in its ability to combine all of these aspects into a very simple and elegant system. That being said, PBTh remains severely hindered by its low catalytic activity and low overall efficiency; especially when considering the total photo energy and electrochemical potential input *vs* hydrogen produced. Further modification may help alleviate this but it is not guaranteed. Reproducibility is also an issue, where films produced via the same method can have widely varying photo-electrocatalytic performances. A large degree of this is due to PBTh's sensitivity to ambient conditions (temperature/humidity) during production. Without a more controlled environment, it becomes difficult to compare films made on different days. Fortunately, solutions are readily available for these issues though it may take time to implement. Moreover, it should be remembered that the investigations thus far are only just the beginning and there remains enormous potential for optimisation, modification, growth and further discoveries.

Initial Conducting Polymer and Dye Blends

The initial investigation on PEDOT and dye blends was for the most part unsuccessful though it took careful study to finally reveal the true catalytic nature of the system and its dependency on gold. Subsequent electrochemical, optical and computational analysis of a wide range of triarylmethane dyes helped to further reveal the limitations of the PEDOT:dye system. The wealth of data generated is also invaluable as a resource for the commercially important triarylmethane dye family.

Through the characterisation process, much information was gained by the comparison of common literature analytical techniques and their relationships to one another. An important realisation is that the computational modelling of organic molecules, even if relatively simple, is not straight forward and thorough considerations are needed when designing the appropriate model/computation experiment. Because of these issues, we were unable to fully realise our aims of developing computational models to streamline the selection process.

Limitations in experimental techniques were also encountered and included the lack of purity for various dye species. However, it was more difficult to reconcile the absence of clear redox couples with which to easily assign band energies. Though unfortunate, it revealed short-comings in the electrochemical techniques, particularly with regards to species with poor redox performance. Further adjustments using alternate electrodes, electrolytes, supporting electrolyte, scan rates as well as proper purification of the dyes could help improve the CV data. However, for our initial aims of focusing on the characterisation of commercially available dyes

for the purpose of inclusion in electrochemical systems, the data was an accurate reflection of the dye's expected behaviour.

Finally, comparison of the band gap determined using optical spectroscopy revealed that they do not always agree with electrochemical band positions. A number of reasons were used to account for this, the most important of which being that optical spectroscopy probes vertical, singlet transitions, whereas the longer timescale of electrochemistry allows the possibility for different interactions (charge transfer, conformational changes, protonation *etc.*). Although this finding is not new, it bares reminding as the practise remains common throughout literature. Critically for the project, the characterisation of such a wide variety of dyes and conducting polymers helped to reveal a new direction of study, namely, that of PBTh and Cresol Red.

Realisation of H_2 Evolution and Cell Set-up

The initial studies on PBTh:Cresol Red revealed the first indications of photo-catalysis and was helpful in establishing the viability of the original concept. Indeed, there were indications that PBTh:Cresol Red films were able to initiate the HER earlier than that of pure PBTh, however the impressive photo-activity of PBTh alone meant that studies on dye blends were placed on hold. Though this proved to be a significant deviation away from our starting aims, it was deemed necessary to establish the role of PBTh as a catalytically active material, without interference from dye species.

It was presumed early in the discovery that the evolution of hydrogen was the only possible explanation to account for the observed photo-currents. However, the eventual confirmation of H_2 evolution was not trivial and included significant efforts into testing, modifying and designing in-situ electrochemical/gas chromatography cells. While time consuming, it forced an improved understanding of the overall set-up and allowed the tailoring of a custom cell to our samples; something which would not have been possible with a commercially obtained product.

The ability to optimise the cell to our sample – instead of the other way around – played a large part in the eventual detection of hydrogen. This was particularly important in our initial films where catalytic performance was not yet optimised and the generated photo-currents were painfully small. More often than not, the hydrogen evolved was below the detection limit of our GC system. However, with the use of our custom cell and care in ensuring proper sealing of the entire system, the decisive H_2 peak was realised.

Our custom cell is by no means perfect and continued improvements are still required. Key of which, is the effective separation of the counter and working electrodes so that cross-over reactions can be prevented. Also, the use of more impermeable materials would help to further counter the high diffusivity of H_2. Nonetheless, irrespective of its limitations, the custom cell played a major role in the success of our discovery and serves as a reminder that proper

experimental design is an important factor in the success of an investigation. Moreover, the convenience of commercially available products should not be the only contributing factor when selecting/designing experimental set-ups.

Exploration of the PBTh system

What initially began as a simple modification of the PBTh system expanded into a much broader investigation into its catalytic capabilities. These experiments and the obtained results were by far the most exciting and cemented the notion of PBTh as a serious photo-electrocatalyst with potential for future applications. The success observed for the wide array of parameters was truly surprising at first but consideration of the inherent stability and band positions of PBTh can account for much of the phenomena.

For the most part, our investigations continued along the path that is normally taken when an electrocatalyst is first discovered. This included the determination of the faradaic efficiency, the long-term stability and operational pH range. In all these aspects, the PBTh system proved to be remarkably stable with a catalytic activity over a wide range of experimental parameters; albeit at a low rate of H_2 evolution. However, this is in many ways ideal as increasing the catalytic activity of a flat film is relatively trivial when compared to the difficulties in prolonging the lifetime of an unstable catalyst or changing the operation pH range. The ease of this improvement is perhaps best demonstrated by the substantial rise in catalytic activity with the simple thinning of the PBTh film and modifications to morphology.

The investigations on the substrate materials also revealed the possibility of catalytic activity on the alternate, cheap and transparent FTO glass which proved of immense value in subsequent in-situ UV-Vis studies. Moreover, it demonstrated that the success of the PBTh system is not tied to the expensive glassy carbon substrate. The similar finding which showed catalytic activity in NaCl solutions further supported the versatility of PBTh in alternate electrochemical environments.

For the wider implications of the PBTh system, it is this customisation and flexibility to operational parameters that make PBTh such a promising catalyst. Together with the stability and simplicity of PBTh, we have an ideal base for which further modifications and improvements can be made. Some of these ideas include:

- The inclusion of dyes and other photo-active components for further photo-enhancement
- The use of rough/porous/3D-mesh substrates to enhance surface area
- Continued study and use of templating techniques to achieve porous structures
- Synthesis of nano-structured PBTh for catalysis
- Incorporation of hydrophilic components such as PEG to enhance electrolyte penetration
- The inclusion of alternate HER catalysts (MoS_2, metal complexes etc.) to enhance catalysis performance

- Expansion of the studies to other members in the polythiophene family
- Inclusion of reducing agents to promote the release of H_2

Examination of the Catalytic Mechanism

The comprehensive mechanistic studies of the PBTh was a particular challenge, mostly brought about by the multiple excitation processes required to trigger the reaction. Early attempts to use only electrochemical potential to substitute photo-excitation was unsuccessful and rendered subsequent spectroscopic techniques much more difficult.

Prior to the probing of the PBTh film, it was important to remove iron as a potential catalyst site in the overall scheme. The eventual inverse relationship between iron content and catalytic performance showed that Fe was detrimental to the overall process. The direct detection of Fe inside the film would have been more ideal but given the extremely low concentrations, we were unable to find a non-destructive technique for this type of analysis. In any case, the clear inverse relationship clearly points to PBTh as the active site for catalysis.

The close correlation of photo-electrocatalytic performance to the absorbance spectra of PBTh also supported its crucial role in the overall catalysis mechanism. At the same time, the photo-intensity tests were able to show a remarkable linear photo-response that has thus far, not yet been fully saturated. We note that we have not calculated a total efficiency for the system (total photo- and electro-energy in *vs* H_2 out), this was because the efficiency is highly variable and dependent on the chosen potential, operational parameters and film quality. A high efficiency could be obtained in $1 \, \text{mol} \, \text{L}^{-1}$ H_2SO_4 with an ideal film thickness and good porosity, even with only modest potentials. On the other hand, alkaline conditions with the standard flat film would yield much lower numbers. Furthermore the proper elucidation of the overall system efficiency would have to take into account the potential on the counter electrode, which we had not optimised or adjusted. While it was certainly possible to determine an efficiency of the film for each individual instance, whether or not that result is meaningful is debatable. For now, we feel that it is much more prudent to focus on first understanding, maximising and reliably reproduce the performance of the film prior to reporting *the* efficiency; particularly in this early stage of development.

Another important step was the determination of an EIS equivalent circuit for the PBTh system. This was not perhaps critical in the elucidation of the chemical mechanism, but it revealed many key electronic interactions. Amongst which was the presence of a two step catalytic process as more negative potentials were applied. Originally this was suggested as being from the initial protonation and subsequent reduction to release H_2. However, with the realisation that the initial protonation is entirely photo-driven, it is possible that these are two different H_2 release mechanisms; perhaps a Heyrovky-like interaction followed by a Tafel-like reaction as potential is decreased. Further confirmation would have to be decided via alternate analysis

techniques. More importantly, the future application of the equivalent circuit to modified PBTh films would reveal exactly how each modification affects the electronic properties; be it decreasing film/charge transfer resistance, enhancing diffusion, increasing the number of charged states *etc*. The model is by no means perfect and in comparison to typical equivalent circuits, it has a relatively large error value though allowances must also be made for the film's catalytic activity and in-situ electrochemical set-up.

As indicated earlier, the need for photo-excitation meant that background and interference from the external light source would adversely affect all spectroscopic techniques. This was made more frustrating by the lack of a narrow spectral light source (laser), and the use of a broad spectrum light removed any chance of obtaining a meaningful in-situ UV-Vis spectra. Fortunately the Raman systems proved to be more resilient, though not immune and the technique was not without its own issues. In spite of this, two critical pieces of information were gained, the first being that fluorescence of an excimer species was strongly tied to that of catalytic activity. The second and most important of which was the observation of the predicted S—H band of the PBTh(S-H)$^+$ intermediate. This not only provided experimental evidence confirming our proposed mechanism but gave a much stronger basis for our subsequent computational studies.

The computational investigation of the PBTh system began initially out of curiosity as a small side project. However, as more progress was made, the usefulness of the results and the computational methods were made clear. The thermodynamic justification of the system was an important step in establishing both the relevancy of the computational techniques and the catalytic activity of PBTh. Subsequent TD-DFT models were also able to accurately point to the formation of a PBTh(S-H)$^+$ intermediate and support our Raman findings. Moreover, the visualisation of the gound, excited and triplet state molecular orbitals were able to give much more insight into how the subsequent reduction and H$_2$ release process could be achieved.

These initial studies have revealed much about the overall mechanism of PBTh and they importantly give justification for this surprising photo-system. That being said, the results are far from definitive and provide only a small part of the overall picture, crucially, solid experimental evidence (beyond the formation of S—H) is still required. Given more time, equipment and expertise, it is highly possible to yield much more definitive answers with regards to fully understanding this system. Ideas for future studies are numerous and include:

- The use of transient spectroscopy to reveal photo-kinetics
- Use of a laser light source for Raman/UV-Vis spectra to significantly reduce adverse background interference
- Design of a tailored in-situ Raman spectroscopy cell to reduce O$_2$ contamination and noise introduced from bubbling
- Optimise a Raman system via objective lens/excitation laser/substrate selection to maximise the Raman signal from the catalytically active surface

- Use of more advanced computational techniques and accurate basis sets for quantitative analysis of the ground, excited, singlet and triplet states as well as the protonation and hydrogen release mechanisms
- Applying molecular dynamics to study system kinetics
- Use of spin resonance spectroscopy to experimentally determine the presence of singlet/triplet states
- The use of photo-quenching/enhancing moieties or additives to probe its effects on the catalytic performance and infer information on the overall mechanism; *i.e.* triplet promoting species, electron withdrawing groups, use of polyselenophene *etc.*.

Summary and Concluding Remarks

The discoveries made herein are significant in the field of hydrogen evolution catalysis, both in the success of the PBTh system and in the justification of the overall mechanism. Despite the low catalytic activity, the inherent properties of PBTh such as light-harvesting capabilities, stability under applied potential and light and operation in a wide range of pH gives it an advantage over alternate systems. PBTh does not yet represent an ideal catalyst but when coupled with the ease of customisability and promising results obtained thus far, there is substantial scope for improvements.

In a broader context, it is possible that these results may lead to a new field of photo-electrocatalytic applications for conducting polymers. However, a much more thorough understanding of the operating mechanism and development of the idea is first required. While much of our mechanistic findings remain preliminary, significant strides have been made in establishing the crucial building blocks for identifying the catalytic process. This is especially noteworthy considering the complex interactions and interferences from the in-situ studies of the photo-electrocatalytic system. An abundance of improvements and future studies have been discussed and proposed. Moreover, the overarching conclusions showing the photo-electrocatalytic abilities of PBTh towards the HER are indisputable.

It is hoped that these findings would contribute significantly to solving the long standing issue of sustainable hydrogen production. Much potential remains in the development of this novel photo-active organic system.

Appendix A: Supplementary Information for Publication 1, Characterisation of a series of triarylmethane dyes as light harvesters for photo-electrochemical systems

Supplementary Information for:

Characterisation of a series of triarylmethane dyes as light harvesters for photo-electrochemical systems

Chun Hin Ng, C. André Ohlin, and Bjorn Winther-Jensen

To be published in *Dyes and Pigments*

Last updated August 11, 2014

Contents

Cyclic Voltammograms

All electrochemical cells and electrodes were cleaned via sonication in a 1:1 solution of water and ethanol for 30 minutes, followed by rinsing with DI water then acetone. They were then dried in an oven at 70°C for 30 minutes before being dried *in vacuo* at room temperature before introduction into the glove box.

The dye and TBA PF_6 salt were weighed and dried at a temperature of 50°C before being sealed and transferred to a nitrogen glove box. Anhydrous acetonitrile solvent (Sigma Aldrich) was extracted onto freshly activated molecular sieves and transferred into the glove box where they were stored for the duration of the experimentation. The analyte solutions were made up in-situ to prevent contamination from air or water.

Cyclic voltammetry was conducted by a variable multichannel potentiostat (Princeton Applied Research) and analysed using EC Lab v10.19. An initial CV without ferrocene was performed to determine the redox behaviours of the neat dye solution; this has been included in the following voltammograms and corrected vs Fc/Fc^+ using redox peaks common to the dye. The internal reference of Fc/Fc^+ was then added to provide an accurate calibration. In accordance with convention, the first clearly identifiable redox couple ($E_{1/2}$) on the oxidation (E_{ox}) and reduction (E_{red}) sides were assigned as the HOMO and LUMO energy levels, respectively. These energy levels were then converted to absolute energies by referencing against Fc/Fc^+ where $E_{1/2}$ of Fc/Fc^+ is -4.988 eV. In cases where $E_{1/2}$ was unable to be determined, E_{peak} was utilised instead with an empirically determined correction factor of ≈ 0.3 V compared with $E_{1/2}$, this has been presented as the error bars in figure 4C of the main article.
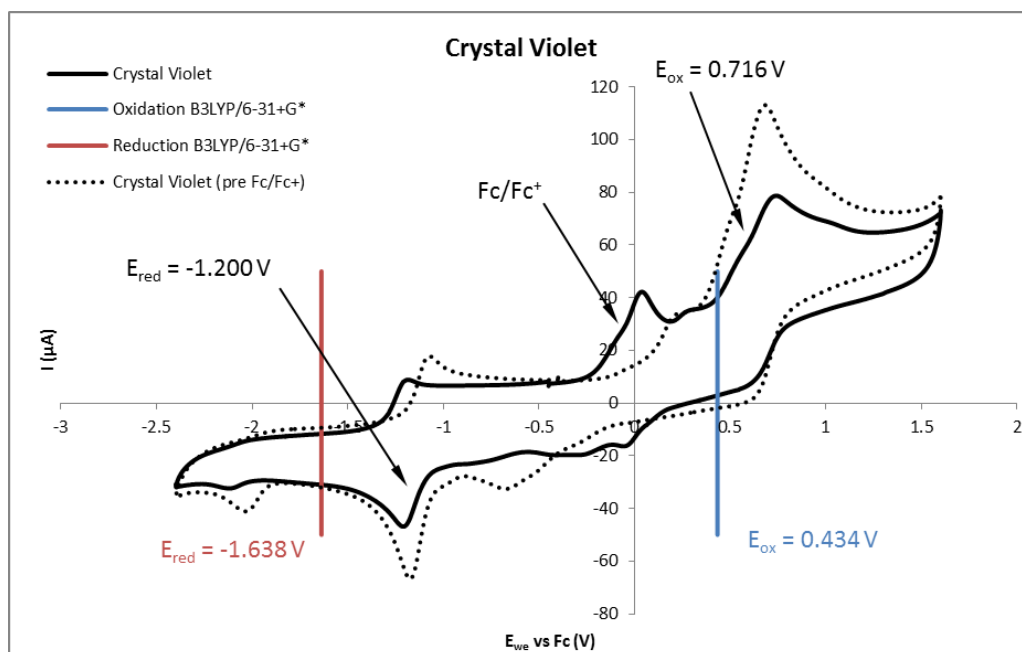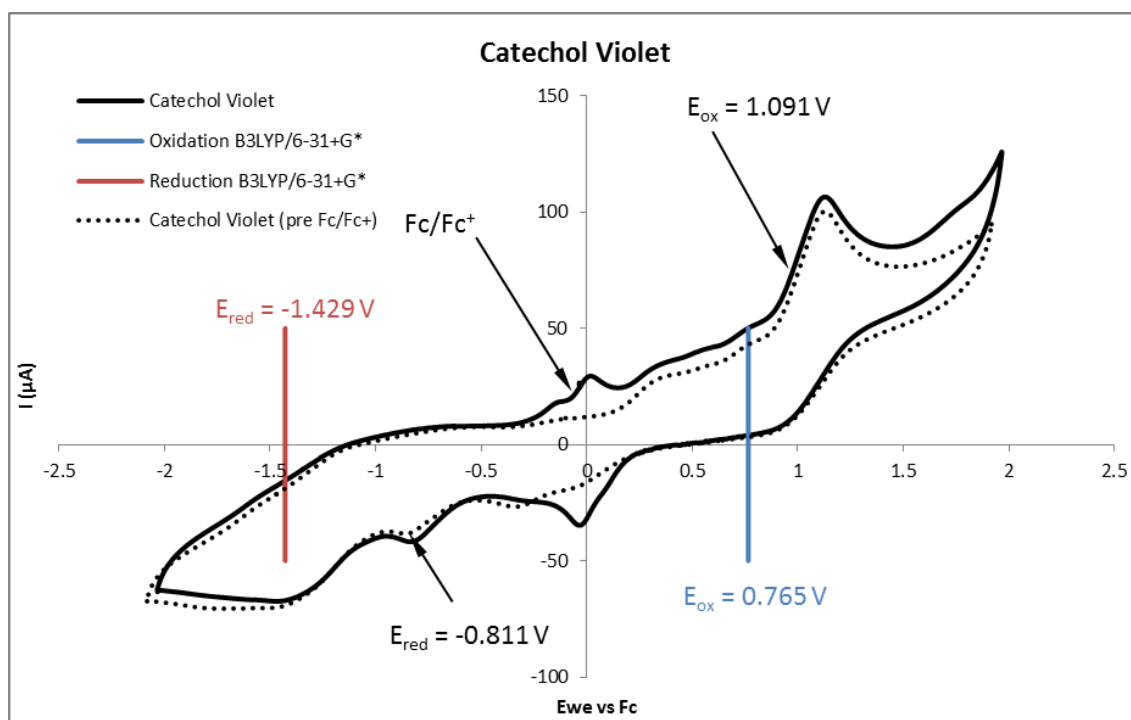

Figure S1: Crystal Violet (0.5 mM) voltammogram, in acetonitrile with 0.1 M [TBA][PF_6] as background salt, and with added Fc/Fc^+ as an internal standard. E_{ox} and E_{red} were determined using $E_{1/2}$.
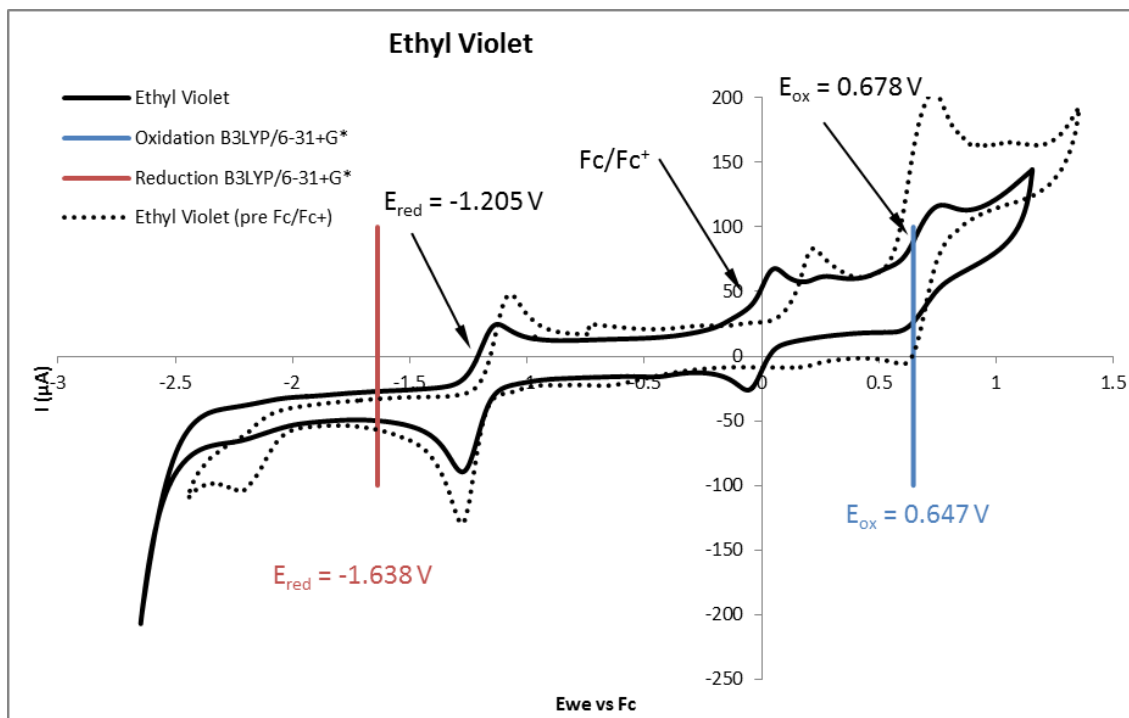
Figure S2: Ethyl Violet (0.5 mM) voltammogram, in acetonitrile with 0.1 M [TBA][PF$_6$] as background salt, and with added Fc/Fc$^+$ as an internal standard. E$_{ox}$ and E$_{red}$ were determined using E$_{1/2}$.
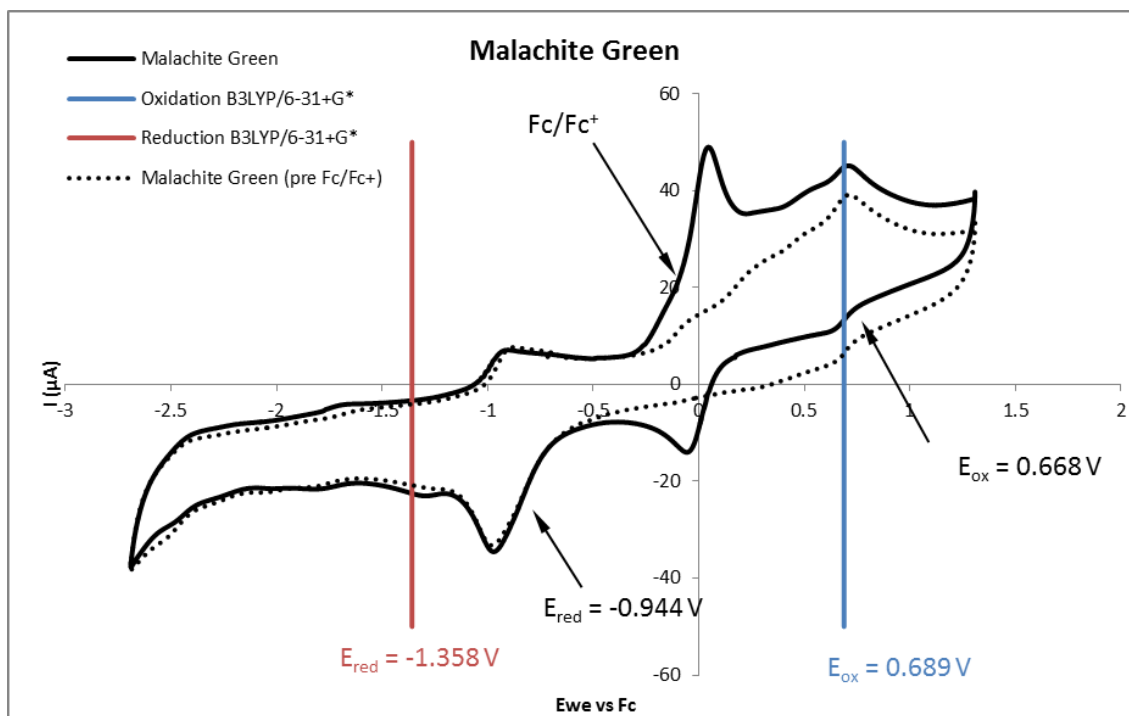
Figure S3: Malachite Green (0.5 mM) voltammogram, in acetonitrile with 0.1 M [TBA][PF$_6$] as background salt, and with added Fc/Fc$^+$ as an internal standard. E$_{ox}$ and E$_{red}$ were determined using E$_{1/2}$.
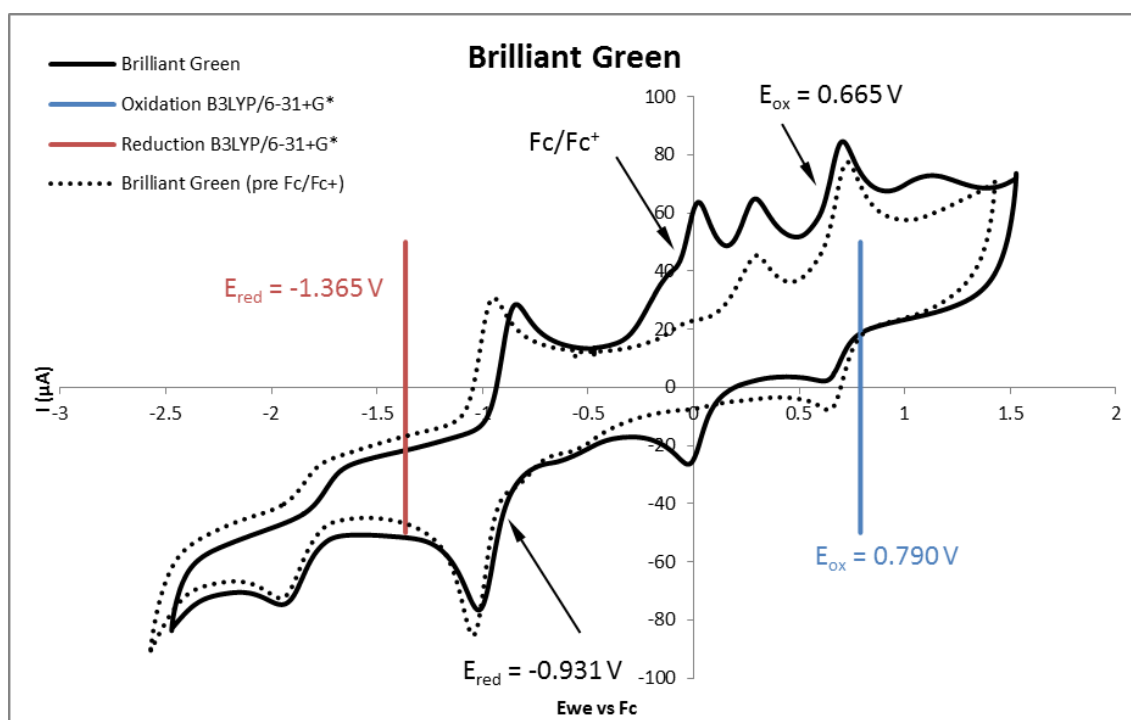
Figure S4: Brilliant Green (0.5 mM) voltammogram, in acetonitrile with 0.1 M [TBA][PF6] as background salt, and with added Fc/Fc+ as an internal standard. E_{ox} and E_{red} were determined using $E_{1/2}$.
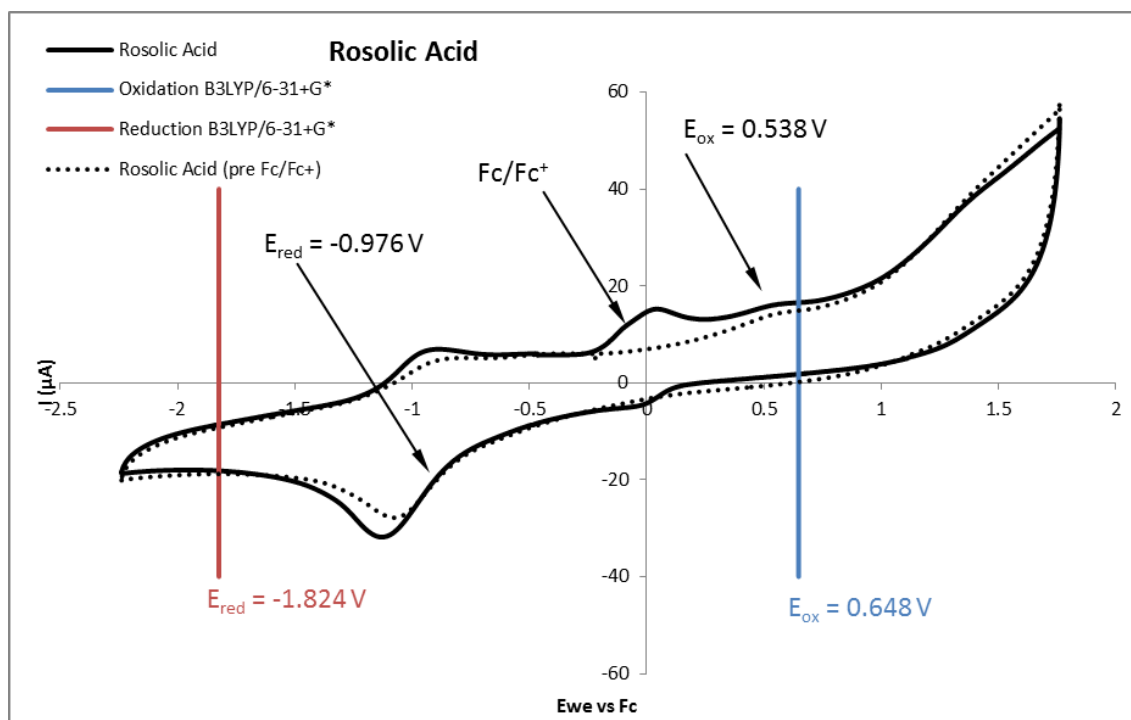
Figure S5: Rosolic Acid (0.5 mM) voltammogram, in acetonitrile with 0.1 M [TBA][PF$_6$] as background salt, and with added Fc/Fc$^+$ as an internal standard. E_{ox} was calculated using E_{peak}, E_{red} was determined using $E_{1/2}$.
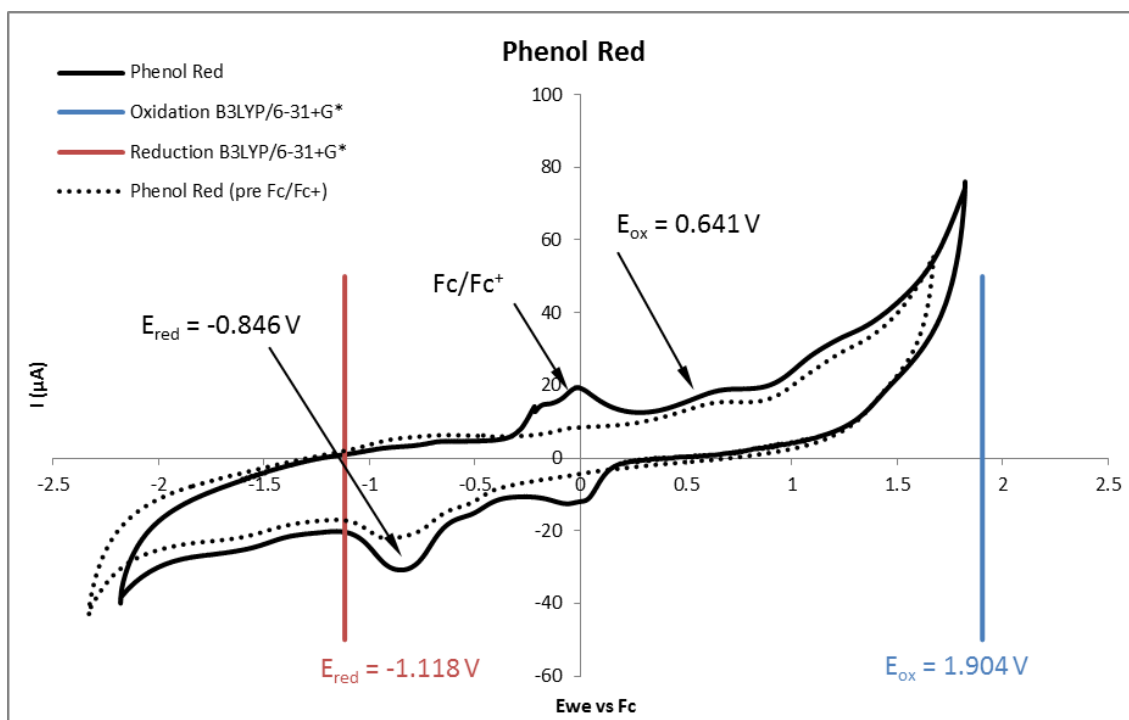
Figure S6: Phenol Red (0.5 mM) voltammogram, in acetonitrile with 0.1 M [TBA][PF$_6$] as background salt, and with added Fc/Fc$^+$ as an internal standard. E$_{ox}$ and E$_{red}$ was calculated using E$_{peak.}$
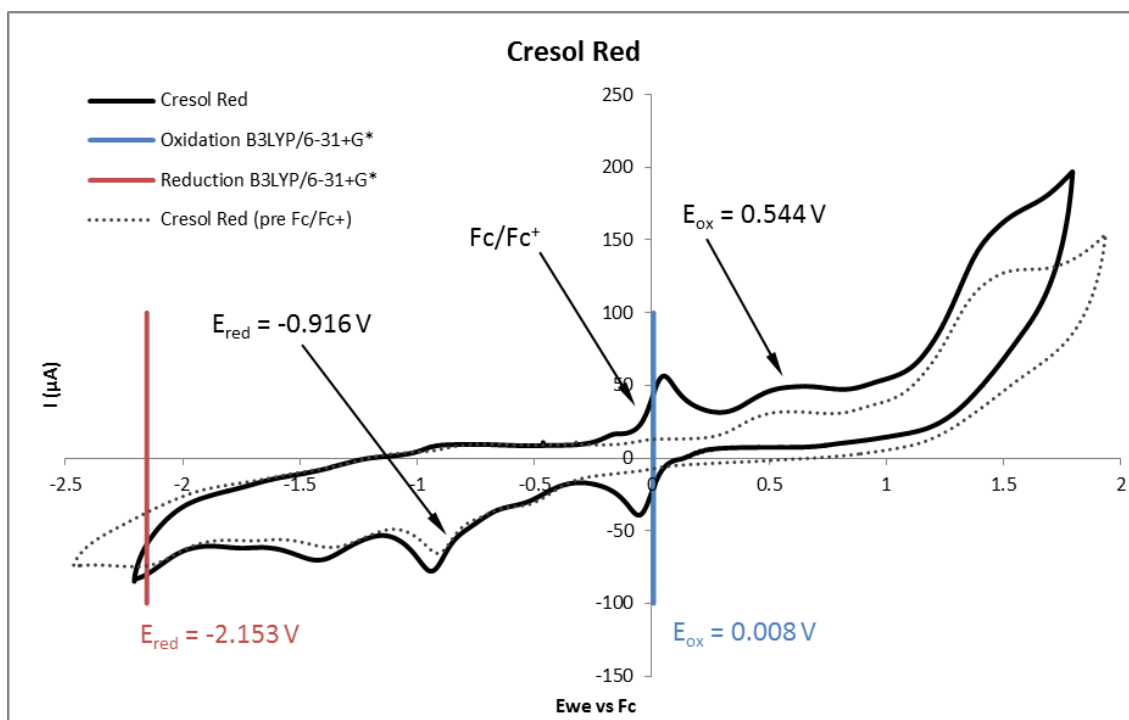
Figure S7: Cresol Red (0.5 mM) voltammogram, in acetonitrile with 0.1 M [TBA][PF$_6$] as background salt, and with added Fc/Fc$^+$ as an internal standard. E$_{ox}$ was determined using E$_{peak}$, E$_{red}$ was calculated using E$_{1/2.}$
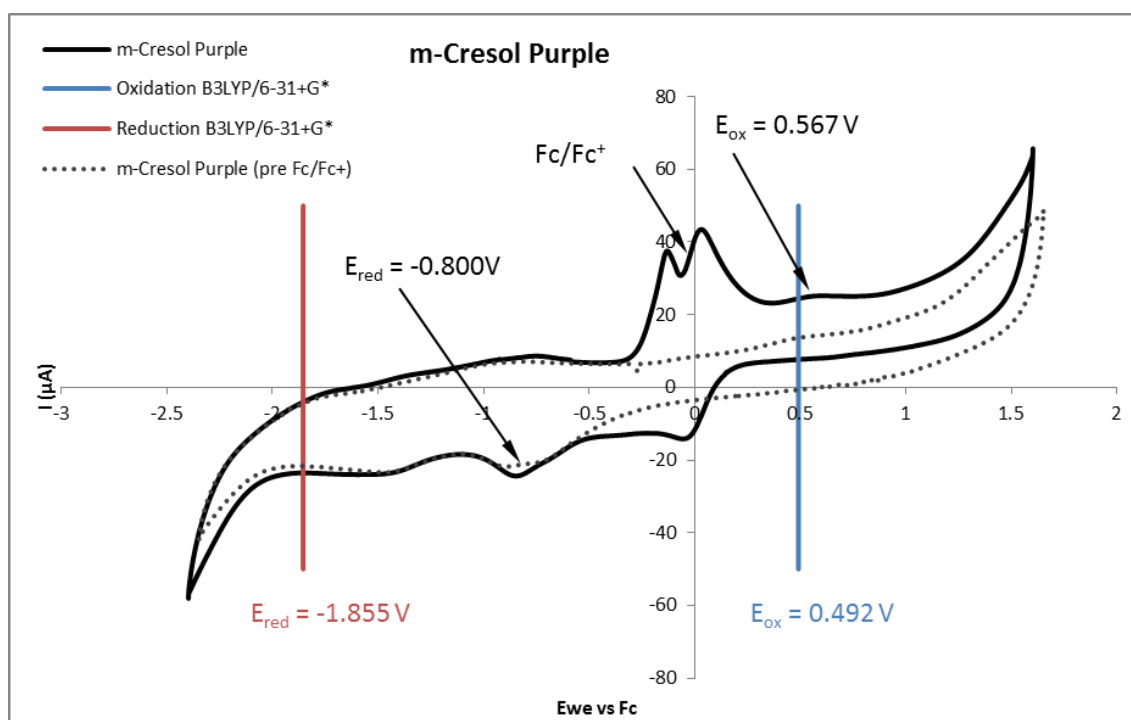
Figure S8: m-Cresol Purple (0.5 mM) voltammogram, in acetonitrile with 0.1 M [TBA][PF$_6$] as background salt, and with added Fc/Fc$^+$ as an internal standard. E$_{ox}$ was determined using E$_{peak}$, E$_{red}$ was calculated using E$_{1/2}$.

Figure S9: Catechol Violet (0.5 mM) voltammogram, in acetonitrile with 0.1 M [TBA][PF$_6$] as background salt, and with added Fc/Fc$^+$ as an internal standard. E$_{ox}$ was determined using E$_{1/2}$, E$_{red}$ was calculated using E$_{peak}$.

Optical Spectroscopy (UV-Vis and Fluorescence)

UV-Vis spectra were acquired using a Jasco V 670 Spectrophotometer. Fluorescence spectra were obtained on a Horiba Fluoromax 4 spectrofluorometer. The experiments were conducted in acetonitrile.

Deconvolution of peaks was occasionally required due to the presence of the oxidized/reduced species. In these cases, the fitted Gaussian peak is displayed and the corresponding intercept labelled.

UV-vis spectroscopy was also conducted on the dyes in a 1:1 H_2O:EtOH solution for confirmation of the dye's purity. Comparison between the experimental and literature λ_{max} for each dye species is presented in Table S1. One drop of 0.1 M NaOH was added to the dyes **4a-c** for consistency with literature values (alkaline conditions).
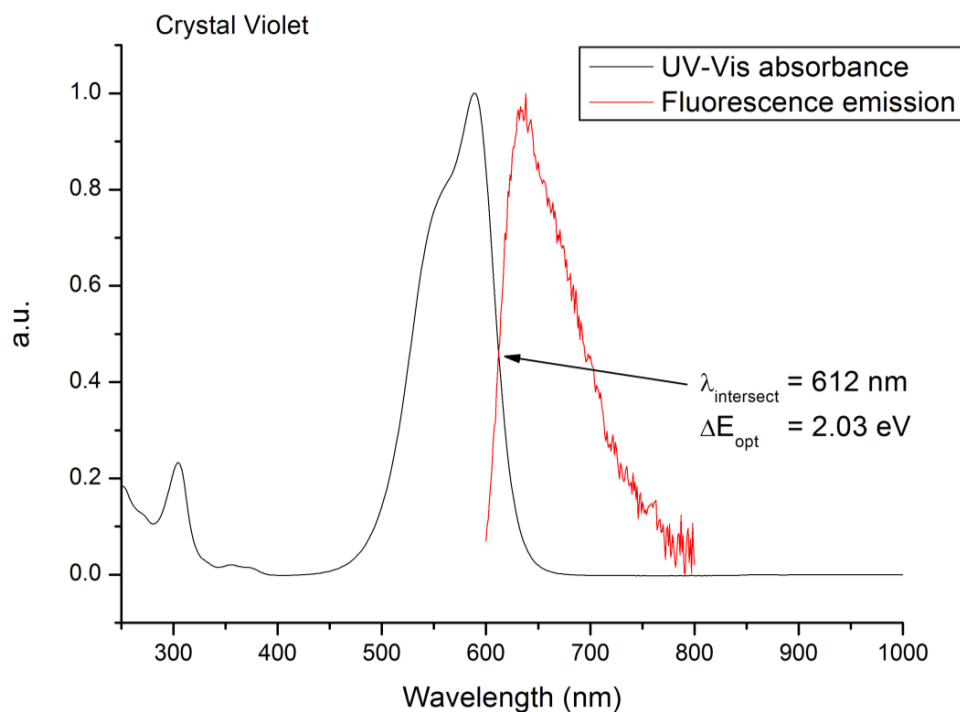
Figure S10: Crystal Violet in acetonitrile. For UV-Vis spectroscopy, 0.03 mM dye was used. For fluorescence spectroscopy, 0.01 mM dye was used.
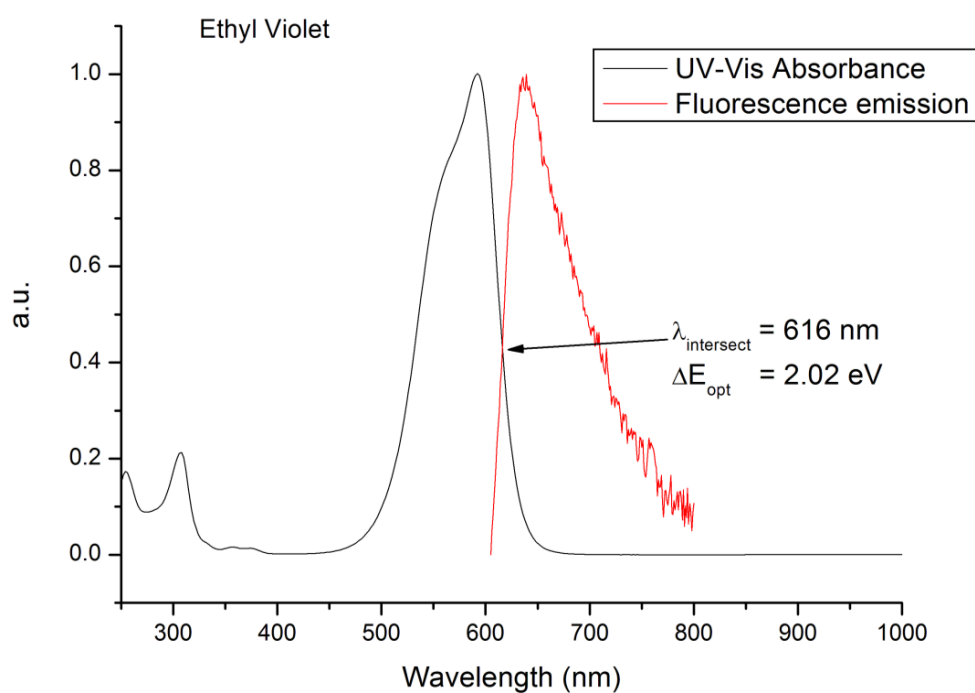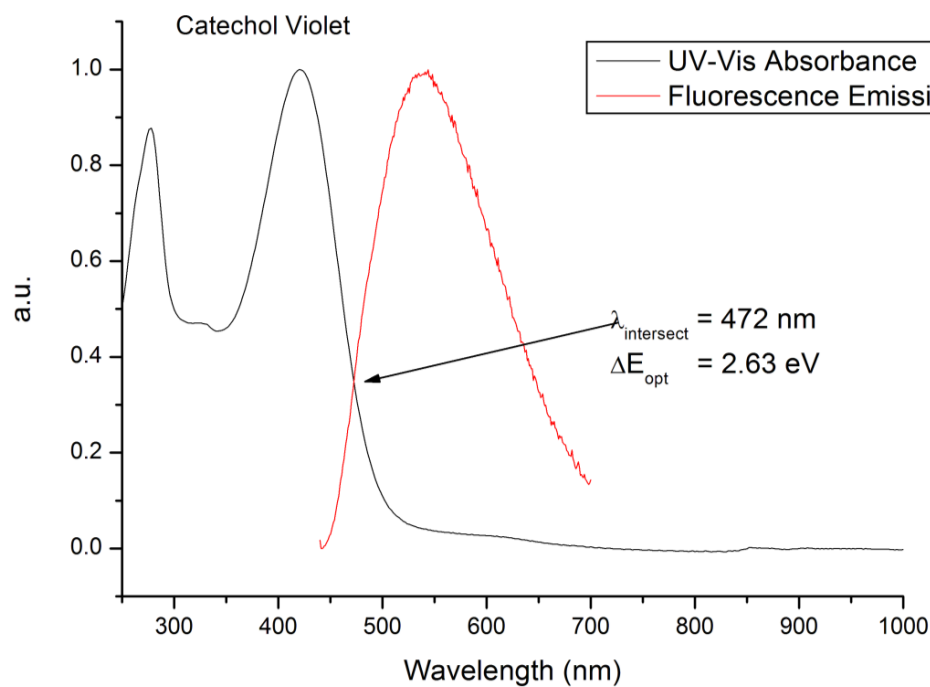
Figure S11: Ethyl Violet in acetonitrile. For UV-Vis spectroscopy, 0.03 mM dye was used. For fluorescence spectroscopy, 0.01 mM dye was used.
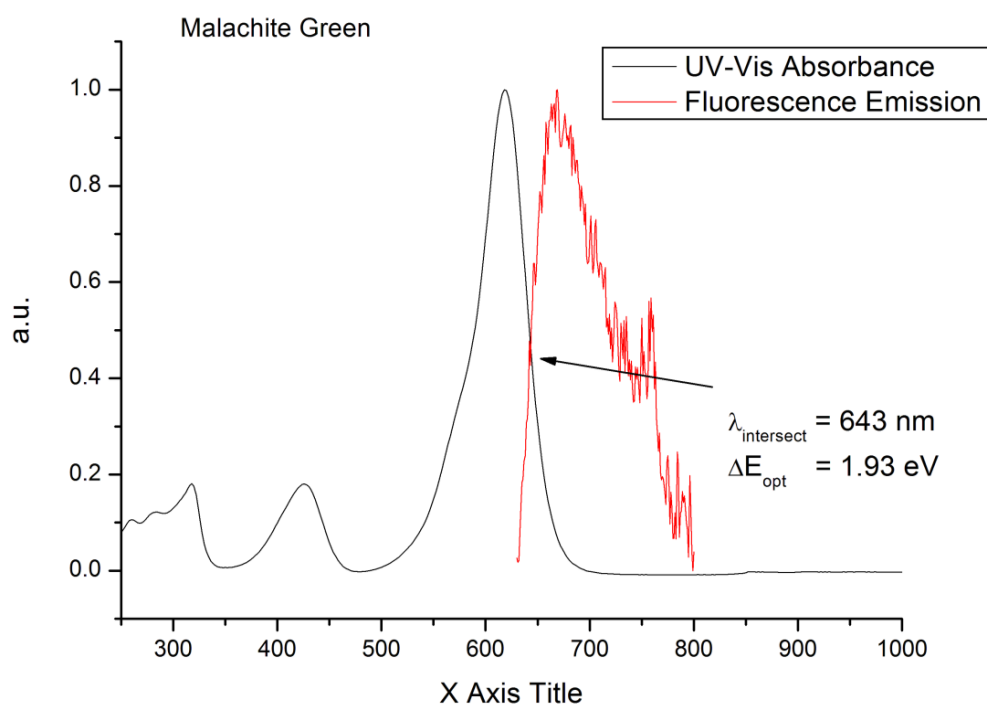
Figure S12: Malachite Green in acetonitrile. For UV-Vis spectroscopy, 0.03 mM dye was used. For fluorescence spectroscopy, 0.01 mM dye was used.
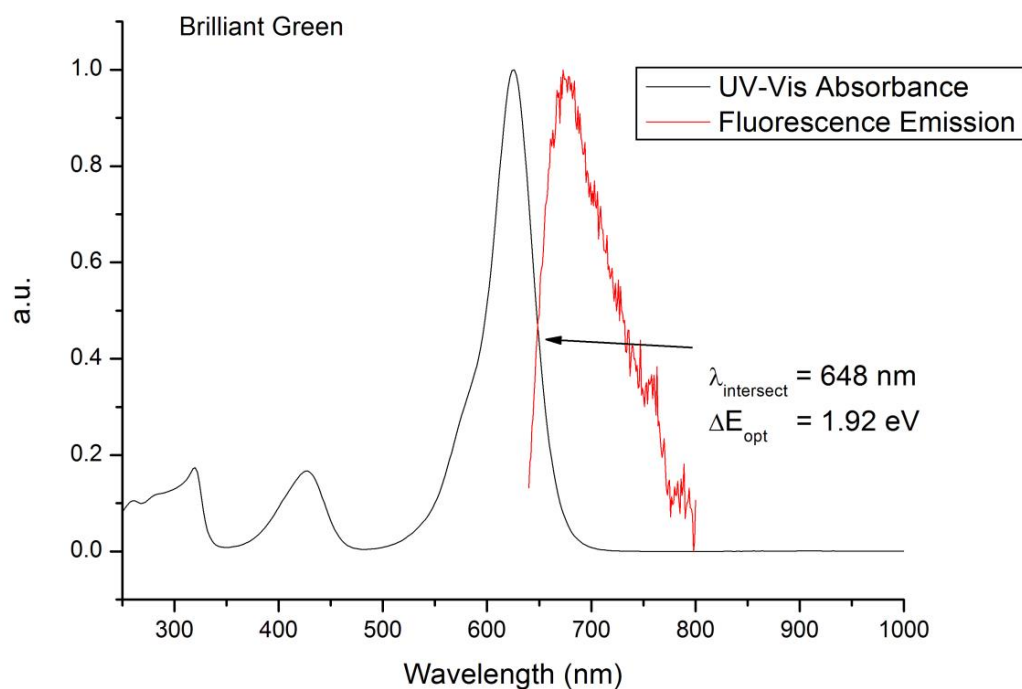
Figure S13: Brilliant Green in acetonitrile. For UV-Vis spectroscopy, 0.03 mM dye was used. For fluorescence spectroscopy, 0.01 mM dye was used.
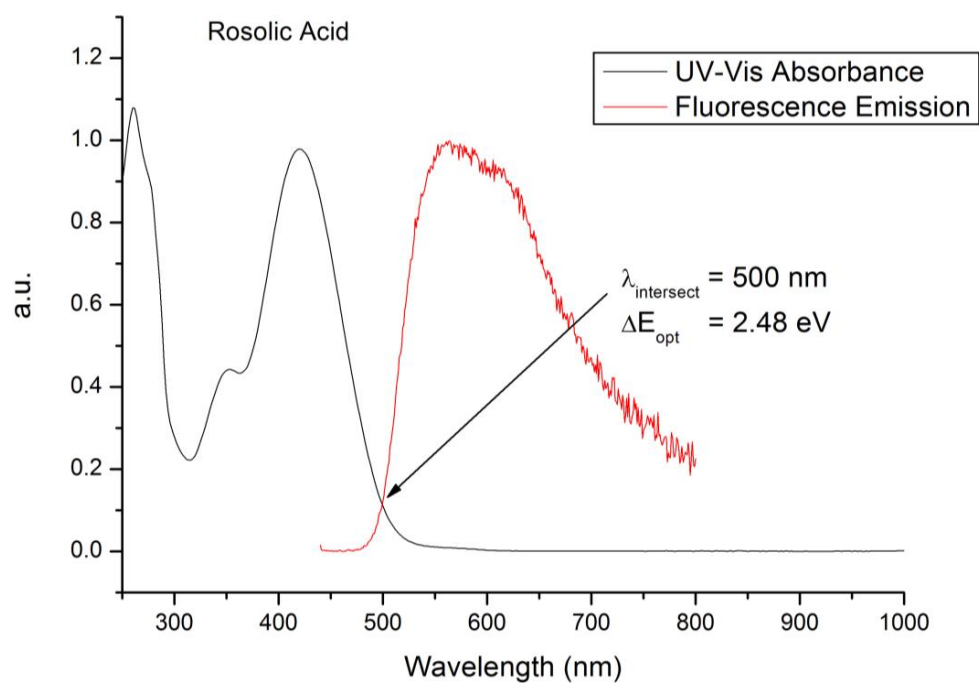
Figure S14: p-Rosolic Acid in acetonitrile. For UV-Vis spectroscopy, 0.03 mM dye was used. For fluorescence spectroscopy, 1.69 mM dye was used.
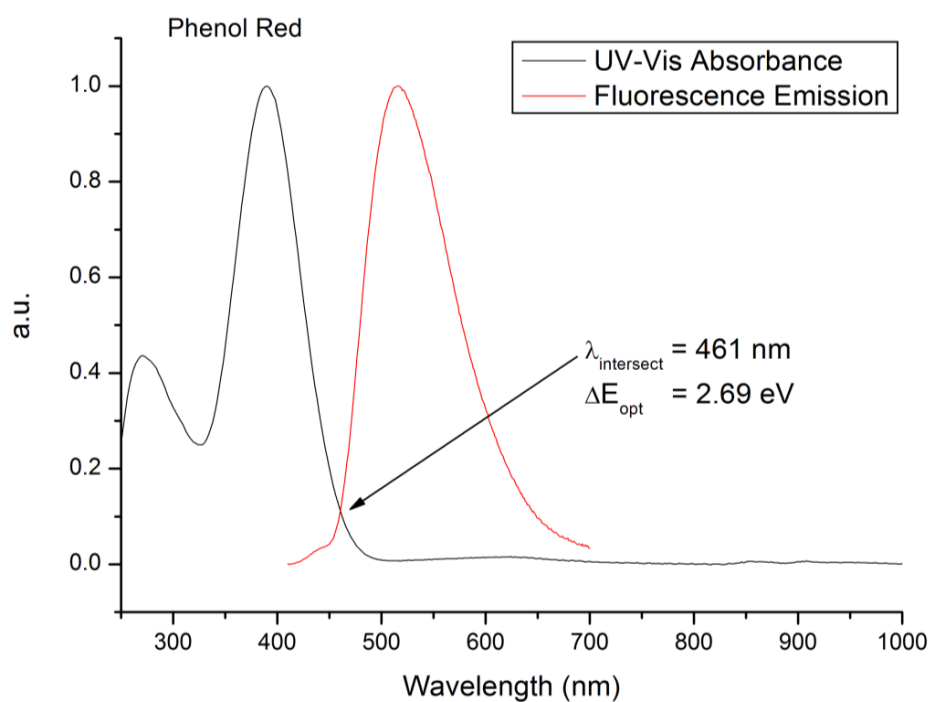
Figure S15: Phenol Red in acetonitrile. For UV-Vis spectroscopy, 0.03 mM dye was used. For fluorescence spectroscopy, 0.31 mM dye was used.
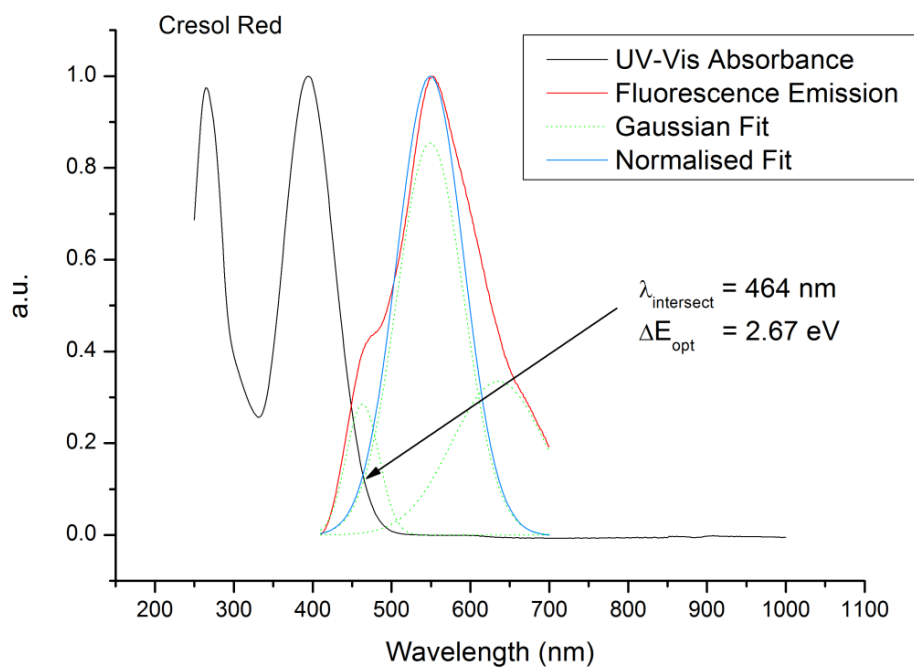
Figure S16: Cresol Red in acetonitrile. For UV-Vis spectroscopy, 0.03 mM dye was used. For fluorescence spectroscopy, 1.28 mM dye was used. The peaks were deconvoluted with the central peak (corresponding to the main fluorescence) was normalised for the determination of the intersection.
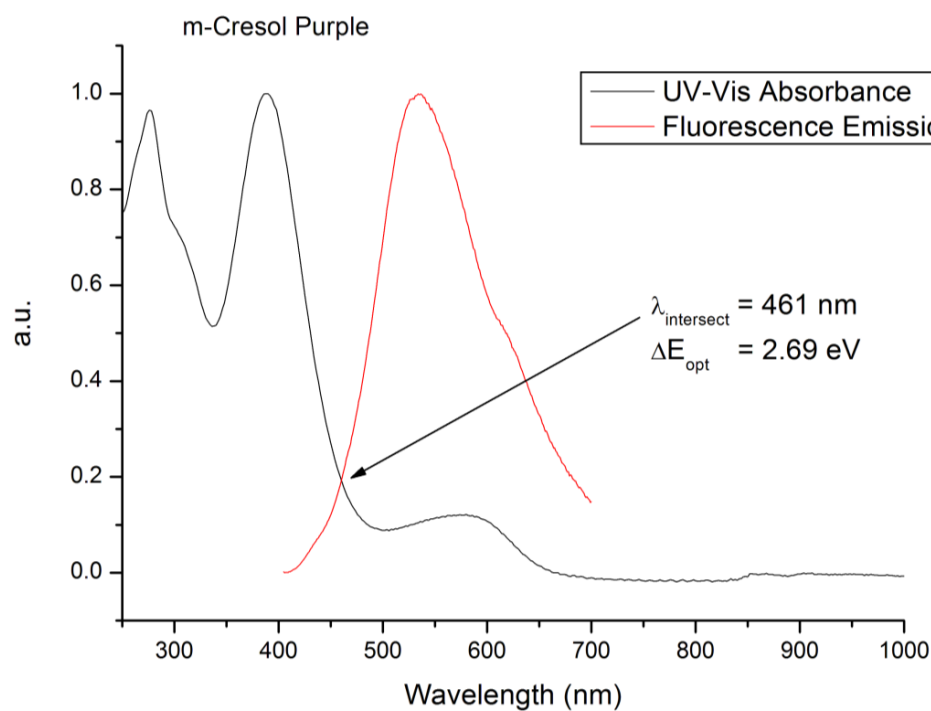
Figure S17: m-Cresol Purple in acetonitrile. For UV-Vis spectroscopy, 0.03 mM dye was used. For fluorescence spectroscopy, 0.54 mM dye was used.

.

Figure S18: Catechol Violet in acetonitrile. For UV-Vis spectroscopy, 0.03 mM dye was used. For fluorescence spectroscopy, 0.30 mM dye was used.

Table S1: Comparison of the experimental and literature λ_{max} for each dye species.

Dye	Experimental λ_{max} (nm)	Literature λ_{max} (nm)[1]
1a – Crystal Violet	592	588
1b – Ethyl Violet	596	595
2a – Malachite Green	622	612-622
2b – Brilliant Green	628	628-632
3 – Rosolic Acid	466	482
4a – Phenol Red	564, 364	555-561, 357-363
4b – Cresol Red	576, 366	570, 367
4c – m-Cresol Purple	586, 376	579, 371
4d – Catechol Violet	444	450

---

[1] Literature λ_{max} were taken from Sigma Aldrich.

Computational Definitions and Conversions

The standard definition of the 6-31+G* basis set was used.[1-4]

The exchange correlation function of B3LYP as implemented in NWChem was used for all calculations and is defined as:

$$E_{XC} = a_0 E_X^{HF} + (1 - a_0)E_X^{Slater} + a_X \delta E_X^{Becke88} + (1 - a_C)E_C^{VWN\_1\_RPA} + a_C \delta E_C^{LYP}$$ ………... (1)

Where

$$a_0 = 0.20, a_X = 0.72, a_C = 0.81$$

The correlation exchange functional (E_{XC}) in equation (1) consists of the Hartree Fock, Slater[5] and Becke88[6] exchange functionals (E_x) as well as the VWN_1_RPA[7] and LYP[8] correlation functionals. Non-local contributions are indicated by δ.

The free energy (G) of each species was calculated via three separate calculations, namely, an initial geometry optimisation and the corresponding ground state energy (ε_0), followed by a single point energy calculation with the COnductor-like Screening Model[9,10] for an implicit solvation energy (G_{solv}) and a vibrational calculation for enthalpy (H_{corr}) and entropy (S) correction. These results are compiled together to give the free energy (G) of single species via equation 2:

$$G = \varepsilon_0 + H_{corr} - T \cdot S - G_{solv}$$ ……………………………………………….…… (2)

Where T = 298 K

The ΔG of each redox reaction (oxidation and reduction) was determined by the difference between the ground state and corresponding redox state. The oxidised and reduced states are defined as the removal and addition of an electron from the ground state respectively. No protonation/deprotonation from the ground state was applied to any of the oxidised/reduced species.

Each ΔG value was then converted to an absolute potential using:

$$E = -\frac{\Delta G}{nF}$$ ………………………………………………………………….…. (3)

The absolute potential (eV) was converted to potential vs Fc/Fc⁺ and vice versa via the relationship:

$$E(eV) = -4.988 \ eV - E(V \ vs \ Fc/Fc^+)$$ ………………………………………….…… (4)

Computational Data

Table S2: Tabulated computational results showing each dye and its species associated calculations.

Dye	Species	ε₀ (Hartree)	H_corr (Hartree)	S (J mol⁻¹ K⁻¹)	G_solv (kJ mol⁻¹)	G (kJ mol⁻¹)	ΔG (kJ mol⁻¹)	E (eV)	E vs Fc (V)	ΔE_calc (eV)
1a - Crystal Violet	Ground	-1134.79	0.53	751.66	135.31	-2975509				
	Oxidized	-1134.46	0.53	762.71	477.36	-2974985	523.131	-5.422	**0.434**	
	Reduced	-1134.95	0.53	753.24	26.79	-2975832	323.249	-3.350	**-1.638**	2.07
1b - Ethyl Violet	Ground	-1370.68	0.71	881.50	126.19	-3593815				
	Oxidized	-1370.36	0.71	880.82	440.32	-3593271	543.685	-5.635	**0.647**	
	Reduced	-1370.84	0.71	903.26	22.45	-3594138	323.222	-3.350	**-1.638**	2.28
2a - Malachite Green	Ground	-1000.81	0.45	661.23	141.49	-2624259				
	Oxidized	-1000.46	0.45	687.20	505.49	-2623711	547.711	-5.677	**0.689**	
	Reduced	-1000.98	0.45	645.22	24.62	-2624609	350.217	-3.630	**-1.358**	2.05
2b - Brilliant Green	Ground	-1158.07	0.57	753.18	131.88	-3036466				
	Oxidized	-1157.73	0.57	747.06	471.04	-3035909	557.511	-5.778	**0.790**	
	Reduced	-1158.24	0.57	762.29	20.94	-3036816	349.543	-3.623	**-1.365**	2.16
3 - p-Rosolic Acid	Ground	-958.11	0.30	576.24	72.44	-2512572				
	Oxidized	-957.86	0.30	570.06	199.68	-2512028	543.776	-5.636	**0.648**	
	Reduced	-958.17	0.30	579.82	217.69	-2512877	305.255	-3.164	**-1.824**	2.47

Table S2 (cont.): Tabulated computational results showing each dye and its species associated calculations.

Dye	Species	ε_0 (Hartree)	H_{corr} (Hartree)	S (J mol⁻¹ K⁻¹)	G_{solv} (kJ mol⁻¹)	G (kJ mol⁻¹)	ΔG (kJ mol⁻¹)	E (eV)	E vs Fc (V)	ΔE_{calc} (eV)
4a - Phenol Red	Ground	-1506.70	0.31	613.06	71.02	-3951483				
	Oxidized	-1506.39	0.31	629.54	199.09	-3950818	664.931	-6.892	**1.904**	
	Reduced	-1506.77	0.31	638.99	246.33	-3951856	373.437	-3.870	**-1.118**	3.02
4b - Cresol Red	Ground	-1584.82	0.35	593.45	225.68	-4156444				
	Oxidized	-1584.70	0.35	601.21	64.83	-4155962	482.003	-4.996	**0.008**	
	Reduced	-1584.78	0.35	593.92	589.63	-4156718	273.521	-2.835	**-2.153**	2.16
4c - m-Cresol Purple	Ground	-1584.81	0.36	666.35	222.67	-4156419				
	Oxidized	-1584.65	0.36	669.05	105.88	-4155890	528.699	-5.480	**0.492**	
	Reduced	-1584.78	0.35	677.74	601.46	-4156721	302.316	-3.133	**-1.855**	2.35
4d - Catechol Violet	Ground	-1657.13	0.32	663.41	79.34	-4346068				
	Oxidized	-1656.87	0.32	667.09	212.09	-4345512	555.107	-5.753	**0.765**	
	Reduced	-1657.21	0.32	663.37	217.23	-4346411	343.430	-3.559	**-1.429**	2.19

Mass spectroscopy

Electrospray-ionisation mass spectroscopy (ESI-MS) was conducted on a Waters micromass ZQ QMS connected to an Agilent 1200 series HPLC system for determination of purity. Flow rate used was 300 uL/min (MeOH) with a cone voltage of 35 V.

The mass spectrum for each dye is presented below. Some peaks are due to the loss of a methyl ($\Delta m/z$ = 14) or ethyl ($\Delta m/z$ = 28) group from the main dye that maybe due to collision induced dissociation. Other peaks are likely due to trace amounts of contaminating species but have been deemed acceptable as our primary goal of the study is to investigate commercially available dyes. We aim to analyse dyes for their electrochemical and optical properties, **in their commercial form**, and determine whether or not they have potential applications in photo-electrochemical systems. The danger of purification is that those findings on chemically pure dyes may lead to conclusions that are not applicable to their commercially available analogues.

It should be further mentioned that the percentage of contaminants is minimal; though we have included Rosolic Acid for completeness of results despite it having a technical purity of 85% and contains more contaminants than other species. Nevertheless, we do not believe that our overall conclusions from the findings will differ. Redox active and reversible dyes such as ethyl violet will remain so while dyes with poor electrochemical properties will not suddenly switch to a redox active state with purification.
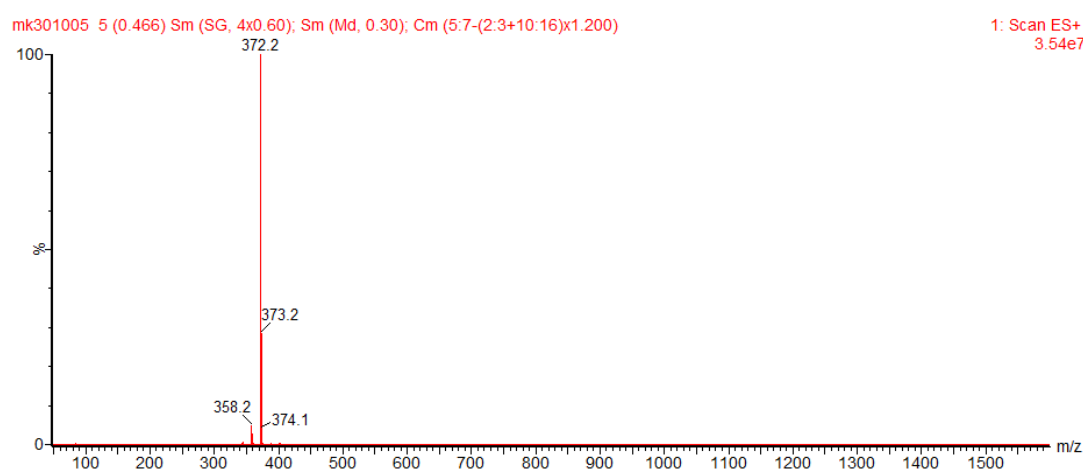
Figure S19: Mass spectrum of **1a** Crystal Violet, m/z = 372.2
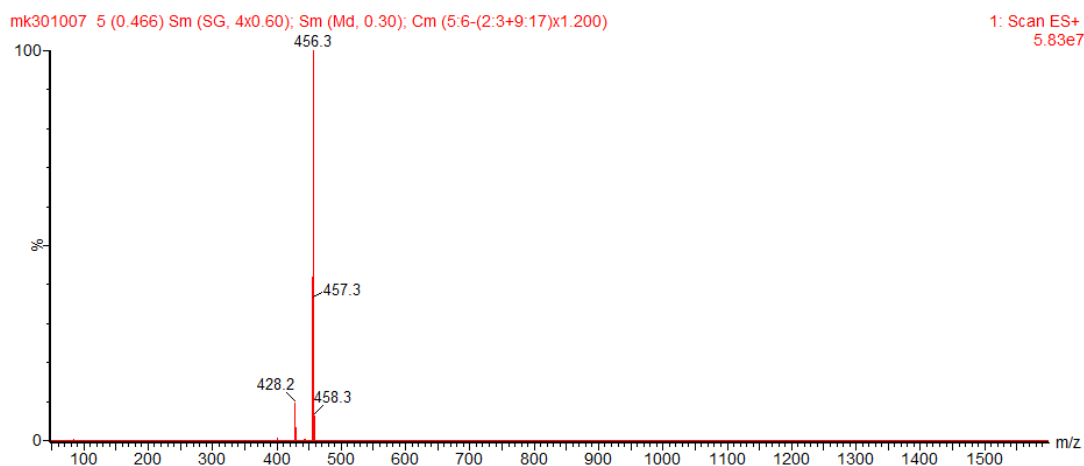
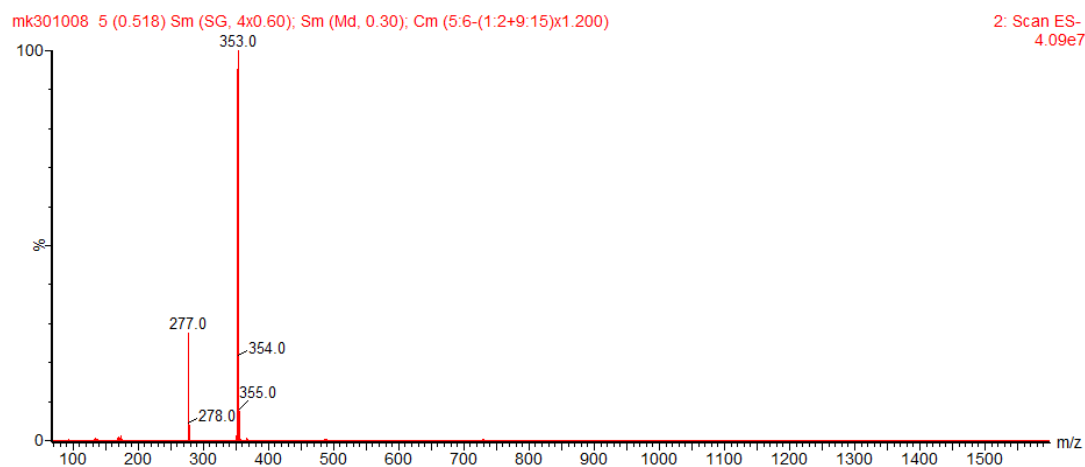**Figure S20:** Mass spectrum of **1b** Ethyl Violet, m/z = 456.3
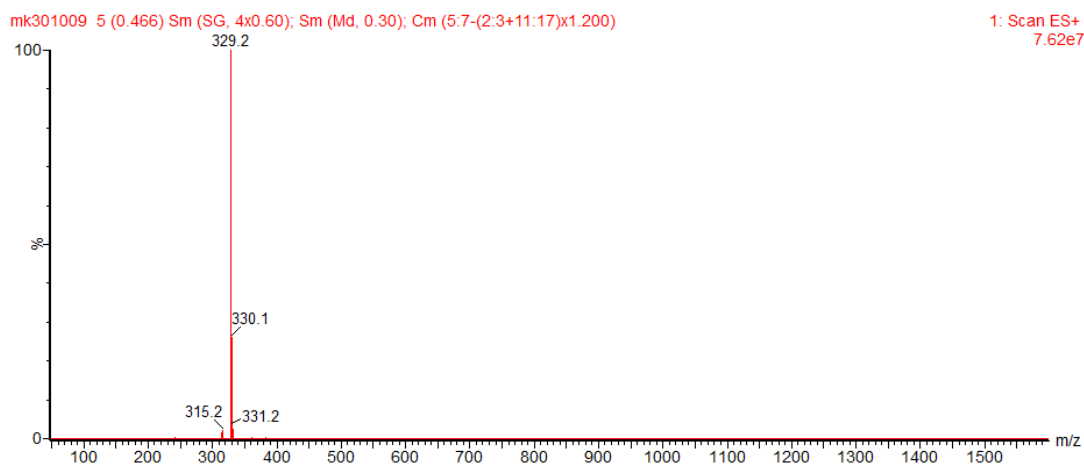
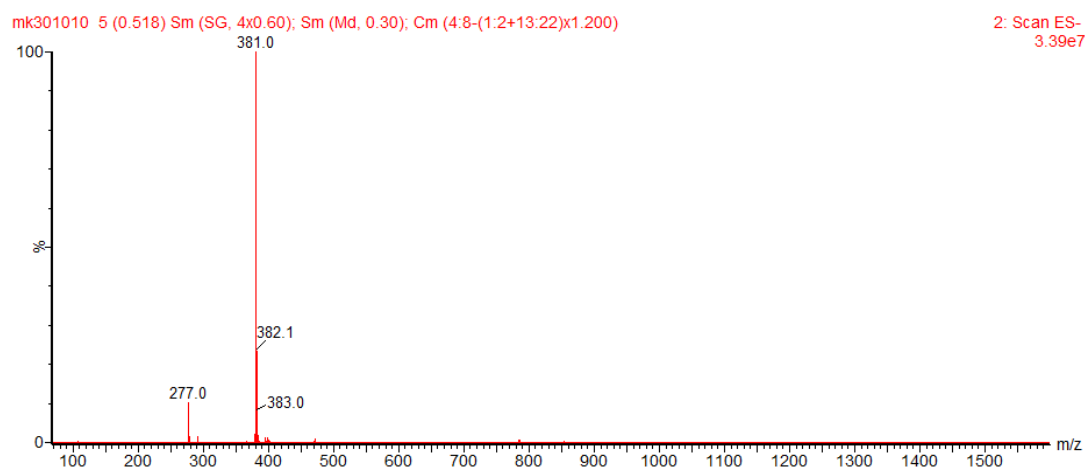**Figure S21:** Mass spectrum of **2a** Malachite Green, m/z = 329.2
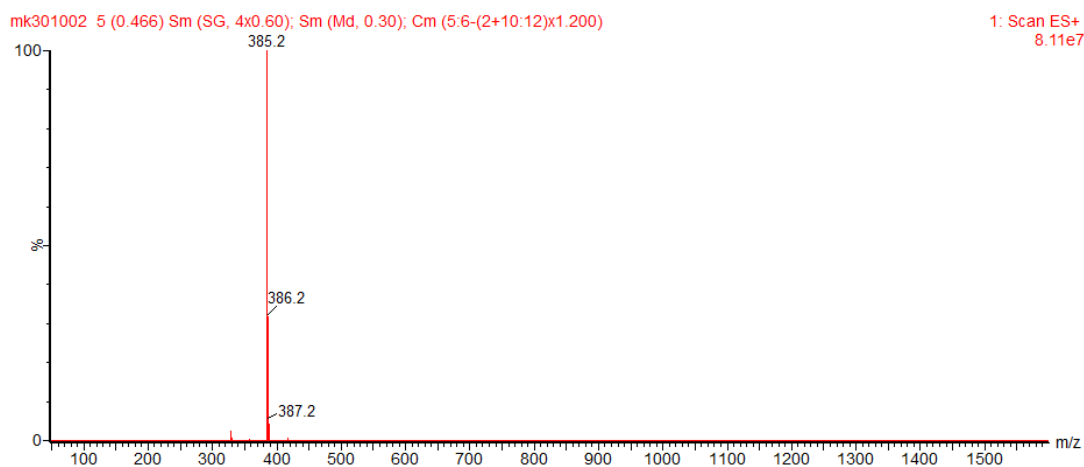
Figure S22: Mass spectrum of **2b** Brilliant Green, m/z = 385.2
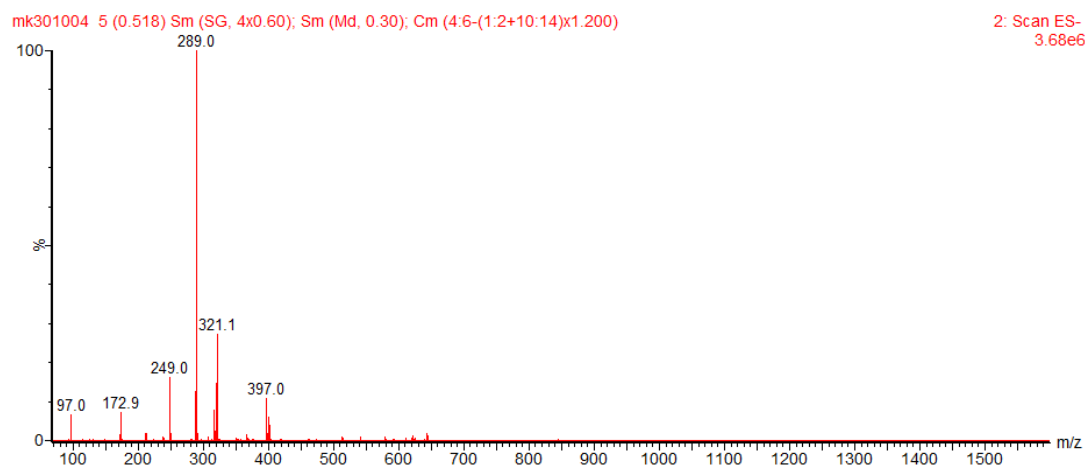
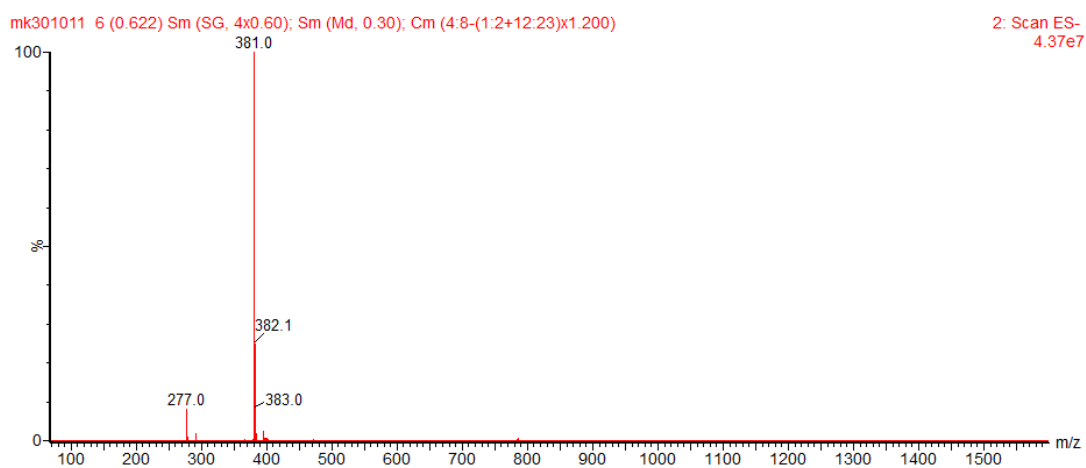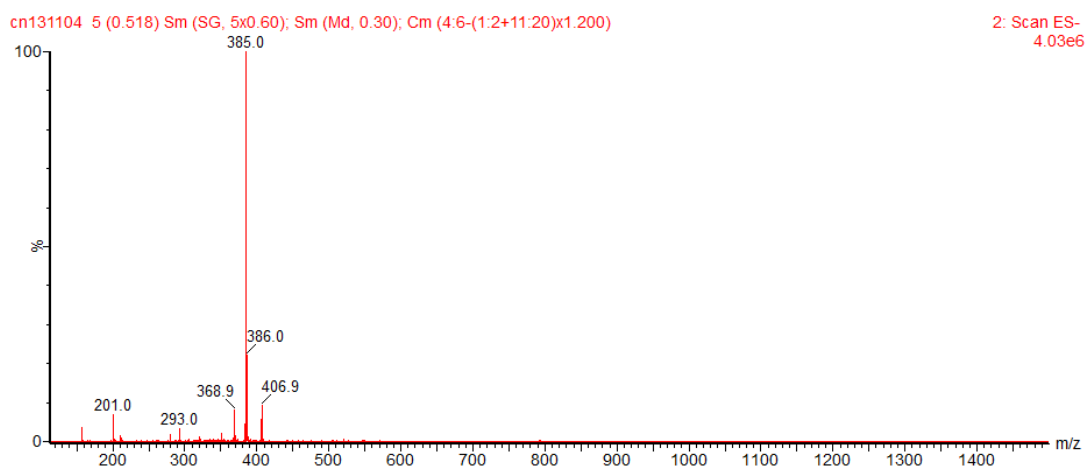**Figure S23:** Mass spectrum of **3** Rosolic Acid, m/z = 289.0

Figure S24: Mass spectrum of **4a** Phenol Red, m/z = 353.0

Figure S25: Mass spectrum of **4b** Cresol Red, m/z = 381.1

Figure S26: Mass spectrum of **4c** m-Cresol Purple, m/z = 381.1

Figure S27: Mass spectrum of **4d** Catechol Violet, m/z = 385.0

Appendix B: Supplementary Information for Publication 2, Photo-electrocatalytic H$_2$ evolution on poly(2,2'-bithiophene) at neutral pH

Supporting Information for:

Photoelectro-catalytic H_2 evolution on poly(2,2-bithiophene) at neutral pH

Chun Hin Ng, Orawan Winther-Jensen, Bartlomiej Kolodziejczyk, C. André Ohlin and Bjørn

Winther-Jensen

To be published in International Journal of Hydrogen Energy

Last updated 12th May, 2014

Polymerisation Process

The glassy carbon substrate was prepared by polishing with a 1 µm diamond suspension to a mirror finish. Following ultrasonication for 15 minutes in a 2:1 mixture of H_2O:EtOH, the substrate was being rinsed in acetone and left to dry. The oxidant for the polymerisation process was deposited by spin coating 40% w/v Fe(III) p-toluene sulphonate in n-butanol (used as is from Yacoo Chemical Reagent Co. Ltd.) onto the glassy carbon substrate (1500 RPM, 30 seconds). The glassy carbon with the Fe(III) oxidant is then placed in a PBTh vapour phase polymerisation (VPP) chamber and left to polymerise for one hour at 70 °C; the VPP chamber consists of a sealed glass jar containing 2,2'-bithiophene monomer, used as is from Sigma Aldrich (CAS No. 492-97-7). The resulting thin film is then rinsed and left to soak in 1 mmol L^{-1} p-toluenesulphonic acid for approximately 15 hours to remove residual iron before being left to dry. This acid wash step has been shown to effectively remove Fe(II) and Fe(III) from the polymer film and is described in an upcoming paper ("The Reduction of Oxygen on Iron(II) Oxide/PEDOT Composite Thin Film Electrodes" by Robert Kerr, Cristina Pozo-Gonzalo, Maria Forsyth and Bjorn Winther-Jensen, under review), the removal of iron is further confirmed by EDX measurements (figure S7).
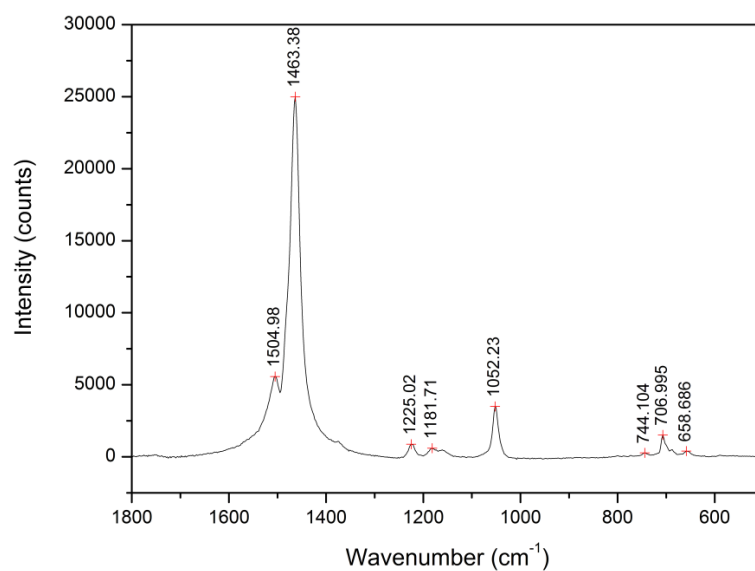
Characterisation

The resulting films were characterised via UV-Vis and Raman spectroscopy using a Jasco V 670 Spectrophotometer and Jobin Yvon T64000 Raman system, respectively. UV-Vis spectra were taken on PBTh films polymerised on glass slides while Raman spectra of PBTh films were obtained on glassy carbon substrates. The polymerisation process was conducted in the same manner as previously mentioned (save for the different substrate).

The mismatch in absorption of the film and the emission of the lamp results in a lower photoefficiency that may be improved by the use of an alternate photo-absorber or light source.
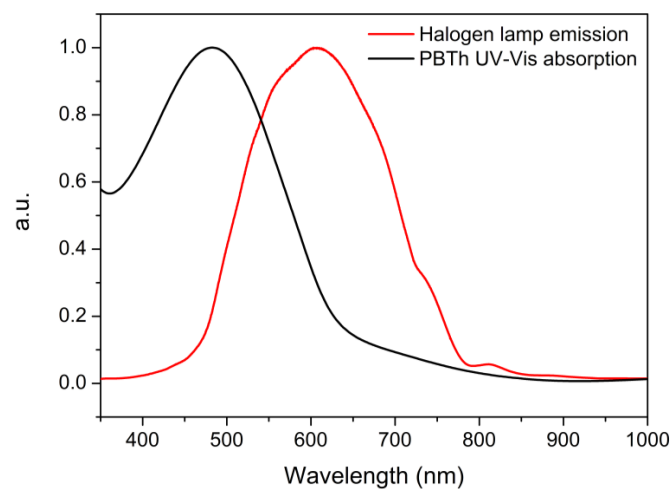

Figure S1: UV-Vis absorption spectrum of PBTh as compared to the spectral emission of the halogen lamp; the spectra has been normalised.

Figure S2: Raman spectrum of VPP PBTh film on glassy carbon showing the characteristic peaks of PBTh, i.e. conjugated coordinate mode at 1505 cm^{-1}, C=C symmetric stretching at 1463 cm^{-1}, in-plane C–C stretch at 1225 cm^{-1} and in-plane C–H bending at 1052 cm^{-1}. Obtained using a 488 nm diode laser at 0.3 mW.

**Electrochemistry, gas chromatography and setup**

Electrochemical tests were conducting using two setups. For preliminary analysis via cyclic voltammetry, a plastic cell was used with a standard calomel reference electrode (SCE, E_0 = 0.241 V vs SHE) reference electrode and was purged using N_2. For subsequent gas chromatography and electrochemistry measurements, a custom designed metal cell with a Ag/AgCl reference electrode (E_0 = 0.222 V vs SHE) was utilised (figure 1 of main article) with bubbled Ar. This set-up was specifically designed to reduce the escape of gaseous H_2 and allow for better GC detection limits. In general a scan rate of 5 mV s^{-1} between -1.1 V and 0.6 V vs Ag/AgCl was used in the metal cell. For ease of reference, all voltages presented are given vs SCE unless otherwise stated. In both cells, a 0.1 mol L^{-1} phosphate buffer of pH 6.9 was used as the electrolyte.
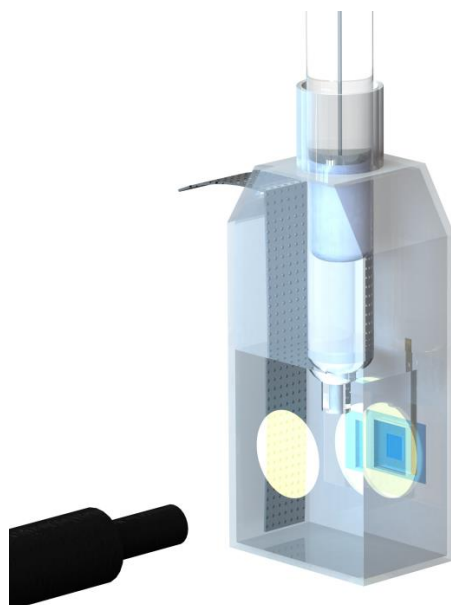
Figure S3: Experimental setup of the plastic cell.

Prior to the experiment, the solution was first purged with Ar to remove oxygen which is a major contaminant and is evident by the presence of a large reduction tail occurring at -0.4 V and 0.2 V vs SCE for dark and illuminated films respectively, fig S3. This effect presents interesting applications for fuel cells, but in this case, the reaction presents an unwanted side-reaction. Once oxygen free (observed from a clean background), the dark CV trace was recorded followed by the application of light and the recording of the illuminated CV trace. If GC was required, a CA experiment holding at -0.5 V vs Ag/AgCl was then performed.
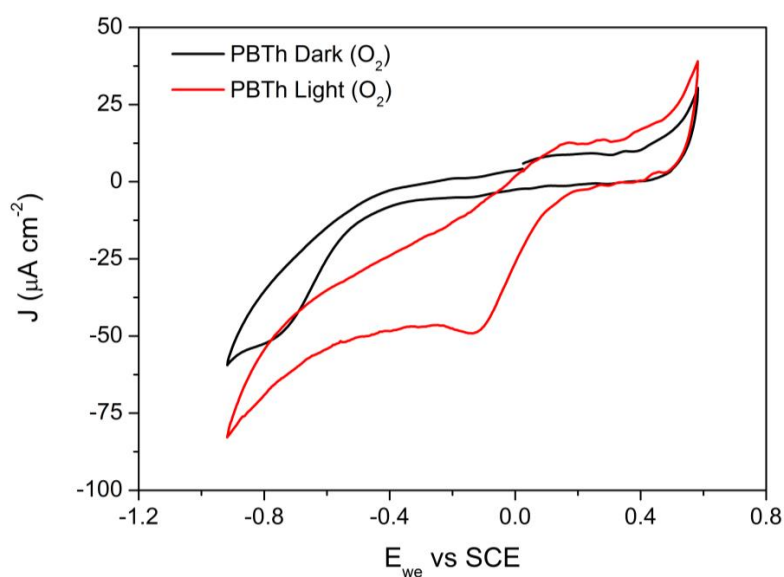
Figure S4: CV of PBTh showing the prominent oxygen reduction tail in both light and dark traces prior to purging with Ar.

GC spectra were acquired by purging the cell by bubbling with argon (0.15 mL min^{-1}) and then sampling the gas stream by injecting a fixed volume into the GC. The dark GC injection was first conducted after holding the -0.5 V vs Ag/AgCl potential for 90 minutes, after which the light was switched on. The light GC injection was then done 90 minutes after the initial illumination of light (whilst holding at -0.5 V vs Ag/AgCl). The resulting GC trace was analysed using Micromath Origin 7. Typically, an automatic baseline correction utilising the "entire data w/smooth" function was undertaken followed by the recording of the H$_2$ peak height. The H$_2$:Ar % was determined using this peak height and comparison to a calibration curve (R^2 = 0.998).

Roughness measurements

Roughness measurements were obtained using a Veeco Dektak 150 profilometer and associated software (Dektak Version 9.3). R_a is used as a measurment of roughness that describes the arithmetic mean deviation away from the mean line and is calculated using

$$R_a = \frac{1}{L} \int_0^L |y(x)| \, dx$$

where L = evaluation length and |y(x)| = the absolute vertical distance away from the mean line. Larger R_a values correspond to a rougher surface. SEM images utilising a FEI Nova NanoSEM 450 were also acquired for a visual comparison on surface morphology (figure S5).
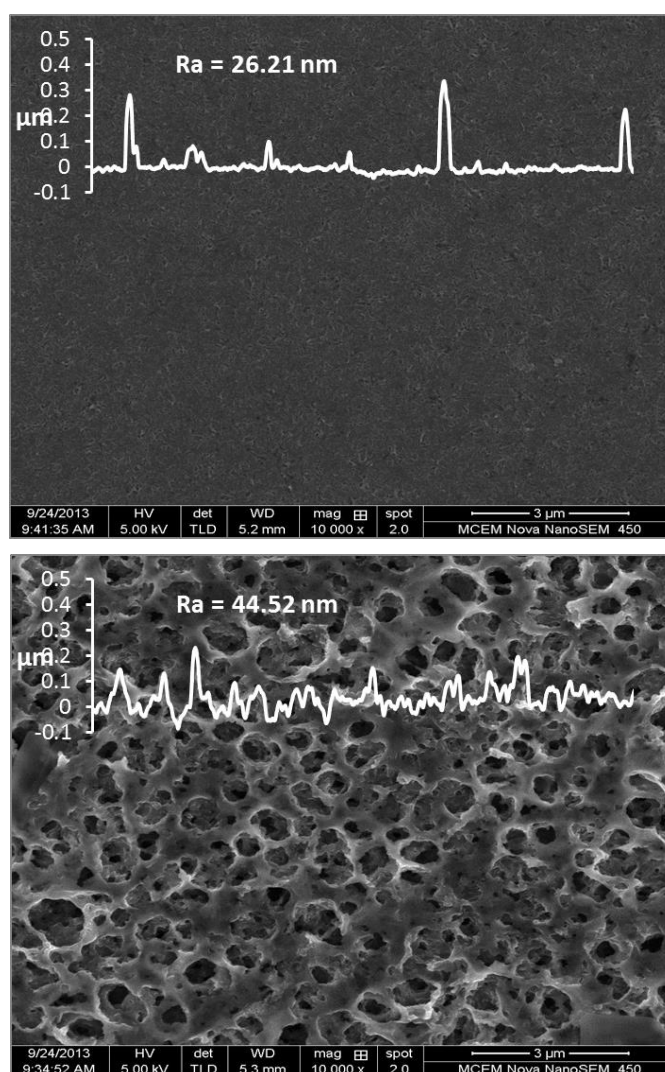
Figure S5: SEM image of a smooth (top) and a rough (bottom) film and their associated profilogrammes that were used to calculated R_a.

Contamination investigations

Long term electrochemical testing showed no decrease in reduction current over a period of 8 hours.
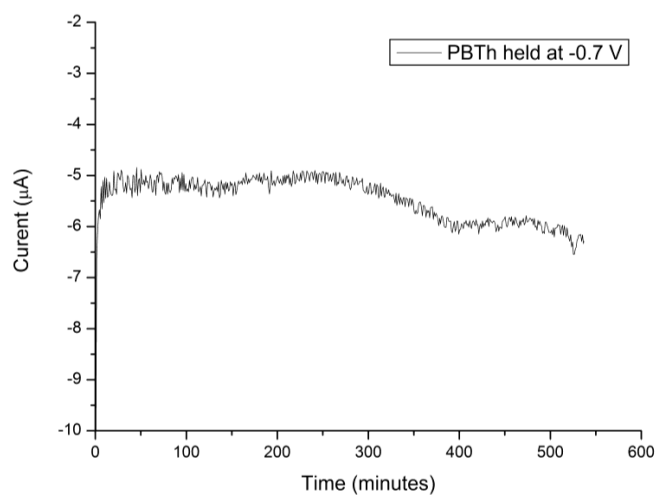
Figure S6: Long term chronoamperometry test (held at -0.7 V vs SCE) on PBTh in 0.1 mol L^{-1} phosphate buffer, pH 6.9; with bubbled N$_2$.

EDX (using a Bruker X-Flash Silicon Drift type EDS detector) was then performed on the smooth PBTh sample to further confirm the absence of contaminants (figure S7).
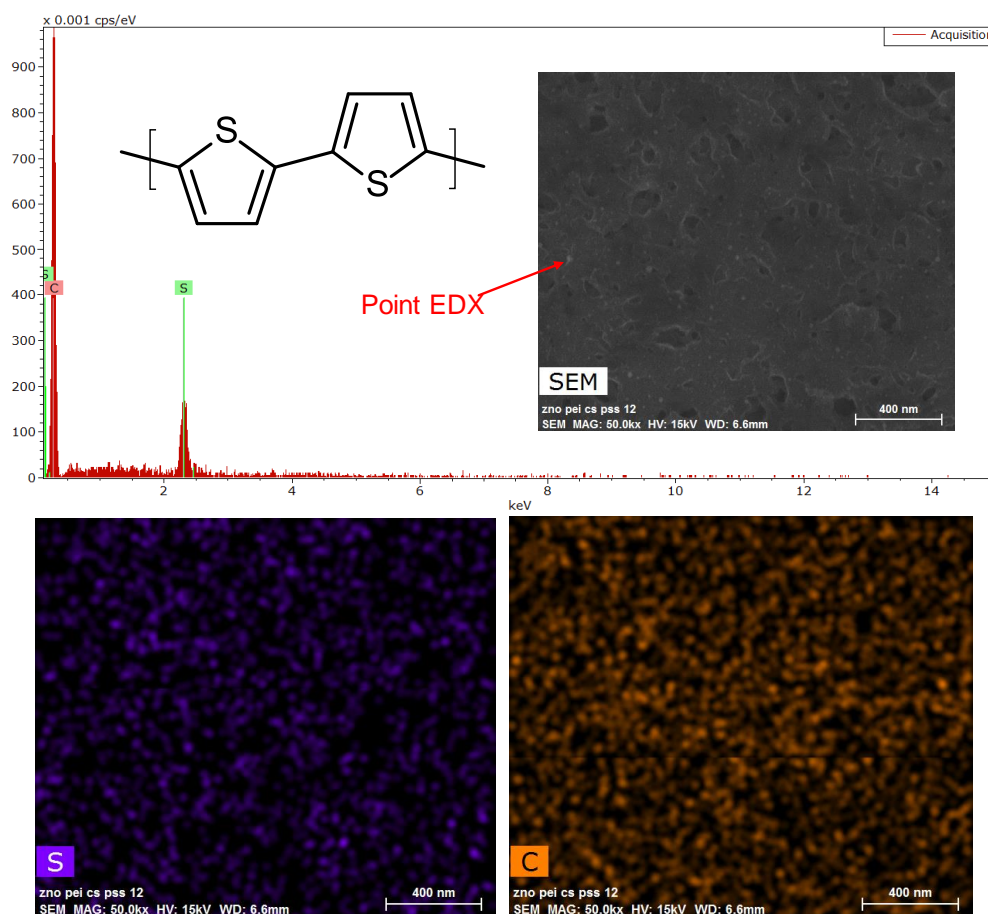
Figure S7: (Top) Point EDX spectrum with chemical structure of PBTh; insert: SEM micrograph of the smooth PBTh film used for EDX measurements. (Bottom) False-colour SEM micrographs of the smooth PBTh film showing the surface morphology and absence of contaminating species.

Appendix C: Miscellaneous Supporting Information for the Thesis, Calibration and Background Data

Supplementary Cyclic Voltammetry

Alternative Redox Species

The photo-catalytic effect of PEDOT and PEDOT:Brilliant Blue films on alternative redox species were also trialled in the initial investigations of Chapter 3. It was hoped that with the application of light, a shift in the onset potential would be obtained. However, this was not observed, nor did it reveal promising leads for the pursuit for further studies.
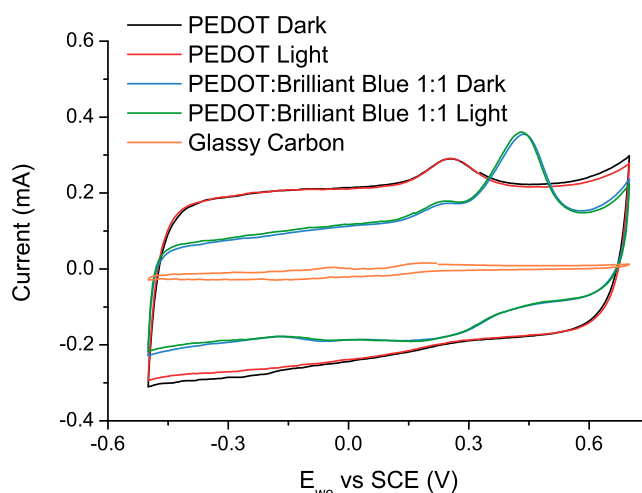

Figure S1: The CV of PEDOT and PEDOT:Brilliant Blue films in $0.17\,\mathrm{mmol\,L^{-1}}$ $FcPF_6$ in $0.1\,\mathrm{mol\,L^{-1}}$ NaPTS at $5\,\mathrm{mV\,s^{-1}}$ under N_2. The redox peak of $FcPF_6$ can be seen $\approx 0.2\,\mathrm{V}$ vs SCE but not photo-effect was observed.
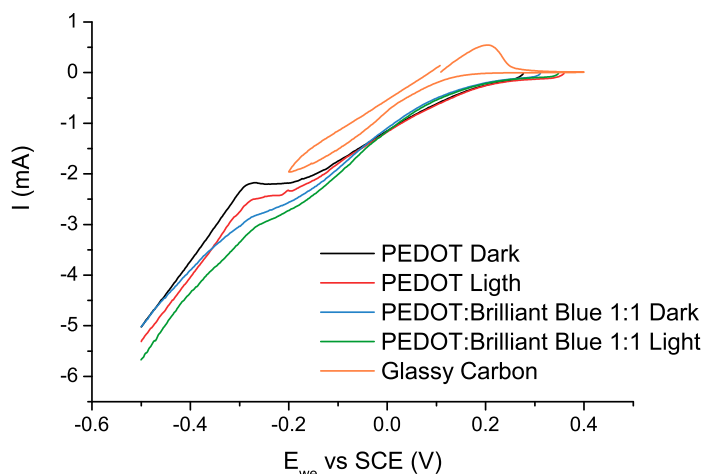
Figure S2: The CV of PEDOT and PEDOT:Brilliant Blue films in aqueous $0.25\,\mathrm{mmol\,L^{-1}}$ $CuCl_2$ (pH 4) at $5\,\mathrm{mV\,s^{-1}}$ under N_2. The reduction and deposition of Cu meant that only the first cycle showed meaningful data. There was a small increase in current with light, but the important shift in E_{onset} was absent.

Characterisation of Conducting Polymers

In order to determine the band energies of conducting polymers, CV of PTTh, PBTh and PEDOT was performed in propylene carbonate. These experiments were conducted by Mr David Mayevski and utilised for analysing conducting polyer/dye blend compatibilities, Chapter 3.
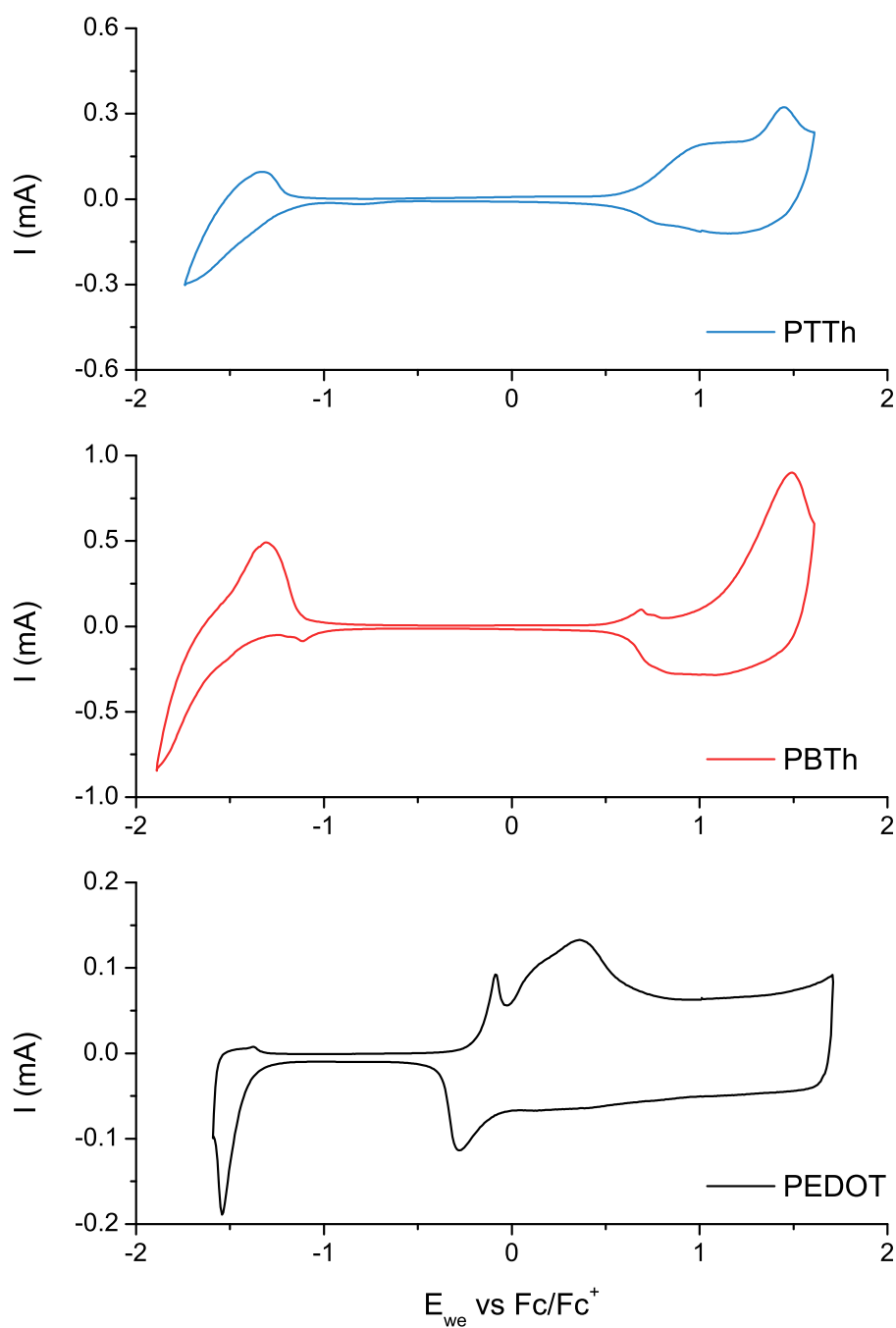
Figure S3: The CV of PTTh, PBTh and PEDOT in propylene carbonate ($0.1 \, mol \, L^{-1}$ TBA PF$_6$) at $25 \, mV \, s^{-1}$ under N$_2$ showing their oxidation (p-doping) and reduction (n-doping) regions.

Substrate Backgrounds

The substrate backgrounds have been presented throughout the thesis though perhaps not obviously so. For clarity, a selection of CVs and CAs are presented showing the background signal from our substrates. Among the most important is glassy carbon which is presented in Figure S4 and shows inertness under the standard operating conditions. Furthermore, the application of light shows no photo-response (Figure S4B); the small reduction current can be attributed to residual O_2 present in the system.
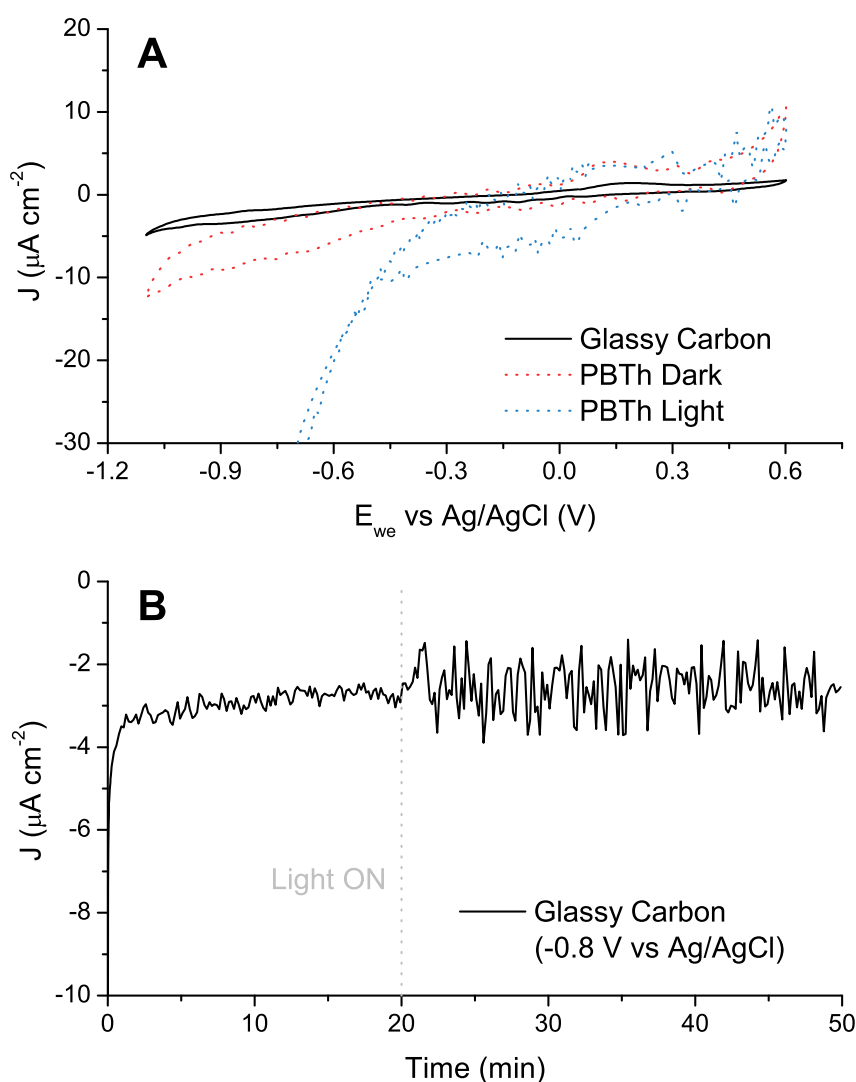
Figure S4: Electrochemical experiments showing the inertness of the glassy carbon substrate in the metal cell, conducted in $0.1\,\mathrm{mol\,L^{-1}}$ PB (pH 7) and under N_2. **A:** The CV results of glassy carbon at a scan rate of $20\,\mathrm{mV\,s^{-1}}$, covering the potential range of 0.6—$1.1\,$V vs Ag/AgCl; a sample PBTh CV is also presented for comparison. **B:** CA results on glassy carbon whilst held at $-0.8\,$V vs Ag/AgCl, light was turned on a t = 20 min.

The background CV of FTO glass is also shown and shows a relatively clean voltammogram. A small redox couple is observed at $-0.5\,V$ and this is attributed to the reduction of phosphate ions in the electrolyte. This was occasionally seen in the films though it is unclear what brings this on. It should be noted that these tests were conducted in slightly alkaline conditions (pH 8.5), nevertheless the results remain applicable in showing the inertness of FTO glass.
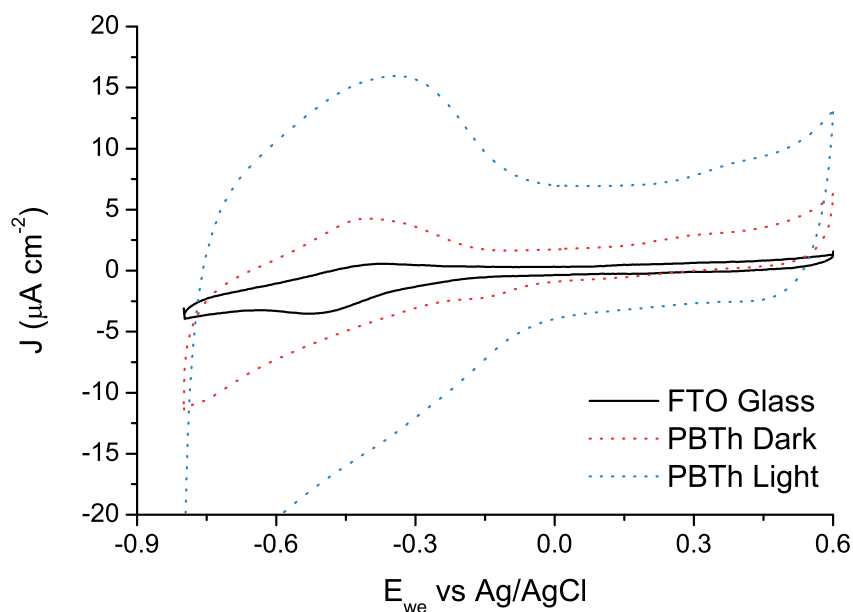
Figure S5: CV on the FTO substrate in the metal cell showing inertness when compared to PBTh films on FTO. The CV was conducted in $0.1\,mol\,L^{-1}$ PB (pH 8.5) and under N_2 at a scan rate of $20\,mV\,s^{-1}$.

Calibration of the Leica KL2500 Halogen Lamp

The calibration of the Leica Lamp was initially conducted using a small Si chip by Dr Bartlomiej Kolodziejczyk and presented in Figure S6; where a photocurrent of 760 mA was equivalent to 1 sun. For our purposes, a light level of "lvl4" (equivalent to a setting of 4E) at a distance of ≈ 2 cm was used and is highlighted.

Date:	25.08.2011		Device name:		Leica KL 2500 LCD #2							
light level	μA at distance to the working electrode [cm]				Suns at distance to the working electrode [cm]				W/m² at distance to the working electrode [cm]			
	1	2	5	10	1	2	5	10	1	2	5	10
lvl1	1060	355	68	17	1.39	0.47	0.09	0.02	1390	466	89	22
lvl2	1560	541	103	26	2.05	0.71	0.14	0.03	2046	710	135	34
lvl3	2200	800	156	39	2.88	1.05	0.20	0.05	2885	1049	205	51
lvl4	2520	1147	222	56	3.30	**1.60**	0.29	0.07	3305	1604	291	73
lvl5	2670	1897	370	93	3.50	2.49	0.49	0.12	3502	2488	485	122
lvl6	2750	2263	481	120	3.61	2.97	0.63	0.16	3607	2968	631	157

**Figure S6:** The photo-intensity calibration results of the Leica KL2500 halogen lamp using a Si chip.

The highlighted value of 1.6 suns was commonly reported and used throughout the earlier sections of the studies. However, later on, the actual lamp intensity was found to be heavily dependent on each individual bulb's spectral output, the age of the bulb, the brand and the even the lamp used. Furthermore, the small size of the Si chip ($\approx 0.1 \, \text{cm}^2$) used for the initial calibration meant it was highly susceptible to directionality, where even a small tilt of a few degrees would dramatically alter the perceived intensity. In response to this, a much larger GaAs chip ($1 \, \text{cm}^2$) with a broader spectra response was used to recalibrate the Leica KL2500 halogen lamp intensities. These results are shown in Table S1 and the latter experiments report the photo-intensity from the Leica KL2500 lamp as 0.4 sun (when at the standard setting of 4E).

Table S1: Recalibration of the Leica KL2500 photo-intensity using a GaAs chip where 12.6 mA = 1 sun. The measurements were made across three different lamps.

| Lamp setting	Average Photocurrent (mA)	Standard Deviation of Photocurrent (mA)	Photo-intensity (sun)
1E	1.7	0.2	0.13 ± 0.02
2E	2.3	0.4	0.18 ± 0.03
3E	3.3	0.9	0.26 ± 0.07
4E	4.6	1.5	0.37 ± 0.12
5E	7.9	3.0	0.63 ± 0.24
6E	10.1	4.0	0.80 ± 0.32

H$_2$ Calibration for Gas Chromatography

The calibration of the GC was conducted by injection of a known H$_2$:Ar ratio and comparison of the height of the resulting GC peak at 2 min. The resulting calibration curve is presented in Figure S7. It should be noted that peak area is typically used for quantitative measurements but a slight oversight led to the use of the peak height. Moreover, the well fitting and linear calibration curve indicates that – while perhaps not ideal – the peak height can provide an accurate quantitative measurement.
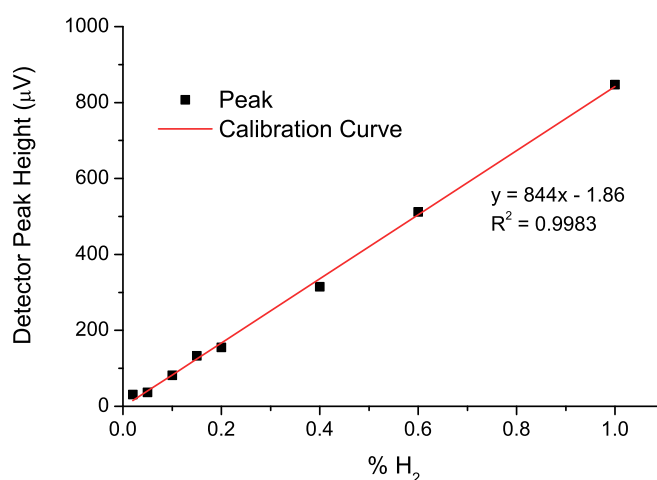
Figure S7: The calibration data of the GC with known percentages of H$_2$ in Ar.

The GC peak of H$_2$ (0.15% in Ar) with an elution time of 2 min is shown in Figure S8. The gas chromatogram of injected air show the peaks of O$_2$ and N$_2$ at 3.5 min and 6.5 min respectively.
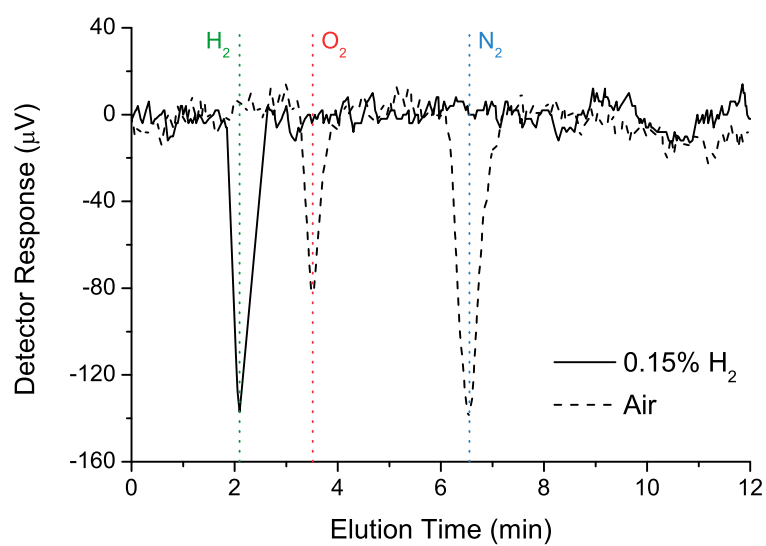
Figure S8: The gas chromatogram with the injection of 0.15% H$_2$ (solid trace) and air (dashed trace)